

Studies on Humidification of PEM Fuel Cells

Thesis Submitted to AcSIR for the Award of
the Degree of
DOCTOR OF PHILOSOPHY
In Engineering Sciences



By
Ramendra Pandey
Reg. No. 32EE14A41008

Under the guidance of
Dr. Ulhas K. Kharul and Dr. Ashish K. Lele

Polymer Science and Engineering Division
CSIR-National Chemical Laboratory, Pune



राष्ट्रीय रासायनिक प्रयोगशाला
(वैज्ञानिक तथा औद्योगिक अनुसंधान परिषद)
डॉ. होमी भाभा मार्ग पुणे - 411 008. भारत
NATIONAL CHEMICAL LABORATORY
(Council of Scientific & Industrial Research)
Dr. Homi Bhabha Road, Pune - 411 008. India.



Certificate

This is to certify that the work incorporated in this Ph.D. thesis entitled "Studies on Humidification of PEM Fuel Cells" submitted by Mr. Ramendra Pandey to Academy of Scientific and Innovative Research (AcSIR) in fulfillment of the requirements for the award of the Degree of Philosophy in Engineering Sciences, embodies original research work under our supervision. We further certify that this work has not been submitted to any other University or Institution in part or full for the award of any degree or diploma. Research material obtained from other sources has been duly acknowledged in the thesis. Any text, illustration, table etc., used in the thesis from other sources, have been duly cited and acknowledged.

It is also certified that this work done by the student, under my supervision, is plagiarism free.

Ramendra Pandey
(Student)

Dr. Ulhas K. Kharul
(Supervisor)

Dr. Ashish K. Lele
(Co-Supervisor)

Declaration by the Candidate

I hereby declare that the thesis entitled **“Studies on Humidification of PEM Fuel Cells”** submitted by me for the Degree of Doctor of Philosophy to Academy of Scientific & Innovative Research (AcSIR) is the record of work carried out by me at Polymer Sciences & Engineering Division (PSE), CSIR- National Chemical Laboratory, Pune - 411008, India, under the supervision of Dr. Ulhas Kharul and Dr. Ashish Lele. The work is original and has not formed the basis for the award of any degree, diploma, associateship and fellowship titles in this or any other university or other institute of higher learning. I further declare that the material obtained from other resources has been duly acknowledged in the thesis.



Ramendra Pandey
AcSIR ID: 32EE14A41008

April 2019

Polymer Science & Engineering Division
CSIR-National Chemical Laboratory
Dr. Homi Bhabha Road, Pashan
Pune – 411008
Maharashtra, India

Synopsis

Introduction

Proton exchange membrane (PEM) fuel cell is an electrochemical energy conversion device which converts chemical energy of hydrogen into electrical energy via redox reactions. The Pt/C (Platinum on carbon) catalyst layers at anode and cathode facilitate oxidation of hydrogen and reduction of oxygen, respectively. These catalyst layers are separated by an ion-exchange membrane. Besides acting as an electrical insulator thereby preventing shorting of the fuel cell, the main purpose of this membrane is to allow protons to migrate selectively from anode to cathode without allowing the gaseous reactants to diffuse across. Such membranes are typically made of Nafion, which is a sulfonated polytetrafluoroethylene (PTFE) random co-polymer. The co-polymer consists of PTFE backbone and pendant side chains each ending in a sulphonate (SO_3^-) group. The dissimilar nature of the covalently bonded pendant group and backbone chain results in microphase separation, which is enhanced by solvation (uptake of water or solvent molecules). The microphase separated morphology comprises micelles, which upon water uptake self-assemble into an inter-connected network of nanochannels comprising solvated sulfonic acid groups and water molecules. The sulphonate groups are responsible for water retention and transport in the membrane [1]. This phase-separated morphology gives Nafion its unique ion and solvent transport properties [2].

The hydration of Nafion membranes is achieved partially by water generated at the cathode because of the oxygen reduction reaction. However, it is often observed that the water generated at the cathode is insufficient for optimal hydration of the membrane because of the water lost due to convective evaporation on the cathode, thereby resulting in lower fuel cell performance [3]. Therefore, a common practice is to externally humidify the feed gases supplied to PEM fuel cell using humidification devices such as bubble humidifier, membrane humidifier, evaporators etc. Among these, membrane humidifiers due to their large surface area, compactness and easy-to-use module setup, are the most popular choice for fuel cell humidification. Other methods include passive humidification of cells using novel techniques based on the principle of evaporative cooling such as wicks, direct liquid water injection, porous water transport plates

etc. In any case, achieving optimum humidification is critical for water management in PEM fuel cells and its durable performance. In this work, we have focused on membrane humidifiers in the class of active humidification methods and wick based humidification in the class of passive humidification methods.

Statement of Problem, Aim and Objectives

While there is myriad literature on membrane humidifiers and passive humidification methods for PEM fuel cells, there are several important lacunae which have remained unaddressed. These are:

- i) comprehensive understanding of mechanisms involved in membrane (both porous and non-porous) based gas humidification
- ii) rigorous experimental validation of models developed for heat and mass transport in membranes
- iii) poor pressure tolerance and high cost of dense membrane humidifiers
- iv) dry-feed operation of PEM fuel cell using passive humidification technique for large active areas.

The aim of this thesis is to address these lacunae. Specifically, the work presented in this thesis is aimed at contributing to the field of membrane technology and PEM fuel cells by delineating the following research objectives covering both active and passive methods of humidification.

Research objectives and methodology:

1. Understanding gas humidification through dense membranes. The methodology for achieving this objective includes:
 - 1.1. Mathematical modelling of water-to-gas hollow fiber membrane humidifier and
 - 1.2. Validation of model with experimental results on commercial scale Perma Pure humidifier
2. Developing cost effective (up to 5 – 10 folds cost reduction from commercial benchmark humidifier) hollow fiber membranes for gas humidification. The methodology for achieving this objective includes:
 - 2.1. Developing polysulfone based asymmetric hollow fiber membranes for gas humidification.

- 2.2. Characterizing the hollow fiber membranes for microstructure elucidation.
- 2.3. Mathematical modelling of water-to-gas asymmetric hollow fiber membrane humidifier
- 2.4. Validation of model with experimental results on developed humidifiers.
- 3. Understanding maldistribution of flow inside hollow fiber membrane humidifier. The methodology for achieving this objective includes:
 - 3.1. Flow simulations using COMSOL multi-physics CFD tool.
 - 3.2. Studying the effect of tube symmetry and header geometry on flow distribution.
- 4. Investigate wick based passive humidification technique for water management in PEM fuel cells under dry-feed operation. The methodology for achieving this objective includes:
 - 4.1. Characterizing carbon cloth for its feasibility to be used as a wicking material.
 - 4.2. Testing single cell with a hydrophilic carbon cloth over the MEA extending out of the cell and dipping in a water reservoir to facilitate wicking action.
 - 4.3. Testing different configurations of fuel cell with wick.
 - 4.4. Electrochemical impedance measurements for comparison of different configurations with control experiments without wick.

Key findings of the research work

The work presented on membrane humidifiers in this thesis is a combination of analytical theory, numerical simulations and experimental investigations. The summary and key results of each of the major working scheme is provided below.

Scheme-1: Mathematical modelling of gas humidification using dense nafion membranes

This work focusses on improving the understanding of the mechanisms involved in water-to-gas membrane humidification using dense membranes. It presents a quasi-2D model for water-to-gas hollow fiber membrane humidifier and its validation with experiments performed on commercial Perma Pure FC200 humidifier module. The model takes into account the relevant phase equilibria along with coupled heat and mass transport across dense Nafion hollow fiber membranes. The model is shown to predict the humidifier performance within 8 % deviation from the experimental results.

Scheme-2: Experimental and theoretical investigations on polysulfone based membrane humidifiers

This work focusses on developing cost effective polysulfone asymmetric membranes which can be used for gas humidification over more expensive dense Nafion membrane-based humidifiers. It presents experimental and theoretical investigations of polysulfone based asymmetric hollow fiber membranes. The experimental section includes development of polysulfone based hollow fiber membranes, their characterization and humidification performance tests. The humidification performance was found to decrease with increasing polymer concentration. Membranes developed from polymer concentration of 27 % were shown to provide high humidification performance without any flooding or entrainment issues. A mathematical model based on resistance-in-series approach is proposed for these membranes and is shown to fit the experimental observations in humidification tests. It is found that in asymmetric membranes, the skin and bulk resistances govern the mass transport whereas heat transport is limited by the interfacial resistance. Membranes made from 27 wt % polymer concentration are found to work comparably with bubble humidifiers for fuel cell operation.

Scheme-3: Flow behavior inside humidifiers using CFD simulations

This work presents a computational fluid dynamics study on flow behavior inside humidifier module. The effect of symmetry in tube arrangement inside the humidifier module helps provide relevant design guidelines for minimizing flow maldistribution in tubes. Further, shell side flow simulations based on current humidifier design provide suggestions for reducing the dead volume inside humidifier. On tube side, a perfectly symmetric tube arrangement along with a small truncated conical header is observed to show uniform flow distribution. On shell side, a dead volume zone is developed near the inlet/outlet ports because of the current design. It is therefore suggested to have the inlet and outlet ports on the end caps to reduce the dead volume.

Scheme-4: Wick based passive humidification of PEM fuel cells.

This work focusses on reducing parasitic power loss in PEM fuel cell operation by providing passive means of fuel cell hydration and dry-feed operation. It presents a novel wick based

internal humidification technique for low temperature PEM fuel cells. The technique leverages on hydrophilic carbon cloth as a wick placed over the MEA for passive water transport inside the cell without external aid of membrane humidifiers. Configurations with wick placed over anode (Configuration-B) or cathode (Configuration-C) were shown to have performance comparable with a fuel cell operated with external humidifiers on both sides.

References

- [1] A. Kusoglu, A.Z. Weber, New Insights into Perfluorinated Sulfonic-Acid Ionomers, *Chem. Rev.* 117 (2017) 987–1104. doi:10.1021/acs.chemrev.6b00159.
- [2] A. Dicks, J. Larminie, *Fuel Cell Systems Explained*, 2003. doi:10.1002/9781118878330.
- [3] J. Zhang, H. Zhang, J. Wu, J. Zhang, *Pem Fuel Cell Testing and Diagnosis*, 2013. doi:10.1016/B978-0-444-53688-4.00007-3.

Acknowledgement

It is my extreme pleasure to be acknowledging the contributions of some wonderful people to my PhD journey without whom the time spent at CSIR-NCL would be extremely mundane. Often the key moments which bring out some key insights and help you move forward during a PhD are spent on brainstorming with your mentors, friends, colleagues and sometimes with family as well. I also went through a similar journey. Although I must confess my journey was a little less stressful, thanks to my supercool advisor and my PhD mate Aniket Thosar who went through the highs and lows along with me.

First and foremost, I would like to extend my sincerest gratitude to all my secondary and higher secondary school teachers for laying a strong foundation for me to be a good student in life. Without that foundation, I may not have chosen this path.

I am forever indebted to my co-supervisor Dr. Ashish Lele, for all his help, support and guidance with minimal supervision at both professional and personal levels. His way of mentoring has clearly helped me become more independent and confident in taking decisions and approaching a problem. The time spent with him, be it serious hours spent in meetings, casual discussions over coffee or over several lunches/dinners that he sponsored, were truly the most intellectually enriching times of my PhD. Besides his knowledge on almost everything, I also admire his supercool and humble nature. I would also like to thank my supervisor Dr. Ulhas Kharul for giving me an opportunity to learn about membrane technology in his excellent lab at CSIR-NCL. His experience on membranes made my life easy and helped me finish my experimental work in minimum time. I also thank him for being patient with me despite my several mistakes. I also extend my gratitude to my DAC members Dr. Ashish Orpe, Dr. Santoshkumar Bhat, and Dr. Ashok Giri for continuous evaluation of my research work.

I would like to thank Council of Scientific and Industrial Research (CSIR), India for providing research fellowship. I acknowledge CSIR-National Chemical Laboratory, Pune for providing infrastructure for carrying out research.

I would like to thank my chemical engineering course instructors, Dr. Ashish Orpe, Dr. Amol Kulkarni, and Dr. Rajnish Kumar, who helped get my basics right and advance my knowledge of chemical engineering. I am extremely grateful to them for their lectures which have clearly improved my understanding of key chemical engineering subjects. I am also extremely grateful to Dr. K. Guruswamy who has taken teaching to a whole another level at NCL. The amount of efforts that he puts in teaching and improving students is truly commendable. I also thank him for his excellent support to all the student driven activities like Research Discussions Forum, NCL-Technology and Entrepreneurship Club, Macromet and many formal and informal requests that he had patiently agreed to.

Being involved with NCL-TEC has been a major positive of my PhD for my all-round development. My association with NCL-TEC would not be possible without the initiative by Dr. V. Premnath. I am extremely grateful to him and Venture Center for hosting this exciting club and giving innumerable opportunities to students to expand their horizons beyond their routine PhD work. I thank my dynamic NCL-TEC team Aniket, Pravin, Indravadan, Vishwanath, Emmanuel and Meenakshi for volunteering and conducting so many events together. Organizing the events together definitely made learning so much fun. I would also like to thank Dr. Magesh Nandagopal for his support to NCL-TEC and to me at a professional level. I would always keep the lessons learned from his professional development workshop while navigating my workspace in my career. I will always remain grateful to the efforts that Dr. Premnath, Dr. Guruswamy and Dr. Magesh had put for the betterment of the students at NCL. I was lucky to be associated with all of them. The support received from Dr. Chetan Gadgil, Dr. Kumar Vanka, Dr. B.L.V. Prasad, Dr. Amol Kulkarni, Dr. M.V. Badiger, Dr. Anuya Nisal, and Prof. Ashwini Kumar Nangia also need to be acknowledged. I thank them for their support and encouragement to NCL-TEC and the student community at NCL.

I am extremely thankful to my NCL mates Aniket, Ajinkya and Harshal Agarwal for all the fun times keeping the stress at bay. Special thanks to Aniket for all the brainstorming sessions in D-103 and J-119. A lot of credit goes to Aniket for technically correcting me when I was wrong. I have really learnt a lot from him. I thank my J-wing mates Aakash, Bipul and Karthika, and other lab mates Indravadan, Amruta, Krishnaroop and Sameer for fun pass times and several

brainstorming sessions. I would also like to thank my membrane lab mates Supriya, Anita, Anand, Sayali, Harshal, Shebeeb, Vijay, Harsha, Nishina, Varsha, and Kiran with whom I conducted experiments and had fun. Special thanks to Shebeeb and Harshal for extending help beyond lab work. I had a memorable one year spent at the membrane lab.

I would also like to thank my mentors at the CSIR-CEERI and CSIR-CECRI units at Chennai, Dr. Balaji Rao, Dr. P. Sridhar, Dr. Bala Pasela, Dr. S. Subba Rao and Dr. Santoshkumar Bhat, for their never-ending support and encouragement. I also am extremely thankful to my 8-variables group (Anand, Meraj, Sreeja, Harshal, Balakrishna, Ashok, Shubhangi) and Shatabdi for the three wonderful years spent at CSIR-SERC for the Renewable Energy program.

Lastly and most importantly, I am grateful to the grace of God and Guru which has motivated me to improve myself along this journey. I also thank my world-best sister Priya and my parents for their love and affection.

Ramendra Pandey

15th April 2019

Table of Contents

Chapter 1: Introduction

1.1. Gas Humidification.....	1
1.2. Strategies for gas humidification	1
1.2.1. Direct methods	1
1.2.1.1. <i>Bubble column</i>	1
1.2.1.2. <i>Simple reservoir humidifiers</i>	2
1.2.1.3. <i>Liquid water injection</i>	3
1.2.2. Indirect methods.....	3
1.2.2.1. <i>Wick humidifier</i>	3
1.2.2.2. <i>Ultrasonic nebulizer</i>	4
1.2.2.3. <i>Membrane contactors</i>	5
1.2.2.4. <i>Water permeating membranes</i>	5
1.3. Gas humidification for water management in PEM fuel cells	6
1.4. Internal humidification in PEM fuel cells	9
References	10

Chapter 2: Background

2.1. Solution-diffusion process in membranes.....	13
2.1.1. Overview	13
2.1.2. General solution-diffusion model.....	14
2.1.3. Solution-diffusion model for pervaporation	16
2.2. Dense membranes for gas humidification.....	19
2.2.1. Overview	19
2.2.2. Nafion® flat sheet and hollow fiber membranes	19
2.2.3. Water transport through Nafion® membranes	20
2.2.4. Models on membrane based gas humidification	25
2.3. Porous membranes for gas humidification	30
2.3.1. Overview	30
2.3.2. Asymmetric membranes	30
2.3.3. Asymmetric membranes for gas humidification.....	33

2.3.4. Models on asymmetric membrane based gas humidification	36
2.4. Internal humidification in PEM fuel cells	43
2.4.1. Overview	43
2.4.2. Water management in PEM fuel cells	44
2.4.3. Internal humidification with evaporative cooling techniques in PEM fuel cell	45
2.4.3.1. <i>Liquid water injection into the fuel cell</i>	46
2.4.3.2. <i>Porous water transport plates</i>	46
2.4.3.3. <i>Wicks as lands or channels</i>	47
2.5. Research Objectives	50
2.6. Thesis structure	51
References.....	53

Chapter 3: Modelling of Water-to-Gas Hollow Fiber Membrane Humidifier

3.1. Introduction	61
3.2. Model	64
3.3. Results and Discussion	76
3.3.1. Liquid-Vapor Permeation (LVP).....	76
3.3.2. Model Validation.....	79
3.3.3. Non-dimensional analysis	82
3.3.4. Quantification of resistances to heat and mass transfer	86
3.3.5. Effect of flow configuration	87
3.3.6. Effect of geometric parameters	89
3.4. Conclusions	93
Appendix A:	94
Appendix B:	94
Nomenclature	96
References	97

Chapter 4: Experimental Investigation and Modelling of Asymmetric Hollow Fiber Membranes for Gas Humidification

4.1. Introduction	102
4.2. Experimental	105

4.2.1. Materials	105
4.2.2. Preparation of spinning dope	105
4.2.3. Spinning of hollow fibers	105
4.2.4. Preparation of hollow fiber membrane modules	106
4.2.5. Field emission scanning electron microscopy (FE-SEM) of hollow fiber membranes	108
4.2.6. Water flux and entrainment tests.....	108
4.2.7. Bubble point, pore size distribution and membrane porosity tests	109
4.2.8. Measuring humidifier performance.....	110
4.3. Mathematical model.....	111
4.4. Results and discussion	120
4.4.1. Membrane Microstructure	120
4.4.2. Quantification of porosity.....	123
4.4.3. Estimating resistance for transport of moisture through porous microstructure	127
4.4.4. Bubble point and pore size distribution analysis.....	128
4.4.5. Water flux and entrainment	132
4.4.6. Humidifier performance: Effects of air flow rate and membrane type.....	133
4.4.7. Humidifier performance: Effects of water temperature and water flow rate	135
4.4.8. Effect of tube length and tube number	138
4.4.9. Comparison of humidifier performance with literature	143
4.5. Conclusions	144
Nomenclature	146
Appendix A.....	148
Appendix B	150
References	152

Chapter 5: Flow Distribution in Humidifiers Using Flow Simulations

5.1. Introduction	159
5.2. CAD models.....	160
5.3. Governing Equations.....	163
5.4. Simulation Methodology	163
5.5. Results and Discussion	165
5.5.1. Effect of symmetry on tube flow distribution	165
5.5.2. Effect of header design	168

5.5.3. Effect of symmetry on shell flow distribution.....	169
5.6. Conclusions	171
References	172

Chapter 6: Internal Humidification in PEM Fuel Cells Using Wick Based Water Transport

6.1. Introduction	173
6.2. Experimental	177
6.2.1. Determination of pore size, permeability, contact angle and thermal stability.....	177
6.3. Results and Discussion	183
6.3.1. Determination of pore size, permeability, contact angle and thermal stability of wicking material	183
6.3.2. Theoretical calculation for water uptake from capillary action of wick	185
6.3.3. Polarization curves.....	188
6.3.4. Effect of air stoichiometry on wicking action	191
6.3.5. Electrochemical impedance spectroscopy (EIS) measurements	194
6.4. Conclusions	201
References	202

Chapter 7: Conclusions and Future Scope

7.1. Membrane-based active humidification	208
7.1.1. Dense hollow fiber membranes.....	208
7.1.2. Asymmetric hollow membranes	210
7.1.2.1 <i>Model development for asymmetric membrane humidifiers</i>	212
7.1.2.2 <i>Flow distribution in HFM humidifiers</i>	214
7.2. Wick-based passive humidification	215
7.3. Future Scope	216
7.3.1. Dense Nafion™ hollow fiber membrane humidifier	216
7.3.2. Asymmetric polysulfone membrane humidifier	217
7.3.3. Wick based passive humidification	219
References	219
List of Publications	221

List of Figures

Fig. 1.1. Bubble column humidifier.....	2
Fig. 1.2. Simple reservoir humidifier.....	2
Fig. 1.3. Liquid water injection	3
Fig. 1.4. Wick humidifier	4
Fig. 1.5. Ultrasonic nebulizer	4
Fig. 1.6. Membrane contactor	5
Fig. 1.7. Water permeating membranes	6
Fig. 1.8. Cluster network model	7
Fig. 1.9. Effect of humidity on fuel cell performance.....	8
Fig. 1.10. Hollow fiber membrane humidifier.....	9
Fig. 2.1. Solution-diffusion process in membranes	14
Fig. 2.2. Pressure-driven permeation of a one-component solution through a membrane according to solution-diffusion model	15
Fig. 2.3. Membrane water content as a function of (a) water activity (b) temperature in vapor and liquid equilibrium and (c) equilibrium time and temperature	21
Fig. 2.4. Resistance to steady-state water transport in the membrane as a function of membrane thickness showing the mass-transport resistance at the interface	23
Fig. 2.5. Measured flux with respect to chemical potential gradient for various permeation cases: liquid-liquid permeation (LLP), vapor-vapor permeation (VVP) and liquid-vapor permeation (LVP).....	24
Fig. 2.6. Variation of physical properties of air with temperature and humidity	26
Fig. 2.7. (a) Spinning process (dry-wet phase inversion) for hollow fiber membranes (b) typical asymmetric hollow fiber membrane.....	32
Fig. 2.8. Typical asymmetric flat sheet membrane	33
Fig. 2.9. (a) SEM cross-section image of PES hollow fiber (b) Outlet gas relative humidity as a function of liquid velocity and gas flow rates	34
Fig. 2.10. Relative humidity (RH %) of outlet gas for different membranes in various gas flow rate of 60, 120 and 180 L/h	35

Fig. 2.11. Effect gas flow rate on (a) water vapor concentration in outlet stream and (b) average mass transfer rate of water. Temperature 25 °C. Symbols represent experimental data, and the solid lines are calculated values based on the cross flow model.....	36
Fig. 2.12. (a) SEM cross-section image of PVDF flat sheet membrane (b) water vapor concentration profile across the membrane	38
Fig. 2.13. (a) Schematic illustration of an enthalpy exchanger system (b) Zoomed image of the flow channels and membrane unit inside the enthalpy exchanger (c)SEM image of the membrane cross-section, (d) Schematic representation of the heat and moisture transfer through the asymmetric composite membrane.....	39
Fig. 2.14. a) Metallic foil used by Intelligent Energy Ltd. and b) Plate design used by Intelligent Energy Ltd.....	46
Fig. 2.15. Schematic of PEMFC with WTPs allowing liquid water exchange	47
Fig. 2.16. Wick material a) as lands or b) placed over channels of the cathode bipolar plates	48
Fig. 2.17. Porous fiber channels for water transport	50
Fig. 2.18. Schematic illustration of the thesis overview.....	53
Fig. 3.1. Schematic representation of the model	68
Fig. 3.2. Comparison of sorption isotherms for liquid equilibrated (LE) Nafion membranes. The filled symbols are the experimentally obtained values in different studies. The hollow symbols represent maximum water concentration in the membrane when predicted by the polynomial expressions proposed for vapor equilibrated (VE) membranes ($a_w = 1$). For liquid equilibrated Nafion™ membranes, empirical expression given by Springer et al. (1991) [21] or Eq. (36) may be used.....	74
Fig. 3.3. Comparison of LVP fluxes with membrane-air interface equilibrium expressions from Monroe et al. (2007) (red lines) [31] and Springer et al. (1991) (blue lines) [21] for (a) 50 °C (b) 70 °C and (c) 80 °C...77	77
Fig. 3.4. Water flux predictions when both the membrane interface equilibrium are modelled using Eq. (8) for (a) 50 °C (b) 70 °C and (c) 80 °C	78
Fig. 3.5. Schematic representation of the test rig.....	80
Fig. 3.6. Model predictions vs. Perma Pure's data, $T_w = 40$ °C (triangles), 60 °C (squares) and 80 °C (circles).....	81
Fig. 3.7. Model validation with experiments performed on test rig with water flow rates (a) 1 lpm, (b) 2 lpm and (c) 3 lpm; , $T_w = 40 \pm 2$ °C (triangles), 60 ± 2 °C (squares) and 80 ± 2 °C (circles)	82
Fig. 3.8. Variation with respect to dimensionless tube length for (a) Dimensionless numbers (b) β with air flow rate for different water temperatures (c) outlet gas temperature and relative humidity (d) Heat transfer rate (HTR) and Vapor transfer rate (VTR) and (e) air and water mass flow rates. These calculations are shown for the reference case (PermaPure FC200-780-7LP humidifier; inlet air temperature of 25 °C relative humidity of 10 %, inlet water temperature of 60 °C, inlet air flow rate of 650 lpm and inlet water flow rate of 26 lpm).....	86

Fig. 3.9. Effect of flow configuration on (a) outlet air temperature (squares) and vapor pressure (circles) (b) mixing ratio (absolute humidity) (circles) and percentage relative humidity (squares).....	88
Fig. 3.10. Effect of tube number on (a) air outlet temperature (b) percentage relative humidity.....	89
Fig. 3.11. Effect of membrane thickness on (a) air outlet temperature (b) percentage relative humidity...	91
Fig. 3.12. Effect of tube length on (a) air outlet temperature (b) percentage relative humidity.....	91
Fig. 3.13. Effect of tube inner diameter on (a) air outlet temperature (b) percentage relative humidity..	92
Fig. 3.B1 Variation in (a) air mass flow rate and (b) water mass flow rate along the tube length for different water temperatures and counter-flow mode of operation at 10 L/min inlet air flow rate.....	95
Fig. 3.B2 Variation in (a) air mass flow rate and (b) water mass flow rate along the tube length for different water temperatures and counter-flow mode of operation at 1138 L/min inlet air flow rate.....	95
Fig. 4.1. Humidification test setup	110
Fig. 4.2. Schematic representation of (a) resistance-in-series model for asymmetric membranes (b) temperature and concentration profiles along transverse (x-) direction.....	113
Fig. 4.3. FE-SEM images of entire fiber cross-section (top row; left to right: (a1) HFM25, (b1) HFM27, (c1) HFM30), fiber thickness cross-section (second row; left to right: (a2) HFM25, (b2) HFM27, (c2) HFM30), shell-side membrane microstructure (third row; left to right: (a3) HFM25, (b3) HFM27, (c3) HFM30) and tube-side membrane microstructure (bottom row; left to right: (a4) HFM25, (b4) HFM27, (c4) HFM30).....	123
Fig. 4.4. (a) Representative images for HFM25 (a1), HFM27 (a2), and HFM30 (a3) used for image processing. The representative rectangular segment of the cross-section marked in red is used for calculations presented in Table 4.4. The zoomed-in image of macrovoids in the segment is presented as domains (1, 2, and 3) which were used for calculating areal fractions using ImageJ as shown in Table 4.5. (b) Representative micrographs for HFM25 (b1), HFM27 (b2), and HFM30 (b3) are shown with the spatial domains (marked as R_1 , R_2 , and R_3) containing macrovoids and smaller interconnected pores.....	126
Fig. 4.5. (a) Bubble point (b) IBA flux and (c) Pore size distribution of PSF hollow fiber membranes.....	130
Fig. 4.6. (a) Water flux and (b) Entrainment rate for membranes made with different polymer concentration in the dope.	132
Fig. 4.7. (a) Air outlet temperature, (b) Absolute humidity of outlet air, (c) Thermal effectiveness factor, and (d) Humidity effectiveness factor. Solid lines through the data are model fits. The Pearson's correlation coefficients (r_{25} , r_{27} and r_{30}) close to 1 suggests a positive correlation between model and experimental results.....	134
Fig. 4.8. Overall heat transfer coefficient variation with air flow rate for different HFMs. The error bars represent 1 standard deviation from the mean values.....	135
Fig. 4.9. (a) Air outlet temperature, (b) Absolute humidity of outlet air, (c) Thermal effectiveness factor and (d) Humidity effectiveness factor measured on PS27-N30-L15 modules for different water inlet	

temperatures. Lines through the data are model fits. The Pearson's correlation coefficient (r) greater than 0.9 suggests an excellent positive correlation between model and experimental results.....	136
Fig. 4.10. (a) Air outlet temperature, (b) Absolute humidity of outlet air, (c) Thermal effectiveness factor and (d) Humidity effectiveness factor measured on PS27-N30-L15 modules for different water inlet flow rates. Lines through the data are model fits. The Pearson's correlation coefficient (r) greater than 0.9 suggests an excellent positive correlation between model and experimental results.....	138
Fig. 4.11. Overall heat transfer coefficient variation with air flow rate for different inlet water temperatures in HFM27 test module. The error bars represent 1 standard deviation from the mean values.....	138
Fig. 4.12. (a) Air outlet temperature, (b) Absolute humidity of outlet air, (c) Thermal effectiveness factor and (d) Humidity effectiveness factor for modules having different tube lengths. Lines through the data are model fits. The Pearson's correlation coefficient (r) greater than 0.9 suggests an excellent positive correlation between model and experimental results.....	140
Fig. 4.13. (a) Air outlet temperature, (b) Absolute humidity of outlet air, (c) Thermal effectiveness factor and (d) Humidity effectiveness factor for modules having different tube numbers. Lines through the data are model fits. The Pearson's correlation coefficient (r) greater than 0.9 suggests an excellent positive correlation between model and experimental results for $N=30$ and $N=60$. However, for $N=10$, a good correlation could not be obtained due to the anomalous behaviour observed at $AFR=10$ L/min (see text).....	141
Fig. 4.14. Effect of membrane area on thermal effectiveness. The solid line and data point for $N=30$, $L=30$ cm are model fits. The humidity effectiveness factor also follows a similar trend.....	142
Fig. 4A.1. Schematic representation of phase inversion hollow fiber spinning setup and microscope image of the annular spinneret.....	148
Fig. 4A.2. Schematic representation of bubble point setup.....	149
Fig. 4A.3. Schematic representation of pore size distribution setup using liquid-liquid displacement method.....	150
Fig. 4B.1. Comparison of model predictions for the cases of liquid water vs water vapor transport for the reference membrane HFM27 (a) Normalized concentration gradients; (b) flux of liquid water (blue line) vs water vapor (red line); (c) outlet gas temperature and (d) outlet gas humidity in the two cases. The normalization in (a) is done using C_{max}^{liq} for liquid water and using C_{max}^{vap} for water vapor.....	152
Fig. 5.1. Variation of outlet gas temperature and humidity with air flow rate. The green region is the monotonic region which is captured by the transport model presented in Chapter-4 and the red region corresponds to low humidifier performance which is studied in this chapter.....	159
Fig. 5.2. Front and isometric views of the CAD models (a) Tube_C1/C2/C3 (b) Tube_C4 and (c) Tube_C5.....	162
Fig. 5.3. Cross-sectional view of CAD models (a) Tube_C1 (b) Tube_C2 and (c) Tube_C3/C4/C5.....	162

Fig. 5.4. (a) Front and isometric views of Shell_C1/C2/C3, (b) Cross-sectional/Top view of Shell_C1, Shell_C2, and Shell_C3.....	162
Fig. 5.5. Physics controlled mesh for (a) shell side geometry and (b) tube side geometry.....	164
Fig. 5.6. Schematic illustration of the simulation procedure.....	164
Fig. 5.7. (a) Velocity distribution inside tubes (b) flow velocity streamlines inside inlet header and (c) flow streamlines inside outlet header for Tube_C1 model. The red circles represent tubes receiving higher flow than other tubes.....	166
Fig. 5.8. (a) Velocity distribution inside tubes (b) flow velocity streamlines inside inlet header and (c) flow streamlines inside outlet header for Tube_C2 model. The red circles represent tubes receiving higher flow than other tubes.....	166
Fig. 5.9. (a) Velocity distribution inside tubes (b) flow velocity streamlines inside inlet header and (c) flow streamlines inside outlet header for Tube_C3 model. The red circles represent tubes receiving higher flow than other tubes.....	167
Fig. 5.10. (a) Velocity distribution inside tubes (b) flow velocity streamlines inside inlet header and (c) flow streamlines inside outlet header for Tube_C4 model. The red circles represent tubes receiving higher flow than other tubes.....	168
Fig. 5.11. (a) Velocity distribution inside tubes (b) flow velocity streamlines inside inlet header and (c) flow streamlines inside outlet header for Tube_C5 model.....	169
Fig. 5.12. Velocity profile inside the shell for (a) Shell_C1 (b) Shell_C2 and (c) Shell_C3.....	170
Fig. 5.13. Flow velocity streamlines inside the shell for (a) Shell_C1 (b) Shell_C2 and (c) Shell_C3.....	171
Fig. 6.1. Schematic representation of the flow modes in a single cell. Counter-flow: Gas inlet – (2), Gas outlet – (1); Co-flow: Gas inlet – (1), Gas outlet – (2). In counter-flow mode, the gas flow is opposite to the capillary action while in co-flow mode, the gas flow is in the direction of capillary action.....	179
Fig. 6.2. Schematic representation of different configurations in a single cell.....	180
Fig. 6.3. Wick characterization: (a) Pore diameter vs. differential air pressure across the wick, (b) Gas permeability through wick vs. differential air pressure across the wick, (c) Contact angle measurement and (d) TGA/DSC plot for variation in mass % and heat flow with respect to temperature. The error bars represent the standard deviation values for a data set of average pore diameter and gas permeability....	183
Fig. 6.4. Block diagram representation of the differential pressure measurement for (a) Counter-flow and (b) co-flow mode, in a 100 cm ² PEM fuel cell.....	186
Fig. 6.5. Polarization curves for different single cell configurations at $\lambda_{H_2} = 1.2$ and $\lambda_{Air} = 3$: (a) Counter-flow mode and (b) Co-flow mode. Error bars represent the standard deviation values obtained for the set of experiments performed for each configuration.....	190
Fig. 6.6. Polarization curves for configuration-C in co-flow mode at air stoichiometry of 1.5, 2 & 3: (a) without external water supply to the wick (configuration-C ₁) and (b) with external water supply to the	

wick (configuration-C ₂). Error bars represent the standard deviation values obtained for the set of experiments performed for each air stoichiometry.....	193
Fig. 6.7. Equivalent circuit for the Nyquist plots.....	194
Fig. 6.8. Nyquist plots under counter-flow mode: (a) configuration-A (b) configuration-B (c) configuration-C and (d) configuration-D. Experimental data (o) and simulated curve (□) are compared for their Ohmic resistance and charge transfer resistance values, which are the major losses incurred in the experimental setup.....	196
Fig. 6.9. Nyquist plots under co-flow mode: (a) Configuration-A (b) Configuration-B (c) Configuration-C and (d) Configuration-D. Experimental data (o) and simulated curve (□) are compared for their Ohmic resistance and charge transfer resistance.....	199
Fig. 6.10. Nyquist plots for configuration (a) C ₁ and (b) C ₂ compared at air stoichiometry of 1.5 (o), 2 (Δ) and 3 (□).....	200
Fig. 7.1. Fuel cell performance comparison with different humidification systems (a) Bubble humidifier (black markers) (b) HFM27 (red markers) and (c) HFM30 (blue markers).....	210
Fig. 7.2. Resistance-on-series model for (a) HFM25, (b) HFM27 / HFM30.....	212
Fig. 7.3. Utility of the model. The black lines are the model predictions. The dashed red and blue lines represent the upper and lower bounds respectively for a wide range of flow conditions. In all cases, the water flow rate is 1/25 th of air flow rate.....	216
Fig. 7.4. Challenges to be addressed for asymmetric HFM humidifiers.....	217
Fig. 7.5. Proposed header design for minimizing dead volume and improving flow distribution. The figure is not drawn to scale. The dimensions will be based on the flow capacity.....	218

List of Tables

Table 2.1: Classification of membrane processes.....	13
Table 2.2: Existing models on dense membrane humidifier.....	26
Table 2.3: Spinning process conditions.....	33
Table 2.4: Literature on porous/asymmetric membranes used for gas humidification.....	40
Table 3.1: Values of input parameters.....	70
Table 3.2: Dimensionless numbers and their physical significance.....	72
Table 3.3: Humidifier parameters for Perma Pure FC 200-780-7LP.....	79
Table 3.4: Various resistances for heat and mass transfer in the humidifier.....	87
Table 4.1: Hollow fiber spinning parameters.....	106
Table 4.2: Details of modules and test parameters.....	107
Table 4.3: Value of input parameters.....	119
Table 4.4: Estimated porosity for each membrane type.....	124
Table 4.5: Calculation of porosity in the macro-porous bulk of the membranes.....	125
Table 4.6: Individual resistances and effective diffusion coefficient of liquid water for different HFMs.....	131
Table 4.7: Comparison of humidifier performance between this study and the literature.....	144
Table 4.B1: Individual resistances and effective diffusion coefficient of water vapor for different HFMs.....	151
Table 5.1: Design parameters for different CAD models.....	161
Table 6.1: Description of different configurations.....	179
Table 6.2: Experimental parameters for fuel cell testing.....	181
Table 6.3: Comparison of properties for selection of wicking material.....	183
Table 6.4: Determination of water uptake through capillary action in counter-flow and co-flow modes.....	187
Table 6.5: Experimental and simulated values of Ohmic and charge transfer resistances for different configurations.....	196
Table 6.6: Comparison of Ohmic resistances between different configurations.....	197
Table 6.7: Comparison of charge transfer resistances (CTR) between different configurations.....	198

Table 7.1: Cost comparison of different membrane humidifiers.....	211
-------------------------------------------------------------------	-----

Chapter 1

Introduction

1.1. Gas humidification

Humidification of gas in simple terms means the addition of moisture to gas. It is also sometimes referred to as conditioning of gas based on application. Storage of several moisture sensitive products such as drugs, vaccines, chemical reagents, food etc. require maintaining optimum humidity levels for preventing degradation [1–3]. In industries, several chemical operations require maintaining specific humidity levels for obtaining high product yield. The importance of gas humidification can be understood from the fact that even human functioning is hampered under adverse humidity conditions [4]. Under very low humidity conditions, people suffer from dryness of eyes, skin cracking, difficulty in breathing and dehydration whereas under very high humidity conditions, people often suffer from microbial infections, excess sweating etc., causing uneasiness. Analogous to human response towards humidity, energy systems such as PEM fuel cells are also susceptible to gas humidification which controls hydration of membrane used for proton conduction [5–8]. Thus, gas humidification is a crucial objective for a variety of applications and for satiating scientific curiosity.

1.2. Strategies for gas humidification

Gas humidification can be either achieved by bringing the gas to be humidified in direct contact with water or indirectly by using a medium to introduce moisture in the gas.

1.2.1. Direct methods

1.2.1.1. Bubble column

A bubble column is an apparatus typically used to generate and control gas-liquid absorption reactions. It is also used as a humidifier when a water-insoluble gas is passed through a water column as shown in the schematic below in Fig. 1.1. The gas is supplied from the bottom of the column using a sparger arrangement and bubbles upwards through the water column towards the outlet. In the process, the gas picks up moisture and gets humidified. The water column can be optionally heated or circulated with hot water to achieve the required amount of moisture

and temperature of the gas. Bubble humidifier typically works well at low gas flow rates due to the limitation on pressure tolerance and bubbling inside the column.

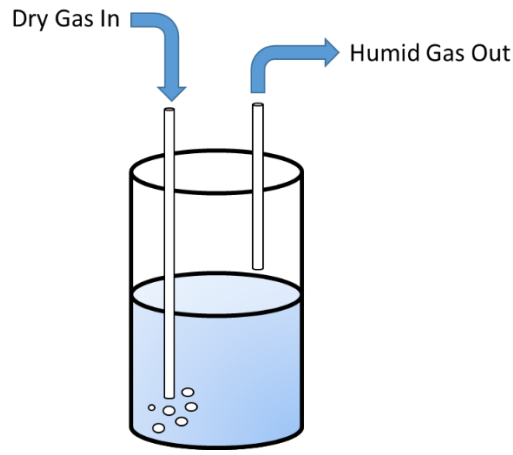


Fig. 1.1. Bubble column humidifier

1.2.1.2. Simple reservoir humidifiers

Simple reservoir humidifiers are similar to bubble column except that in this type of humidifier, gas is supplied over the surface of the heated water which adds water vapor to the gas stream. The schematic is shown below in Fig. 1.2. These type of humidifiers are limited by the small surface area available for heat and moisture exchange.

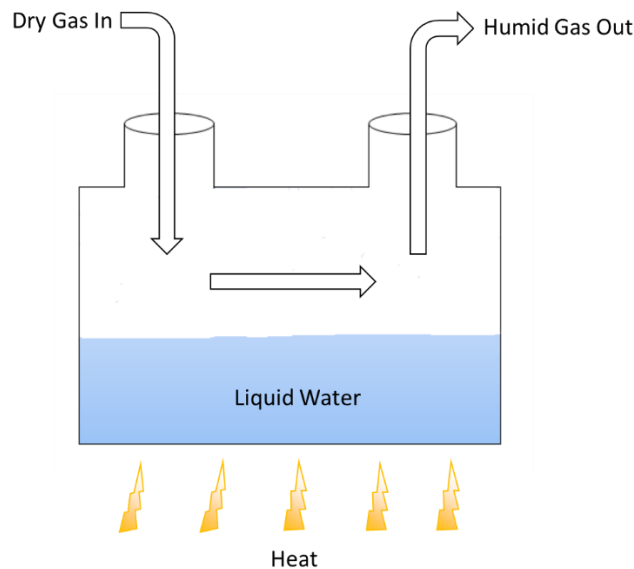


Fig. 1.2. Simple reservoir humidifier

1.2.1.3. Liquid water injection

Direct liquid water injection is used in a variety of configurations. The commonly used configuration makes use of injecting liquid over a hot plate which evaporates the film of fluid formed over the plate to humidify the air flowing over it. The injected liquid flow rate, plate temperature, and gas flow rate can be tuned to achieve the desired humidification. The schematic of this type of humidification is shown in Fig. 1.3.

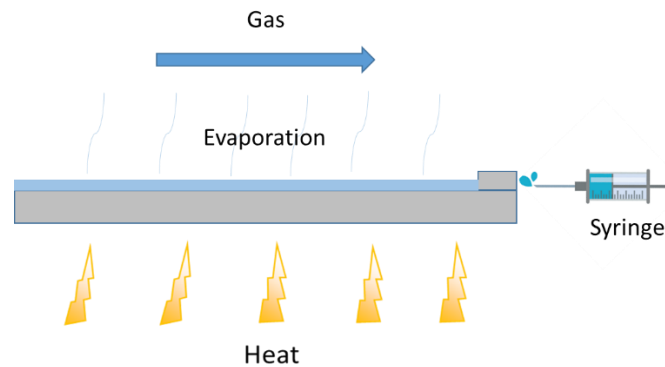


Fig. 1.3. Liquid water injection

1.2.2. Indirect methods

1.2.2.1. Wick humidifier

Wick humidifiers are a modified version of simple reservoir humidifier consisting of water absorbing material placed upright and partially dipped in the water column to enhance the available surface area for heat and moisture exchange. The dry gas moves in the chamber, flows around the wick and absorbs heat and moisture and leave the chamber through the outlet. The schematic is shown below in Fig. 1.4.

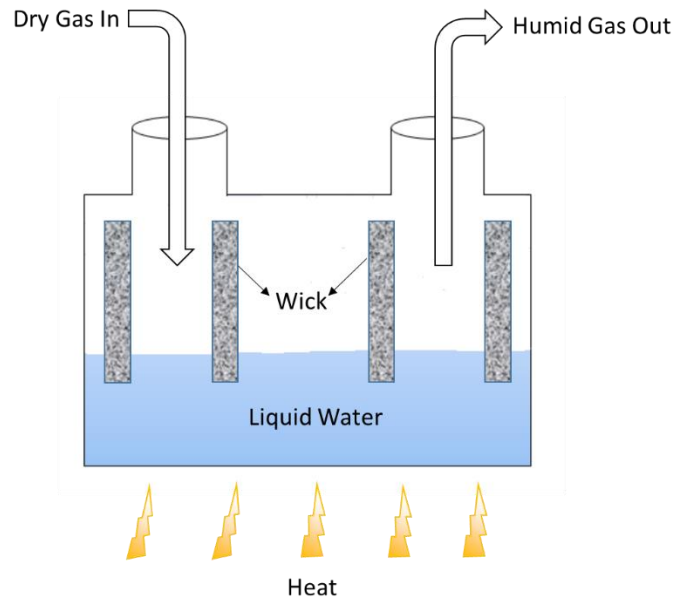


Fig. 1.4. Wick humidifier

1.2.2.2. Ultrasonic nebulizer

Ultrasonic nebulizer uses piezoelectric crystals which contract and expand when supplied with electric current and produce radio waves. These radio waves are converted into high frequency mechanical vibrations using a crystal transducer. These high energy mechanical vibrations create cavitation inside the fluid and generates fine dispersed water particles. The frequency of oscillation determines the size of water particles dispersed. Nebulizers are extremely energy intensive besides being also limited by gas flow rate capacities. The schematic representation of the working principle of a typical ultrasonic nebulizer is shown in Fig. 1.5 [9].

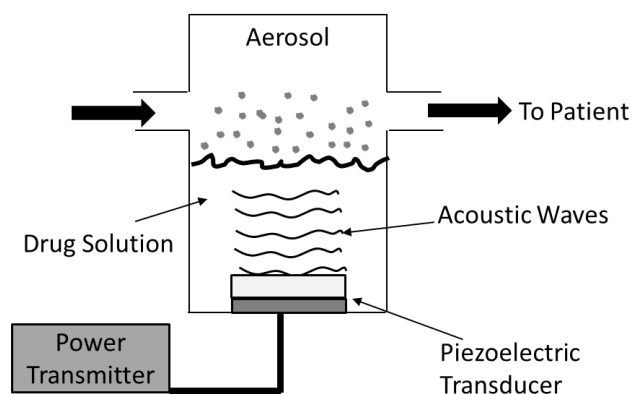


Fig. 1.5. Ultrasonic nebulizer

1.2.2.3. Membrane contactors

Membrane contactors are typically used for degassing liquids and are made of hydrophobic microporous membranes such as polypropylene which separates the liquid from the gas stream [10]. Since the membranes are hydrophobic, liquid water does not enter the pores thereby avoiding entrainment. At the pore, the gas lies in direct contact with the liquid for heat and moisture exchange. Membrane contactors require precise control over pore size and number to control the performance which is one of its major limiting factors. A schematic illustration of the working of membrane contactors is shown in Fig. 1.6.

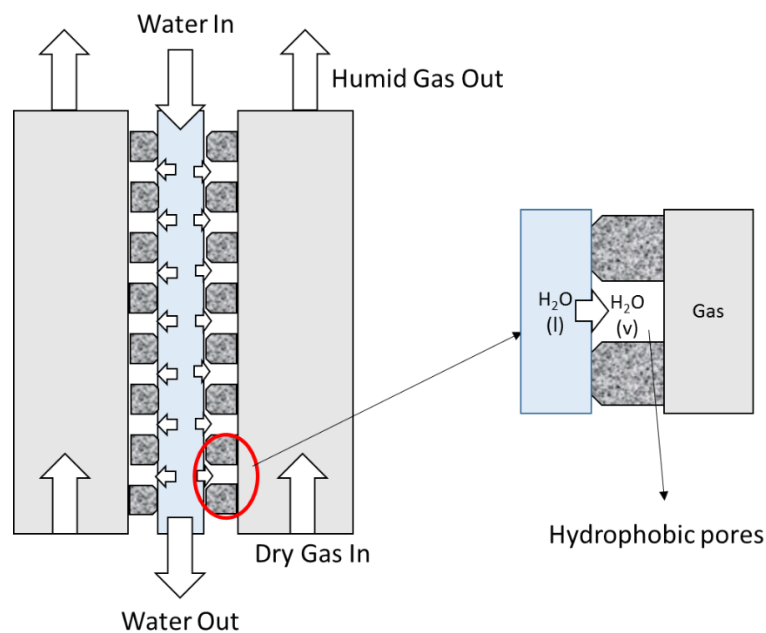


Fig. 1.6. Membrane contactor

1.2.2.4. Water permeating membranes

Water permeating membranes work on the principle of solution-diffusion phenomenon wherein the water molecules sorb at the membrane surface and diffuse across a concentration gradient to desorb on the other side of the membrane facing a dry gas stream. Due to their dense nature, these membranes prevent flooding and entrainment that might be caused due to liquid crossover. However, the dense nature also provides major resistance to moisture transport. Therefore, such membranes are typically made thin for achieving high humidification performance. Such thin membranes often fail under high trans-membrane pressures which is a

major drawback of these membranes besides also being costly. The schematic illustration of the working principle of these membranes is shown in Fig. 1.7.

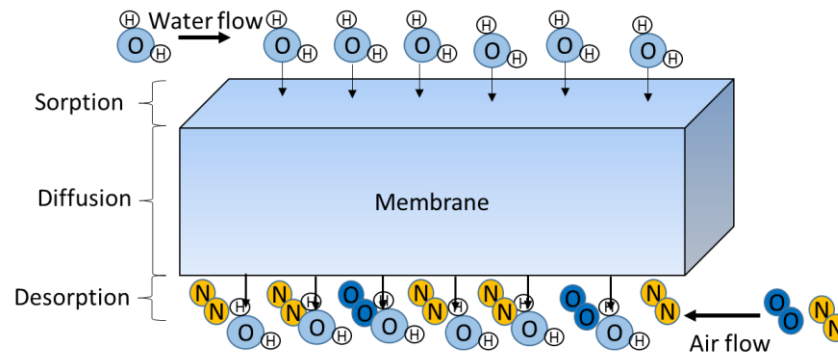


Fig. 1.7. Water permeating membranes

1.3. Gas humidification for water management in PEM fuel cells

Gas humidification is a critical component of water management in PEM fuel cells, which in turn is essential for durable and reliable fuel cell performance [6]. Low temperature PEM fuel cells typically use Nafion membrane and an ionomer, which is usually a sulfonated polytetrafluoroethylene polymer. The sulfonated pendant chain is responsible for proton transport across the membrane. The proton conductivity of the Nafion membrane is dependent on the hydration state of the sulfonated pendant chain [11,12]. Fig. 1.8. below gives a schematic representation of the cluster network model which illustrates the effect of hydration on proton conduction in Nafion [13,14]. Under dry conditions, the sulphonate groups remain as isolated clusters because of which the proton migration becomes difficult. Under humid conditions which are maintained because of either external humidifiers or by water generated at the cathode of PEM fuel cell or both, the sulphonate groups start solvating and create water nano-domains. These domains facilitate effective proton transport by allowing different sulphonate groups to communicate with each other.

It is widely reported that when Nafion is in contact with liquid water, the water content (mol H_2O /mol SO_3^-) in the membrane can reach as high as 22 whereas when it is in contact with water vapor with unit activity i.e. saturated water vapor, the equilibrium water content reaches only 14 [12,15]. This phenomenon where a material absorbs different amount of water based on the physical state of water is more commonly referred to as the Schroeder's Paradox [16–18]. In any

case, higher the water content higher is the proton conductivity. However, presence of liquid water at the fuel cell electrodes often cause mass transport limitations commonly known as flooding of the fuel cell [19]. Flooding is undesirable because although it increases the proton conductivity of the membrane and the electrode, it also provides resistance for feed gas diffusion in the gas diffusion layer and catalyst layer which reduces the fuel cell performance. Hence, an optimum balance between hydration of membrane and removal of liquid water from the fuel cell is desirable. Maintaining this balance inside the fuel cell is known as water management.

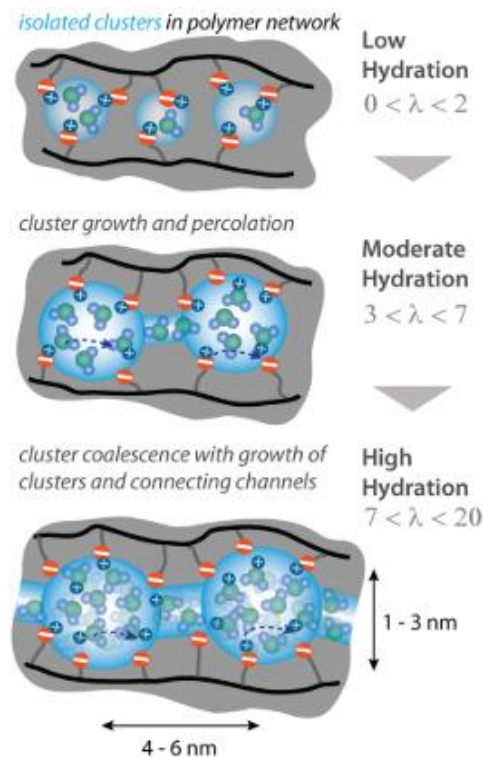


Fig. 1.8. Cluster network model (reproduced with permission from [15])

Hydration of fuel cell is achieved partially by the water generated at the cathode due to electrochemical reaction. However, since air flow rates at cathode are typically much higher than hydrogen flow rate at anode, water retention in the membrane is difficult due to vaporization at the cathode. Therefore, fuel cell stacks are often employed with external gas humidifiers which maintain the required hydration level inside the stack. Figure 1.9. shows the effect of gas humidity on fuel cell performance (represented by the V-I characteristic curve known as fuel cell polarization curve) which suggests that higher the humidity better is the fuel cell performance. Since liquid water entering the fuel cell can exacerbate its performance due to possible flooding

of electrodes, it is critical that the chosen humidifier type does not allow flooding and entrainment in the gas stream. An ideal humidifier for fuel cell application should add only water vapor and heat to the gas (the latter enabling the gas to raise its temperature up to the fuel cell operating temperature) with minimum size, volume, and parasitic power loss.

As discussed earlier, there are several options for achieving gas humidification. However, for PEM fuel cells, the most commonly used methods are bubble humidifiers and membrane based humidifiers. Among these, hollow fiber membrane based humidifiers, which offer excellent performance in a compact and easy-to-use module setup are the most preferred candidates for use as external humidifiers for a wide range of fuel cell capacities. In this research work, we study gas humidification from dense and porous hollow fiber membrane humidifiers. Detailed background literature on hollow fiber membrane humidifiers is provided in Chapter 2.

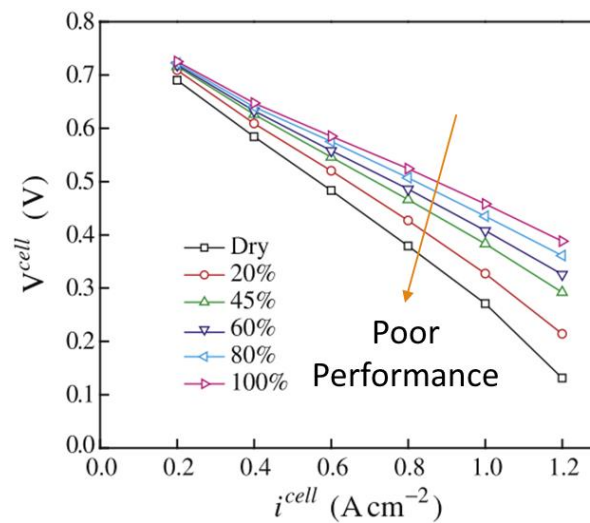


Fig. 1.9. Effect of humidity on fuel cell performance (reproduced with permission from [20])

Hollow fiber membrane humidifiers are similar to a conventional shell and tube heat exchangers except for the coupled moisture exchanged between the shell and tube side fluids along with heat exchange. The schematic of a hollow fiber membrane humidifier is shown in Fig. 1.10. Within the given set of constraints of size and volume, hollow fiber membrane humidifier performance is determined by the available residence time and interfacial area for gas to exchange heat and moisture with water. Thus, by proper selection of membrane material, tube length, tube

diameter, tube number and the process conditions, desired humidity and temperature of the outlet gas to be supplied to PEM fuel cells can be achieved.

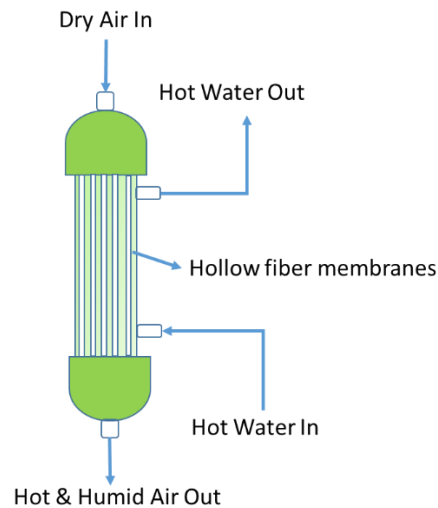


Fig. 1.10. Hollow fiber membrane humidifier

1.4. Internal humidification in PEM fuel cells

While external humidification of gases improves fuel cell performance, dry feed operation of PEM fuel cell is desirable in order to reduce the parasitic power loss and system complexity caused by external humidifiers [21]. However, operating under such conditions leads to large Ohmic loss (voltage drop due to resistance in proton and electron transport) in fuel cell performance caused because of excessive drying of the membrane and ionomer [22,23]. Often with dry feed, fuel cells are operated at low temperatures (40 – 50 °C) to reduce the evaporation loss and help retain the water generated [19]. However, reducing cell temperature slows down the reaction kinetics at the catalyst thereby increasing the activation losses (voltage drop towards driving the chemical reaction that transfers electrons to and from the electrodes). Hence, water management under dry feed operation is a challenge that needs to be addressed. Several internal humidification techniques (discussed in detail in Chapter 2) have been devised to tackle the issue. In this work, we investigate a novel passive internal humidification technique devised on the principle of capillary action in electrically conducting and hydrophilic wicks.

References

- [1] M.E.K. Ngcobo, M.A. Delele, L. Chen, U. Linus, Postharvest Biology and Technology Investigating the potential of a humidification system to control moisture loss and quality of 'Crimson Seedless' table grapes during cold storage, *Postharvest Biol. Technol.* 86 (2013) 201–211. doi:10.1016/j.postharvbio.2013.06.037.
- [2] I. Koutsourelakis, E. Vagiakis, E. Perraki, M. Karatza, C. Magkou, M. Kopaka, C. Roussos, S. Zakyntinos, Nasal inflammation in sleep apnoea patients using CPAP and effect of heated humidification, *Eur. Respir. J.* 2011; 37: 587–594. doi:10.1183/09031936.00036910.
- [3] A. Schulze, Respiratory Gas Conditioning and Humidification, *Clin. Perinatol.* 34 (2007) 19–33. doi:10.1016/j.clp.2006.12.009.
- [4] D.K. Milton, P.M. Glencross, and M.D. Walters, Risk of Sick Leave Associated with Outdoor Air Supply Rate, Humidification, and Occupant Complaints, *Indoor Air* 10 (2000) 212–221.
- [5] P. Berg, K. Promislow, J. St. Pierre, J. Stumper, B. Wetton, Water Management in PEM Fuel Cells, *J. Electrochem. Soc.* 151 (2004) A341. doi:10.1149/1.1641033.
- [6] D.N. Ozen, B. Timurkutluk, K. Altinisik, Effects of operation temperature and reactant gas humidity levels on performance of PEM fuel cells, *Renew. Sustain. Energy Rev.* 59 (2016) 1298–1306. doi:10.1016/j.rser.2016.01.040.
- [7] S.-K. Park, E.A. Cho, I.-H. Oh, Characteristics of membrane humidifiers for polymer electrolyte membrane fuel cells, *Korean J. Chem. Eng.* 22 (2005) 877–881. doi:10.1007/BF02705668.
- [8] R. Pandey, H. Agarwal, B. Saravanan, P. Sridhar, S.D. Bhat, Internal Humidification in PEM Fuel Cells Using Wick Based Water Transport, *J. Electrochem. Soc.* 162 (2015) F1000–F1010. doi:10.1149/2.0621509jes.
- [9] T.R. Myers, D.S. Gardenhire, A. Ari, *A Guide to Aerosol Delivery Devices for Respiratory Therapists* 3rd Edition, (2013).

- [10] A. Gabelman, S.-T. Hwang, Hollow fiber membrane contactors, *J. Memb. Sci.* 159 (1999) 61–106. doi:10.1016/S0376-7388(99)00040-X.
- [11] J. Peron, A. Mani, X. Zhao, D. Edwards, M. Adachi, T. Soboleva, Z. Shi, Z. Xie, T. Navessin, S. Holdcroft, Properties of Nafion®NR-211 membranes for PEMFCs, *J. Memb. Sci.* 356 (2010) 44–51. doi:10.1016/j.memsci.2010.03.025.
- [12] T.A. Zawodzinski, Water Uptake by and Transport Through Nafion® 117 Membranes, *J. Electrochem. Soc.* 140 (1993) 1041. doi:10.1149/1.2056194.
- [13] P. Products, E. Station, The Morphology in Nafion* Perfluorinated Membrane Products, as Determined by Wide- and Small- Angle X-Ray Studies, 19 (1981) 1687–1704.
- [14] W.Y. Hsu, T.D. Gierke, Ion Transport And Clustering In Nafion* Perfluorinated Membranes, *J. Memb. Sci.*, 13 (1983) 307–326.
- [15] A. Kusoglu, A.Z. Weber, New Insights into Perfluorinated Sulfonic-Acid Ionomers, *Chem. Rev.* 117 (2017) 987–1104. doi:10.1021/acs.chemrev.6b00159.
- [16] P. Choi, R. Datta, Sorption in Proton-Exchange Membranes, *J. Electrochem. Soc.* 150 (2003) E601. doi:10.1149/1.1623495.
- [17] V. Freger, Hydration of Ionomers and Schroeder ' s Paradox in Nafion, *J. Phys. Chem. B.* 113 (2009) 24–36.
- [18] L.M. Onishi, J.M. Prausnitz, J. Newman, Water-Nafion Equilibria. Absence of Schroeder's Paradox, *J. Phys. Chem. B.* 111 (2007) 10166–10173. doi:10.1021/jp073242v.
- [19] A. Dicks, J. Larminie, *Fuel Cell Systems Explained*, 2003. doi:10.1002/9781118878330.
- [20] D.H. Jeon, K.N. Kim, S.M. Baek, J.H. Nam, The effect of relative humidity of the cathode on the performance and the uniformity of PEM fuel cells, *Int. J. Hydrogen Energy.* 36 (2011) 12499–12511. doi:10.1016/j.ijhydene.2011.06.136.
- [21] P.K. Jithesh, T. Sundararajan, S.K. Das, Experimental investigation of dry feed operation in a polymer electrolyte membrane fuel cell, *J. Power Sources.* 260 (2014) 243–250.

doi:10.1016/j.jpowsour.2014.03.002.

- [22] J. Zhang, H. Zhang, J. Wu, J. Zhang, Pem Fuel Cell Testing and Diagnosis, 2013.

doi:10.1016/B978-0-444-53688-4.00007-3.

- [23] J. Zhang, PEM Fuel Cell Electrocatalysts and Catalyst Layers, 2008. doi:10.1007/978-1-

84800-936-3.

Chapter 2

Background

This Chapter provides necessary background based on the available literature to help understand the process of external gas humidification using membranes and internal gas humidification using passive water management strategies in PEM fuel cells. The research objectives of this work and the structure of the thesis are also presented at the end of this chapter.

2.1. Solution-diffusion process in membranes

2.1.1. Overview

The principal property of a membrane is to selectively allow for permeation of certain species. Membranes used for separation processes can be classified into groups based on the driving force used for separation as shown in Table 2.1.

Table 2.1: Classification of membrane processes

Driving force	Separation Process
Pressure difference	<ul style="list-style-type: none">• Reverse osmosis• Ultrafiltration• Microfiltration• Gas/Vapor separation• Pervaporation
Concentration difference	<ul style="list-style-type: none">• Dialysis• Membrane extraction
Temperature difference	<ul style="list-style-type: none">• Membrane distillation
Electric potential difference	<ul style="list-style-type: none">• Electrodialysis

Interestingly, the solution-diffusion model is widely accepted to represent membrane processes like dialysis, pervaporation, gas separation and reverse osmosis [1–4]. A schematic illustration of

the solution-diffusion process is shown in Fig. 2.1. The permeant molecules first adsorb on to the membrane surface, dissolve in the membrane phase and diffuse across a concentration gradient to desorb on the other side of the membrane. Separation is achieved based on the difference in solubility and diffusion coefficient of different species in the feed mixture [3].

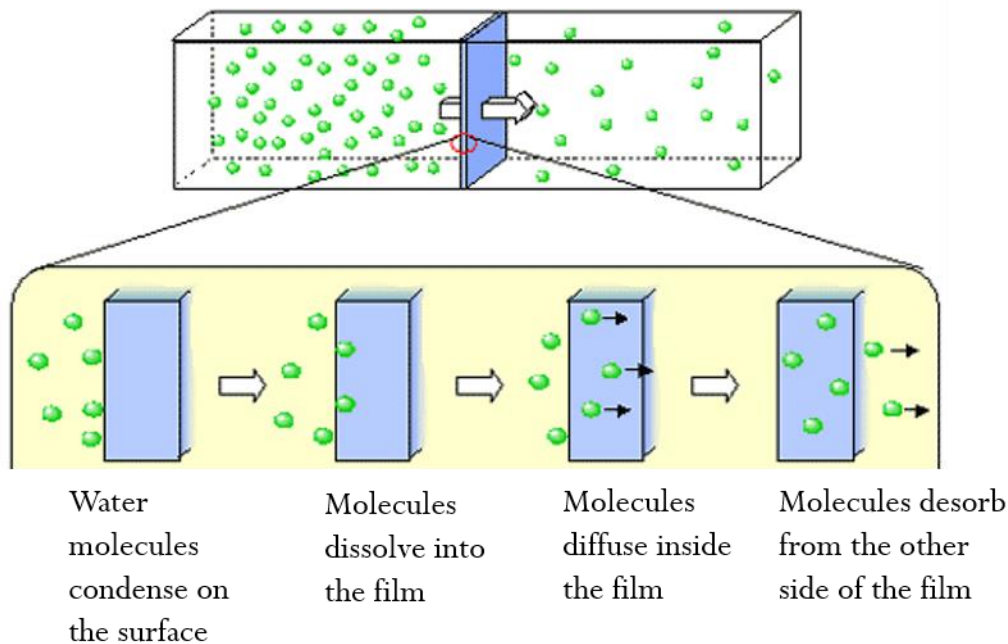


Fig. 2.1. Solution-diffusion process in membranes

In this chapter, we will focus on the solution-diffusion model for pervaporation as it closely resembles the process of gas humidification.

2.1.2. General solution-diffusion model

The fundamental thermodynamic quantity that governs transport across membranes is the gradient in chemical potential. This gradient in chemical potential produces a movement of the permeant inside the membrane. Thus the molar flux of a component 'i' can be given as

$$J_i = -L_i \frac{d\mu_i}{dx} \dots\dots\dots(1)$$

Where, $\frac{d\mu_i}{dx}$ is the chemical potential gradient and L_i is a constant of proportionality linking the flux to gradient in the chemical potential.

Taking into account the driving forces for mass transfer as concentration and pressure gradients, the chemical potential can be expressed as [4]

$$d\mu_i = RTd(\ln(\gamma_i c_i)) + v_i dP \dots \dots \dots (2)$$

Where, c_i is the molar concentration (mol/mol) of component i , γ_i is the activity coefficient linking concentration with activity, P is the pressure, and v_i is the molar volume of component i .

A schematic illustration of the gradients involved in a typical solution-diffusion process is shown in Fig. 2.2. Here, the high-pressure solution is the feed which consists of the component 'i' to be separated. The pressure within the dense membrane is assumed uniform and at the same high pressure value as the feed. Additionally, the chemical potential gradient across the membrane is expressed only as a concentration gradient. On the contrary, the pore-flow model assumes that the concentration of solvent and solute within the membrane are uniform and that the chemical potential gradient is expressed only as a pressure gradient [4–7]. This is the primary difference between solution-diffusion and pore-flow models. In processes like pervaporation, the pressure difference between the high and low pressure sides is primarily responsible for the chemical potential gradient according to Eq. (2).

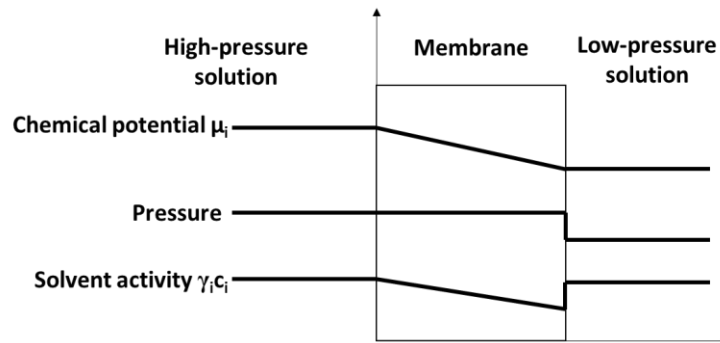


Fig. 2.2. Pressure-driven permeation of a one-component solution through a membrane according to solution-diffusion model [4]

Integrating Eq. (2) for incompressible phases like liquids or solids, we get

$$\mu_i = \mu_i^0 + RT\ln(\gamma_i c_i) + v_i(P - P_i^0) \dots \dots \dots (3)$$

Where μ_i^0 is the chemical potential of pure 'i' at a reference pressure P_i^0 .

Similarly, for compressible phases such as gases assumed to follow ideal gas behavior where the molar volume is a function of pressure, we get from Eq. (2)

$$\mu_i = \mu_i^0 + RT \ln(\gamma_i c_i) + RT \ln(P/P_i^0) \dots \dots \dots (4)$$

In Eqs. (3) and (4), the reference pressure is $P_i^0 = P_{i,sat}$ i.e., the saturation vapor pressure of component 'i'.

The underlying assumptions of this model are

- The fluids on either side of the membrane are in equilibrium with the membrane at the interface
- The rate of sorption/desorption is much faster than the rate of diffusion through the membrane

These assumptions are valid for most membrane transport processes except for transport processes involving chemical reactions or facilitated diffusion and for diffusion of gases through metals in which case the interfacial sorption/desorption can be slow [4].

2.1.3. Solution-diffusion model for pervaporation

Pervaporation is a membrane process that combines permeation and vaporization. Pervaporation is typically used to separate liquid mixtures. The membranes used typically are dense and non-porous and display an affinity towards the component that needs to be separated. Specifically, for this process, the permeating component is converted into a vapor phase, due to the low (partial) vapor pressure on the permeate-side. The low vapor pressure is normally achieved by placing a slight vacuum on the permeate-side of the membrane. In most cases, the collected permeate is re-condensed for use. The pervaporation process contains three steps:

- Selective sorption in the membrane on the feed side;
- Selective diffusion through the membrane;
- Desorption in the gas phase on the permeate-side.

The key equations describing pervaporation process can be found in [3,4,6,7] and are summarized below.

At the liquid-membrane interface, the chemical potential of liquid is equilibrated with the chemical potential of liquid in the membrane phase. This gives,

$$\mu_i^o + RT\ln(\gamma_i c_i) + v_i(P_l - P_{i,sat}) = \mu_i^o + RT\ln(\gamma_{i,m} c_{i,m}) + v_i(P_l - P_{i,sat}) \dots \dots \dots (5)$$

Where the subscript 'm' refers to membrane-liquid interface.

From Eq. (5) we get

$$c_{i,m} = \frac{\gamma_i}{\gamma_{i,m}} c_i = K_i c_i \dots \dots \dots (6)$$

Where, K_i is the liquid-phase sorption coefficient.

At the membrane-gas interface, the chemical potential of the liquid in the membrane phase is equilibrated with the chemical potential of vapor in the gas phase. This gives,

$$\mu_i^o + RT\ln(\gamma_{i,m,o} c_{i,m,o}) + v_i(P_l - P_{i,sat}) = \mu_i^o + RT\ln(\gamma_{i,o} c_{i,o}) + RT\ln(P_o / P_{i,sat}) \dots \dots \dots (7)$$

Where the subscript 'o' refers to the membrane-gas interface.

From Eq. (7) we get

$$c_{i,m,o} = \frac{\gamma_{i,o}}{\gamma_{i,m,o}} c_{i,o} \left(\frac{P_o}{P_{i,sat}} \right) \exp \left(\frac{-v_i}{RT} (P_l - P_{i,sat}) \right) \dots \dots \dots (8)$$

In Eq. (8), because the term $\left(\frac{-v_i}{RT} (P_l - P_{i,sat}) \right)$ is small ($O(v_i = \frac{RT}{p_i}) \approx O(\frac{(P_l - P_{i,sat})}{RT})$) the exponential term is close to 1 and thus Eq. (8) can be written as

$$c_{i,m,o} = \frac{\gamma_{i,o}}{\gamma_{i,m,o}} c_{i,o} \left(\frac{P_o}{P_{i,sat}} \right) = \frac{\gamma_{i,o}}{\gamma_{i,m,o}} \left(\frac{p_{i,o}}{P_{i,sat}} \right) = K_i^G p_{i,o} \dots \dots \dots (9)$$

Where, K_i^G is the gas phase sorption coefficient and $p_{i,o}$ is the partial vapor pressure of component i in the gas phase.

The flux across the membrane can be estimated as

$$J_i = -D_i \frac{(c_{i,m,o} - c_{i,m})}{L} \dots \dots \dots (10)$$

Where, D_i is the diffusion coefficient of component 'i' in the membrane and L is the membrane thickness.

It must be noted that the sorption coefficient in Eq. (6) is for liquid phase and the sorption coefficient in Eq. (9) is for the gas phase. Thus, an interconversion is required to account for the change in phase. This can be achieved by assuming a hypothetical equilibrium between the feed liquid and its vapor [4,8]. This gives

$$\mu_i^o + RT \ln(\gamma_i^L c_{i,o}^L) + v_i(P - P_{i,sat}) = \mu_i^o + RT \ln(\gamma_i^G c_i^G) + RT \ln(P/P_{i,sat}) \dots \dots \dots (11)$$

Where, γ_i^L and γ_i^G are the activity coefficients of component i in the liquid and gas phase respectively. Please note that γ_i^L can be replaced with γ_i for liquid phase.

Solving for c_i^L in Eq. (11), we get

$$c_i^L = c_i = \frac{\gamma_i^G}{\gamma_i^L P_{i,sat}} p_i \dots \dots \dots (12)$$

Where, p_i is the partial pressure of component 'i' in equilibrium with feed liquid. The term $\frac{\gamma_i^G}{\gamma_i^L P_{i,sat}}$ in Eq. (12) is sometimes referred to as Henry's law coefficient. Substituting Eq. (12) in Eq. (6), we get

$$c_{i,m} = \frac{\gamma_i^G \gamma_i}{\gamma_i^L \gamma_{i,m}} \left(\frac{p_i}{P_{i,sat}} \right) \dots \dots \dots (13)$$

Now, using Eqs. (9), (10) and (13) one can estimate the flux in a pervaporation process. Gas humidification process is similar to pervaporation in terms of dual equilibrium established on either side of the membrane, one at the membrane-liquid interface and other at the membrane-gas interface. However, gas humidification differs in terms of the heat transport coupled with mass transport while a pervaporation process, the coupling between mass and heat transfer is not likely to be strong in most cases. Hence, a general solution diffusion model is insufficient to model a membrane based gas humidification process.

2.2. Dense membranes for gas humidification

2.2.1. Overview

Non-porous membranes also known as dense membranes are widely used for gas humidification. Typical examples include Nafion[®], silicone (PDMS), SPEEK etc. Although all these membranes have different chemical structures, the mechanism of water transport in all of them is based on solution-diffusion phenomenon. It must be noted that in a water-to-gas membrane humidifier, the gas pressure is typically similar to or slightly higher than the water side pressure. Therefore, the affinity of the membrane material towards water is primarily responsible for sorption at the membrane-water interface. The chemical potential gradient is therefore a consequence of difference in water concentration across the membrane. No pressure driven transport of water is thus considered in this work. This is another key difference in pervaporation and membrane based gas humidification. In this thesis, we pay special attention to Nafion[®] membranes as these are common to membrane humidifiers as well as PEM fuel cells.

2.2.2. Nafion[®] flat sheet and hollow fiber membranes

Nafion[®] belongs to the class of ion conducting polymers known for their excellent ion conductivity and physico-chemical properties [9–13]. Nafion[®] is a sulfonated polytetrafluoroethylene random co-polymer which consists of a Teflon[®] (PTFE) backbone and pendant side chains each ending in a sulphonate (SO_3^-) group. The dissimilar nature of the covalently bonded pendant group and backbone results in natural micro-phase separation, which is enhanced by solvation (upon introduction of water or solvent molecules). This phase-separated morphology gives Nafion[®] its unique ion and solvent-transport properties. The sulphonate groups present on the pendant chains are responsible for water retention and transport in the membrane [9]. Under its optimal hydration state, Nafion[®] membranes can store up to 22 mol H_2O / mol SO_3^- . This high hydration state is also responsible for its excellent performance in water-to-gas and gas-to-gas humidifiers. Besides, the high hydration state is also responsible for better proton transport from anode to cathode in PEM fuel cells [12,14,15].

Nafion[®] membranes can be processed either as flat sheet or hollow fibers based on the type of humidifier i.e. plate-and-frame or shell-and-tube type. Nafion[®] membranes used in PEM fuel cells are flat sheet. While flat sheet membranes are manufactured either using solution casting or melt

extrusion, Nafion® hollow fibers are usually made using extrusion through a tube-in-orifice assembly. Nafion® derivatives are first synthesized by copolymerization of tetrafluoroethylene and the derivative of perfluorovinyl sulfonyl acid fluoride. The latter reagent can be prepared by the pyrolysis of its respective oxide or carboxylic acid. The resulting product is an SO₂F containing thermoplastic that can be extruded into films. The process conditions govern the physico-chemical properties of these membranes. For instance, casting with different solvents changes its ionic conductivity, and casting at higher temperatures forms a more entangled network of chains, higher crystallinity, better solvent resistance and overall mechanical properties [16–19].

2.2.3. Water transport through Nafion® membranes

Determining water transport through Nafion® membrane starts with the determination of its water uptake capacity. The sorption of water in Nafion® membrane is an extensively studied subject primarily because of the long-standing debate on sorption in the presence of liquid water versus saturated vapor. In both cases, the water activity $a_w = 1$. However, despite being under similar thermodynamic equilibrium conditions, the water content of Nafion® in presence of liquid water is ~ 22 mol H₂O/ mol SO₃⁻ whereas in presence of saturated vapor, the water content is only ~ 14 mol H₂O/ mol SO₃⁻ as shown in Fig. 2.3(a,b). For a vapor equilibrated membrane (Fig. 2.3a), the difference between the water content of an as-received membrane versus a pre-treated membrane is < 2 . The difference between the water uptakes of membranes that are equilibrated in liquid water versus saturated vapor increases when the membranes are pre-boiled instead of pre-dried (Fig. 2.3b). This anomaly in water uptake of Nafion® and several other polymeric systems is commonly known as the Schroeder's paradox based on the work of Schroeder, who reported that gelatins swell more in liquid water than in saturated water vapor [20].

The causes of membrane interaction with liquid/vapor are considered to be of interfacial origin [21–23] or thermal history [11,24]. While the former is responsible for altering the membrane morphology at the interface alone, the latter changes the entire bulk morphology. Some reports suggest that a pre-dried membrane absorbs a similar amount of water in saturated vapor or liquid water i.e. $\lambda_{vap} \approx \lambda_{liq} \approx 14 \pm 1$ mol H₂O/ mol SO₃⁻, but a pre-boiled membrane does not i.e. for pre-boiled membrane, $\lambda_{vap} \approx 14 \pm 1 < \lambda_{liq} \approx 22 \pm 1$ [25,26]. These observations have led

some research to conclude that the difference in water content is a matter of achieving or not achieving equilibrium. It is further known that the water content of Nafion® and other PFSA ionomers increases and approaches that of a pre-boiled membrane upon increasing liquid water temperature (see Fig. 2.3c) [10]. For as-received membranes, the water content increases with temperature. However, for pre-boiled membranes, the liquid-water uptake does not change with temperature indicating that the membrane is already in quasi- equilibrium (see Fig. 2.3b).

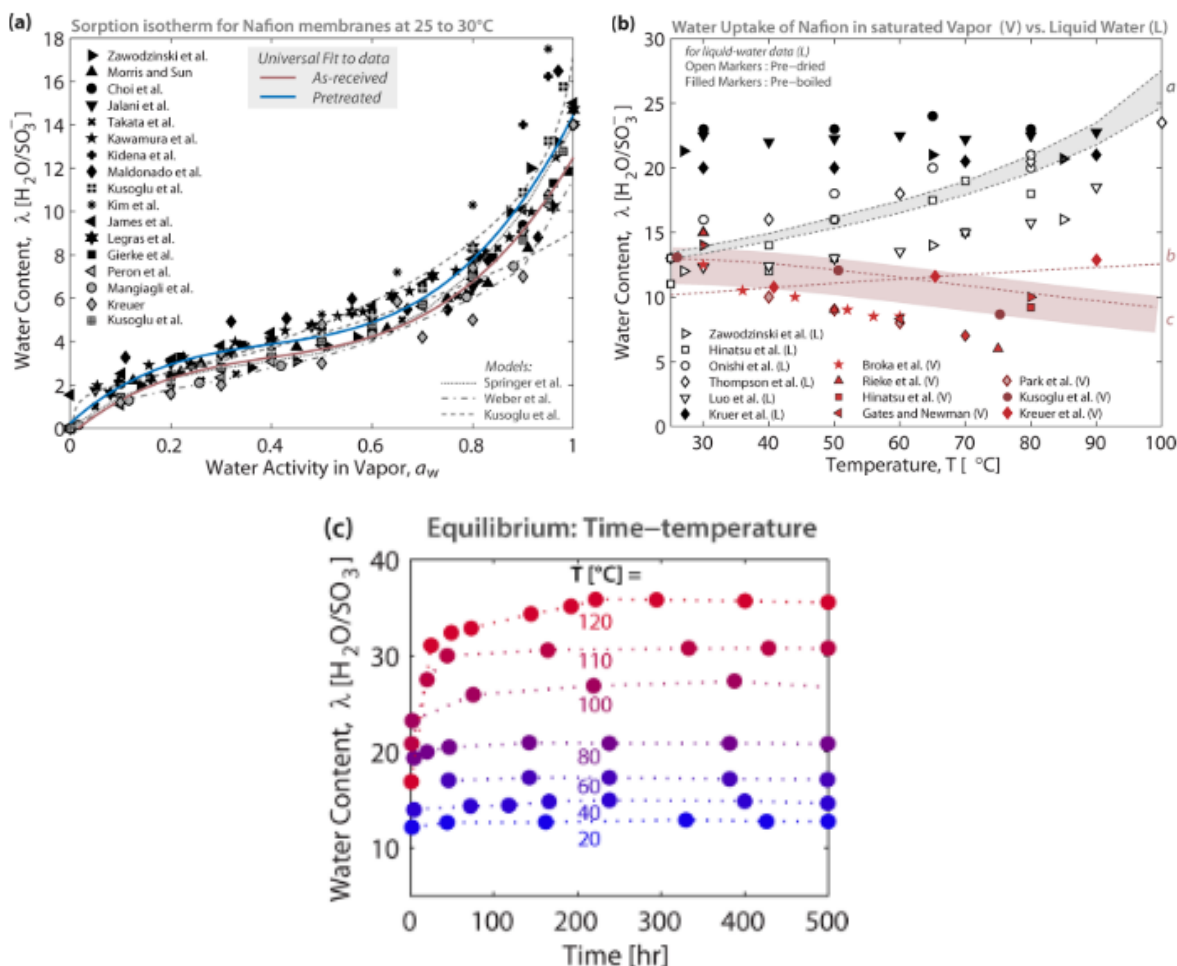


Fig. 2.3. Membrane water content as a function of (a) water activity (b) temperature in vapor and liquid equilibrium and (c) equilibrium time and temperature (Reproduced with permission from [10])

In order to demonstrate the origin and nature of Schroeder's paradox, Bass and Freger [26] carried out water uptake study for Nafion® for activities $a_w < 1$ using solutions of polyvinylsulfonic acid salts, which allowed for measuring isopiestic sorption isotherms in vapor

and liquid equilibrium conditions. They concluded that the Schroeder's paradox is not just an anomaly at $a_w = 1$ but also extends up to $a_w = 0.5$, thereby confirming the difference between vapor and liquid equilibrium. They also investigated the membrane morphology and showed that the membrane surface is hydrophobic in presence of vapor but becomes hydrophilic in liquid. Kusoglu et al. [24] further showed using time-resolved SAXS that a membrane's average d-spacing reaches steady-state in seconds when equilibrated in liquid water. Whereas in vapor, the d-spacing does not reach a steady-state even after a month and is found to be still lower than that in liquid water. It must be noted that it is difficult to achieve truly unit vapor activity ($a_w = 1$) in the presence of thermal fluctuations and liquid–water condensation on the surface, since the latter effect, if occurring, would change the membrane's interfacial condition from vapor to liquid.

Water transport across Nafion® takes place through hydrophilic nano-domains formed because of restructured morphology upon water uptake. The transport process can then be described taking into account the bulk and interfacial resistances. Often Fick's law (Eq. (14)) is used to describe water transport within the membrane under a concentration gradient.

$$N_w = -D_f \nabla c_w \dots\dots\dots(14)$$

Where D_f is the Fickian diffusion coefficient, which is a function of membrane water concentration (c_w) and temperature ($D_f = D_f(c_w, T)$). The interfacial resistance and the bulk resistance to water transport can be determined from a steady- state diffusion experiment by measuring the water flux through the membrane at different water activity gradients, $\Delta a_w = a_{w1} - a_{w2}$, and using samples with different thicknesses (L) (see Fig. 2.4) [10]. The diffusivity can then be determined as a function of average water activity in the membrane from the measured flux.

$$N_w = \bar{c}_w \frac{\Delta a_w}{R} = \bar{c}_w \frac{a_{w1} - a_{w2}}{\frac{1}{k_{m1}} + \frac{L}{D_f} + \frac{1}{k_{m2}}} \dots\dots\dots(15)$$

Where the resistance (R) is the sum of the interfacial resistances ($1/k_m$) at both sides of the membrane and the bulk resistance, which is inversely proportional to the steady-state diffusivity ($1/D_f$) and \bar{c}_w is the average water concentration in the membrane between the two activities.

Thus, a plot of the measured membrane resistance as a function of membrane thickness, L , gives a straight line where the slope yields the diffusivity and the nonzero intercept, if it exists, gives the interfacial resistance. Note that if the intercept is zero, the interfacial resistance does not exist, and Eq. (15) reduces to the original expression, $N_w = c_w D_f \Delta a_w / L$, which means that the process is not limited by interfacial mass transport. A typical resistance vs thickness plot is demonstrated in Fig. 2.4. The interfacial resistance changes with activity and must be considered in modelling water transport across membranes, more so at the membrane-gas interface.

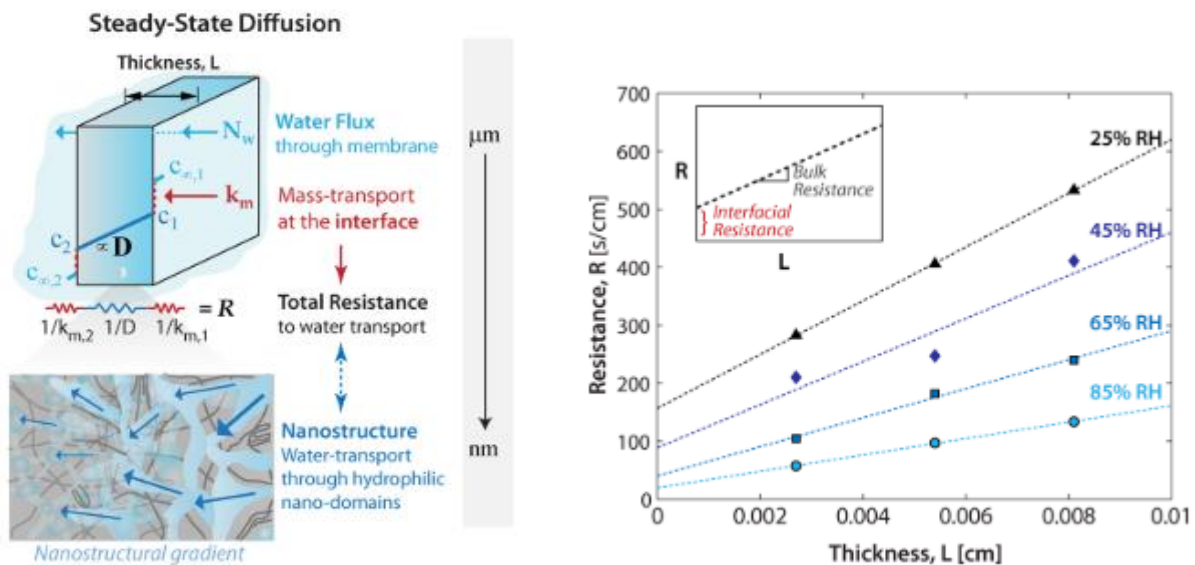


Fig. 2.4. Resistance to steady-state water transport in the membrane as a function of membrane thickness showing the mass-transport resistance at the interface. (Reproduced with permission from [10])

Adachi et al. [27] measured the water flux with liquid-liquid, liquid-vapor and vapor-vapor boundaries and concluded that liquid-liquid equilibrated membrane had the highest transport coefficient (determined as the slope of flux vs chemical potential) and vapor-vapor equilibrated membrane had the lowest flux as shown in Fig. 2.5 below. As noted earlier, the water content and morphology are different based on the phase of water that is in contact with the membrane surface (Schroder's paradox). These results therefore suggest a difference in the nature of the transport mechanism and the membrane microstructure under varied interfacial conditions.

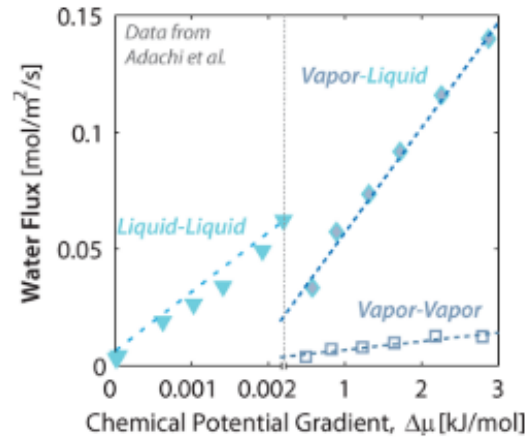


Fig. 2.5. Measured flux with respect to chemical potential gradient for various permeation cases: liquid-liquid permeation (LLP), vapor-vapor permeation (VVP) and liquid-vapor permeation (LVP) (Reproduced with permission from [10])

A possible way to determine the limiting transport mechanism for steady-state water transport, is through the Biot number [10], which is the ratio of diffusion time scale to the interfacial mass transport time scale (Eq. (16)).

$$Bi = \frac{t_{\text{diffusion}}}{t_{\text{interface}}} = \frac{L^2/D}{L/k_m} \dots\dots\dots(16)$$

When $Bi \ll 1$, the transport is limited by interfacial mass transport and when $Bi \gg 1$, the transport is diffusion limited. Eq.(16) suggests that membrane thickness can alter the limiting transport process; transport limitation would be of interfacial origin with decreasing membrane thickness and vice-versa. The problem however with this approach of estimation of limiting resistance is that the characteristic length scale for interfacial transport is often difficult to estimate and hence is assumed as the entire membrane thickness which is possibly incorrect.

Based on the evidence presented above, it becomes clear that in case of water-to-gas humidification which has different equilibration conditions on either interface, contributions of bulk diffusion as well as interfacial resistance must be accounted for while modelling water transport across Nafion® membranes.

2.2.4. Models on membrane based gas humidification

As discussed earlier, membrane based gas humidification is a coupled heat and mass transport process. In addition, there is a different thermodynamic equilibrium at either interface controlling the water concentration gradient for diffusion within the membrane. These two essential physics need to be captured in a model to understand humidification from membranes. Several models have been proposed in the literature to understand gas humidification. Table 2.2 below lists earlier models proposed for membrane-based gas humidification and the lacunae that each of these studies have not addressed.

While few macroscopic models have not studied the interfacial transport, other microscopic models make use of an empirical correlation proposed by Springer et al. [28] which relates water content in Nafion (λ) and water vapor activity (a), for modelling both the membrane interfaces. The problem with such an approach in modelling interfacial equilibrium, lies in two primary factors which are not considered while choosing this empirical correlation: i) Nafion's water uptake is temperature dependent, whereas the empirical correlation is proposed for water vapor uptake at 30 °C only, and ii) Nafion's water uptake differs in the presence of liquid water vs water vapor. Due to these incorrect considerations, the interfacial equilibrium in a water-to-gas Nafion humidifier has not been captured appropriately thus far. Additionally, physical property like specific heat of air which has strong dependence on humidity (see Fig. 2.6), has been considered as constant. This assumption often leads to erroneous predictions since a higher specific heat of humid gas is expected to require more input heat for increasing gas temperature or in other words, a higher specific heat leads to lower outlet gas temperature than the predictions made with a lower constant specific heat.

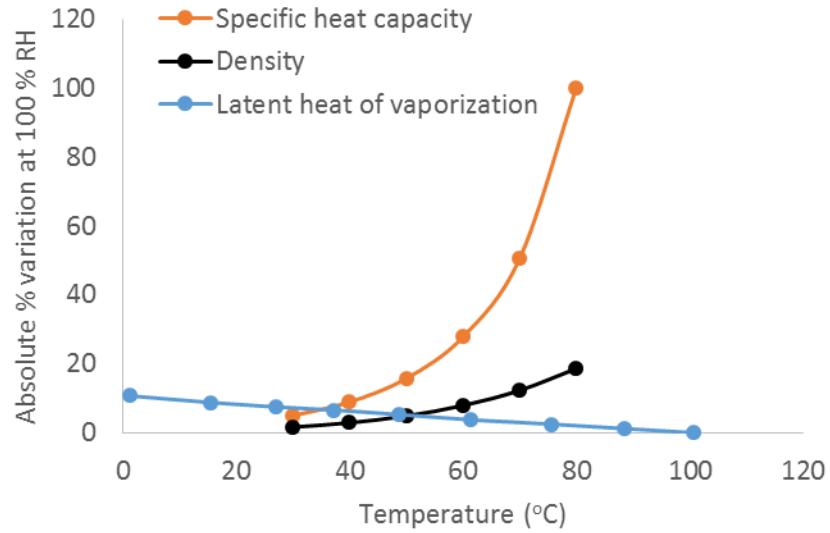


Fig. 2.6. Variation of physical properties of air with temperature and humidity

Table 2.2: Existing models on dense membrane humidifier

Model	Humidifier Type	Heat and Mass Coupling	Equilibrium law	Lacunae
Bhatia et al. 2013 [29]	Nafion, Gas-to-Gas Shell and Tube	Yes	No (Macroscopic model)	<ul style="list-style-type: none"> Accounting for interfacial equilibrium Variation of C_p with humidity

Park and Jung, 2013 [30]	Nafion, Water-to-Gas Shell and Tube	Yes	λ $= 0.043$ $+ 17.81a - 39.85a^2$ $+ 36a^3$	<ul style="list-style-type: none"> Accounting for membrane-water interfacial equilibrium with empirical equation meant for VVP. Variation of C_p with humidity Accounting for thermal gradient across the membrane
Sabharwal et al. 2012 [31]	Nafion, Gas-to-Gas Plate and Frame	Yes	λ $= 0.043$ $+ 17.81a - 39.85a^2$ $+ 36a^3$	<ul style="list-style-type: none"> Accounting for membrane-water interfacial equilibrium with empirical equation meant for VVP. Variation of C_p with humidity
Zhang, 2012 [32]	Modified porous membranes, Water-to-Gas Shell and Tube	Yes	No (Macroscopic model)	<ul style="list-style-type: none"> Accounting for interfacial equilibrium Variation of C_p with humidity

Zhang and Huang, 2011 [33]	PVDF-PVAL Composite, Water-to-Gas Shell and Tube	Yes	No (Macroscopic model)	<ul style="list-style-type: none"> Accounting for interfacial equilibrium Variation of C_p with humidity
Kang et al. 2010 [34]	Nafion, Water-to-Gas Shell and Tube	Yes	λ $= 0.043$ $+ 17.81a - 39.85a^2$ $+ 36a^3$	<ul style="list-style-type: none"> Accounting for membrane-water interfacial equilibrium with empirical equation meant for VVP. Variation of C_p with humidity
Park and Oh, 2009 [35]	Nafion, Water-to-Gas Plate and Frame	No	No (Macroscopic model)	<ul style="list-style-type: none"> Accounting for interfacial equilibrium Variation of C_p with humidity Accounting for the coupling between heat and mass transfer
Park et al. 2008 [36]	Nafion, Gas-to-Gas Shell and Tube	No	λ $= 0.043$ $+ 17.81a - 39.85a^2$ $+ 36a^3$	<ul style="list-style-type: none"> Variation of C_p with humidity Accounting for the coupling between heat and mass transfer

Chen et al. 2008 [37]	Nafion, Water-to- Gas Shell and Tube	No	λ $= 0.043$ $+ 17.81a - 39.85a^2$ $+ 36a^3$	<ul style="list-style-type: none"> Accounting for membrane-water interfacial equilibrium with empirical equation meant for VVP. Variation of C_p with humidity Accounting for the coupling between heat and mass transfer
--------------------------	--------------------------------------------------	----	--------------------------------------------------------------	-------------------------------------------------------------------------------------------------------------------------------------------------------------------------------------------------------------------------------------------------------------------------

The lacunae mentioned in Table 2.2 have been addressed in this thesis by careful consideration of

- Dual equilibrium laws at the membrane interfaces:* The membrane-air equilibrium has been modeled using a modified form of Henry's law (Eq.(17)) as proposed by Monroe et al. [38]. The membrane-water equilibrium has been modeled using an empirical correlation developed from experiments performed on Nafion 212 (50 μm) membrane.
- Intricate couplings of heat and mass transport, for a Nafion® hollow fiber membrane humidifier (PermaPure FC200 module):* This is primarily achieved by coupling the governing energy and mass balance equations.
- Variation in specific heat capacity of air with humidity:* This is achieved using Eq. (18) which related the specific heat of air to its specific humidity.

$$P_{eq} = P_{v,sat} \frac{C_L}{C_{max}^{liq}} \dots\dots\dots(17)$$

$$C_{pa} = C_{pa,dry} + C_{pv}X \dots\dots\dots(18)$$

In Eqs. (17), P_{eq} is the vapor pressure at the membrane-air interface which is in equilibrium with water concentration in the membrane C_L , $P_{v,sat}$ is the saturation vapor pressure at water temperature, C_{max}^{liq} is the maximum water concentration in membrane. In Eq. (18), $C_{pa,dry}$ (1.005

(kJ/kg K)) is the specific heat of dry air and C_{pv} (1.82 (kJ/kg K)) is the specific heat of water vapor. X is known as the mixing ratio (grams of water vapor per kg of dry air).

2.3. Porous membranes for gas humidification

2.3.1. Overview

Porous membranes are widely used for separation processes like ultrafiltration, microfiltration etc. However, in all these processes, the separation is achieved based on size exclusion under a differential transmembrane pressure. Typical porous membranes used in gas humidification in the form of membrane contactors differ from membranes used in typical separation processes. Membrane contactors although popularly used for gas absorption and liquid-liquid extraction, do not offer any selectivity for a particular species with respect to another, but simply act as a barrier between the phases involved by allowing their contact over a well-defined interfacial area [39]. The two phases are separated by the membrane and do not mix or disperse. The species are transferred from one phase to the other by only diffusion. The membranes are usually microporous, symmetric, and hydrophobic (examples: expanded PTFE, polypropylene, silicone rubber)[40]. The hydrophobic pores prevent liquid water from wetting the pores below capillary pressure. Thus, the water vapor has to diffuse across the membrane thickness to humidify the gas. This adds to the membrane mass transport resistance. Being symmetric, hydrophobic and typically used for different applications, the limitations with membrane contactors used for gas humidification are i) the narrow handle on the pore size distribution, and ii) slow heat and mass transfer. Hence, an integrally skinned asymmetric membrane treated for the macrovoids to act as water reservoirs is hypothesized to reduce this resistance and improve heat and mass transport for gas humidification application.

2.3.2. Asymmetric membranes

Asymmetric membranes consist of pores ranging from a few nm to a few microns along the thickness of the membrane, with bulk of the membrane being macro-porous matrix sandwiched between extremely thin (few hundred nm) nano-porous or dense skin layers. For a dense skin, the solubility of the permeant in the polymer dictates the flux. However, for a porous skin, the flux can be regulated by both bulk and skin resistances. A variety of polymers can be used for making asymmetric membranes. These membranes are prepared using phase inversion in a

spinning machine (for hollow fibers) or via solution casting (for flat sheet). In this thesis, we focus only on hollow fiber membranes since they provide a major advantage of high surface area per unit volume for heat and mass exchange [39].

A hollow fiber spinning process is shown in Fig. 2.7a. The process known as dry-wet phase inversion consists of three stages once the dope and the non-solvent are extruded simultaneously from a spinneret (tube-in-orifice arrangement):

- i. Air gap, responsible for
 - a. quenching of inner layer and inner skin formation
 - b. slower phase inversion at the outer layer due to moisture present in the air gap
- ii. Coagulation bath, responsible for
 - a. quenching of the outer layer and outer skin formation
 - b. rapid exchange of solvent and non-solvent
- iii. Post treatment, responsible for
 - a. removal of excess solvent and complete phase separation
 - b. controlling porosity and hydrophilicity of the membrane

Together, the spinning process conditions viz. dope composition, coagulation bath composition, air gap distance, air gap temperature, air gap humidity, bore non-solvent flow rate, coagulation bath temperature, take up speed and post treatment, contribute towards the resulting hollow fiber membrane microstructure. A typical asymmetric hollow fiber structure is shown in Fig. 2.7b.

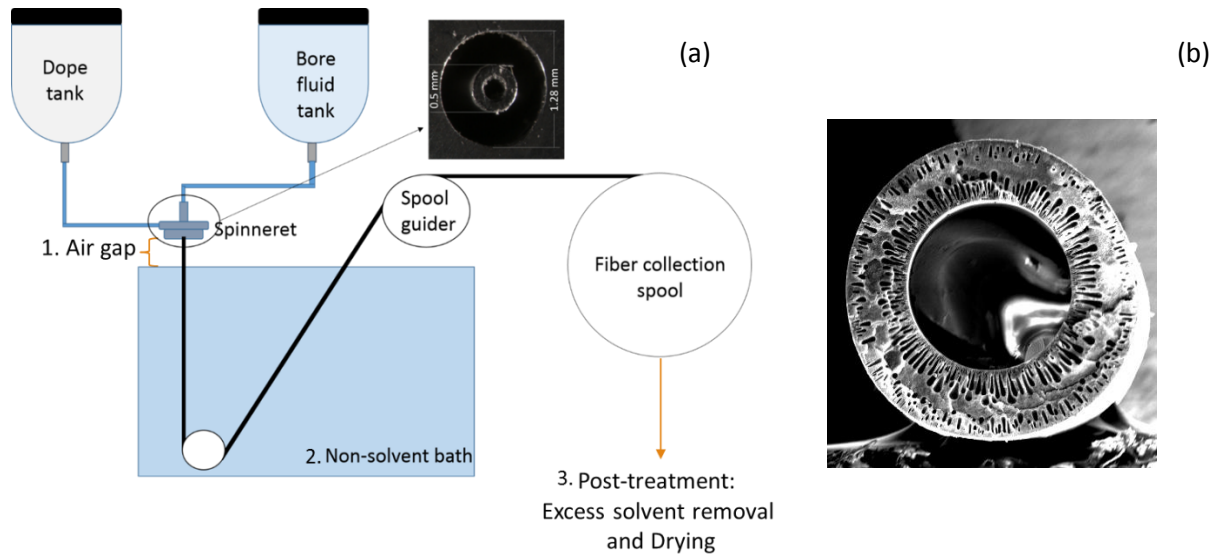


Fig. 2.7. (a) Spinning process (dry-wet phase inversion) for hollow fiber membranes (b) typical asymmetric hollow fiber membrane

In case of flat-sheet membranes, the dope solution is knife casted on a glass plate. The dope composition, exposure time prior to coagulation and temperature of the coagulation bath together contribute to the resulting membrane microstructure. Often, in flat sheet, the membrane region near the glass surface is spongy due to slow phase separation and the outer surface facing the non-solvent is prone to develop macrovoids due to rapid unmixing of solvent and non-solvent. A schematic illustration of an asymmetric flat sheet membrane is shown in Fig. 2.8. Again, the skin can be porous or non-porous based on the process parameters. While a dense skin is formed with higher exposure time before coagulation or a thin-film polymer coating, a porous skin is usually a consequence of small exposure time or immediate coagulation after casting [41].

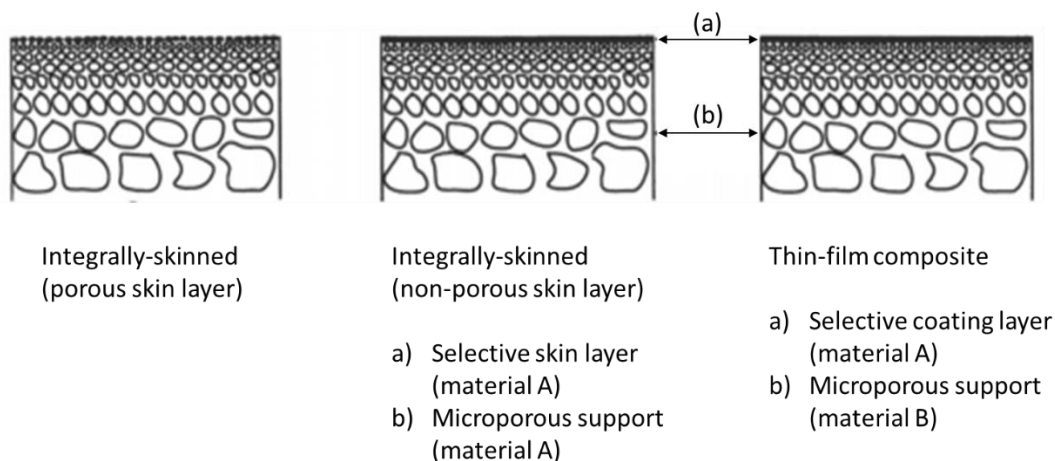


Fig. 2.8. Typical asymmetric flat sheet membrane

2.3.3. Asymmetric membranes for gas humidification

Asymmetric membranes have been widely used for applications like gas separation, water treatment etc. However, not many studies have been reported for its use in gas humidification. Among the studies reported, polymers like polyethersulfone (PES) [42,43], polysulfone (PSF) [43], poly(N,N-dimethylaminoethyl methacrylate)/polyacrylonitrile (PDMAEMA/PAN) composite [44] membrane have been used.

Bakeri et al. [42] developed PES hollow fiber membranes using a dry-wet phase inversion spinning process. The spinning parameters used are provided in Table 2.3 below. Some of the important spinning parameters like take-up speed, dope pressure, bore flow rate etc., were not provided by the authors.

Table 2.3: Spinning process conditions

Dope composition wt% (PES/Water-NMP)	15/85
Air gap	1 cm
Bore fluid	Distilled water
External coagulant	Tap water
Bore fluid temperature	Room temperature
External coagulant temperature	Room temperature

The resultant membrane microstructure is shown in Fig. 2.9a below. The irregular tube ID suggests that the spinning process was not optimized. The developed membranes were reported to have a bulk porosity of 0.834, effective surface porosity (porosity per unit length) of 28 m^{-1} ,

mean pore size of 653 nm and liquid entry pressure of water of 4.2 bar. They tested the membranes for gas humidification for different air (shell side fluid) and water (tube side fluid) flow rates. Fig. 2.9b shows the variation of outlet gas RH with increasing air and water flow rates at a temperature of 60 °C and air pressure of 1 bar. The membrane area used for obtaining the performance was not reported and thus any evidence of the system's superior performance over other membrane systems remains inconclusive. In addition, the developed membranes were found to have poor thermal performance with approach temperature ($T_{w,in}-T_{a,out}$) @ 3 L/min gas flow rate and 1 m/s water velocity, found to be > 29 °C. The reason for poor humidification performance can be attributed to the hydrophobic nature of PES, poor thermal conductivity of dry polymer and possibly small membrane area (which was not reported).

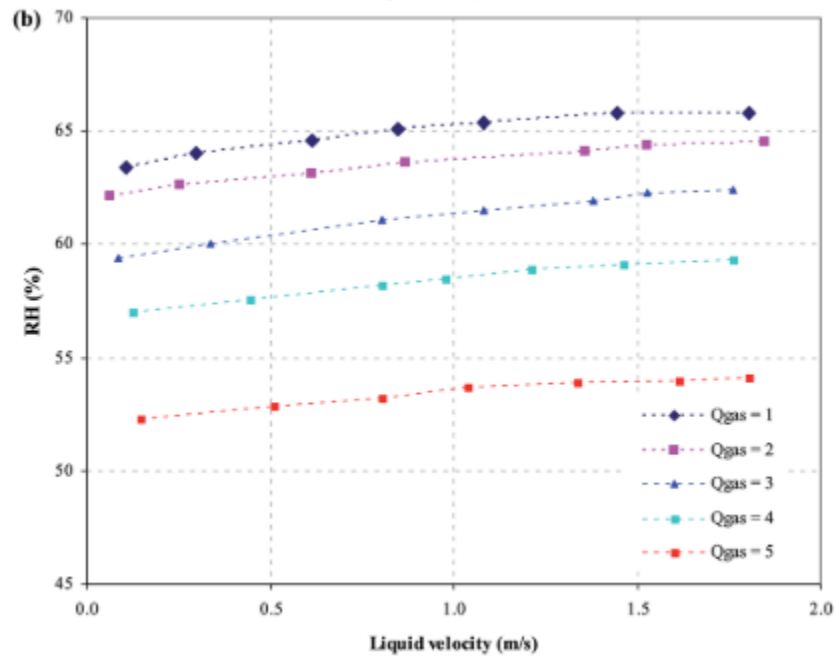
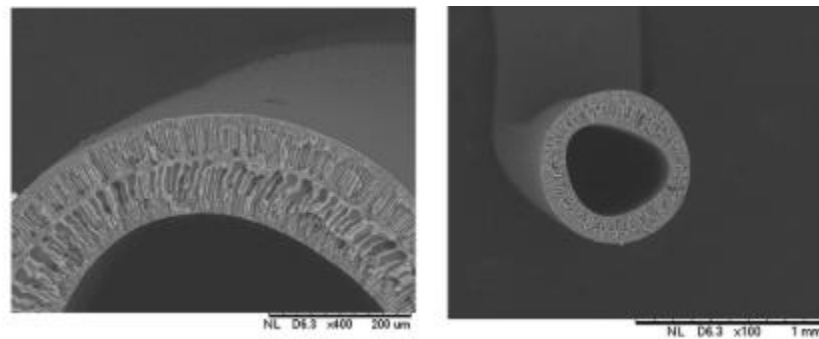


Fig. 2.9. (a) SEM cross-section image of PES hollow fiber (b) Outlet gas relative humidity as a function of liquid velocity and gas flow rates (Reproduced with permission from [42])

Samimi et al. [43] studied a series of polyethersulfone and polysulfone flat sheet membranes by varying polymer concentration (7, 10, 16 wt %), solvent (DMF/NMP) and incorporating TiO_2 (0/0.1 wt %) nanoparticles to improve hydrophilicity of the membranes. The membranes were prepared by wet phase inversion solution casting with water as a non-solvent. The active area of the membranes tested on a plate and frame module setup was 47.3 cm^2 . The measured outlet gas relative humidity for the different membranes operated at 25°C is shown in Fig. 2.10. It can be seen that incorporation of 0.1 wt % TiO_2 although improves gas humidity but only marginally and thus does not provide appreciable cost-performance benefits for such a composite system. In addition, the study does not discuss the heat transfer across these asymmetric membrane systems which is a major lacuna especially in studying gas humidification.

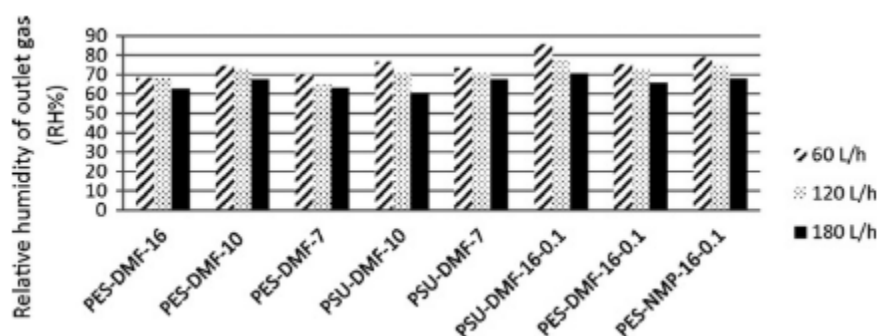


Fig. 2.10. Relative humidity (RH %) of outlet gas for different membranes in various gas flow rate of 60, 120 and 180 L/h. (Reproduced with permission from [43])

Runhong et al. [44] studied a PDMAEMA/PAN composite membrane system for gas humidification. They used a commercial PAN ultrafiltration membrane of thickness $70 \mu\text{m}$ which was rinsed with deionized water prior to use as a substrate. The PDMAEMA/PAN composite membranes (area = 16.6 cm^2) were prepared by interfacial crosslinking of a thin layer of PDMAEMA coated onto the PAN substrate. The humidification tests were conducted at isothermal conditions of 25°C with liquid water as feed on one side and dry nitrogen gas as sweeping gas on the other side of the membrane. The outlet water mole fraction in humidified gas and average water transfer rate are plotted as a function of air flow rate in Fig. 2.11(a,b). As expected, the water mole fraction reduces with increasing air flow rate due to the effect of

residence time. However, the water transfer rate increases due to higher transport gradients developed at higher gas flow rates. The study does not address heat transport across the membrane since isothermal conditions were considered. This too leads towards inconclusive evidence in support of these membranes to be used for gas humidification application over a wide range of operating conditions.

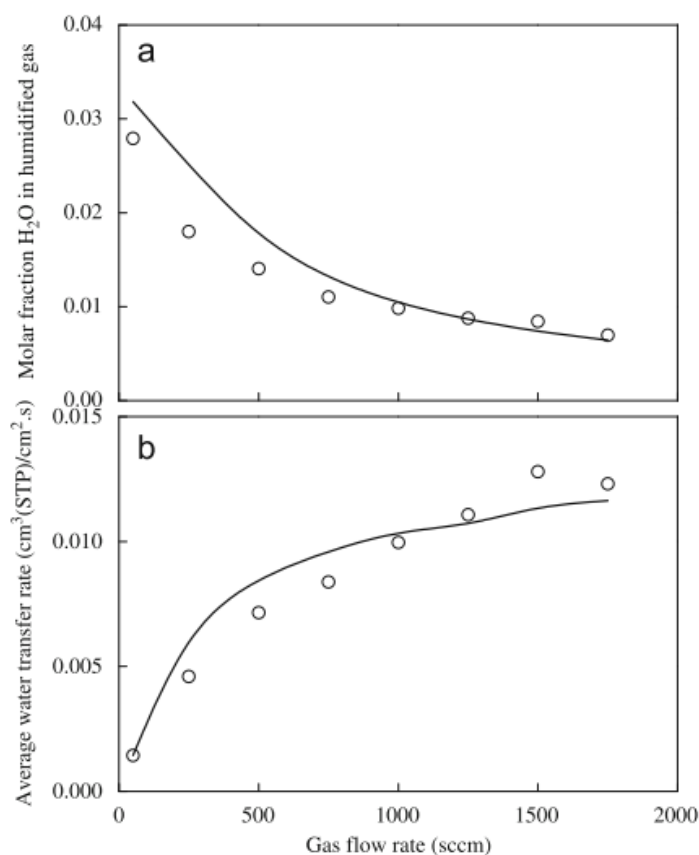


Fig. 2.11. Effect gas flow rate on (a) water vapor concentration in outlet stream and (b) average mass transfer rate of water. Temperature 25 °C. Symbols represent experimental data, and the solid lines are calculated values based on the cross flow model. (Reproduced with permission from [44])

As can be seen from the literature presented above on asymmetric membranes developed for gas humidification application, major experimental lacunae have been in evaluating the thermal performance, and in understanding the coupling of heat and mass transport. This is a critical gap in using asymmetric membranes for gas humidification, which has been addressed in this thesis.

2.3.4. Models on asymmetric membrane based gas humidification

In most previous studies attempting to model membrane based gas humidification, the membrane has been considered as a “black box” with constant transport properties, which are

usually determined by a single permeation experiment or adjusted as floating parameters to best fit the experimental results [45–49]. While this approach simplifies the modeling of the complex membrane microstructures, it is destined to fail in making accurate humidifier performance predictions under conditions different from those of the experiment using which the parameters were derived, especially for asymmetric membranes. The role of membrane microstructure in heat and mass transport must be inherent to the model in order to avoid these model limitations.

Zhang [50] proposed a model for heat and mass transport across asymmetric flat sheet membrane with finger like macrovoids. The study was performed for an in-house PVDF asymmetric membrane shown in Fig. 2.12a. The model is built for gas-to-gas humidification on the following considerations

- The membrane is considered to have three layers
 - Sponge like porous support layer
 - Sponge layer with finger like macrovoids
 - Porous skin layer
- Due to no transmembrane pressure, the mass transport is governed by a combination of Knudsen and ordinary diffusion
- Porosity of each layer is estimated from SEM
- Resistance model is used for estimation of effective diffusivity and effective thermal conductivity
- NTU method is used for heat and mass transport
- No phase change was considered
- The anticipated concentration profile of water vapor across the membrane is shown in Fig. 2.12b

While, the model considers the role of membrane microstructure on heat and mass transport, there are few major flaws or limitations:

- Considering Knudsen transport despite Knudsen number $\ll 1$, raises severe concerns on the correctness of the model.
- Interfacial equilibrium at the respective membrane interfaces is not considered.

- Constitutive layer porosity estimation from SEM is not discussed.
- Effect of operating temperature is not considered in model validation.

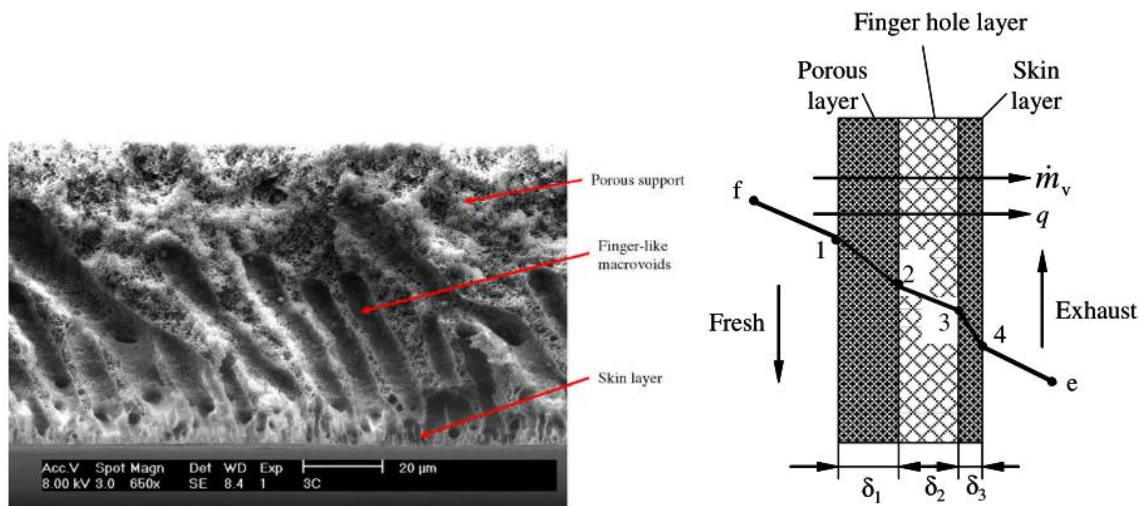


Fig. 2.12. (a) SEM cross-section image of PVDF flat sheet membrane (b) water vapor concentration profile across the membrane (Reproduced with permission from [50])

Zhang [51] also reported a mesoscale Lattice-Boltzmann simulation approach to model moisture transport through composite membranes with a porous support layer and a dense skin layer. While a very detailed analysis of mass transport was presented, no discussion was provided on the heat transport and the coupled nature of heat and mass transport in asymmetric membranes.

More recently, a comprehensive model was proposed by Amin et al. [49] for an enthalpy exchanger (see Fig. 2.13(a,b)) consisting of an asymmetric composite membrane (see Fig. 2.13c) having a dense skin (5 μm thick) and a porous substrate layer (~100 μm thick, pore size of 38 – 100 nm). Fig. 2.13d shows a representation of the vapor pressure and moisture concentration profiles in the composite membrane model. The transport mechanism across dense skin is considered to originate from solution-diffusion and transport through the porous substrate is assumed to be due to vapor pressure difference driven pore-diffusion. While the model is comprehensive and effectively captures the role of membrane microstructure in mass transport, it is only applicable for a gas-to-gas (VVP) transport. The same is not applicable for water-to-gas (LVP) transport, which undergoes two phase change processes: liquid water to membrane phase at membrane-water interface followed by water in membrane phase to vapor phase at the membrane-gas interface. Hence, different equilibrium laws govern the membrane phase water

concentration at each interface. Additionally, the membrane system considered by Amin et al. is a composite asymmetric membrane with a dense membrane coated on a porous support. This system differs from an integrally-skinned asymmetric membrane which typically has a nanoporous skin on one or both sides of the membrane. Thus, the proposed model by Amin et al. is not applicable for the membrane system under consideration in this thesis.

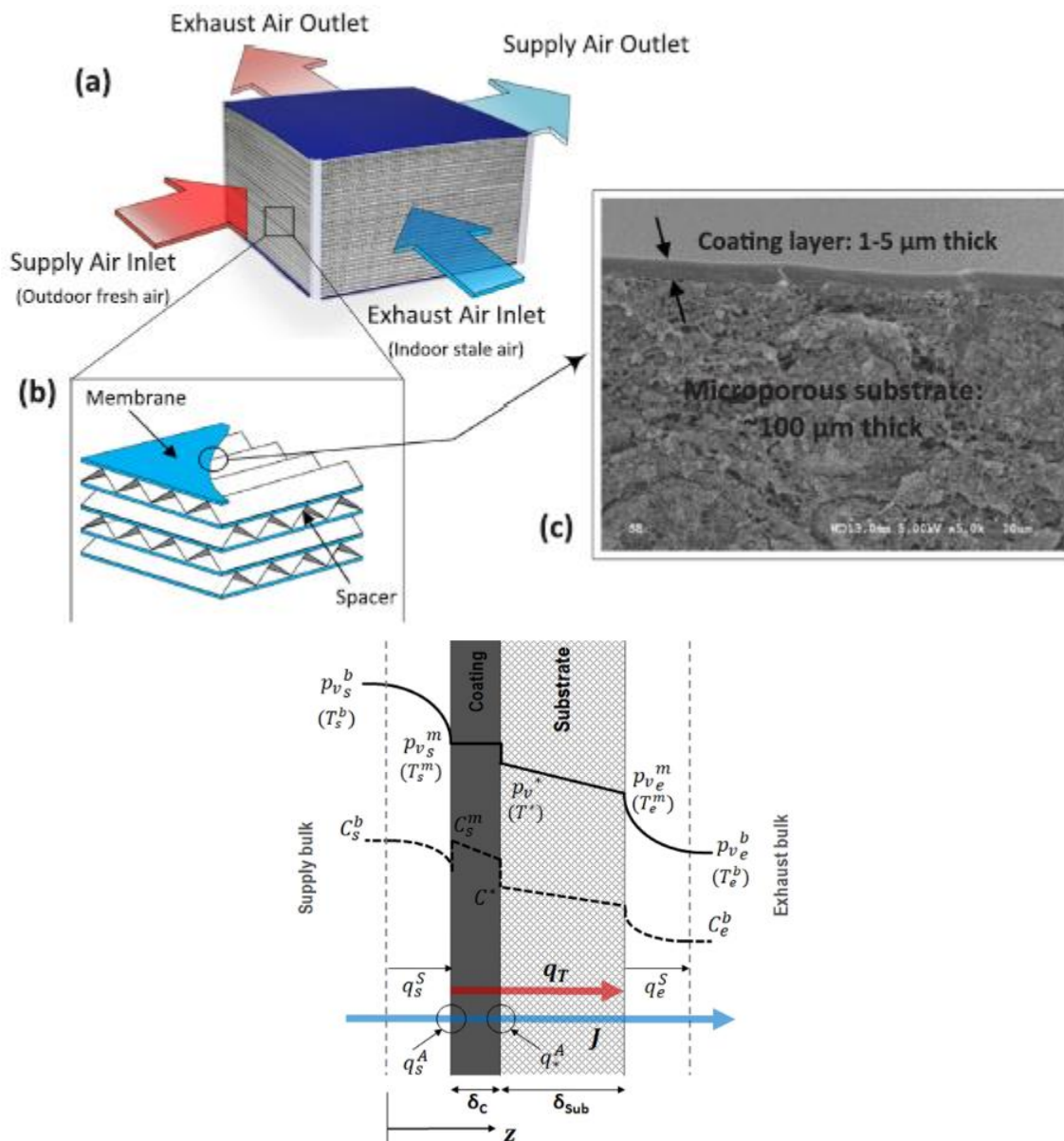


Fig. 2.13. (a) Schematic illustration of an enthalpy exchanger system (b) Zoomed image of the flow channels and membrane unit inside the enthalpy exchanger (c) SEM image of the membrane cross-section, (d) Schematic representation of the heat and moisture transfer through the asymmetric composite membrane. (Reproduced with permission from [49])

Table 2.4 below summarizes the most relevant literature on asymmetric membranes used for heat and mass exchange. The table also lists the lacunae or remarks for the presented literature which have been addressed in this thesis.

Table 2.4: Literature on porous/asymmetric membranes used for gas humidification

Reference	Membrane	Study	Remarks
Park et al. (2005) [52]	PSF flat sheet	Experimental Liquid-Vapor Permeation (LVP)	<ul style="list-style-type: none"> Experimentally compared PSF flat sheet UF membranes with Nafion based plate-and-frame humidifiers for fuel cell humidification Demonstrated superior outlet gas humidity from PSF humidifiers in comparison to Nafion Did not study thermal performance of the humidifier
Zhang (2009) [50]	PVDF flat sheet	Experimental + Modelling Vapor-Vapor Permeation (VVP)	<ul style="list-style-type: none"> Proposed a phenomenological model based on resistance-in-series approach for estimating membrane mass transport resistance Studied coupling of heat and mass transport in gas humidification using flat sheet PVDF asymmetric membranes Knudsen diffusion was considered as a transport mechanism despite $Kn \ll 1$ which is a major concern in the model. No experimental evidence in support of constitutive layer porosity was presented Interfacial equilibrium was neglected
Runhong et al. (2010) [44]	PDMAEMA/PAN composite flat sheet	Experimental Liquid-Vapor Permeation (LVP)	<ul style="list-style-type: none"> Experimentally evaluated PDMAEMA/PAN composite flat sheet membrane for gas dehydration ($\text{CH}_4/\text{H}_2\text{O}$ feed) and humidification application. A phenomenological mass transfer equation was proposed

			<p>to correlate the water transport rate with membrane area and overall mass transfer coefficient.</p> <ul style="list-style-type: none"> • Non-isothermal operation of membrane humidifier was not studied
Ramya et al. (2011) [53]	Expanded PTFE	Experimental Liquid-Vapor Permeation (LVP)	<ul style="list-style-type: none"> • Experimentally evaluated porous PTFE membrane for gas humidification in PEM fuel cell • Demonstrated comparable fuel cell performance with bubble humidification • Did not study thermal performance of the humidifier
Samimi et al. (2011) [43]	PES and PSF flat sheet	Experimental Liquid-Vapor Permeation (LVP)	<ul style="list-style-type: none"> • Experimentally demonstrated humidification from PES/PSF membranes and PES/PSF membrane with TiO₂ nanoparticles • A small improvement in humidity with incorporation of TiO₂ nanoparticles was observed • Non-isothermal operation of membrane humidifier was not studied
Min et al. (2011) [54]	PES and Cellulose	Experiment + Modelling Vapor-Vapor Permeation (VVP)	<ul style="list-style-type: none"> • Experimentally tested commercial porous PES and cellulose membranes • Experimentally estimated the contribution of interfacial and bulk membrane resistances to mass transport. • Theory for mass transport was proposed taking into account a normal pore size distribution but not validated • Knudsen diffusion as a transport process was considered despite $Kn \ll 1$ (pore size $\sim 0.45 \mu\text{m}$)
Min et al. (2013) [55]	-	Modelling	<ul style="list-style-type: none"> • A macroscopic model was proposed for heat and mass transport (VVP) across a

		Vapor-Vapor Permeation (VVP)	<p>membrane which is considered as a black-box with fixed transport and material properties.</p> <ul style="list-style-type: none"> • Coupling of heat and mass transport was considered using Chilton-Colburn analogy • Model was not validated with experimental results
Yang et al. (2014) [56]	Porous PVDF and PTFE flat sheet	Experimental Liquid-Vapor Permeation (LVP)	<ul style="list-style-type: none"> • Experimental studied the effect of flow arrangement of humidification effectiveness of a flat-sheet porous membrane humidifier • PVDF membranes were found to provide higher humidity effectiveness over PTFE membranes • Thermal effectiveness was not studied
Bakeri et al. (2015) [42]	PES hollow fiber	Experimental Liquid-Vapor Permeation (LVP)	<ul style="list-style-type: none"> • Demonstrated PES hollow fiber membranes for gas humidification • Studied the effect of water flow rate, gas flow rate, water temperature, and gas pressure on outlet gas relative humidity • No discussion was presented on the thermal effectiveness of the developed membranes
Amin et al. (2018) [49]	dPoint MX4™	Experimental + Modelling Vapor-Vapor Permeation (VVP)	<ul style="list-style-type: none"> • Proposed a model for heat and mass exchange in an enthalpy exchanger comprising of a commercial composite membrane having a dense layer on top of a porous support. • Role of membrane microstructure on mass transport was modelled based on resistance-in-series approach • Role of membrane microstructure on heat transport was assumed

			negligible due to membrane thermal resistance contribution being < 5% to the overall resistance.
--	--	--	--------------------------------------------------------------------------------------------------

2.4. Internal humidification in PEM fuel cells

2.4.1. Overview

Proton exchange membrane fuel cells have been looked upon as one of the most promising clean energy solution for automotive applications [9,57]. With the world facing energy crisis and global warming issues in an alarming state, the need of the hour is to switch from conventional energy sources like coal and petroleum to sustainable renewable/clean energy sources. However, the challenges that persist in widespread adoption and market penetration of clean technologies are their high capital costs and lack of technology maturity [58,59].

Presently, the cost of a PEM fuel cell stack has decreased drastically to less than 50% of the overall system [60]. Two major and persistent issues that have been nagging ever since proton exchange membrane were introduced for fuel cells are its water and thermal management [61–64]. Several methods have been adopted to address the same but at the expense of high parasitic power loss, increased system complexity and high cost. These methods invariably make use of external humidifiers and cooling system for providing humidified gases to retain sufficient moisture content in the MEA and remove excess heat to prevent drying out of membrane, respectively. Such external units consume significant power for their operation and make the system bulky and costly. Therefore, more advanced techniques in the form of internal humidification and evaporative cooling have been sought out by researchers that render passive means of water and thermal management in PEMFC without significant addition to the cost and parasitic power loss of the overall system.

2.4.2. Water management in PEM fuel cells

As discussed in Chapter 1, PEM fuel cells require both gas streams to be humidified in order to maintain the moisture content of the Nafion® membrane. Often, more humidification is required at the anode side due to electro-osmotic drag while less on the cathode due to water generated from the reaction. On one hand, while it is necessary to provide humidification of gas streams for maintaining the ionic conductivity of membrane, it is also necessary to remove the product water from the fuel cell, and then either reuse it for humidification and/or dispose of the excess product water. The balance of these two tasks comprises water management of PEM fuel cells.

In order to provide water management in a PEMFC system there are certain well-established methods which have been widely accepted. While on the one hand these methods solve water management issue, on the other hand they trade off with increased space requirements and balance-of-plant components resulting in high system cost and parasitic power loss.

One of the conventional methods of humidifying the reactant gas streams is to use a bubble humidification unit (discussed in Chapter-1) wherein each gas stream is bubbled separately through a column of water at a temperature slightly below or at the operating temperature of the fuel cell depending on the percentage relative humidity required. The temperature of the bubbler needs to be controlled in order to provide sufficient humidity levels at each electrode. If the water temperature in the bubbler is far below the fuel cell temperature, the amount of water vapor ($\text{kg H}_2\text{O}/\text{kg gas}$) thus generated will be insufficient for the gas stream to provide enough humidification. Whereas if the water temperature is higher than the fuel cell temperature, the water vapor might condense inside the relatively cool stack and cause waterlogging (flooding) of the active sites of the electro-catalyst (especially on the cathode).

Other methods of humidification of gases include using a membrane-based external humidifier for each gas stream which selectively permeate water to the gas streams flowing across it. The humidification is provided in a gas-to-gas or water-to-gas manner. In the former, the hot and humid exhaust of the fuel cell outlet gas stream is used for inlet gas humidification. In case of water-to-gas humidification, hot water is supplied by a water pump to the humidifier. Water bath maintains the necessary temperature of water for achieving the desired humidity levels.

Alternatively, water used for cooling fuel cell stacks can also be used for gas humidification in a water-to-gas humidifier.

The removal of water from the cathode is one of the major aspects of water management in PEMFC. Several techniques have been used wherein the gas diffusion layer is teflonized to some degree to provide hydrophobicity to the cathode and drive water out by a combination of gravity and convection of gas flowing downwards through the flow field [65]. Other non-conventional methods include incorporation of wicking materials in channels or forming channels using the wicking materials as bipolar plates [66,67]. The wicking materials take up water using capillary action and distribute it uniformly throughout the channel. Such techniques are very useful in preventing flooding by ensuring uniform distribution of water at cathode. However, placing electrically non-conducting wicking materials reduces effective active area and increases Ohmic resistance of the cell thereby reducing the performance. Yet another way to remove water is to simply operate the fuel cell without any humidification of the reactant gases (commonly known as dry-feed operation) and allow evaporation of water at the cathode to evaporate into the rather dry cathode gas stream. Operating the cell without any cathode humidification causes the Nafion® membrane to have lower moisture content, and consequently, such an arrangement leads to fuel cell operation at low current densities due to poor ionic conductivity of the partially dehydrated membrane. This method essentially sacrifices power density and conversion efficiency for the convenience of being able to dispose of the product water as a gas that is vented with the cathode exhaust stream.

2.4.3. Internal humidification with evaporative cooling techniques in PEM fuel cell

Several fuel cell manufacturers like Intelligent Energy, UTC Ltd., General Motors, etc. have carried out years of research in successfully developing PEMFC stacks using evaporative cooling concept for water and thermal management. In order for evaporative cooling to operate, all that is needed is a porous matrix that can hold water or a substrate that can facilitate water transport over it, a source of heat, and air flow which is preferably dry. The wet surface when in contact with a heat source, loses latent heat to evaporate water which simultaneously humidifies the gas and cools down the surface. The concept of internal humidification with evaporative cooling has been incorporated into the fuel cells in several forms.

2.4.3.1. Liquid water injection into the fuel cell

A method that has been proposed by Intelligent Energy is a modified design of bipolar plates to provide liquid water directly into the channels to facilitate simultaneous internal humidification of membranes and cooling [68,69]. Figure 2.14(a, b) shows a schematic representation of a metallic foil and a modified bipolar design used by Intelligent Energy Ltd. for their metallic bipolar plate stacks. Required thickness of the metallic foil was reported to be ~40 microns. The complicated design of the bipolar plate involves manufacturing limitation.

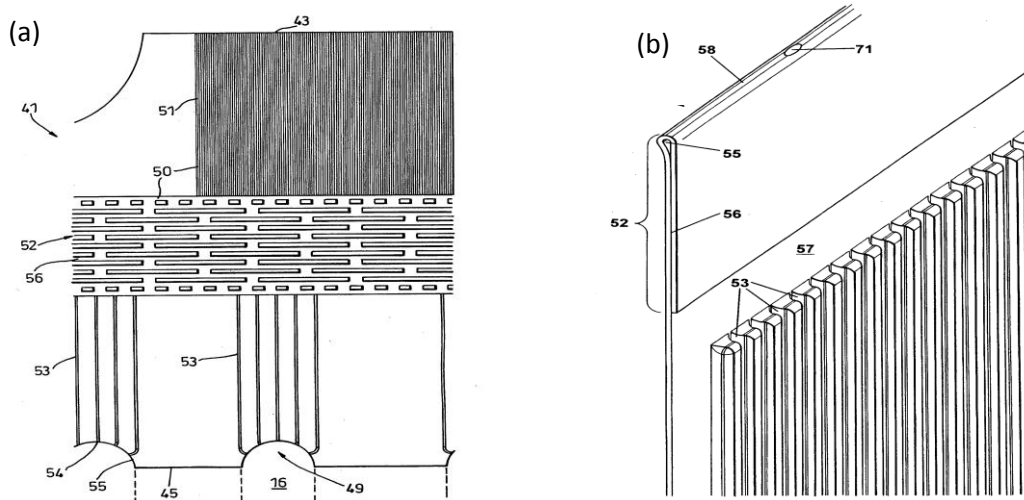


Fig. 2.14. a) Metallic foil used by Intelligent Energy Ltd. and b) Plate design used by Intelligent Energy Ltd. [68,69]

2.4.3.2. Porous water transport plates

Concept of porous water transport plates for fuel cell operation was proposed and continuously advanced by UTC power. The porous bipolar plates, known as water transport plates (WTPs), allow direct exchange of liquid water between the gas channels and the cooling channels through the pores. With proper design of the size, the distribution and the surface hydrophobicity of the pores to form a wet seal to prevent hydrogen or oxygen entering the coolant stream, simultaneous internal humidification and evaporative cooling of the PEMFC stacks can be realized [70]. The membrane dry out or flooding issues can also be prevented. It works based on differential pressure flow of anode and cathode gas streams where the water movement occurs across the WTP (Fig. 2.15., [71]) Moisture in the membrane is maintained due to inherent electro-osmotic drag process. Cooling occurs when the low humid air passes over the porous plates and evaporates the water. The disadvantages of this method however are that the pores have to

always remain filled with water to prevent gas leakage to opposite sides. Besides, the side facing the gas stream must have hydrophobic pores to facilitate water transfer from pores to the stream. Thus, manufacturing of such plates becomes expensive.

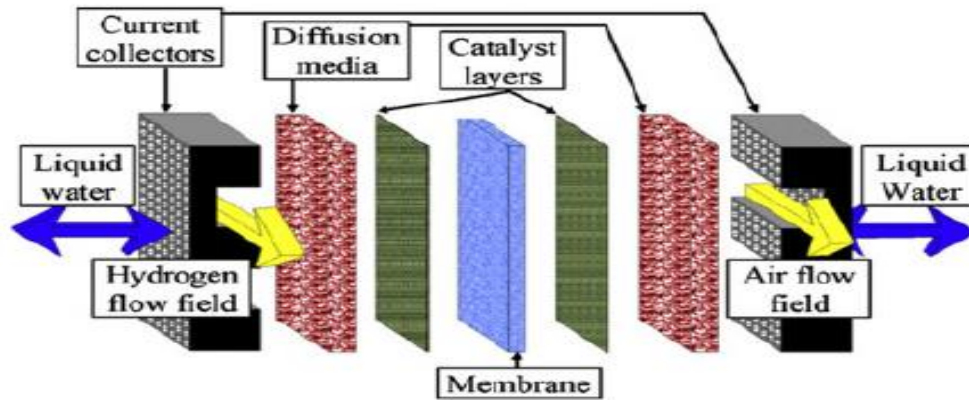


Fig. 2.15. Schematic of PEMFC with WTPs allowing liquid water exchange (reproduced with permission from [71])

2.4.3.3. Wicks as lands or channels

Incorporation of wicks as lands or channels typically makes use of materials that can facilitate capillary action of water for transport into the fuel cell internally. They may be electrically non-conducting when used as lands or channels in the bipolar plate as shown in Fig. 2.16., [72]. The liquid water transported along the wicking material is used to maintain the hydration levels and cool the fuel cell due to the endothermic latent heat of vaporization of the water. In most operating circumstances (especially at high current densities), the water generated at the cathode is insufficient to achieve the necessary cooling. The heat generated during normal operations generally exceeds the cooling effects provided by the heat of vaporization of the product water. Thus, unless a region experiences localized cooling, or the cell is under start-up conditions where the heat is used to increase the thermal mass of the stack, there will be a need to cool the cell by introducing external water for vaporization. As the water is evaporated, the wicking material will draw additional liquid from the liquid reservoir to the fuel cell via the header and into the rows of wicking material to provide additional necessary cooling effects.

Wicking material is preferably a porous material, which has a wicking rate that is dependent upon both the pore size and permeability of the material. Goebel et al. [72] suggested suitable characteristics of a wicking material which can be used in PEM fuel cells. Preferred ranges of pore size diameter in wicking materials are within the range of about 5 - 30 μm and the void fraction ranges from about 60 - 80%. Preferred thickness of each row of wicking material is between 0.2 mm and 1 mm. The wicking material should have good thermal conductivity values $> 2 \text{ W/mK}$ and an electrical resistivity of $< 500 \text{ mOhm-cm}$. Other factors include the wicking velocity of the material determined by the pore size (and void fraction), and the hydrophobic and hydrophilic properties of the material. Examples for wicking materials include fiber mats, mesh, screen, metal foams, sprayed metal powders, polymers with conductive particles dispersed therein, and mixtures and equivalents thereof.

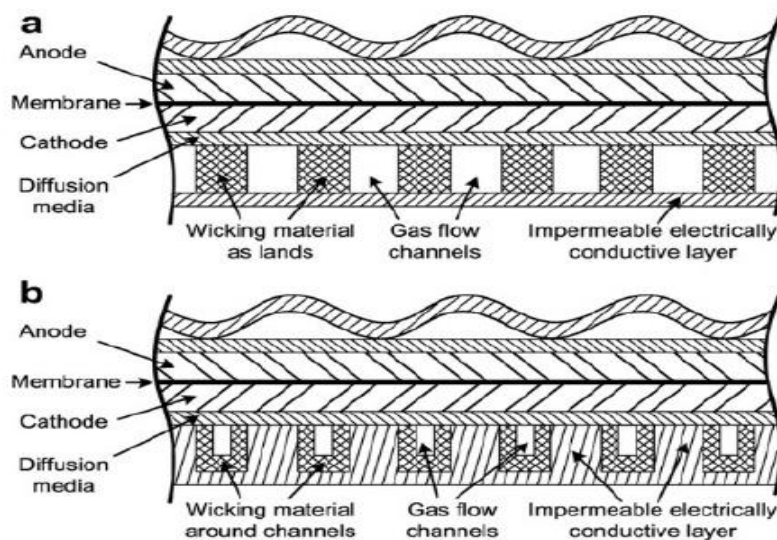


Fig. 2.16. Wick material a) as lands or b) placed over channels of the cathode bipolar plates [72]

The pore diameter of a felted fiber porous material can be found by [72]

$$\text{Pore diameter, } d_{\text{pore}} = \frac{d}{2(1-\epsilon)} \dots\dots\dots(19)$$

Here 'd' is the fiber diameter and ϵ is the void fraction of the material with the void fraction being defined by

ε = Void volume in material/ total volume of material

A capillary pressure (differential pressure dP_{cap}) is generally determined in a porous material by the Young-Laplace equation,

$$dP_{cap} = \frac{4\sigma\cos\theta}{d_{pore}} \dots\dots\dots(20)$$

where σ is the surface tension of water, θ is the wetting angle, and d_{pore} is the pore diameter. The wicking velocity (or volumetric flow rate of liquid per unit area– V_{wick}) is generally determined by

$$V_{wick} = \frac{K(dP_{cap}-dP_{flowfield})}{\mu L} \dots\dots\dots(21)$$

Here K is the permeability of the porous material, $dP_{flowfield}$ is the flow field pressure drop, μ is the water viscosity, and L is the flow field length. The flow of the cathode gas in the gas flow channels can also be co-current i.e., in the same direction as the wicking flow so that the flow field pressure drop adds to the capillary pressure to assist the wicking flow.

US Patent 6,960,404 [72] describes the wicking action over the cathode in the form of channels in order to supply the water inside the cell for internal humidification. The wicking material should be porous and hydrophilic although it does not need to be electrically conducting. However, the drawbacks of such a configuration of fuel cell is that it is difficult to fabricate bipolar plates with wicking materials as channels. In addition, the usage of electrically insulating wicking material shall render increased resistance to charge transfer across the cells in a fuel cell stack.

Another form of wicking technique used for in-situ humidification in PEMFC, which is shown in US 2004/0170878 [73], describes porous fibers that can be used as channels for direct water transport into the cell which is briefly illustrated in Fig. 2.17. herein. A fuel cell (11) has strips of wicking (12) disposed over a diffusion layer (13) which is in immediate contact with the cathode catalyst layer in the membrane electrode assembly (MEA) (14). The fuel cell is separated from the next cell in the series (20) by a separator plate (21). To provide water to the wick (12), a wicking header (22) extends across the ends of all the individual cells opposite to the flow of air into the spaces (24) between the wicks (12) that comprises the oxidant reactant gas flow field. Air is supplied by a pump (26) through a manifold (27) to the inlets (28) of each fuel cell. In Fig.

2.16., the air flow is exhausted through an outlet header (31) to a condenser (32) which vents the air to exhaust and delivers the condensate to a reservoir (33). Water in the reservoir (33) is conducted back to the wicking header (22).

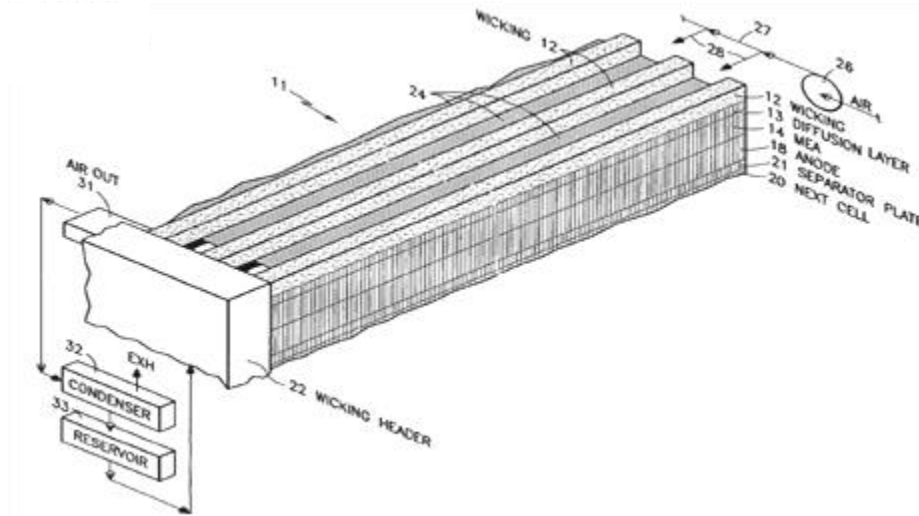


Fig. 2.17. Porous fiber channels for water transport [73]

The wick based internal humidification and evaporative cooling described in the aforementioned publication is stated to require external water from a source outside the fuel cell. The water generated at the cathode (process water) is said to be insufficient, except at startup, to achieve the necessary cooling. This is also true in an evaporative cooled fuel cell stack which relies on wicking in US 4,826,741 [74]. Therein, 100 cm² cells when tested, deliver a performance of only 0.7-0.8 V at 100-120 mA/cm². Furthermore, the differential capillary pressure along the length of each of the wicks must be greater than the pressure drop along the adjacent air flow field channels in order to have a positive wicking velocity. Although, it is stated that having air flow in the same direction as the flow of water in the wicking means would overcome that problem. In this thesis, we propose and investigate a novel internal humidification technique based on wicking for dry-feed operation of PEM fuel cell.

2.5. Research Objectives

To address the lacunae in the literature presented above, a comprehensive study on humidification of PEM fuel cell is carried out in this work with the following objectives.

- Understanding gas humidification from dense membranes by developing a multi-physics mathematical model and validate the same with experimental results obtained for a commercial humidifier module.
- Developing cost effective asymmetric hollow fiber membranes for gas humidification using dry-wet phase inversion method.
- Understanding gas humidification from asymmetric membranes by developing a phenomenological and multi-physics mathematical model and validate the same with experimental results obtained on variety of humidifier modules.
- Understanding flow behavior inside humidifiers using computational fluid dynamics simulations and provide design guidelines for humidifiers.
- Investigate wick based passive humidification technique for dry feed operation of PEM fuel cells and compare the performance with conventional operation.

2.6. Thesis structure

In this thesis, we contribute to the field of membrane technology and PEM fuel cells through several studies. The thesis is categorized into 7 chapters. Figure 2.18. provides a schematic illustration of the thesis overview. A brief introduction to the chapters is given below.

Chapter 1 gives a brief introduction about various gas humidification strategies and the importance of humidification in PEM fuel cells.

Chapter 2 gives a detailed background on the state-of-the-art literature on water-to-gas humidifier, porous membrane humidifiers, and passive water management techniques in PEM fuel cells. It also describes the research objectives and thesis structure.

Chapter 3 presents work done for improving our understanding of the mechanisms involved in water-to-gas membrane humidification. It presents a quasi-2D model for water-to-gas hollow fiber membrane humidifier and its validation with experiments performed on a commercial humidifier module. The model takes into account the relevant phase equilibria along with coupled heat and mass transport across dense Nafion hollow fiber membranes. The model is shown to predict the humidifier performance within 8 % deviation from the experimental results.

Chapter 4 focusses on efforts made on developing cost effective polysulfone asymmetric membranes which can be used for gas humidification over costly dense Nafion membrane based humidifiers. It presents an experimental and numerical investigation of polysulfone based asymmetric hollow fiber membranes. The experimental section includes development of polysulfone based hollow fiber membranes, their characterization and humidification performance tests. A mathematical model based on resistance-in-series approach is proposed for these membranes and is shown to fit the experimental observations in humidification tests.

Chapter 5 presents a computational fluid dynamic study on the flow distribution inside the tubes and shell of the humidifier. Based on the flow simulations, some design guidelines are presented to achieve uniform flow distribution inside the humidifiers.

Chapter 6 focusses on the work done on dry-feed operation of PEM fuel cell by providing passive means of hydration. It presents a novel wick based internal humidification technique for low temperature PEM fuel cells. The technique leverages the use of a hydrophilic modified carbon cloth as a wick over the MEA for passive water transport inside the cell without external aid of membrane humidifiers.

Chapter 7 provides a summary of the conclusions of this work and recommends path for further study and investigation.

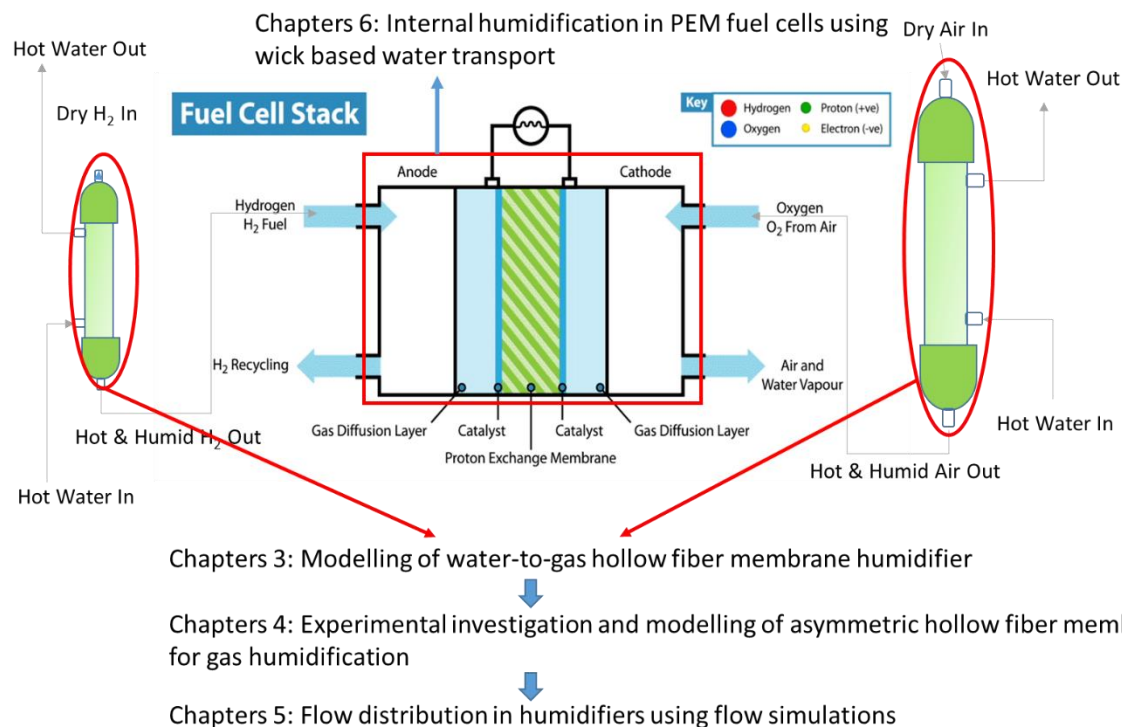


Fig. 2.18. Schematic illustration of the thesis overview

References

- [1] P.M. Bungay, H.K. Lonsdale, M.N. de Pinho, Synthetic Membranes: Science, Engineering and Applications, D. Reidel Publishing Company, 1st edition 1986. doi:10.1016/S0376-7388(00)83175-0.
- [2] J. Min, L. Wang, Membrane sorption property effects on transmembrane permeation, Chinese Sci. Bull. 56 (2011) 2394–2399. doi:10.1007/s11434-011-4562-4.
- [3] N. Valentínyi, E. Cséfalvay, P. Mizsey, Modelling of pervaporation: Parameter estimation and model development, Chem. Eng. Res. Des. 91 (2013) 174–183. doi:10.1016/j.cherd.2012.07.001.
- [4] J.G. Wijmans, R.W. Baker, The solution-diffusion model: a review, J. Memb. Sci. 107 (1995) 1–21. doi:10.1016/0376-7388(95)00102-1.
- [5] P. Taylor, Modelling Of Pervaporation : Models To Analyze And Predict The Mass Transport

- In Modelling Of Pervaporation, Separation & Purification Reviews (2007) 37–41.
- [6] R.K. Tyagi, A.E. Fouda, T. Matsuura, A pervaporation model: Membrane design, *Chem. Eng. Sci.* 50 (1995) 3105–3114. doi:10.1016/0009-2509(95)00148-X.
 - [7] T. Okada, T. Matsuura, A new transport model for pervaporation, *Journal of Membrane Science*, 59 (1991) 133-150.
 - [8] J.G. Wijmans, R.W. Baker, A simple predictive treatment of the permeation process in pervaporation ", 79 (1993) 101–113.
 - [9] J. Larminie, A. Dicks, *Fuel Cell Systems Explained*, 2001. doi:10.1016/S0378-7753(00)00571-1.
 - [10] A. Kusoglu, A.Z. Weber, New Insights into Perfluorinated Sulfonic-Acid Ionomers, *Chem. Rev.* 117 (2017) 987–1104. doi:10.1021/acs.chemrev.6b00159.
 - [11] L. Maldonado, J.C. Perrin, J. Dillet, O. Lottin, Characterization of polymer electrolyte Nafion membranes: Influence of temperature, heat treatment and drying protocol on sorption and transport properties, *J. Memb. Sci.* 389 (2012) 43–56. doi:10.1016/j.memsci.2011.10.014.
 - [12] J. Peron, A. Mani, X. Zhao, D. Edwards, M. Adachi, T. Soboleva, Z. Shi, Z. Xie, T. Navessin, S. Holdcroft, Properties of Nafion®NR-211 membranes for PEMFCs, *J. Memb. Sci.* 356 (2010) 44–51. doi:10.1016/j.memsci.2010.03.025.
 - [13] S. Shi, A.Z. Weber, A. Kusoglu, Structure/property relationship of Nafion XL composite membranes, *J. Memb. Sci.* 516 (2016) 123–134. doi:10.1016/j.memsci.2016.06.004.
 - [14] T.A. Zawodzinski, Water Uptake by and Transport Through Nafion® 117 Membranes, *J. Electrochem. Soc.* 140 (1993) 1041. doi:10.1149/1.2056194.
 - [15] V. Liso, S. Simon Araya, A.C. Olesen, M.P. Nielsen, S.K. Kær, Modeling and experimental validation of water mass balance in a PEM fuel cell stack, *Int. J. Hydrogen Energy.* 41 (2016) 3079–3092. doi:10.1016/j.ijhydene.2015.10.095.

- [16] G. Gebel, P. Aldebert, and M. Pineri, Structure and Related Properties of Solution-Cast Perfluorosulfonated Ionomer Films, *Macromolecules*, 1987, 20 (6), pp 1425–1428.
- [17] Y.S. Kim, C.F. Welch, R.P. Hjelm, N.H. Mack, A. Labouriau, E.B. Orlor, Origin of Toughness in Dispersion-Cast Nafion Membranes, (2015). doi:10.1021/ma502538k.
- [18] K.A. Mauritz, R.B. Moore, State of Understanding of Nafion, (2004). doi:10.1021/cr0207123.
- [19] C. Ma, T.L. Yu, H. Lin, Y. Huang, Y. Chen, U. Jeng, Y. Lai, Y. Sun, Morphology and properties of Nafion membranes prepared by solution casting, *Polymer (Guildf)*. 50 (2009) 1764–1777. doi:10.1016/j.polymer.2009.01.060.
- [20] D. Winkelmann, D. Roizard, E. Favre, P. Scharfer, M. Kind, On Schroeder ' s paradox, 278 (2006) 357–364. doi:10.1016/j.memsci.2005.11.020.
- [21] P.W. Majsztik, M.B. Satterfield, A.B. Bocarsly, J.B. Benziger, Water sorption, desorption and transport in Nafion membranes, *J. Memb. Sci.* 301 (2007) 93–106. doi:10.1016/j.memsci.2007.06.022.
- [22] T. Romero, W. Mérida, Water transport in liquid and vapour equilibrated Nafion™ membranes, *J. Memb. Sci.* 338 (2009) 135–144. doi:10.1016/j.memsci.2009.04.018.
- [23] M.B. Satterfield, J.B. Benziger, Non-Fickian water vapor sorption dynamics by nafion membranes, *J. Phys. Chem. B.* 112 (2008) 3693–3704. doi:10.1021/jp7103243.
- [24] A. Kusoglu, S. Savagatrup, K.T. Clark, A.Z. Weber, Role of Mechanical Factors in Controlling the Structure – Function Relationship of PFSA Ionomers, *Macromolecules*. 45 (2012) 7467–7476. doi:10.1021/ma301419s.
- [25] G. Alberti, R. Narducci, M. Sganappa, Effects of hydrothermal / thermal treatments on the water-uptake of Nafion membranes and relations with changes of conformation , counter-elastic force and tensile modulus of the matrix, 178 (2008) 575–583. doi:10.1016/j.jpowsour.2007.09.034.
- [26] V. Freger, Hydration of Nafion and Dowex in liquid and vapor environment : Schroeder ' s

- paradox and microstructure, (2018). doi:10.1016/j.polymer.2007.11.054.
- [27] M. Adachi, T. Navessin, Z. Xie, B. Frisken, Correlation of In Situ and Ex Situ Measurements of Water Permeation Through Nafion NRE211 Proton Exchange, (2009) 9–11. doi:10.1149/1.3116922.
 - [28] T.E. Springer, Polymer Electrolyte Fuel Cell Model, J. Electrochem. Soc. 138 (1991) 2334. doi:10.1149/1.2085971.
 - [29] D. Bhatia, M. Sabharwal, C. Duell, Analytical model of a membrane humidifier for polymer electrolyte membrane fuel cell systems, Int. J. Heat Mass Transf. 58 (2013) 702–717. doi:10.1016/j.ijheatmasstransfer.2012.11.033.
 - [30] S. Park, D. Jung, Effect of operating parameters on dynamic response of water-to-gas membrane humidifier for proton exchange membrane fuel cell vehicle, Int. J. Hydrogen Energy. 38 (2013) 7114–7125. doi:10.1016/j.ijhydene.2013.03.170.
 - [31] M. Sabharwal, C. Duell, D. Bhatia, Two-dimensional modeling of a cross flow plate and frame membrane humidifier for fuel cell applications, J. Memb. Sci. 409–410 (2012) 285–301. doi:10.1016/j.memsci.2012.03.066.
 - [32] L.-Z. Zhang, Coupled heat and mass transfer in an application-scale cross-flow hollow fiber membrane module for air humidification, Int. J. Heat Mass Transf. 55 (2012) 5861–5869. doi:10.1016/j.ijheatmasstransfer.2012.05.083.
 - [33] L.Z. Zhang, S.M. Huang, Coupled heat and mass transfer in a counter flow hollow fiber membrane module for air humidification, Int. J. Heat Mass Transf. 54 (2011) 1055–1063. doi:10.1016/j.ijheatmasstransfer.2010.11.025.
 - [34] S. Kang, K. Min, S. Yu, Two dimensional dynamic modeling of a shell-and-tube water-to-gas membrane humidifier for proton exchange membrane fuel cell, Int. J. Hydrogen Energy. 35 (2010) 1727–1741. doi:10.1016/j.ijhydene.2009.11.105.
 - [35] S. Park, I. Oh, An analytical model of Nafion™ membrane humidifier for proton exchange membrane fuel cells, J. Power Sources. 188 (2009) 498–501. doi:10.1016/j.jpowsour.

2008.12.018.

- [36] S.K. Park, S.Y. Choe, S. ho Choi, Dynamic modeling and analysis of a shell-and-tube type gas-to-gas membrane humidifier for PEM fuel cell applications, *Int. J. Hydrogen Energy*. 33 (2008) 2273–2282. doi:10.1016/j.ijhydene.2008.02.058.
- [37] D. Chen, W. Li, H. Peng, An experimental study and model validation of a membrane humidifier for PEM fuel cell humidification control, *J. Power Sources*. 180 (2008) 461–467. doi:10.1016/j.jpowsour.2008.02.055.
- [38] C.W. Monroe, T. Romero, W. Mérida, M. Eikerling, A vaporization-exchange model for water sorption and flux in Nafion, *J. Memb. Sci.* 324 (2008) 1–6. doi:10.1016/j.memsci.2008.05.080.
- [39] A. Gabelman, S.-T. Hwang, Hollow fiber membrane contactors, *J. Memb. Sci.* 159 (1999) 61–106. doi:10.1016/S0376-7388(99)00040-X.
- [40] E. Drioli, A. Criscuoli E. Curcio, *Membrane Contactors: Fundamentals, Applications and Potentialities*, Elsevier Science, 1st edition (2005).
- [41] G. Bakeri, A.F. Ismail, M.R. DashtArzhandi, T. Matsuura, Porous PES and PEI hollow fiber membranes in a gas-liquid contacting process-A comparative study, *J. Memb. Sci.* 475 (2015) 57–64. doi:10.1016/j.memsci.2014.09.037.
- [42] G. Bakeri, S. Naeimifard, T. Matsuura, A.F. Ismail, A porous polyethersulfone hollow fiber membrane in a gas humidification process, *RSC Adv.* 5 (2015) 14448–14457. doi:10.1039/C4RA14180F.
- [43] A. Samimi, S.A. Mousavi, A. Moallemzadeh, R. Roostaazad, M. Hesampour, A. Pihlajamäki, M. Mänttari, Preparation and characterization of PES and PSU membrane humidifiers, *J. Memb. Sci.* 383 (2011) 197–205. doi:10.1016/j.memsci.2011.08.043.
- [44] J.R. Du, L. Liu, A. Chakma, X. Feng, Using poly(N,N-dimethylaminoethyl methacrylate)/polyacrylonitrile composite membranes for gas dehydration and humidification, *Chem. Eng. Sci.* 65 (2010) 4372–4381. doi:10.1016/j.ces.2010.05.005.

- [45] W. Yaïci, M. Ghorab, E. Entchev, Numerical analysis of heat and energy recovery ventilators performance based on CFD for detailed design, *Appl. Therm. Eng.* 51 (2013) 770–780. doi:10.1016/j.applthermaleng.2012.10.003.
- [46] L. Zhang, International Journal of Heat and Mass Transfer Heat and mass transfer in plate-fin enthalpy exchangers with different plate and fin materials, *Int. J. Heat Mass Transf.* 52 (2009) 2704–2713. doi:10.1016/j.ijheatmasstransfer.2008.12.014.
- [47] L.Z. Zhang, Y. Jiang, Heat and mass transfer in a membrane-based energy recovery ventilator, 163 (1999) 29–38.
- [48] S. Koester, M. Falkenberg, M. Logemann, M. Wessling, Modeling heat and mass transfer in cross-counter flow enthalpy exchangers, *J. Memb. Sci.* 525 (2017) 68–76. doi:10.1016/j.memsci.2016.10.030.
- [49] A. Engarnevis, R. Huizing, S. Green, S. Rogak, Heat and mass transfer modeling in enthalpy exchangers using asymmetric composite membranes, *J. Memb. Sci.* 556 (2018) 248–262. doi:10.1016/j.memsci.2018.03.007.
- [50] L.Z. Zhang, Coupled heat and mass transfer through asymmetric porous membranes with finger-like macrovoids structure, *Int. J. Heat Mass Transf.* 52 (2009) 751–759. doi:10.1016/j.ijheatmasstransfer.2008.07.029.
- [51] L. Zhang, A Lattice Boltzmann Simulation of Mass Transport Through Composite Membranes, 60 (2014) 3925–3938. doi:10.1002/aic.
- [52] S.-K. Park, E.A. Cho, I.-H. Oh, Characteristics of membrane humidifiers for polymer electrolyte membrane fuel cells, *Korean J. Chem. Eng.* 22 (2005) 877–881. doi:10.1007/BF02705668.
- [53] K. Ramya, J. Sreenivas, K.S. Dhathathreyan, Study of a porous membrane humidification method in polymer electrolyte fuel cells, *Int. J. Hydrogen Energy.* 36 (2011) 14866–14872. doi:10.1016/j.ijhydene.2010.12.088.
- [54] J. Min, T. Hu, Moisture permeation through porous membranes, *J. Memb. Sci.* 379 (2011)

- 496–503. doi:10.1016/j.memsci.2011.06.028.
- [55] J. Min, L. Wang, Coupled heat and mass transfer during moisture exchange across a membrane, *J. Memb. Sci.* 430 (2013) 150–157. doi:10.1016/j.memsci.2012.12.018.
 - [56] M. Yang, S.M. Huang, X. Yang, Experimental investigations of a quasi-counter flow parallel-plate membrane contactor used for air humidification, *Energy Build.* 80 (2014) 640–644. doi:10.1016/j.enbuild.2014.07.058.
 - [57] J.H. Wee, Applications of proton exchange membrane fuel cell systems, *Renew. Sustain. Energy Rev.* 11 (2007) 1720–1738. doi:10.1016/j.rser.2006.01.005.
 - [58] F. Barbir, S. Yazici, Status and development of PEM fuel cell technology, (2008) 369–378. doi:10.1002/er.
 - [59] Y. Wang, K.S. Chen, J. Mishler, S.C. Cho, X.C. Adroher, A review of polymer electrolyte membrane fuel cells: Technology, applications, and needs on fundamental research, *Appl. Energy.* 88 (2011) 981–1007. doi:10.1016/j.apenergy.2010.09.030.
 - [60] S. Santyapal, Fuel Cell Technologies Program Overview Fuel Cells, US DOE (2012).
 - [61] J. Yu, T. Matsuura, Y. Yoshikawa, M. Hori, Lifetime behavior of a PEM fuel cell with low humidification of feed stream, (2005).
 - [62] D. Candusso, D. Hissel, A. Hernandez, A. Aslanides, A review on PEM voltage degradation associated with water management : Impacts , influent factors and characterization, 183 (2008) 260–274. doi:10.1016/j.jpowsour.2008.04.037.
 - [63] D.G. Strickland, J.G. Santiago, In situ -polymerized wicks for passive water management in proton exchange membrane fuel cells, 195 (2010) 1667–1675. doi:10.1016/j.jpowsour.2009.09.034.
 - [64] G. Zhang, S.G. Kandlikar, A critical review of cooling techniques in proton exchange membrane fuel cell stacks, *Int. J. Hydrogen Energy.* 37 (2012) 2412–2429. doi:10.1016/j.ijhydene.2011.11.010.

- [65] H. Su, C. Sita, S. Pasupathi, The Effect of Gas Diffusion Layer PTFE Content on The Performance of High Temperature Proton Exchange Membrane Fuel Cell, 11 (2016) 2919–2926.
- [66] D.G. Strickland, J.G. Santiago, In situ-polymerized wicks for passive water management in proton exchange membrane fuel cells, J. Power Sources. 195 (2010) 1667–1675. doi:10.1016/j.jpowsour.2009.09.034.
- [67] S.-H. Ge, X.-G. Li, I.-M. Hsing, Water Management in PEMFCs Using Absorbent Wicks, J. Electrochem. Soc. 151 (2004) B523. doi:10.1149/1.1781591.
- [68] Intelligent Energy Ltd., Fuel Cell Fluid Distribution Plates, EP 2016640 B1 (2010).
- [69] Intelligent Energy Ltd., Fuel Cell Direct Water Injection, EP 1530813 B1 (2012).
- [70] J.S. Yi, J.D. Yang, C. King, Water Management along the Flow Channels of PEM Fuel Cells, 50 (2004). doi:10.1002/aic.10307.
- [71] A.Z. Weber, R.M. Darling, Understanding porous water-transport plates in polymer-electrolyte fuel cells, 168 (2007) 191–199. doi:10.1016/j.jpowsour.2007.02.078.
- [72] General Motors Corp., Evaporative Cooled Fuel Cell, US 6960404 B2 (2005).
- [73] S.G. Goebel, Evaporative Cooled Fuel Cell, US 0170878A1 (2004).
- [74] Ergenics Power Systems Inc., Ion Exchange Fuel Cell Assembly With Improved Water And Thermal Management, US 4826741 (1989).

Chapter 3

Modelling of Water-to-Gas Hollow Fiber Membrane Humidifier

In this chapter, a microscopic mathematical model is developed for membrane-based water-to-gas humidification by rigorously accounting for phase equilibrium between the membrane and water phases as well as membrane and gas phases in addition to the coupled heat and mass transfer occurring across the membrane. The model is then integrated along the length of the hollow fiber membrane humidifier in order to predict humidifier performance as a function of design variables, operating variables and operational strategies. For realistic values of membrane thickness and flow parameters, the model suggests that while membrane-gas interfacial resistance is crucial for heat transfer, the vapor transfer is governed by the combined resistances of diffusion within the membrane and at the membrane-gas interface. The model is validated against experimental data obtained using a commercial hollow fiber membrane module.

The content of this chapter is published in,

"Chemical Engineering Science, [Volume 192](#), 31 December 2018, Pages 955-971".

Reproduced with permission from Elsevier.

3.1. Introduction

The performance of a low-temperature PEM fuel cell stack (LT-PEMFC) is largely governed by the hydration state of the proton exchange membrane (PEM) [1-4]. In a closed-cathode LT-PEMFC stack, membranes are kept hydrated using external gas humidifiers which come in various configurations such as bottle humidifiers, plate and frame membrane humidifiers, and shell and tube membrane humidifiers [5-7]. Of these, the shell and tube membrane humidifiers, also called hollow fiber membrane (HFM) humidifiers, offer advantages of low pressure drop, high active surface area for moisture transfer, compactness and ease of handling [8,9]. Most HFM humidifiers use dense Nafion™ membranes. The shell side of a HFM humidifier has liquid water

(in a water-to-gas humidifier) or moist gas (in a gas-to-gas humidifier), whereas the process gas which is to be humidified, flows through Nafion™ tubes.

In the case of gas-to-gas humidifiers, humidification happens by vapor-vapor permeation (VVP) wherein moisture from the shell side moist gas is transferred to the tube side process gas through the membrane. Here, the membrane is interfaced with gases on both sides [10 – 12]. In the case of water-to-gas humidifiers, humidification happens by liquid-vapor permeation (LVP) wherein moisture from the shell side water is transferred to the tube side process gas through the membrane. Here, the membrane is interfaced with water on the shell side and gas on the tube side [13 – 15]. In this thesis we are concerned with water-to-gas humidification because this is the most common configuration for humidification of a PEM fuel cell. Hence this chapter focuses on equilibrium and transport phenomena involving sorption of liquid water in the membrane, permeation across the membrane and evaporation in the gas stream. The extent of humidification of process gas ultimately depends on design (or geometric) parameters of the HFM, membrane properties, operating parameters and operational strategies (eg. counter-current or co-current) [13, 16, 17]. Mathematical modelling of humidification helps in the optimization of these parameters to achieve enhanced humidifier performance.

Several analytical and numerical models have been proposed in the past for membrane-based gas humidification [10 – 15, 17 – 19]. Any modelling effort for a water-to-gas membrane humidifier must account for phase change of water from liquid state on one side of the membrane to vapor on the other side. Thus mathematical models must account for two phenomena: (a) coupling of heat and mass transfer by way of latent and sensible heat carried by the water that is transported from one side to the other, (b) simultaneous dual equilibration of the membrane with liquid water on one side, and with gas on the other side. With regards to coupling of heat and mass transfer, there exist models in the literature which do not account for any coupling between heat and mass transfer [10,14,17,20], those which account for limited coupling between heat and vapor transfer across the membrane through the latent heat carried by the permeating water [13,18,19], and those which account for full coupling of mass transfer

and heat transfer by accounting for both latent heat and sensible heat carried by the moisture [11,12]. These models were reviewed in Chapter 2.

Insofar as equilibrium considerations are concerned, most of the theoretical models available in the literature use an empirical fit given by Springer et al. [21] to the isopiestic moisture uptake measurements conducted by Zawodzinski et al. [22, 23] to model equilibrium at membrane interfaces. Zawodzinski et al. [22, 23] reported moisture uptake of Nafion™ 117 membrane equilibrated with vapor of different activities under static and isothermal (30 °C) conditions. Yet another study by Hinatsu et al. [24] reported vapor sorption isotherms for Nafion™ 117 membranes at 80°C and provided an empirical equation for moisture uptake by the membrane as a function of vapor activity. While these empirical correlations may be appropriate for modelling equilibrium at the membrane-gas interface, their applicability to model interfacial equilibrium at the membrane-water interface needs careful consideration. This is because of the fact that uptake of moisture in the membrane is typically higher when the membrane is equilibrated with liquid water than with vapor, a condition known as the so-called Schroeder's paradox [23, 25 – 27] (as discussed in Chapter 2). Consequently, several studies have demonstrated that the flux of moisture transported in Nafion membranes by liquid-vapor permeation (LVP) is higher than by vapor-vapor permeation (VVP) [16,27,28]. Existing models for water-to-gas membrane humidifiers have ignored this dual equilibrium condition, which can be a serious concern since interfacial equilibrium is expected to play a key role in determining the rate of mass transfer by virtue of setting up concentration gradients [27 – 32].

Thus it is incumbent to refine existing models to capture the physics appropriate for a water-to-gas membrane humidifier. In this chapter, we develop a microscopic model that not only rigorously accounts for full coupling between vapor transfer and heat transfer but also takes into consideration appropriate phase equilibrium equations at the membrane-water and membrane-gas interfaces. The process gas of interest in this chapter is air. Our model is built on the following premises:

- (a) The membrane is in equilibrium with water on the shell side and with moist air on the tube side thereby allowing LVP. The water-membrane equilibrium is accounted for by empirically

modelling the experimental sorption isotherm in liquid water, while the air-membrane equilibrium is modelled using an appropriate equilibrium law that is chosen by fitting independent experimental LVP data.

- (b) The heat of vaporization required to convert water from the shell side into vapor is taken from the shell side [15, 33]. The vapor is subsequently added into the air on the tube side.

3.2. Model

In this study, we focus on modelling a shell and tube type HFM humidifier with low humidity air entering the tubes at a mass flow rate per tube given by (\dot{m}_a/N) and hot water entering the shell at a nominal mass flow rate per tube given by (\dot{m}_w/N) in counter-current or co-current flow modes. Here N is the number of tubes in the HFM humidifier, and \dot{m}_a and \dot{m}_w are total mass flow rates of air and water respectively in the humidifier. Nafion™ tubes allow the water from shell side to diffuse through the membrane and evaporate into the gas stream on tube side by LVP. Thus, when dry air enters the humidifier, it picks up heat and moisture from the membrane and gets humidified. Figure 3.1. illustrates a schematic representation of the model wherein x and z represent the transverse and axial directions, respectively.

The assumptions underlying the model are as follows:

- Cartesian coordinate system is chosen despite the cylindrical nature of tubes. This is reasonable because the ratio of membrane thickness (L) to average tube diameter(\bar{d}) is $L/\bar{d} \ll 1$, and the ratio of tube length to average tube diameter is $H/\bar{d} \gg 1$.
- The problem is quasi-2D with local inter-phase heat and mass exchange occurring across the membrane along transverse direction (x -direction in Fig. 3.1.) while the overall addition of heat and mass occurs along the length of the humidifier in the axial direction (z -direction in Fig. 3.1.). The quasi-2D assumption is reasonable since $H/\bar{d} \gg 1$ so that locally for any infinitesimal segment Δz along the fiber length, the gradients in concentration and temperature are much higher along the x -direction than along the z -direction.
- Heat and mass losses from the boundary of the humidifier are neglected. In other words, the humidifier is perfectly insulated.

- The heat required for vaporization of water is taken from the shell side.
- While the variation of specific heat in x and z directions is accounted for in the model, the other physical properties such as thermal conductivity, density and latent heat are assumed constant along x and z directions since they vary weakly with humidity and temperature.
- Flow is fully developed over the entire length of the humidifier.
- Air is considered as an ideal gas.

At any axial location z , the elemental balance in the x -direction gives the concentration profile (Eq. (1)) and temperature profile (Eq. (2)) within the membrane. Eq. (2) implies that the quantum of sensible heat carried by the vapor diffusing through the membrane is negligible compared to the heat conducted through the membrane. This is discussed later in the chapter and is also validated in Appendix A. Here, C and T are respectively the water concentration (mol/m³) and temperature (K) in the membrane. Eqs. (1) and (2) result into linear concentration and temperature profiles across the membrane given by Eqs. (3) and (4).

$$\frac{\partial^2 C}{\partial x^2} = 0 \dots\dots\dots(1)$$

$$\frac{\partial^2 T}{\partial x^2} = 0 \dots\dots\dots(2)$$

$$C = \left(\frac{C_L - C_{\max}^{liq}}{L} \right) x + C_{\max}^{liq} \dots\dots\dots(3)$$

$$T = \left(\frac{T_m - T_w'}{L} \right) x + T_w' \dots\dots\dots(4)$$

T_w' in Eq. (4) is the temperature of membrane at the membrane-water interface on the shell side with T_w being the water temperature. It turns out that $T_w' \approx T_w$ because the heat transfer coefficient on shell side (h_s) \gg heat transfer coefficient on tube side (h_t), as will be discussed later.

C_{\max}^{liq} in Eq. (3) is the concentration of water in the membrane at the membrane-water interface which is in equilibrium with water on shell side. C_L is concentration of water in

membrane at membrane-air interface, and T_m is the membrane temperature at membrane-air interface.

The boundary conditions given in Eqs. (5) and (6) respectively for mass transfer and heat transfer at the membrane-air interface reflect the steady-state condition at which diffusion flux through the membrane equals convection flux into the air.

Boundary conditions for mass transfer across the membrane are given as

$$\begin{aligned} x=0, C &= C_{\max}^{liq} \\ x=L, -D_m \frac{\partial C}{\partial x} \Big|_L &= K_t \left(\frac{P_{eq}}{RT_m} - \frac{P_v}{RT_a} \right) \end{aligned} \quad (5)$$

Boundary conditions for heat transfer across the membrane are given as

$$\begin{aligned} x=0, T &= T_w \\ x=L, -k_m \frac{\partial T}{\partial x} \Big|_L &= h_t (T_m - T_a) \end{aligned} \quad (6)$$

In Eq. (5), D_m (m^2/s) is the diffusion coefficient of water in the membrane, K_t (m/s) is the convective mass transfer coefficient on the tube side and P_{eq} (Pa) is the vapor pressure at the membrane-air interface which is in equilibrium with water concentration in the membrane, C_L (mol/m^3). P_v (Pa) is the vapor pressure of moisture in the bulk air. In Eq. (6), k_m (W/mK) is the thermal conductivity of the membrane, T_a (K) is the bulk air temperature at z and h_t (W/m^2K) is the heat transfer coefficient on air side.

In principle, P_{eq} can be determined independently by equilibrium measurements of vapor pressure on the air side of membranes which are uniformly hydrated by liquid water on the other side. Such experiments were conducted by Monroe et al. [31], who suggested that the relation between P_{eq} and C_L can be approximated by a modified form of Henry's law (Eq. (7)) with Henry's constant being the ratio of saturation vapor pressure ($P_{v,sat}$) and maximum water concentration in membrane (C_{\max}^{liq}). Here it must be noted that the Henry's constant is obtained at T_w .

$$P_{eq} = \frac{P_{v,sat}}{C_{\max}^{liq}} C_L \quad (7)$$

Yet another widely used method of modelling the membrane-air equilibrium is a cubic polynomial (Eq. (8)) proposed by Springer et al. (1991) [21] for a vapor equilibrated Nafion™ 117 membrane.

$$\lambda_m = 0.043 + 17.81(a_w) - 39.85(a_w^2) + 36(a_w^3) \quad 0 < a_w \leq 1 \quad \dots\dots\dots(8)$$

Here, a_w is the activity of water in the gas phase which is equivalent to relative humidity ($P_{eq}/P_{v,sat}$), λ_m is the water content (mol H₂O/ mol SO₃⁻) in the membrane at the membrane-air interface, which can be expressed in terms of concentration using Eq. (9).

$$C_L = \frac{\lambda_m \rho_m}{E.W.} \quad \dots\dots\dots(9)$$

Here, ρ_m and $E.W$ are the density and equivalent weight of the membrane. The choice between Eq. (7) and Eq. (8) can be made by comparing them against independent LVP experimental data, as will be shown later in the article.

Assuming for now that the Monroe equation (Eq. (8)) can be used to model the membrane-air interface, it is now possible to obtain expressions for C_L and T_m from Eqs. (3) – (7) and these are given below in Eqs. (10) - (12).

$$C_L = C_{\max}^{liq} \left(\frac{T_m}{T_a} \right) \left[\frac{D_m R T_a C_{\max}^{liq} + K_t L P_v}{D_m R T_m C_{\max}^{liq} + K_t L P_{v,sat}} \right] \quad \dots\dots\dots(10)$$

or equivalently,

$$P_{eq} = P_{v,sat} \left(\frac{T_m}{T_a} \right) \left[\frac{D_m R T_a C_{\max}^{liq} + K_t L P_v}{D_m R T_m C_{\max}^{liq} + K_t L P_{v,sat}} \right] \quad \dots\dots\dots(11)$$

and

$$T_m = \frac{k_m T_w + h_t L T_a}{k_m + h_t L} \quad \dots\dots\dots(12)$$

Note that all concentrations, temperature and vapor pressure in Eqs. (10) and (11) are functions of axial location z .

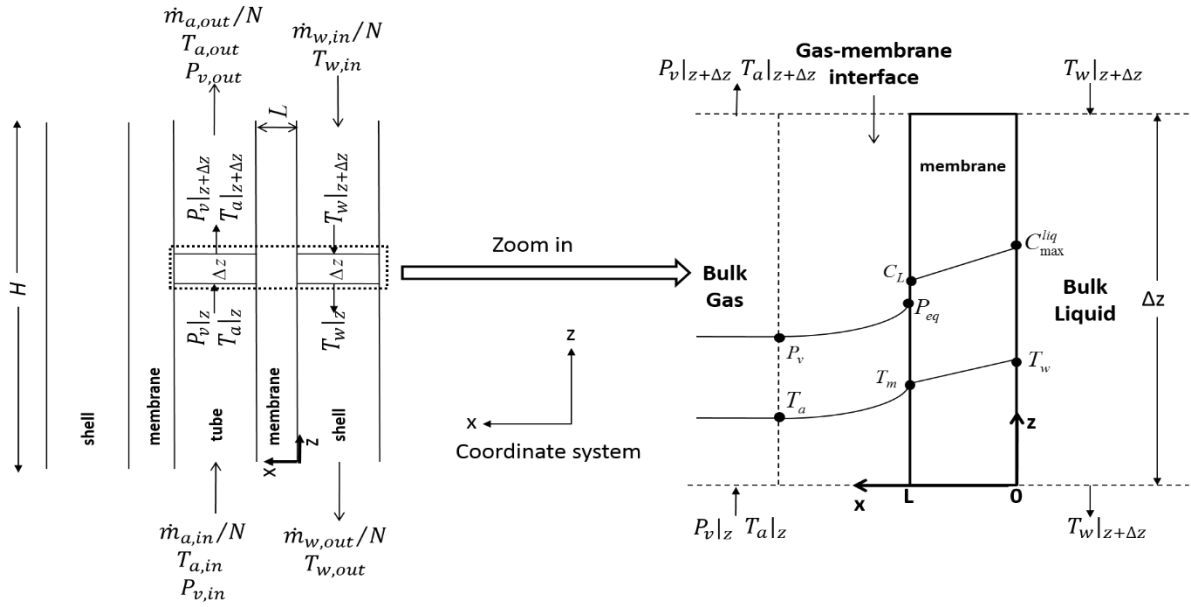


Fig. 3.1. Schematic representation of the model

The saturation vapor pressure of water is given by Antoine's equation [34]

$$P_{v,sat} = A \times 10^{\left(\frac{mT_w}{T_w + T_n} \right)} \quad \dots\dots\dots (13)$$

Where, $A = 611.6441 \text{ (Pa)}$, $m = 7.591386$, $T_n = 240.7263 \text{ }^\circ\text{C}$ for $-20 \leq T_w \leq 50 \text{ }^\circ\text{C}$ and

$A = 600.4918 \text{ (Pa)}$, $m = 7.337936$, $T_n = 229.3975 \text{ }^\circ\text{C}$ for $50 \leq T_w \leq 100 \text{ }^\circ\text{C}$

Writing mass balance equation for water vapor on the tube side along the axial direction in a control volume of length Δz , we get

$$\frac{\pi d_{id}^2}{4RT_a} v_a (P_v|_z - P_v|_{z+\Delta z}) = -K_t \left(\frac{P_{eq}}{RT_m} - \frac{P_v}{RT_a} \right) \pi d_{id} \Delta z \quad \dots\dots\dots (14)$$

Here, $d_{id}(m)$ is the inner diameter of tube, $v_a (m/s)$ is average superficial velocity of air in the tube, and $K_t(m/s)$ is the tube side convective mass transfer coefficient.

As vapor is added to air, the mass flow rate of air increases while the mass flow rate of water decreases along the length of the humidifier. Writing mass balance equation for air on tube side and water on shell side along the axial direction, we get

$$\dot{m}_a|_z - \dot{m}_a|_{z+\Delta z} = -NK_t M_w \pi d_{id} \Delta z \left(\frac{P_{eq}}{RT_m} - \frac{P_v}{RT_a} \right) \quad \dots\dots\dots (15)$$

$$\dot{m}_w|_{z+\Delta z} - \dot{m}_a|_z = -NM_w\pi d_{od}\Delta z(C_L - C_{max}^{liq})\frac{D_m}{L} \dots\dots\dots(16)$$

The energy balance on the shell side given in Eq. (17) indicates that the energy loss is due to latent heat of evaporation of water as well as the heat transferred by conduction and convection.

$$C_{pw}(\dot{m}_w T_w)|_{z+\Delta z} - C_{pw}(\dot{m}_w T_w)|_z = NU\pi d_{od}\Delta z(T_w - T_a) + NK_t M_w \lambda_{vap} \pi d_{od} \Delta z \left(\frac{P_{eq}}{RT_m} - \frac{P_v}{RT_a} \right) \dots\dots\dots(17)$$

Here, \dot{m}_w (kg/s) is mass flow rate of water on shell side, C_{pw} (J/kg K) is specific heat of water, U (W/m²K) is overall heat transfer coefficient, d_{od} (m) is outer diameter of tube, N is number of tubes, M_w (kg/mol) is molecular weight of water, and λ_{vap} (J/kg) is latent heat of vaporization of water.

Energy balance on tube side accounts for increase in air temperature due to the heat gained from conductive and convective heat transfer and the sensible heat gained due to addition of water vapor. The tube side energy balance can thus be written in the form given in Eq. (18).

$$(\dot{m}_a C_{pa} T_a)|_z - (\dot{m}_a C_{pa} T_a)|_{z+\Delta z} = -NU\pi d_{id}\Delta z(T_w - T_a) - NK_t M_w C_{pv} (T_m - T_a) \pi d_{id} \Delta z \left(\frac{P_{eq}}{RT_m} - \frac{P_v}{RT_a} \right) \dots\dots\dots(18)$$

It is to be noted that specific heat of air can vary significantly with the addition of moisture and is therefore considered as a function of moisture content given by [35]

$$C_{pa} = C_{pa,dry} + C_{pv}X \dots\dots\dots(19)$$

In Eq. (19), $C_{pa,dry}$ (1.005 (kJ/kg K)) is the specific heat of dry air and C_{pv} (1.82 (kJ/kg K)) is the specific heat of water vapor. X is known as the mixing ratio (grams of water vapor per kg of dry air) and is given in Eq. (20) below [34].

$$X = B \times \frac{P_v}{P_{tot} - P_v} \text{ where } P_{tot} = 101325 Pa \text{ and } B = \frac{M_w}{M_{air}} = 621.9907 \text{ g/kg} \dots\dots\dots(20)$$

The overall heat transfer coefficient is defined as [36]

$$U = \frac{1}{\frac{1}{h_t} \left(\frac{d_{od}}{d_{id}} \right) + \frac{L}{k_m} \left(\frac{d_{od}}{\bar{d}} \right) + \frac{1}{h_s}} \dots\dots\dots(21)$$

Where, h_s (W/m^2K) is convective heat transfer coefficient on shell side, d_{id} (m) and d_{od} (m) are the tube inlet and outlet diameters respectively, and \bar{d} is average diameter of tube given by

$$\bar{d} = \frac{d_{id} + d_{od}}{2} \dots\dots\dots(22)$$

Eqs. (14) – (18) can be written in the form of ordinary differential equations (ODEs) as given below.

$$\frac{dP_v}{dz} = \frac{4K_t}{v_a d_{id}} \left(P_{eq} \left(\frac{T_a}{T_a} \right) - P_v \right) \dots\dots\dots(23)$$

$$\frac{dm_a}{dz} = NK_t M_w \pi d_{id} \left(\frac{P_{eq}}{RT_m} - \frac{P_v}{RT_a} \right) \dots\dots\dots(24)$$

$$\frac{dm_w}{dz} = \frac{D_m}{L} NM_w \pi d_{od} (C_L - C_{max}^{liq}) \dots\dots\dots(25)$$

$$\frac{dT_w}{dz} = \frac{NU\pi d_{od}(T_w - T_a)}{\dot{m}_w C_{pw}} + \frac{NK_t M_w \lambda_{vap} \pi d_{od}}{\dot{m}_w C_{pw}} \left(\frac{P_{eq}}{RT_m} - \frac{P_v}{RT_a} \right) - \frac{\beta}{1+\beta} \left(\frac{ND_m M_w \pi d_{od} C_{max}^{liq} T_w}{L \dot{m}_w} \right) \times \left(\frac{P_v}{P_{v,sat}} \left(\frac{T_m}{T_a} \right) - 1 \right) \dots\dots\dots(26)$$

$$\frac{dT_a}{dz} = \frac{NU\pi d_{id}(T_w - T_a)}{\dot{m}_a C_{pa}} + \frac{NK_t M_w C_{pv} \pi d_{id}(T_m - T_a)}{\dot{m}_a C_{pa}} \left(\frac{P_{eq}}{RT_m} - \frac{P_v}{RT_a} \right) - \frac{NK_t \pi d_{id} M_w}{\dot{m}_a} \left(\frac{P_{eq}}{RT_m} - \frac{P_v}{RT_a} \right) - \frac{2.488 K_t C_{pv} R T_a^2 P_T}{v_a d_{id} C_{pa} (P_T - P_v)^2} \left(\frac{P_{eq}}{RT_m} - \frac{P_v}{RT_a} \right) \dots\dots\dots(27)$$

In Eq. (23), $v_a = \frac{4\dot{m}_{a,in}}{\rho_a N \pi d_{id}^2}$, and in Eq. (26), β is a dimensionless number given as $\beta = \frac{K_t L P_{v,sat}}{D_m R T_m C_{max}^{liq}}$ discussed later in this section. The boundary conditions are the inlet conditions $P_{v,in}$ (Pa), $T_{a,in}$ (K) and $T_{w,in}$ (K), which are operating parameters. The other known quantities are the remaining operating parameters: \dot{m}_w , \dot{m}_a ; the design parameters: d_{id} , d_{od} , L , H ; and physical properties like C_{pw} , $C_{pa,dry}$, C_{pv} , ρ_a , ρ_w , μ_a , μ_w , k_a , k_w , k_m of the fluids. The values of these different input parameters of the model are provided in Table 3.1.

Table 3.1: Values of input parameters.

Property	Value
Specific heat of water, C_{pw} (J/kg K)	4186
Specific heat of dry air, $C_{pa,dry}$ (J/kg K)	1005
Specific heat of water vapor, C_{pv} (J/kg K)	1820
Molecular weight of water M_w (kg/mol)	0.018
Molecular weight of air M_{air} (kg/mol)	0.0289
Density of air, ρ_a (kg/m ³)	1.166
Density of water, ρ_w (kg/m ³)	1000
Viscosity of water, μ_w (Pa s)	8.9×10^{-4}
Viscosity of air, μ_a (Pa s)	1.83×10^{-5}
Thermal conductivity of air, k_a (W/m K)	0.0264
Thermal conductivity of water, k_w (W/m K)	0.6
Thermal conductivity of membrane, k_m (W/m K)	0.254
Diffusivity of water in air, D_{wa} (m ² /s)	2.52×10^{-4}
Latent heat of vaporization of water, λ_{vap} (J/kg)	2.265×10^6

Eqs. (23) – (27) constitute the governing equations in dimensional form. The coupling between heat and mass transfer is evident in these equations. Non-dimensionalizing these equations using the following variables, we get

$$\xi = \frac{z}{H}, \theta_v = \frac{P_v - P_{v,in}}{P_{v,sat,in} - P_{v,in}}, \theta_{vs} = \frac{P_{v,sat} - P_{v,in}}{P_{v,sat,in} - P_{v,in}}, T_w^* = \frac{T_w - T_{ref}}{T_{w,in} - T_{ref}}, T_a^* = \frac{T_a - T_{ref}}{T_{a,in} - T_{ref}}, T_{ref} = 273K,$$

$$\dot{m}_a^* = \frac{\dot{m}_a}{\dot{m}_{a,in}}, \dot{m}_w^* = \frac{\dot{m}_w}{\dot{m}_{w,in}} \dots \dots \dots (28)$$

$$\frac{d\theta_v}{d\xi} = \frac{4\alpha}{1+\beta} \left[\left(\frac{T_a}{T_m} \right) \left(\theta_{vs} + \frac{P_{v,in}}{P_{v,sat,in} - P_{v,in}} \right) - \left(\theta_v + \frac{P_{v,in}}{P_{v,sat,in} - P_{v,in}} \right) \right] \dots \dots \dots (29)$$

$$\frac{d\dot{m}_w^*}{d\xi} = \frac{\phi\beta}{1+\beta} \left[\left(\frac{\theta_v(P_{v,sat,in} - P_{v,in}) + P_{v,in}}{(\theta_{vs}(P_{v,sat,in} - P_{v,in}) + P_{v,in})} \right) \left(\frac{T_m}{T_a} \right) - 1 \right] \dots \dots \dots (30)$$

$$\frac{d\dot{m}_a^*}{d\xi} = \left(\frac{\phi'}{1+\beta} \right) \times \left[\left(\frac{T_a}{T_m} \right) \left(\theta_{vs} + \frac{P_{v,in}}{P_{v,sat,in} - P_{v,in}} \right) - \left(\theta_v + \frac{P_{v,in}}{P_{v,sat,in} - P_{v,in}} \right) \right] \dots \dots \dots (31)$$

$$\begin{aligned} \frac{dT_w^*}{d\xi} = & \gamma \left[T_w^* - \left(\frac{T_{a,in} - T_{ref}}{T_{w,in} - T_{ref}} \right) \times T_a^* \right] + \left(\frac{\delta}{1+\beta} \right) \times \left[\left(\frac{T_a}{T_m} \right) \left(\theta_{vs} + \frac{P_{v,in}}{P_{v,sat,in} - P_{v,in}} \right) - \left(\theta_v + \frac{P_{v,in}}{P_{v,sat,in} - P_{v,in}} \right) \right] - \\ & \frac{\eta\beta}{1+\beta} \left[\left(\frac{\theta_v(P_{v,sat,in} - P_{v,in}) - P_{v,in}}{(\theta_{vs}(P_{v,sat,in} - P_{v,in}) - P_{v,in})} \right) \left(\frac{T_m}{T_a} \right) - 1 \right] \dots \dots \dots (32) \end{aligned}$$

$$\begin{aligned} \frac{dT_a^*}{d\xi} = & \gamma' \left[T_w^* \times \left(\frac{T_{w,in} - T_{ref}}{T_{a,in} - T_{ref}} \right) - T_a^* \right] + \left(\frac{\delta' - \sigma - \sigma'}{1+\beta} \right) \times \left[\left(\frac{T_a}{T_m} \right) \left(\theta_{vs} + \frac{P_{v,in}}{P_{v,sat,in} - P_{v,in}} \right) - \left(\theta_v + \frac{P_{v,in}}{P_{v,sat,in} - P_{v,in}} \right) \right] \\ & \dots \dots \dots (33) \end{aligned}$$

The following dimensionless numbers emerge during the non-dimensionalization and are discussed later in the chapter. These numbers along with their physical significance are presented in Table 3.2 below.

$$\begin{aligned}\alpha &= \frac{K_t H}{v_a d_{id}}; \beta = \frac{K_t L P_{v,sat}}{D_m R T_m C_{max}^{liq}}; \gamma = \frac{N U \pi d_{od} H}{\dot{m}_w C_{pw}}; \gamma' = \frac{N U \pi d_{id} H}{\dot{m}_a C_{pa}}; \delta = \frac{N K_t M_w \pi d_{od} H \lambda_{vap} (P_{v,sat,in} - P_{v,in})}{R T_a \dot{m}_w C_{pw} (T_{w,in} - T_{ref})}; \\ \delta' &= \frac{N K_t M_w \pi d_{id} H C_{pv} (T_m - T_a) (P_{v,sat,in} - P_{v,in})}{R T_a \dot{m}_a C_{pa} (T_{a,in} - T_{ref})}; \sigma = \frac{N K_t M_w \pi d_{id} H T_m (P_{v,sat,in} - P_{v,in})}{R T_a \dot{m}_a (T_{a,in} - T_{ref})}; \\ \sigma' &= \frac{2.488 K_t T_a C_{pv} P_T H (P_{v,sat,in} - P_{v,in})}{v_a d_{id} C_{pa} (P_T - P_v)^2 (T_{a,in} - T_{ref})}; \eta = \frac{N D_m M_w \pi d_{od} H C_{max}^{liq} T_w}{\dot{m}_w L (T_{w,in} - T_{ref})}; \phi = \frac{N D_m M_w \pi d_{od} H C_{max}^{liq}}{\dot{m}_w L}; \\ \phi' &= \frac{N K_t M_w \pi d_{id} H (P_{v,sat,in} - P_{v,in})}{\dot{m}_a R T_a} \dots\dots\dots(34)\end{aligned}$$

Table 3.2: Dimensionless numbers and their physical significance.

Dimensionless Number	Physical Meaning
α	Ratio of residence time of air in tube to the time taken for mass transfer through convection Similar to Stanton number
β	Ratio of maximum convective mass flux in air to maximum diffusive mass flux in the membrane Similar to Sherwood number $Sh = K_t L / D_m$
γ	Ratio of overall heat transfer rate to the heat capacity of water Equivalent to NTU or Effectiveness on Shell Side
γ'	Ratio of overall heat transfer rate to the heat capacity rate of air Equivalent to NTU or Effectiveness on Tube Side
δ	Ratio of total latent heat lost due to evaporation to the total available heat of inlet water Latent heat ratio (LHR)
δ'	Ratio of sensible heat of vapor transferred to the total available heat of inlet air Sensible heat ratio (SHR)

σ	Ratio of amount of moisture added per unit increase in air temperature to the total increase in air mass per unit increase in membrane temperature.
σ'	Ratio of heat carrying capacity of water vapor to the heat carrying capacity of humidified air
η	Ratio of thermal flux due to water diffusion in membrane to the total thermal flux of inlet water
ϕ	Ratio of rate of water diffusion in the membrane to the inlet mass flow rate of water
ϕ'	Ratio of rate of mass convection at the membrane-gas interface to the inlet mass flow rate of air

Eqs. (29) – (33) can be integrated numerically to obtain steady-state solutions for outlet vapor pressure on tube side, outlet mass flow rate of air on tube side, outlet mass flow rate of water on shell side, outlet air temperature on the tube side and outlet water temperature on the shell side. Further, these output parameters yield the relative humidity or the dew point temperature of air at tube outlet. The latter is given below in Eq. (35) [34].

$$T_{d,out} = \frac{T_n}{\frac{m}{\log_{10}\left(\frac{P_{v,out}}{A}\right)} - 1} \dots\dots\dots(35)$$

Here, the constants m , T_n and A are same as defined in Eq. (13).

For determining the dimensionless numbers in Eq. (34), K_t , D_m , C_{\max}^{liq} , U and $P_{v,sat,in}$ must be obtained either experimentally or through standard correlations. In this study, C_{\max}^{liq} was obtained by immersing as-received Nafion™ membranes of known weights in a water bath at varying temperatures for 3 h. The difference between initial and final weights were then used to calculate C_{\max}^{liq} in the membrane phase. The time period of 3 h was decided based on dynamic sorption measurements conducted by Majsztrik et al. [28], which suggest that the time required for equilibration of Nafion™ with liquid water was found to be less than 2 h for different membrane thickness. Figure 3.2. records the water-membrane isotherm obtained for Nafion™

212 ($\approx 50 \mu\text{m}$ thickness) membrane. Our experimental observations for water uptake in liquid equilibrated system is in excellent agreement with the observations made in the temperature range of $40 - 80^\circ\text{C}$ by Shi et al. [37] for 1 h liquid water equilibrated as-received Nafion™ 212 membrane as well as with the study by Springer et al. [21] for Nafion™ 117 sample. The sorption data shown in Fig. 3.2. was fit to a third order polynomial (Eq. (36)) to interpolate $C_{\text{max}}^{\text{liq}}$ at any desired water temperature. In Fig. 3.2., we also show the predictions of water concentration in membrane as obtained using the empirical correlations for vapor equilibrated membranes (Eqs. (8-9)) suggested by Springer et al. [21], Kusoglu et al. [38] and Hinatsu et al. [24] by considering water activity to be 1 at the membrane-water interface. It is to be noted that these correlations have been used in several previous humidifier models [10, 11,13,15,17,39]. It is evident that these correlations under-predict the equilibrium water concentration in Nafion™ membrane leading to erroneous prediction of moisture flux in a LVP process.

$$C_{\text{max}}^{\text{liq}} = -99467.411 + 5312.483T_w - 70.255T_w^2 + 0.313T_w^3 \dots\dots\dots (36)$$

where, T_w is the water temperature in $^\circ\text{C}$.

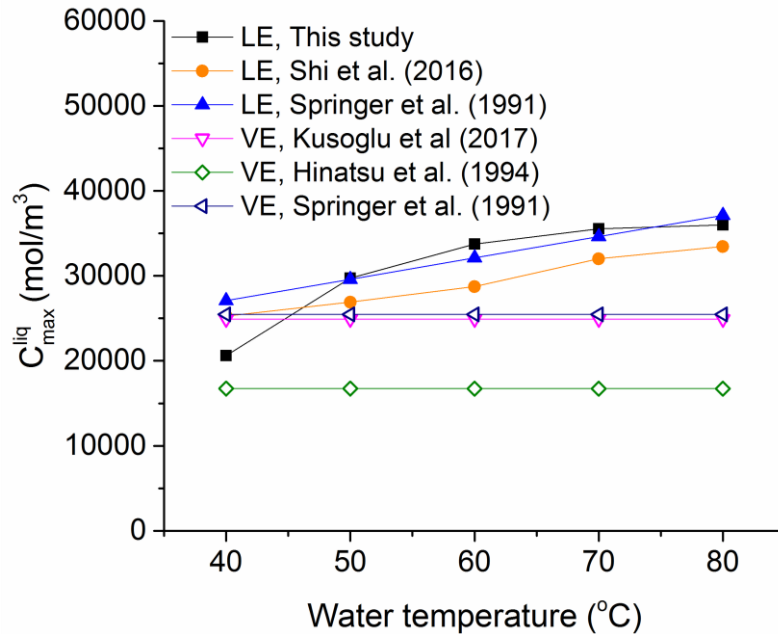


Fig. 3.2. Comparison of sorption isotherms for liquid equilibrated (LE) Nafion membranes. The filled symbols are the experimentally obtained values in different studies. The hollow symbols represent maximum water concentration in the membrane when predicted by the polynomial expressions proposed

for vapor equilibrated (VE) membranes ($a_w = 1$). For liquid equilibrated Nafion™ membranes, empirical expression given by Springer et al. (1991) [21] or Eq. (36) may be used.

Tube side convective mass transfer coefficient(K_t), and convective heat transfer coefficient (h_t), are obtained in terms of Sherwood number(Sh), and Nusselt number(Nu), respectively, and are calculated using standard correlations given below for smooth tubes [35].

$$Sh = \frac{K_t d_{id}}{D_a} \dots\dots\dots(37)$$

$$Nu = \frac{h_t d_{id}}{k_a} \dots\dots\dots(38)$$

$$Nu = 3.658 + \left(\frac{0.085 \left(Re \cdot Pr \frac{d_{id}}{H} \right)}{1 + \left(0.047 \left(Re \cdot Pr \frac{d_{id}}{H} \right)^{2/3} \right)} \right) \dots\dots\dots(39)$$

$$Sh = 3.658 + \left(\frac{0.0668 \left(Re \cdot Sc \frac{d_{id}}{H} \right)}{1 + \left(0.04 \left(Re \cdot Sc \frac{d_{id}}{H} \right)^{2/3} \right)} \right) \dots\dots\dots(40)$$

In the above equations, Reynolds number (Re), Prandtl number (Pr), and Schmidt number (Sc) have their usual definitions

$$Re = \frac{\rho_a v_a d_{id}}{\mu_a}, Pr = \frac{c_{pa,dry} \mu_a}{k_a}, Sc = \frac{\mu_a}{\rho_a D_a}$$

Eqs. (38) and (39) are also used to calculate the shell side heat transfer coefficient by replacing the thermal conductivity of air with that of water and by replacing tube inner diameter by the hydraulic diameter of the shell after accounting for the packing fraction of the tubes as shown in Eq. (41) [18]

$$D = \frac{(1-\phi)(D_s^2)}{N d_{od} + D_s} \dots\dots\dots(41)$$

Where, D (m) is the Hydraulic diameter for shell side water flow, ϕ is the packing fraction, N is the number of tubes, d_{od} (m) is the tube outer diameter and D_s (m) is the shell diameter.

3.3. Results and Discussion

3.3.1. Liquid-Vapor Permeation (LVP)

We start by answering the question: “which of the two equations, Eq. (7) or Eqs. (8-9) would better represent the equilibrium condition at the membrane-air interface in the case of LVP i.e., when the membrane has an interface with liquid water on one side and air on the other?” Majsztrik et al. [28] studied LVP in Nafion™ 115 by measuring the moisture flux through the membrane at different gas flow rates. The moisture flux J_o (mol/m²s) was calculated as

$$J_o = \frac{P_v \dot{Q}}{RTA_m} \dots\dots\dots (42)$$

Here, \dot{Q} (L/min or lpm) is the nitrogen gas flow rate, T (K) is the temperature at which the experiment was carried out, A_m (m²) is the membrane area, and at steady state, $P_v = P_{eq}$.

The flux is also given by Fick's law of diffusion

$$J_o = D_m \frac{(C_{max}^{liq} - C_L)}{L} \dots\dots\dots (43)$$

Where the various terms on the right hand side of Eq. (43) have already been defined earlier. Note that C_L is in equilibrium with P_{eq} at the membrane-gas interface. Substituting C_L from Eq. (7) in Eq. (43) and deriving for P_{eq} , we get

$$P_{eq} = \frac{D_m C_{max}^{liq} RT A_m P_{v,sat}}{\dot{Q} L P_{v,sat} + D_m C_{max}^{liq} RT A_m} \dots\dots\dots (44)$$

Similarly, C_L from Eq. (9) was substituted into Eq. (43) to get another expression for P_{eq} as below

$$C_{max}^{liq} \frac{E.W.}{\rho_m} - 0.043 - \left[\frac{\dot{Q} L E.W.}{RT A_m D_m \rho_m} + \frac{17.81}{P_{v,sat}} \right] \times P_{eq} + \left(\frac{39.85}{P_{v,sat}^2} \right) \times P_{eq}^2 - \left(\frac{36}{P_{v,sat}^3} \right) \times P_{eq}^3 = 0 \dots\dots\dots (45)$$

C_{max}^{liq} in Eqs. (44) and (45) was obtained using the polynomial expression of Eq. (36). P_{eq} values predicted from Eqs. (44) and (45) are then substituted in Eq. (42) to predict the fluxes, which are presented as solid lines in Fig. 3.3. for three different temperatures and are compared with experimental data of Majsztrik et al. [28]. By choosing diffusion coefficient values of 8×10^{-10} , 13

$\times 10^{-10}$ and $18 \times 10^{-10} \text{ m}^2/\text{s}$ respectively for 50, 70 and 80 °C, the predictions of model Eq. (42) and Eq. (44) are found to be in close agreement with the experimental data of Majsztrik et al. [28].

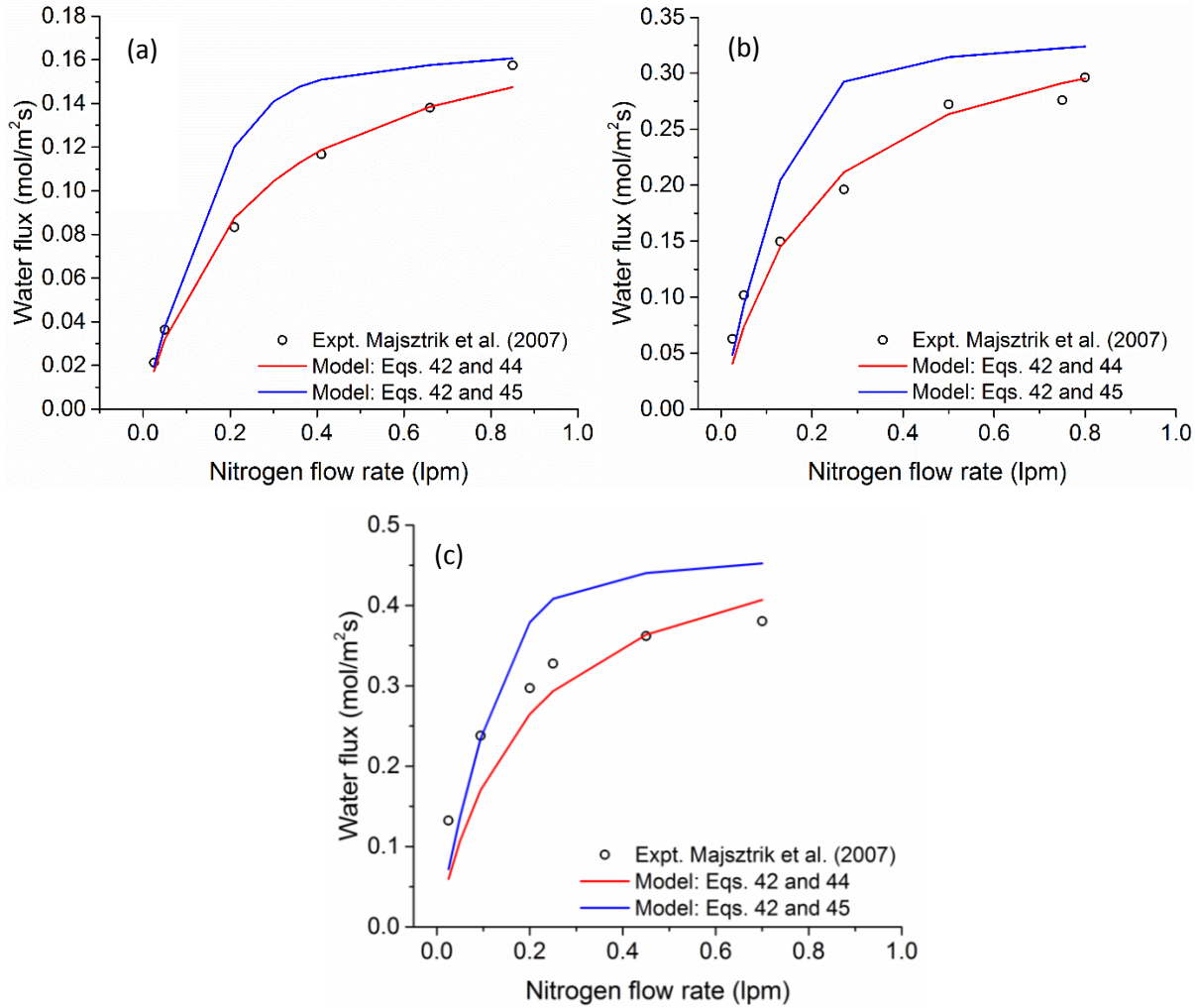


Fig. 3.3. Comparison of LVP fluxes with membrane-air interface equilibrium expressions from Monroe et al. (2007) (red lines) [31] and Springer et al. (1991) (blue lines) [21] for (a) 50 °C (b) 70 °C and (c) 80 °C

As can be seen in Fig. 3.3., for all temperatures, Monroe's equilibrium expression (Eq. (7)) seems to better match the experimental data for LVP quantitatively as well as in terms of behavior with respect to nitrogen flow rate. The over prediction of fluxes in case of Springer et al.'s [21] equilibrium expression (Eq. (8)) is attributed to the estimation of lower λ_m at the membrane-air interface, which is typically obtained because of the equation's origin in modelling VVP systems.

As mentioned earlier, it has been a common practice in humidifier models [10, 11, 13, 15, 39] to use the empirical expression proposed by Springer et al. [21] at both the membrane interfaces.

While this could be appropriate for a gas-to-gas humidifier which involves VVP, the same cannot be expected to work for a water-to-gas humidifier which involves LVP. In Fig. 3.4. below, we show how the empirical correlation (Eq. (8)) either over-predicts or under-predicts the fluxes when the membrane-water interface is also modelled using Eq. (8) keeping water activity as 1. This happens because the maximum water content predicted by Eq. (8) is 14, which amounts to a temperature independent $C_{max}^{liq} \approx 30545 \text{ mol/m}^3$ thereby enabling a higher concentration gradient at lower temperatures (when the actual $C_{max}^{liq} < 30545 \text{ mol/m}^3$) and a lower concentration gradient at higher temperatures (when the actual $C_{max}^{liq} > 30545 \text{ mol/m}^3$).

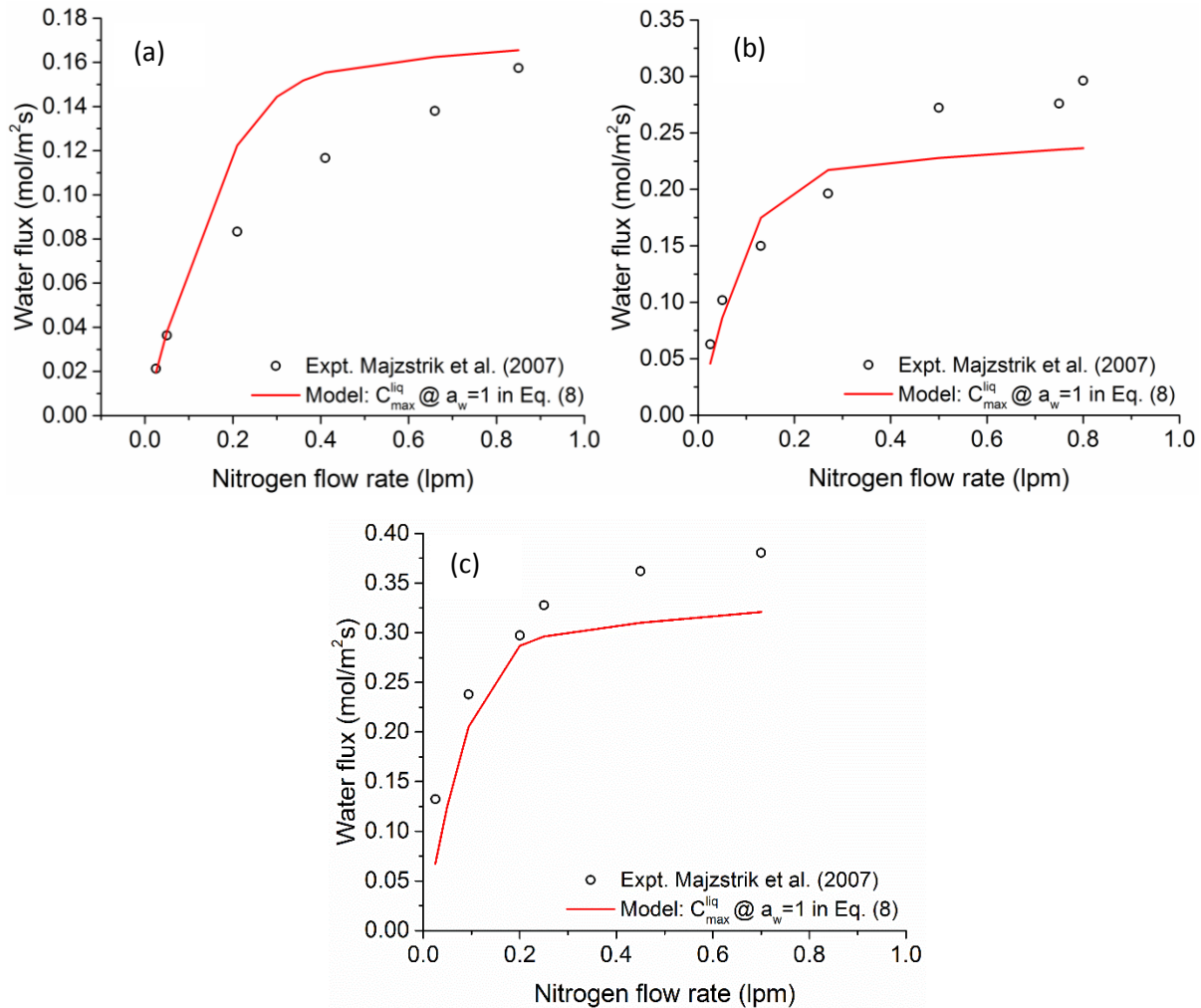


Fig. 3.4. Water flux predictions when both the membrane interface equilibrium are modelled using Eq. (8) for (a) 50 °C (b) 70 °C and (c) 80 °C

In summary, it can be said that appropriate equilibrium expressions at the membrane-water interface and membrane-air interface should be used to model humidification in a water-to-gas humidifier. We find that the empirical cubic polynomial expression as a function of temperature (Eq. (36)) is well suited to model equilibrium at the membrane-water interface, while Monroe's expression (Eq. (7)) is well suited to model equilibrium at the membrane-air interface. It must be noted that Monroe's expression (Eq. (7)) is a generalized expression and is independent of the membrane material and would thus be applicable for a variety of membranes and not just Nafion™ unlike Eq. (8) proposed by Springer et al. [21].

3.3.2. Model Validation

We take the case of Perma Pure's FC200-780-7LP humidifier module of known geometric parameters to validate our model. The details of the Perma Pure humidifier are presented in Table 3.3.

Table 3.3: Humidifier parameters for Perma Pure FC 200-780-7LP.

Parameters	Value
Membrane thickness (L)	0.00005 m
Membrane tube inner diameter (d_{id})	0.00097 m
Membrane tube outer diameter (d_{od})	0.00107 m
Active length of membrane tube (H)	0.1778 m
Number of membrane tubes (N)	780
Inner diameter of shell (d_s)	0.056 m
Membrane dry density (ρ_m)	0.002 kg/cm ³
Membrane dry equivalent weight ($E.W.$)	1.1 kg/mol

Experimental results on this Perma Pure humidifier module were obtained using a test rig shown schematically in Fig. 3.5. The experiments were carried out for various air and water flow rates at different water inlet temperatures. The inlet and outlet temperatures of water and air were carefully measured along with the relative humidity of inlet and outlet air flow. Water temperature was set using a constant temperature water bath (Typ011-0794, Thermo Electron

(Karlsruhe) GmbH, Germany) having a temperature accuracy of ± 2 °C. All tubes were insulated in order to avoid heat loss through them. A mass flow controller (Alicat, Model: MCR-1000SLPM-D/5M) was used for measuring the flow rate of gas. A pressure transducer (Wika S-11 series) with a range of 0-100 psi was used for gas pressure measurements. A warmed probe optical mirror based humidity sensor (Vaisala HMT-337 series) was used for measurement of inlet and outlet gas temperature and relative humidity. In addition to our experimental data, the model was also validated against the performance curves obtained from Perma Pure's datasheet [40].

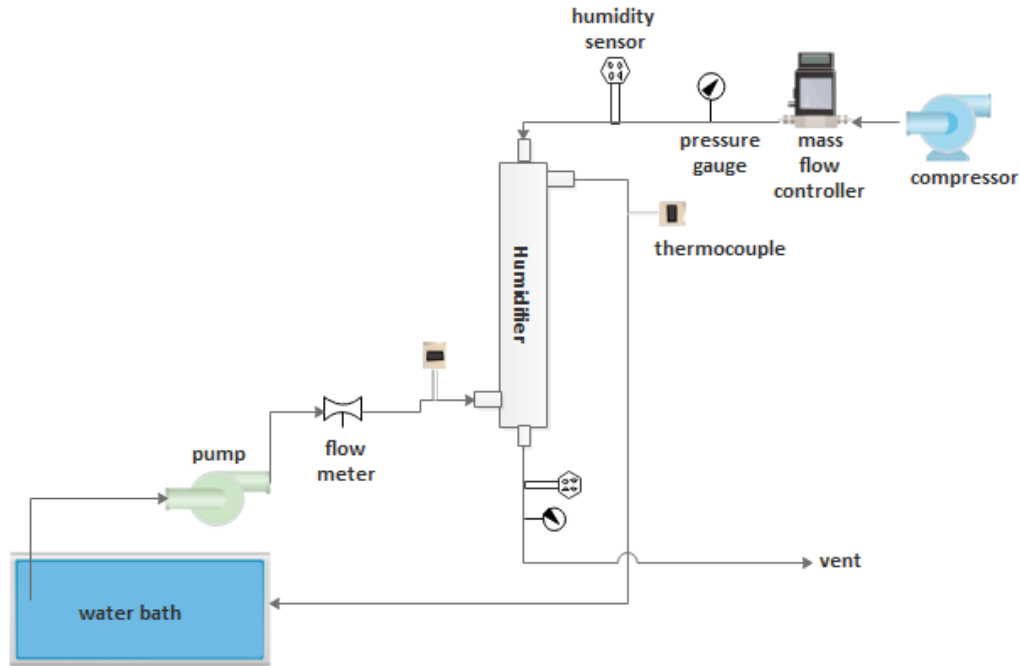


Fig. 3.5. Schematic representation of the test rig.

We begin by calibrating our model against a reference case selected from Perma Pure's datasheet. This reference case pertains to an inlet air temperature of 25 °C, relative humidity of 10 %, inlet water temperature of 60 °C, inlet air flow rate of 650 lpm and inlet water flow rate of 26 lpm. Near quantitative fit of model predictions were possible with Perma Pure's data for the reference case by selecting $D_m = 6 \times 10^{-10}$ m²/s, which is in excellent agreement with widely reported experimental data [22, 23, 32, 38, 41]. For instance, the value of D_m calculated from the empirical correlation proposed by Motupally et al. [42] (see Eq. (46)) for water content (λ_m , mol H₂O / mol SO₃⁻) that corresponds to C_{max}^{liq} (from Fig. 3.2.) is very close to the value used in our calculations. Equation 46 corresponds to the case of liquid-vapor permeation experiments

carried out for Nafion 115 wherein one interface was equilibrated with liquid water and the other interface was equilibrated with nitrogen gas flow. The overall heat transfer coefficient required to obtain good model fit to experimental data was found to be $U_{fit} = 2.3 U$ where U was obtained from the standard correlation Eq. (21). A possible reason for the higher heat transfer coefficient relative to that predicted by Eq (21) was suggested by Karlsson et al. [43] and Rautenbach et al. [44]. The authors proposed that in pervaporation process the mass flux through membrane results in enhancing the effective convective heat transfer coefficient. With these values of parameters, model predictions were made for the other air flow rates at inlet water temperature of 60°C and for all air flow rates at inlet water temperatures of 40 °C and 80 °C. The water to air flow rate ratio was kept at 1:25 as suggested by Perma Pure’s datasheet [40]. As can be seen from Fig. 3.6., the model predicts the outlet dew point of gases with reasonable accuracy.

$$D_m = 4.17 \times 10^{-4} \lambda_m \left(1 + 161 e^{\lambda_m} \right) \exp \left[\frac{-2436}{T_m} \right] \quad 3 < \lambda_m < 16.8 \quad \dots\dots\dots (46)$$

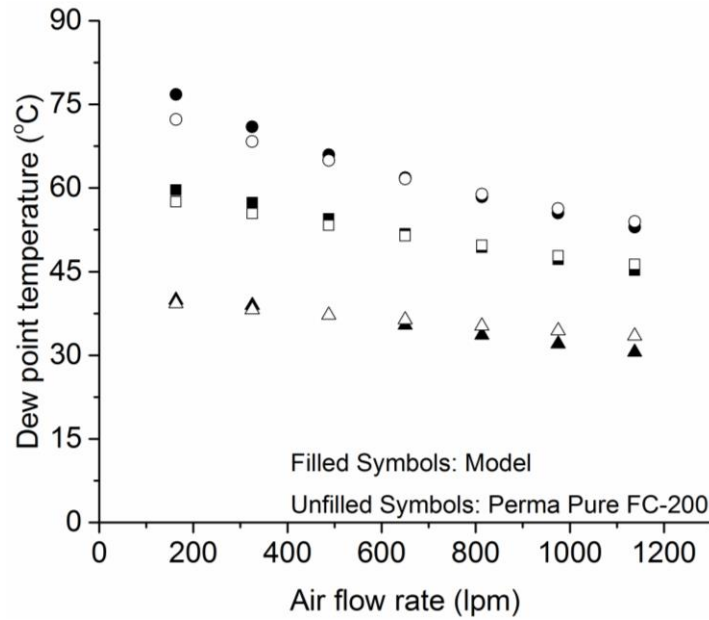


Fig. 3.6. Model predictions vs. Perma Pure’s data, $T_w = 40$ °C (triangles), 60 °C (squares) and 80 °C (circles)

Next, we compare the model predictions with experiments performed on the test-rig. In each test, the inlet conditions were recorded and the same conditions were used in the model to predict the performance. It can be observed from the graphs in Fig. 3.7(a-c) that as air flow rate was increased the dew point remained nearly constant for the water temperatures of 40 and 60

°C, but decreased slightly for water temperature of 80 °C. Model predictions capture this trend reasonably well with a small (<10%) over-prediction for $T_w = 80$ °C case. This deviation is likely due to heat loss from the humidifier surface to ambient, which is not accounted for in model.

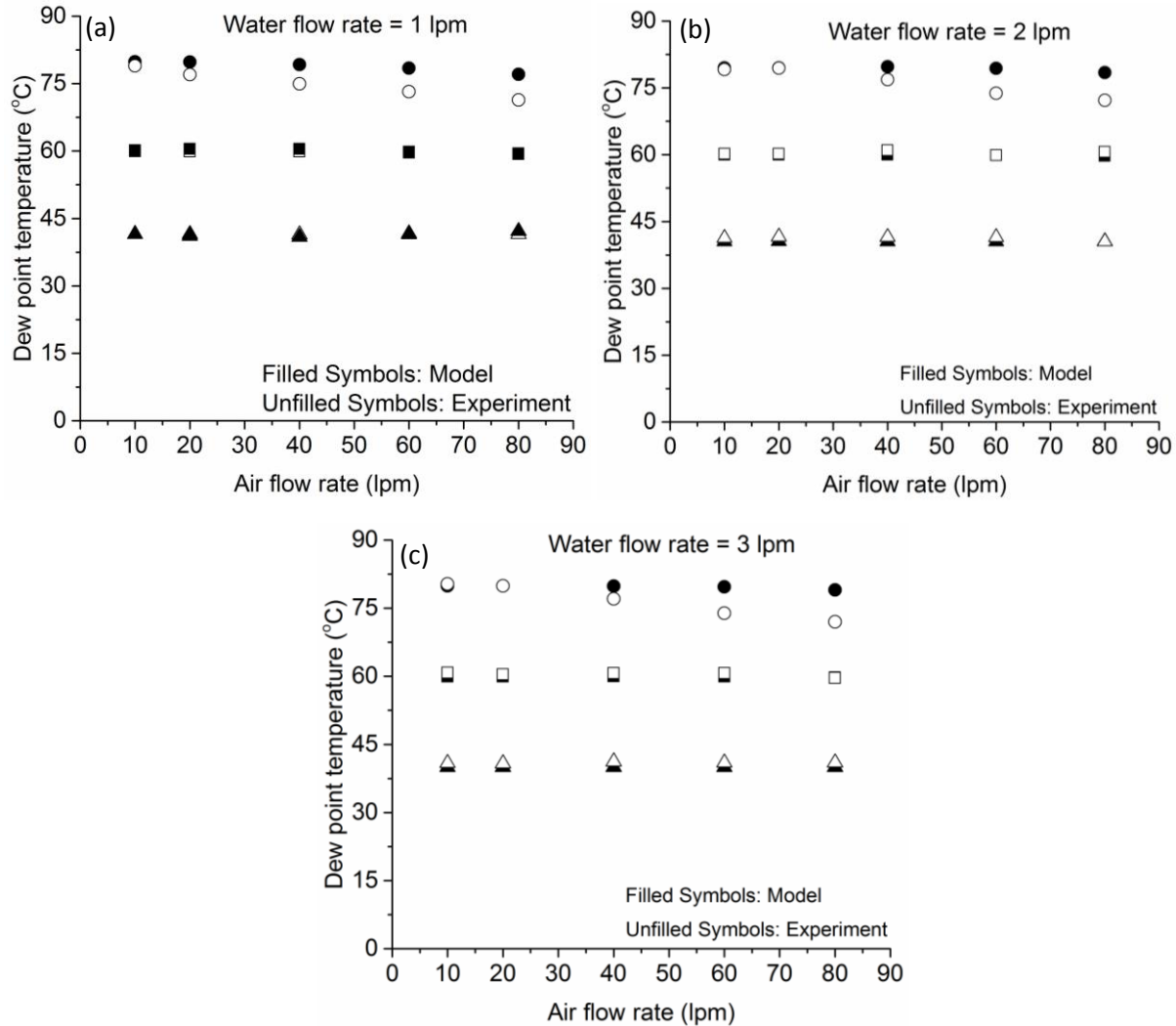


Fig. 3.7. Model validation with experiments performed on test rig with water flow rates (a) 1 lpm, (b) 2 lpm and (c) 3 lpm; , $T_w = 40 \pm 2$ °C (triangles), 60 ± 2 °C (squares) and 80 ± 2 °C (circles)

3.3.3. Non-dimensional analysis

The dimensionless numbers that are obtained from the non-dimensional governing equations indicate significance of heat and mass transport processes occurring on shell and tube sides. Table 3.2 lists all the dimensionless numbers along with their physical significance. Fig. 3.8. shows a plot of the dimensionless numbers as a function of dimensionless tube length. It can be seen that except for β and δ' , the dimensionless numbers increase monotonically with tube length.

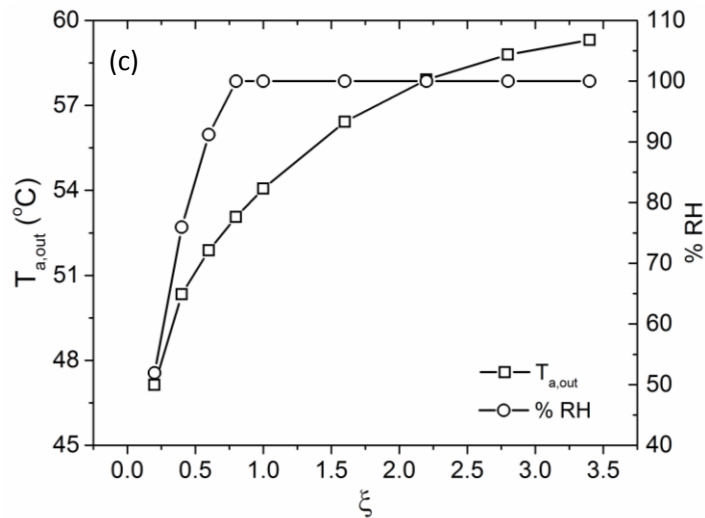
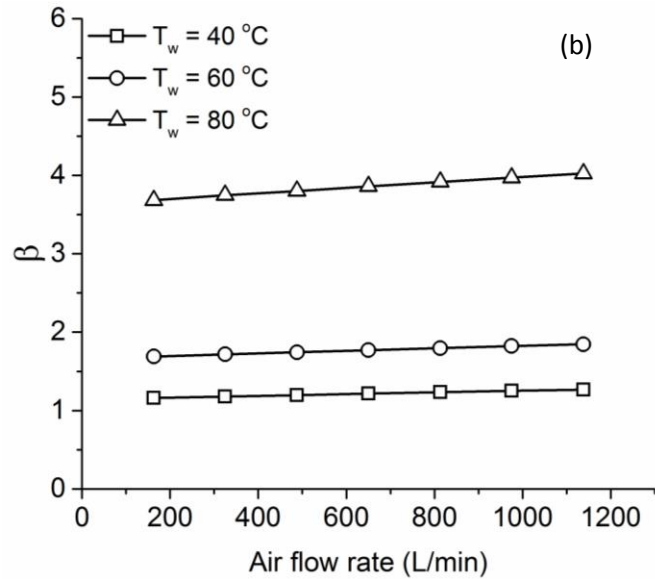
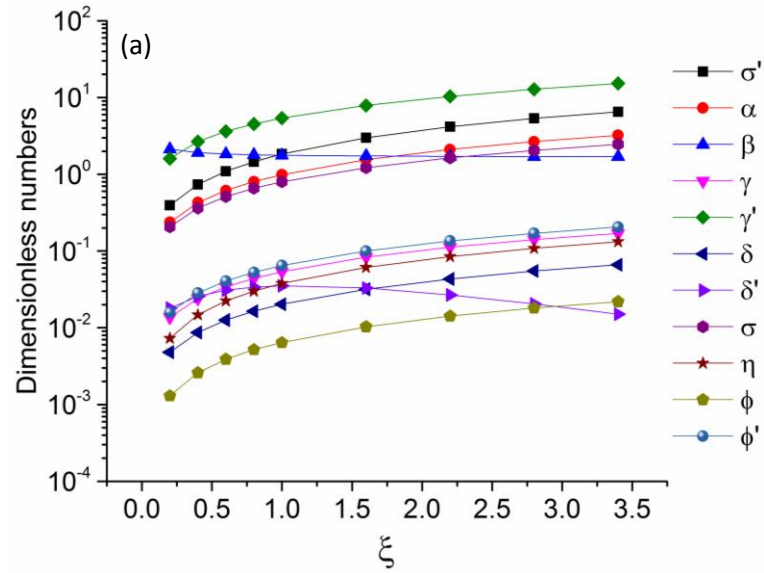
The sensible heat of moisture which is governed by the dimensionless number δ' (SHR) has magnitude two orders smaller than the heat transferred due to convection which is governed by dimensionless number γ' (NTU on tube side). Thus, the sensible heat added due to moisture transfer is a negligible component of overall heat and therefore can be neglected in calculations. Major contributors to tube side heat transfer are the dimensionless numbers γ' and σ' . While γ' governs the sensible heat added by convection, σ' on the other hand governs the enhancement in heat capacity of the gas due to addition of moisture in the air. Another number σ in the tube side energy balance equation also plays a role in controlling the extent of increase in air temperature and is seen to be significant. On the shell side, γ , δ and η are found to have similar magnitudes and are therefore important to be considered in the energy balance equation. Fig. 3.8a also helps to establish a key insight about the variation in mass flow rates on shell and tube sides. The numbers ϕ' and ϕ which govern respectively the variation in tube side air mass flow rate and shell side water mass flow rate suggest that while the latter is small, the former can be significant and therefore cannot be ignored. This is also corroborated with Fig. 3.8e wherein it is seen that the variation in mass flow rate of air can be significant along the tube length whereas the variation in shell side mass flow rate is less than 1 %. Another key observation is that the dimensionless number β which represents the rate of convective mass flux in gas over diffusion flux in the membrane, is greater than unity for $\xi < 1$ suggesting that the diffusion flux through the membrane is the rate limiting step. As the gas travels through the tube and picks up humidity, the driving force for convective mass transfer gradually reduces and eventually matches the diffusion flux through the membrane so that β approaches unity. Simultaneously, the gas temperature and relative humidity also approach near their maximum values as shown in Fig. 3.8(c).

Fig. 3.8(b) shows the effect of air flow rate and water inlet temperature on β . It can be seen that $\beta > 1$ for most cases of gas flow rates and water inlet temperatures indicating that diffusional resistance through the membrane has a greater contribution than interfacial resistance in controlling vapor transport. However, for the case where water inlet temperature is 40°C, $\beta \approx 1$ indicating that membrane-gas interfacial resistance cannot be neglected. This is expected because the diffusion coefficient of Nafion being a function of water content and temperature,

increases with increasing temperature (see Eq. (46)). Thus, both membrane diffusion as well as interfacial resistance can be important for humidity transfer.

On the shell side, comparison of δ and γ suggests that heat transferred from water by latent heat of evaporation is nearly as much as the heat transferred by convection and conduction. Thus, coupling between heat and mass transfer by evaporation is important. However, the values of η in Fig. 3.8a suggest that sensible heat transported by the water diffusing through the membrane is a small fraction of the total heat brought into the humidifier by the incoming water. Therefore, it is safe to neglect this contribution when writing the heat balance across the membrane (see Eq. (2)).

In Fig. 3.8(d), heat and vapor transfer rates are plotted with respect to increasing dimensionless length. It can be seen that both heat transfer rate (HTR) and vapor transfer rate (VTR) follow a non-monotonic trend. The transfer rates first increase with increasing length and then decrease after reaching a maximum. The non-monotonicity is a result of decreasing thermal and concentration gradients along with increasing membrane area along the tube length. In addition, as the gas temperature increases along the length, the saturation vapor pressure of the gas increases thereby increasing the gas phase partial pressure gradient ($P_{eq} - P_v$) for vapor transfer. This however does not increase indefinitely and when the gas temperature reaches its steady state value, the HTR and VTR starts decreasing as expected. Earlier models have not explicitly demonstrated this coupling of heat and mass transfer along the length of the tube.



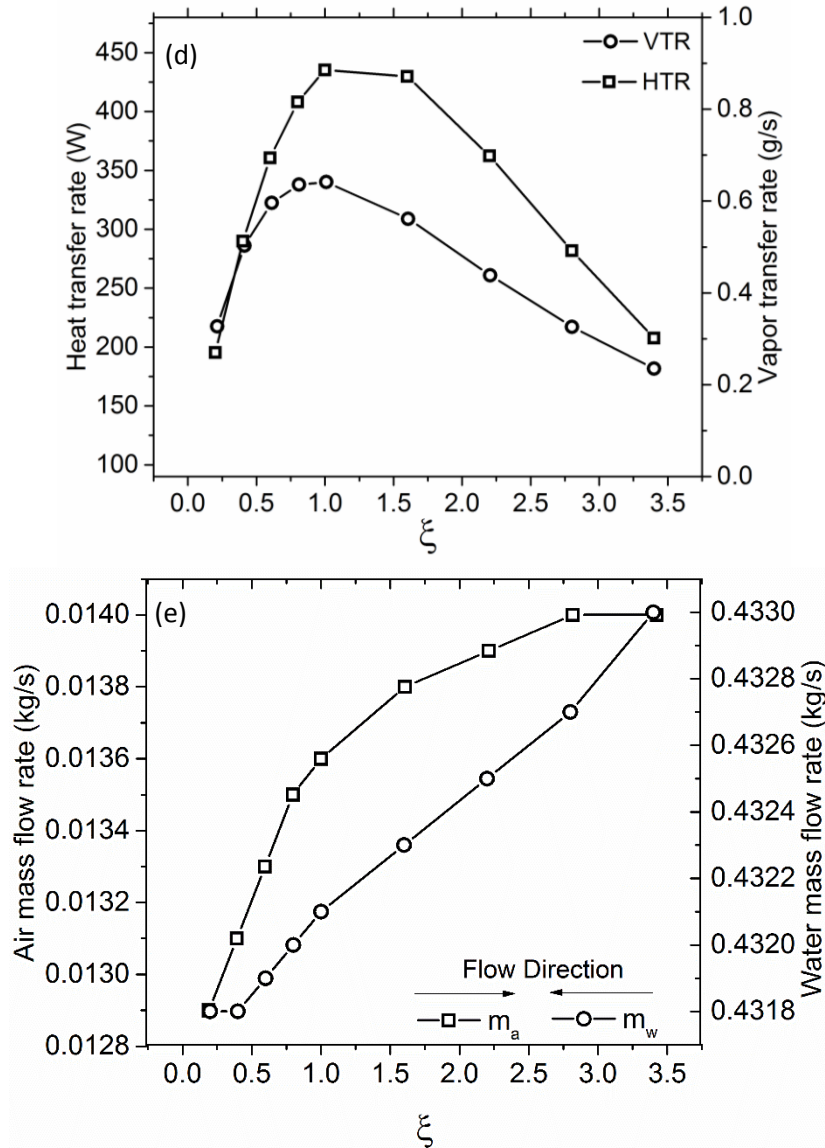


Fig. 3.8. Variation with respect to dimensionless tube length for (a) Dimensionless numbers (b) β with air flow rate for different water temperatures (c) outlet gas temperature and relative humidity (d) Heat transfer rate (HTR) and Vapor transfer rate (VTR) and (e) air and water mass flow rates. These calculations are shown for the reference case (PermaPure FC200-780-7LP humidifier; inlet air temperature of 25 °C relative humidity of 10 %, inlet water temperature of 60 °C, inlet air flow rate of 650 lpm and inlet water flow rate of 26 lpm)

3.3.4. Quantification of resistances to heat and mass transfer

Several resistances act upon the heat and mass transfer during humidification. To shed some light on the relative significance of each of these resistances, it is necessary to quantify them. While the resistances to heat transfer are estimated as the inverse of the respective heat transfer coefficients, the mass transfer resistance on the tube side is estimated as $1/\Gamma K_t$ (where $\Gamma =$

$\frac{P_{v,sat}}{RT_m C_{max}^{liq}}$ is the dimensionless Henry's constant) and the diffusion resistance in the membrane is estimated as L/D_m .

Table 3.4 records various resistances offered to heat and mass transfer in different regions (shell, tube and membrane) of the humidifier for the reference case. It is evident that the shell side resistance to heat transfer is at least an order of magnitude smaller than that on tube side. Therefore, our assumption of $T'_w \approx T_w$ used in Eq. (4) is validated. From Table 3.4 it becomes clear that while the heat transfer rate is mostly limited by the membrane-gas interfacial resistance, the mass transfer rate is governed by both diffusion within the membrane and interfacial resistance. This is in agreement with several earlier reports [16,25,27-29,31,32,38,45-49] who noted that both interfacial transport and bulk diffusion were important for determining water transport across the membrane.

Table 3.4: Various resistances for heat and mass transfer in the humidifier.

Re= 1162 AFR=650 lpm				
Resistances	Heat transfer resistance (m ² K/kW)	Percentage (%)	Mass transfer resistance (s/m)	Percentage (%)
Liquid side	0.62	6.18	0.0	0.0
Membrane	0.197	1.96	8.34 x 10 ⁴	63.91
Air side	9.21	91.85	4.71 x 10 ⁴	36.09
Total	10.027	100	13.05 x 10 ⁴	100

3.3.5. Effect of flow configuration

Typically, hollow fiber membrane based humidifiers are built in the form of shell and tube heat exchanger with the provision to operate them in co-flow or counter-flow mode. However, from basic understanding of heat exchangers it is well known that counter-flow arrangement provides better heat transfer in comparison to co-flow mode due to a higher temperature gradient across the length of the tubes. To check if the same would occur in a HFM humidifier, we study here the effect of flow configuration on humidifier performance. It must be noted that a humidifier is different from a heat exchanger due to coupled heat and mass transfer. Fig. 3.9(a,b) records the outlet air temperature, vapor pressure, absolute humidity and percentage relative humidity that are obtained based on model predictions. It can be clearly seen that

counter-flow offers superior performance in terms of outlet-air temperature, partial pressure of vapor and absolute humidity (mixing ratio). However, relative humidity for co-flow configuration marginally supersedes the counter-flow configuration because even though the outlet air vapor pressure is higher in the counter-flow mode, the corresponding increase in air temperature leads to a higher saturation vapor pressure thereby leading to slightly lower relative humidity in counter-flow mode.

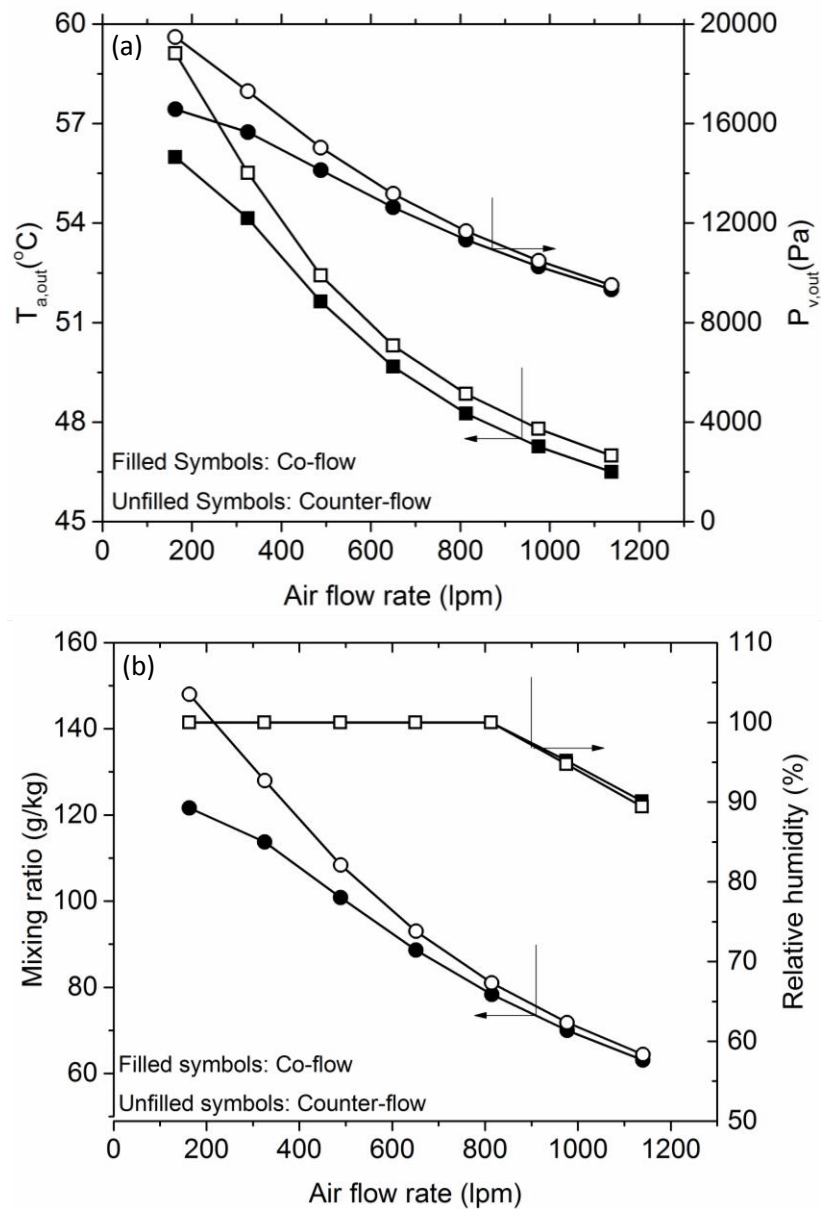


Fig. 3.9. Effect of flow configuration on (a) outlet air temperature (squares) and vapor pressure (circles) (b) mixing ratio (absolute humidity) (circles) and percentage relative humidity (squares)

3.3.6. Effect of geometric parameters

In this section, we present model predictions obtained by varying several geometric parameters that govern the performance of the humidifier. Here we study the effect of all parameters for a single water temperature of 60 °C and vary air and water flow rates in the ratio 25 : 1 as per Perma Pure's datasheet recommendations [40]. While tube length, number of tubes and inner diameter of tube in general affect the active surface area for heat and mass transfer, the membrane thickness also increases the length scale for thermal and mass diffusion. In addition, the cost of humidifier scales with the active area. Therefore, designing humidifiers tailored for specific applications requires optimization of these parameters. Besides these parameters, adjusting flow rates and temperatures of the fluids can also provide the desired performance from humidifiers.

Fig. 3.10(a,b) present the model predictions for variable tube number. It is seen that the lower tube number ($N=200$) drastically reduces the air outlet temperature as well as the relative humidity. As the number of tubes are increased, the air starts to reach closer to the water temperature and saturation vapor pressure at that temperature. The predictions imply that as the number of tubes increase, both heat and mass transfer processes are positively improved. More number of tubes leads to increase in the residence time in each tube and therefore allows for increase in exchange of heat and mass across the length of the humidifier. It is seen that for high tube numbers ($N=1000$), the air relative humidity saturates at all air flow rates whereas air temperature does not. This is in agreement with the predictions shown in Fig. 3.8c. This implies that mass transfer on tube side is a rapid process and achieves saturation before thermal saturation, which may require an even higher active surface area for saturation. This can also be corroborated based on the tube side convective resistance to heat and mass transfer presented in Table 3.4. While, the convective resistance accounts for ~92 % for heat transfer, it only accounts for ~36 % in case of mass transfer.

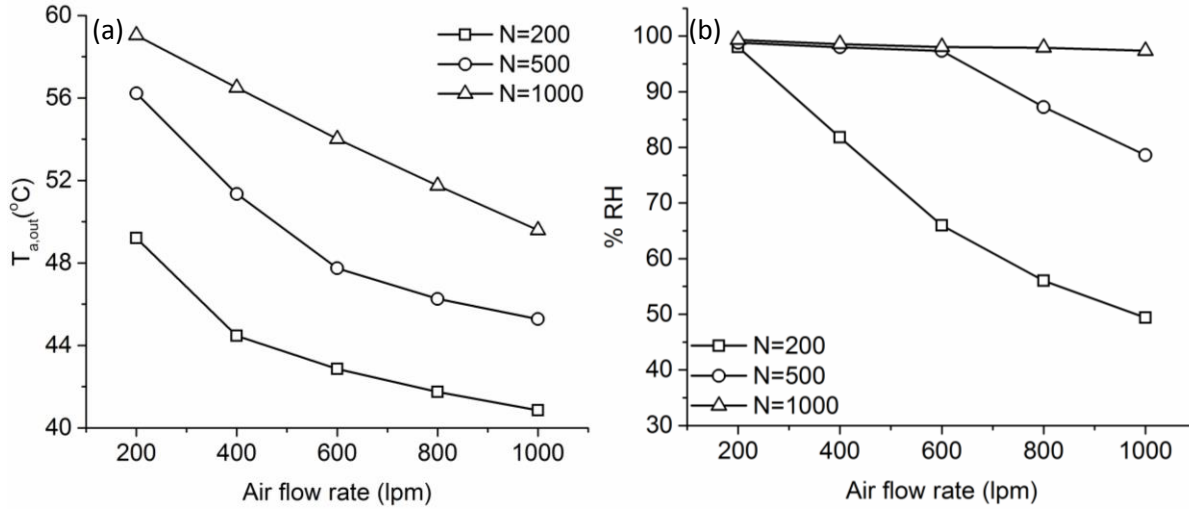


Fig. 3.10. Effect of tube number on (a) air outlet temperature (b) percentage relative humidity.

Fig. 3.11(a,b) shows the effect of membrane thickness on outlet air temperature and relative humidity. It was shown in Table 3.4 that the membrane resistance governs the mass transfer while it has negligible significance on heat transfer. Fig. 3.11a shows the effect of membrane thickness on outlet air temperature. As expected, the outlet air temperature is seen to decrease with increasing membrane thickness for air flow rates <600 L/min. However, beyond 600 L/min the outlet air temperature is observed to increase for membrane with thickness of 100 μ m. This happens because at a certain air flow rate (i.e. 600 L/min in this case), the reduction in mass transport for a thicker membrane (due to higher membrane resistance) leads to reduction of the specific heat capacity of air (see Eq. (27)) resulting in an increase in outlet air temperature. However, effect of thickness on mass transfer is more predominant with lower thickness facilitating higher flux and therefore improving the relative humidity of the outlet air. Decrease in LVP fluxes with increasing membrane thickness was also observed by Adachi et al. [16] who studied the effect of Nafion™ membrane thickness on water transport. Interestingly, using very thin membrane ($L = 25 \mu$) shows a surprising trend in relative humidity which saturates at low air flow rates and remains nearly constant with increasing air flow rates. This observation is similar to RH obtained with $N=1000$ although in this case the membrane-gas interfacial area is not changed. Since, membrane thickness does not affect the heat transfer rate as much as it does the vapor transfer rate, therefore in case of thinner membrane, the increase in vapor transfer due to lower diffusional resistance leads to $P_v \approx P_{v,sat,air}$ at nearly all air flow rates. Further, on

increasing the air flow rate this increased vapor flux is complemented with increasing convective mass transfer coefficient thereby leading to maintaining RH near saturation. At very high air flow rate, the usual trend of decreasing RH with increasing air flow rate is observed since the residence time is not sufficient for vapor transport to reach saturation.

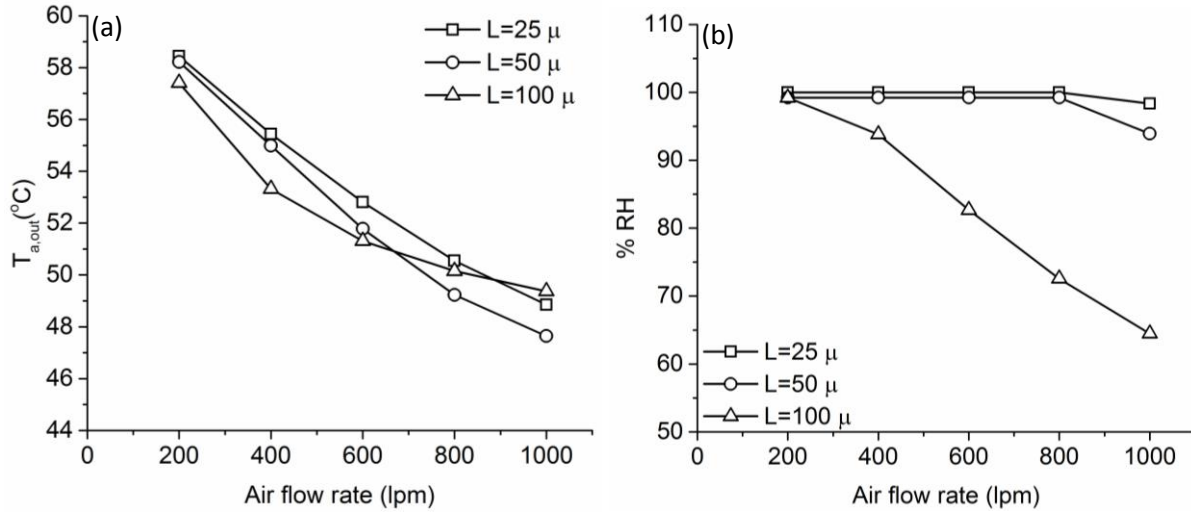


Fig. 3.11. Effect of membrane thickness on (a) air outlet temperature (b) percentage relative humidity.

Fig. 3.12(a,b) shows that tube length is extremely critical for heat transfer, and more so at higher air flow rates. Smaller active area in general leads to lower outlet air temperature as well as lower relative humidity. This is also corroborated by the effect of tube number mentioned earlier where higher membrane area leads to better humidification. A longer tube length provides sufficient residence time to the air for heat and mass uptake from the liquid stream. However, since we cannot have an infinitely long tube for maximizing humidifier performance, there has to be a trade-off between the desired performance and the active area of tubes. The dimensionless number β can provide a suitable means of determining the length of the humidifier as mentioned earlier in section 3.2.

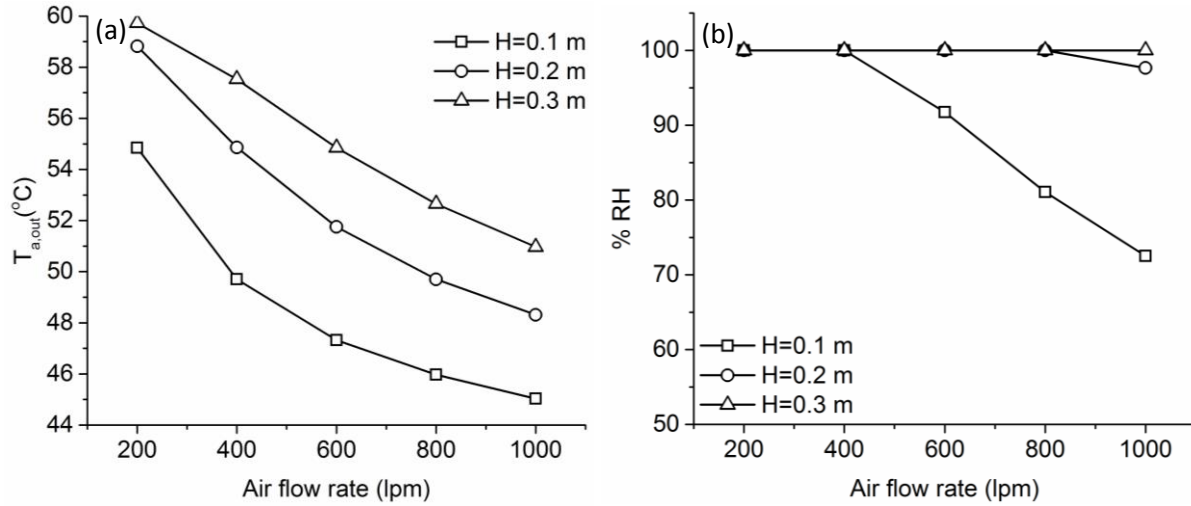


Fig. 3.12. Effect of tube length on (a) air outlet temperature (b) percentage relative humidity.

Effect of tube inner diameter is shown in Fig. 3.13(a,b). The effect is similar to increasing the active surface area thereby improving the moisture transfer rate and therefore the relative humidity. Increasing the diameter leads to increasing the packing fraction which leads to the similar effect as that from increasing the number of tubes. A smaller tube diameter leads to smaller residence time due to increased air velocities. Therefore, both heat and mass uptake suffer poorly from a smaller tube diameters. As the tube diameter is increased, improvement in humidifier performance can be observed due to increase in active surface area facilitated with higher residence time.

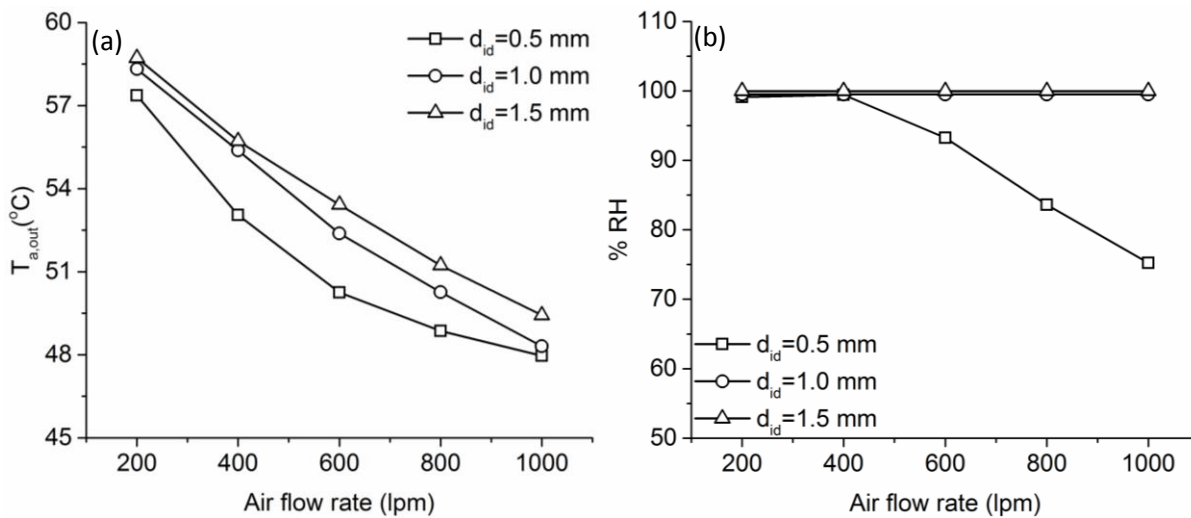


Fig. 3.13. Effect of tube inner diameter on (a) air outlet temperature (b) percentage relative humidity.

3.4. Conclusions

This study presents a comprehensive modelling effort of the steady state humidification process in a water-to-gas humidifier. The model accounts for coupling between heat transport and mass transport in the humidification process. The model also accounts for variation in specific heat of air and the mass flow rates of air and water along the length of the humidifier. Additionally, the model considers appropriate equilibrium conditions at the membrane-gas and membrane-water interfaces for the liquid-to-vapor permeation process occurring in the humidifier. While an empirical sorption isotherm as a function of temperature was shown to adequately model the amount of water sorbed in the membrane (C_{max}^{liq}) at the membrane-water interface, a modified Henry's law served well for simplistic and generalized determination of the equilibrium condition at the membrane-gas interface.

The model predictions were found to be in good agreement with experimental data obtained with a commercial humidifier in which process parameters such as air flow rate and water inlet temperature were varied. The model was further used to investigate the effects of humidifier parameters such as length of hollow fiber membrane tubes, thickness of membrane, number of tubes, diameter of tubes and flow configuration (co-current vs counter-current). It was found that higher membrane area achieved by increasing tube length, tube ID or number of tubes leads to better humidification performance. Under otherwise identical process conditions, counter-flow mode of operation provides better humidification performance than co-flow. However, when relative humidity from the two modes are compared, co-flow marginally exceeds in performance over counter-flow.

The variation in mass flow rate and specific heat of air due to addition of moisture during humidification process were found to be significant at low air inlet flow rates and high water inlet temperature. The variation in water mass flow rate is relatively much smaller and may be neglected. At higher air flow rates the change in air and water mass flow rates along the humidifier length were small.

Dimensionless numbers obtained from non-dimensionalizing the governing equations provided useful insights into the key phenomenon governing the coupled heat and mass

transport across the length of the humidifier. It was found that the membrane-water interface imparts little or no resistance to heat and mass transport due to high shell-side convective transfer coefficients. For practical flow rates in a hollow fiber membrane humidifier where Reynolds number are high, the heat transfer rate is limited by membrane-gas interfacial resistance, while the mass transfer rate is governed by both bulk diffusion in the membrane and membrane-gas interfacial resistance. A consequence of this is seen for the case in which membrane thickness was varied. Increasing membrane thickness increases the resistance to mass transport and consequently the relative humidity decreases. However, this leads to smaller increase in specific heat capacity along the tube length and as a result, increases the air outlet temperature. The heat transfer rate and mass transfer rate were found to vary non-monotonically along the tube length. The initial increase is due to higher thermal and concentration gradients, which later reduce along the tube length.

The comprehensive model presented here would be useful for designing dense hollow fiber membrane water-to-gas humidifiers for any given humidification demand.

Appendix A:

Heat flux due to water diffusion across the membrane is given as:

$$\text{Thermal flux}_{\text{water diffusion}} = \frac{D_m}{L} (C_{\text{max}}^{\text{liq}} - C_L) M_w C_{pv} \Delta T_m \dots \dots \dots (\text{A.1.})$$

Heat flux due to conduction in the membrane is given as:

$$\text{Thermal flux}_{\text{conduction}} = \frac{k_m}{L} \Delta T_m \dots \dots \dots (\text{A.2.})$$

For a representative case of water temperature=60 °C and air flow rate of 650 lpm, the thermal conduction flux from Eq (A.2.) is calculated to be 1270 W/m² whereas the heat flux due to mass diffusion calculated from Eq (A.1.) is only 0.69 W/m² which is three orders of magnitude smaller. Therefore, while deriving the elemental balance for heat transfer across the membrane (see Eq. (2)), contribution due to water diffusion can be neglected.

Appendix B:

Variation of mass flow rates with tube length for inlet $AFR = 10 \text{ L/min}$ is shown in Fig. 3.B1. It is seen that the change in mass flow rate from inlet to outlet increases with increasing water

temperature. Further, the increase in air mass flow rate is nearly ~30 % for water temperature of 80 °C. At this water temperature and low inlet air flow rate, the moisture content at 100 % RH is close to 0.5 g/g_{air} and thus results in significant increase in mass flow rate. Further, it is seen that due to rapid vapor mass transport, the mass flow rate increases significantly within $\xi \leq 0.3$ i.e. within 30 % of the tube length and is constant beyond $\xi > 0.3$. Due to counter-flow operation, the trends for variation in water mass flow rate are reversed i.e. $\dot{m}_w^* = 1$ @ $\xi = 1$. The variation in water mass flow rate is small and can be neglected.

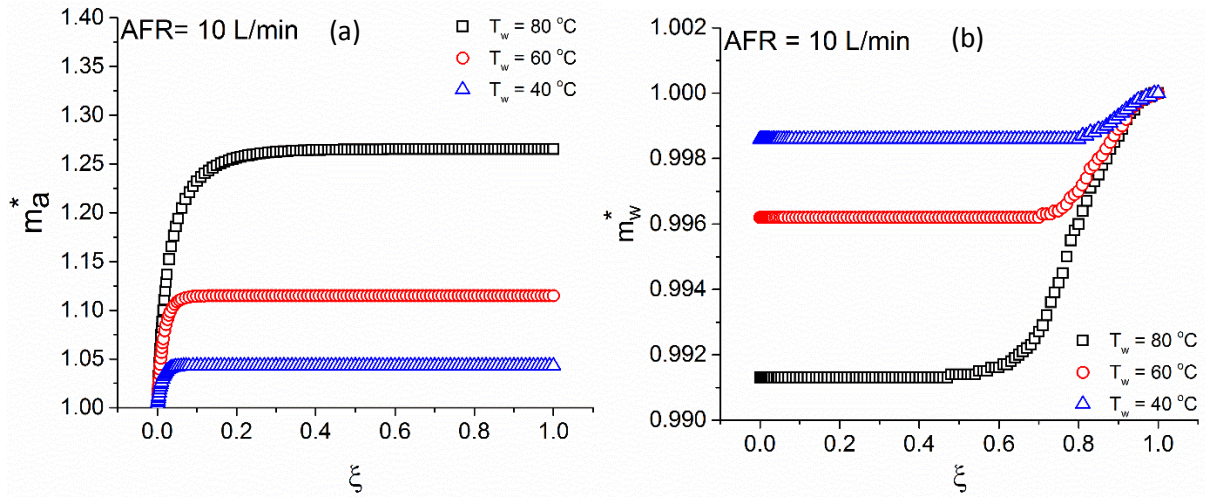


Fig. 3.B1. Variation in (a) air mass flow rate and (b) water mass flow rate along the tube length for different water temperatures and counter-flow mode of operation at 10 L/min inlet air flow rate.

The change in mass flow rates of air and water along the tube length for inlet $AFR = 1138 \text{ L/min}$ is shown in Fig. 3.B2. It is seen that the variation in air mass flow rate is < 10 % at water temperature of 80 °C and is even lower for lower water temperatures. The reason for lower increase in mass flow rate of air for this case is attributed to the drop in air temperature due to reduction in residence time. Reduction in air temperature leads to reducing the moisture content of air at 100 % RH and thus the variation in mass flow rate is small and could be neglected for high air flow rates.

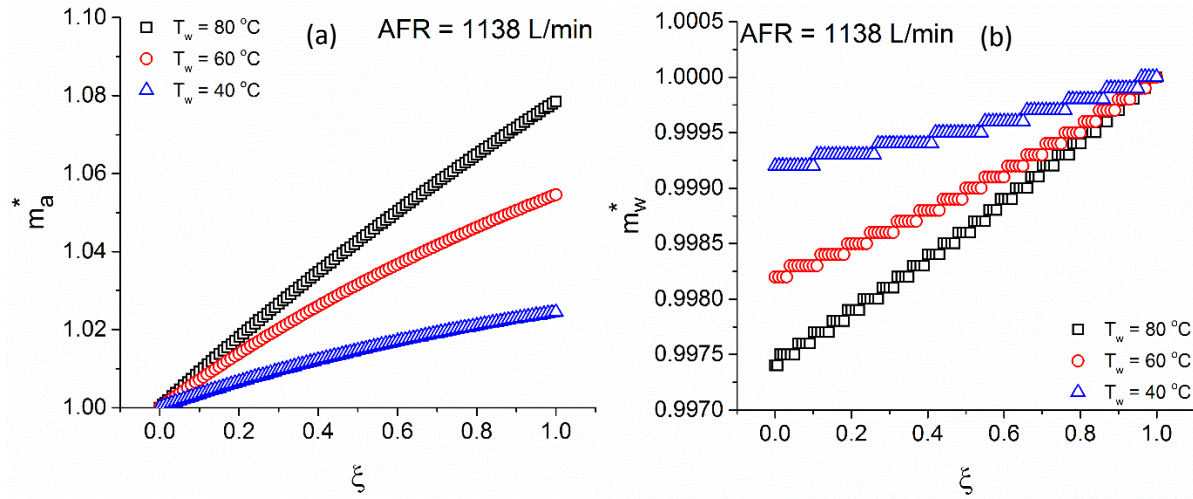


Fig. 3.B2. Variation in (a) air mass flow rate and (b) water mass flow rate along the tube length for different water temperatures and counter-flow mode of operation at 1138 L/min inlet air flow rate.

Nomenclature

a	Air
A	Area (m ²)
A_m	Area of membrane (m ²)
C_L	Concentration of water in the membrane at the membrane-gas interface (mol/m ³)
C_{max}^{liq}	Maximum concentration of water in the membrane at a particular temperature (mol/m ³)
C_{pa}	Specific heat of humid air (J/kg K)
$C_{pa,dry}$	Specific heat of dry air (J/kg K)
C_{pv}	Specific heat of water vapor (J/kgK)
C_{pw}	Specific heat of water (J/kg K)
d_{id}	Tube inner diameter (m)
d_{od}	Tube outer diameter (m)
\bar{d}	Mean tube diameter (m)
D	Hydraulic diameter (m)
D_S	Shell diameter (m)
D_a	Diffusion coefficient of water in air (m ² /s)
D_m	Diffusion coefficient of water in membrane (m ² /s)
$E.W.$	Equivalent weight of membrane (kg/mol)
h_t	Tube side heat transfer coefficient (W/m ² K)
h_s	Shell side heat transfer coefficient (W/m ² K)
H	Tube length (m)
J_o	Water flux across the membrane (mol/m ² K)
K_t	Tube side mass transfer coefficient (m/s)
k_a	Thermal conductivity of air (W/m K)
k_w	Thermal conductivity of water (W/m K)
k_m	Thermal conductivity of membrane (W/m K)
L	Membrane thickness (m)
\dot{m}_a	Mass flow rate of air (kg/s)

\dot{m}_w	Mass flow rate of water (kg/s)
\dot{m}_a^*	Dimensionless air mass flow rate
\dot{m}_w^*	Dimensionless water mass flow rate
M_w	Molecular weight of water (kg/mol)
M_{air}	Molecular weight of air (kg/mol)
N	Number of tubes
$P_{v,in}$	Inlet vapor pressure of water (Pa)
P_v	Vapor pressure of water (Pa)
$P_{v,out}$	Outlet vapor pressure of water (Pa)
$P_{v,sat,in}$	Inlet saturation vapor pressure of water (Pa)
$P_{v,sat}$	Saturation vapor pressure of water at T_w (Pa)
$P_{v,sat,air}$	Saturation vapor pressure of water at T_a (Pa)
P_{eq}	Equilibrium vapor pressure of water at the gas-membrane interface (Pa)
\dot{Q}	Air flow rate (m ³ /s)
R	Universal gas constant (J/mol K)
$T_{a,in}$	Inlet air temperature (K)
$T_{w,in}$	Inlet water temperature (K)
T_{ref}	Reference temperature (K)
$T_{a,out}$	Outlet air temperature (K)
$T_{w,out}$	Outlet water temperature (K)
T_a^*	Dimensionless gas temperature
T_w^*	Dimensionless water temperature
T_d	Dew point temperature (K)
T_m	Membrane temperature at membrane-air interface (K)
U	Overall heat transfer coefficient (W/m ² K)
v_a	Velocity of air (m/s)
v_w	Velocity of water (m/s)
v	Vapor
w	Water
X	Mixing ratio (kg/kg)

Greek letters

$\alpha, \beta, \gamma, \delta, \sigma, \phi, \eta$	Dimensionless numbers
μ	Viscosity (Pa.s)
θ	Dimensionless Vapor pressure
λ_{vap}	Latent heat of vaporization (J/kg)
λ_m	Water content in membrane (mol/mol)
ρ	Density (kg/m ³)
ζ	Dimensionless length
Γ	Dimensionless Henry's constant

References

- [1] J. Larminie, A. Dicks, M.S. McDonald, Fuel cell systems explained, New York, Wiley, (2003).

- [2] P. Berg, K. Promislow, J.S. Pierre, J. Stumper, B. Wetton, Water management in PEM Fuel Cells, *J. Electrochem. Soc.*, 151 (2004) A341-A353.
- [3] M. Ji, Z. Wei, A review of water management in polymer electrolyte membrane fuel cell, *Energies*, 2 (2009) 1057 – 1106.
- [4] D. N. Ozen, B. Timurkutluk, K. Altinisik, Effects of operation temperature and reactant gas humidity levels on performance of PEM fuel cells, *Renewable and Sustainable Energy Reviews*, 59 (2016) 1298 – 1306.
- [5] S.K. Park, E.A. Cho, I.H. Oh, Characteristics of membrane humidifiers for polymer electrolyte membrane fuel cells, *Korean J. Chem. Eng.*, 22 (2005) 877 – 881.
- [6] D.L. Wood III, J.S. Yi, T.V. Nguyen, Effects of direct liquid water injection and interdigitated flow field on the performance of proton exchange membrane fuel cells, *Electrochim. Acta* 43 (1998) 3795 – 3809.
- [7] R. Huizing, M. Fowler, W. Merida, J. Dean, Design methodology for membrane-based plate-and-frame fuel cell humidifiers, *J. Power Sources*, 180 (2008) 265 – 275.
- [8] A. Gabelman, S. Hwang, Hollow fiber membrane contactors, *J. Membr. Sci.*, 159 (1999) 61 – 106.
- [9] Gh. Bakeri, S. Naeimifard, T. Matsuura, A.F. Ismail, A porous polyethersulfone hollow fiber membrane in a gas humidification process, *RSC Advances*, 5 (2015) 14448.
- [10] S.K. Park, S.Y. Choe, S.H. Choi, Dynamic modelling and analysis of a shell-and-tube type gas-to-gas membrane humidifier for PEM fuel cell applications, *Int. J. Hydrogen Energy*, 33 (2008) 2273 – 2282.
- [11] M. Sabharwal, C. Duelk, D. Bhatia, Two-dimensional modelling of a cross flow plate and frame membrane humidifier for fuel cell applications, *J. Membr. Sci.*, 409 – 410 (2012) 285 – 301
- [12] D. Bhatia, M. Sabharwal, C. Duelk, Analytical model of a membrane humidifier for polymer electrolyte membrane fuel cell systems, *Int. J. Heat Mass Tran.* 58 (2013) 702–717.
- [13] S. Kang, K. Min, S. Yu, Two dimensional dynamic modelling of a shell-and-tube water-to-gas membrane humidifier for proton exchange membrane fuel cell, *Int. J. Hydrogen Energ.*, 35 (2010) 1727 – 1741.

- [14] S. Park, I.H. Oh, An analytical model of Nafion™ membrane humidifier for proton exchange membrane fuel cells, *J. Power Sources* 188 (2009) 498–501.
- [15] S. Park, D. Jung, Effect of operating parameters on dynamic response of water-to-gas membrane humidifier for proton exchange membrane fuel cell vehicle, *Intl. J. Hydrogen Energ.* 38 (2013) 7114 – 7125.
- [16] M. Adachi, T. Navessin, Z. Xie, F.H. Li, S. Tanaka, S. Holdcroft, Thickness dependence of water permeation through proton exchange membranes, *J. Membr. Sci.* 364 (2010) 183 – 193.
- [17] D. Chen, W. Li, H. Peng, An experimental study and model validation of a membrane humidifier for PEM fuel cell humidification control, *J. Power Sources* 180 (2008) 461–467.
- [18] L.Z. Zhang, S.M. Huang, Coupled heat and mass transfer in a counter flow hollow fiber membrane module for air humidification, *Int. J. Heat Mass Tran.* 54 (2011) 1055–1063.
- [19] L.Z. Zhang, Coupled heat and mass transfer in an application-scale cross-flow hollow fiber membrane module for air humidification, *Int. J. Heat Mass Tran.* 55 (2012) 5861–5869.
- [20] D.K. Kim, E.J. Choi, H.H. Song, M.S. Kim, Experimental and numerical study on the water transport behavior through Nafion 117 for polymer electrolyte membrane fuel cell, *J. Membrane Sci.* 497 (2016) 194–208.
- [21] T.E. Springer, T.A. Zawodzinski, S. Gottesfeld, Polymer electrolyte fuel cell model, *J. Electrochem. Soc.*, 138 (1991) 2334 – 2342.
- [22] T. Zawodzinski, M. Neeman, L. O. Sillerud, S. Gottesfeld, Determination of water diffusion coefficients in perfluorosulfonate ionomeric Membranes, *J. Phys. Chem.*, 95 (1991) 6041.
- [23] T.A. Zawodzinski, C. Derouin, S. Radzinski, R.J. Sherman, V.T. Smith, T.E. Springer, S. Gottesfeld, Water uptake and transport through Nafion 117 membranes, *J. Electrochem. Soc.* 140 (4) (1993) 1041.
- [24] J.T. Hinatsu, M. Mizuhata, H. Takenaka, Water uptake of perfluorosulfonic acid membranes from liquid water and water vapor, *J. Electrochem. Soc.* 141 (6) (1994) 1493.
- [25] T. Romero, W. Merida, Water transport in liquid and vapor equilibrated Nafion™ membranes, *J. Membr. Sci.*, 338 (2009) 135 – 144.

- [26] P. Choi, R. Dutta, Sorption in proton exchange membranes: An explanation of Schroeder's paradox, *J. Electrochem. Soc.*, 150 (2003) E601 – E607.
- [27] P. Majsztrik, A. Bocarsly, J. Benziger, Water permeation through Nafion membranes: The role of water activity, *J. Phys. Chem. B*, 112 (2008) 16280 – 16289.
- [28] P.W. Majsztrik, M.B. Satterfield, A.B. Bocarsly, J.B. Benziger, Water sorption, desorption and transport in Nafion membranes, *J. Membr. Sci.* 301 (2007) 93 – 106.
- [29] N. Zhao, D. Edwards, Z. Shi, S. Holdcroft, Interfacial vs. Internal Water Transport Resistance of Sulfonated Hydrocarbon Proton-Exchange Membranes, *ECS Electrochem. Letters*, 2 (2013) F22 – F24.
- [30] J.G. Wijmans, R.W. Baker, The solution-diffusion model: a review, *J. Membr. Sci.*, 107 (1995) 1 – 21.
- [31] C.W. Monroe, T. Romero, W. Merida, M. Eikerling, A vaporization-exchange model for water sorption and flux in Nafion, *J. Membr. Sci.* 324 (2008) 1–6.
- [32] Q. Zhao, P. Majsztrik, J. Benziger, Diffusion and interfacial transport of water in Nafion, *J. Phys. Chem. B*, 115 (2011) 2717-2727.
- [33] N. Valentinyi, E. Csefalvay, P. Mizsey, Modelling of pervaporation: parameter estimation and model development, *Chem. Eng. Res. Des.*, 91 (2013) 174 – 183.
- [34] Humidity conversion formulas, Vaisala Oyj, Helsinki, Finland.
http://www.vaisala.com/Vaisala%20Documents/Application%20notes/Humidity_Conversion_Formulas_B210973EN-F.pdf (accessed: 30-01-2019)
- [35] R.H. Perry, D.W. Green, J.O. Maloney, *Perry's Chemical Engineers' Handbook*, Seventh ed., McGraw-Hill publishing 1997.
- [36] F.P. Incropera, D.P. Dewitt, T.L. Bergman, A.S. Lavine, *Fundamentals of Heat and Mass Transfer*, Sixth ed., John Wiley & Sons, New York, 2007.
- [37] S. Shi, A. Z. Weber, A. Kusoglu, Structure/Property relationship of Nafion XL composite membranes, *J. Membr. Sci.*, 516 (2016) 123 – 134.
- [38] A. Kusoglu, A.Z. Weber, New insights into perfluorinated sulfonic-acid ionomers, *Chem. Rev.*, 117 (2017) 987 – 1104.

- [39] D. Chen, H. Peng, A thermodynamic model of membrane humidifiers for PEM fuel cell humidification control, *Trans. ASME*, 127 (2005) 424 – 432.
- [40] Perma Pure FC Series Humidifier User Manual, Perma Pure LLC, New Jersey, USA.
<http://www.permapure.com/wp-content/uploads/2016/01/FC-MAN-001-REV-00.pdf>
(accessed: 30-01-2019)
- [41] T. Okada, S. Moller-Holst, O. Gorseth, S. Kjelstrup, Transport and equilibrium properties of Nafion (R) membranes with H⁺ and Na⁺ ions, *J. Electroanal. Chem.* 442 (1–2) (1998) 137–145.
- [42] S. Motupally, A. J. Becker, J. W. Weidner, Diffusion of water in Nafion 115 membranes, *J. Electrochem. Soc.*, 147 (2000) 3171 – 3177.
- [43] H.O.E. Karlsson, G. Trägårdh, Heat transfer in pervaporation, *J. Membr. Sci.* 119 (1996) 295-306.
- [44] R. Rautenbach, R. Albrecht, Separation of organic binary mixtures by pervaporation, *J. Membr. Sci.* 7 (1980) 203-213.
- [45] C. Mittelsteadt, J. Staser, Simultaneous water uptake, diffusivity and permeability measurement of perfluorinated sulfonic acid polymer electrolyte membranes, *ECS Trans.*, 41 (2011) 101 – 121.
- [46] Q. Duan, H. Wang, J. Benziger, Transport of liquid water through Nafion membranes, *J. Membr. Sci.*, 392-393 (2012) 88 – 94.
- [47] Y. Wang, K.S. Chen, J. Mishler, S.C. Cho, X.C. Adroher, A review of polymer electrolyte membrane fuel cells: Technology, applications, and needs on fundamental research, *App. Energy*, 88 (2011) 981 – 1007.
- [48] M.B. Satterfield, J.B. Benziger, Non-Fickian Water Vapor Sorption Dynamics by Nafion Membranes, *J. Phys. Chem. B*, 112 (2008) 3693 – 3704.
- [49] B. Kientiz, H. Yamada, N. Nonoyama, A.Z. Weber, Interfacial water transport effects in proton-exchange membranes, *J. Fuel Cell Sci. Tech.*, 8 (2011) 011013-1 – 011013-7.

Chapter 4

Experimental Investigation and Modelling of Asymmetric Hollow Fiber Membranes for Gas Humidification

Compared to the widely used dense membranes based on Nafion or SPEEK, asymmetric polysulfone membranes are likely to have favourable cost-performance balance for humidification applications because of their partial hydrophobic character, good physicochemical stability, easy processability, ability to tune porous microstructure and lower cost. In this chapter, we investigate the performance of asymmetric hollow fiber membrane modules based on polysulfone for water-to-gas humidification purposes. Hollow fiber membranes (HFM) made from spinning dopes of different polysulfone concentrations are investigated for their microstructure and humidification performance using a series of experiments and a microscopic transport model. The study aims at drawing guidelines for developing suitable membranes for gas humidification with the desired output parameters of gas temperature and absolute humidity.

4.1. Introduction

A general introduction about humidification and membrane humidifiers can be referred in Chapters 1-2. Humidification through non-porous or dense membranes works on the principle of solution-diffusion, also referred to as pervaporation, wherein water dissolves in the membrane at the wet-side interface and permeates across to vaporize into the gas stream [1,2]. Presently, commercial manufacturing of membrane humidifiers is dominated by non-porous membranes which are based on either Nafion or SPEEK. Being non-porous, these humidifiers are limited by low vapor transfer rates, therefore, requiring a large active surface area. The membranes are typically thin (<100 microns) to reduce mass transfer resistance for moisture diffusion [8,9]. Consequently, they suffer from low-pressure tolerance. Moreover, high material cost for such

membranes makes the humidifiers expensive. An asymmetric membrane typically has gradients of porosity and pore size along its thickness, and dense non-porous or nano-porous skin layers at one or both edges. The larger pores in the bulk, if sufficiently hydrophilic, can act as reservoirs of water and provide minimal resistance to moisture transport. The transport is however modulated by diffusion through the thin dense skin in a manner similar to the solution-diffusion phenomenon in dense membranes [5–8]. Hence asymmetric membranes can be tuned to offer better control on humidification by tailoring the microstructure. Since resistance to mass transport is low because of high porosity and a nanoscale-thin skin layer, hence asymmetric membranes can be thicker than dense non-porous membranes without sacrificing their humidification performance. The higher thickness makes asymmetric membranes sufficiently robust for high-pressure operation, which is not always possible with dense non-porous membranes. Additionally, while high gas flow rates may lead to drying of dense membranes thereby compromising their humidification performance, porous membranes do not dry easily because of the presence of water retaining macrovoids inside the membranes. Furthermore, polymers which are typically used for making porous membranes such as polysulfone are relatively more cost-effective compared to those used to make dense non-porous membranes [9]. Thus, asymmetric porous membrane humidifiers with high-pressure tolerance, better humidification efficiencies, and lower cost can have excellent potential for a variety of applications.

Bakeri et al. [10] studied porous polyethersulfone hollow fiber membrane for gas humidification. The hollow fibers were developed using conventional dry-wet phase inversion technique with a mean pore size of 653 nm. The overall water flux was found to be 2700 % higher than a commercial humidifier Permapure PH-60T-24SS. Runhong Du et al. [11] demonstrated PDMAEMA/PAN composite membrane for gas humidification and dehumidification. They achieved a relative humidity of 30 % with a membrane active area of 16.6 cm² for an air flow rate of 1 L/min in the temperature range of 25 – 45 °C. Ramya et al. [12] reported expanded PTFE porous membranes having a pore size of 0.3 microns for gas humidification using a plate and frame humidifier configuration and coupled it with a PEM fuel cell. They compared fuel cell performances when using the membrane humidifier and a conventional bubble humidifier. The

fuel cell performance obtained by using the membrane humidifier was shown to be at par with that obtained when using bubble humidification. Park et al. [9] studied polysulfone ultrafiltration flat sheet membranes (pore size 70 – 80 Å) for gas humidification and compared the results with Nafion 112, 115 and 117 membranes. On increasing humidifier temperatures from 25 to 75 °C, the relative humidity of the outlet gas from UF membrane decreased from 96 to 82 % whereas the same was found to decrease from 91 to 29 % for Nafion 117. While the polysulfone UF membranes outperformed Nafion in terms of outlet gas relative humidity, it was found to provide comparable humidification to a fuel cell as that by a bubble humidifier. Yang et al. [13] investigated porous PVDF and PTFE membranes in a quasi-counter flow parallel plate membrane contactor (QCFPMC) arrangement for air humidification. They reported a decrease in humidification effectiveness with increasing gas flow rates and increasing pore sizes. They concluded that PTFE membrane showed higher performance than PVDF membrane. Zhang [14] studied coupled heat and mass transport in asymmetric flat sheet membranes having two gases flowing on either side of the membrane. The membranes contained a porous support, finger-shaped macrovoids, and an ultra-thin skin. By using a resistance model, the author showed that the largest resistance to mass transport was offered by the sponge-like porous layer.

As can be seen from the literature review presented above, while several studies have reported on gas humidification using porous membranes, most of them have focused on experimental demonstration of the membranes and their comparison with dense non-porous membranes. Mathematical models proposed so far for membrane-based humidification process are limited to gas-to-gas humidification and have not accounted for membrane-gas interfacial equilibrium in the model. In addition, a detailed microstructure analysis and its influence on membrane transport properties has not been addressed in the literature. Thus, to the best of our knowledge, none of the studies so far have proposed and validated a detailed mathematical model that i) enables understanding of coupled heat and mass transport phenomena in water-to-gas humidification process occurring in asymmetric porous hollow fiber membrane humidifiers, ii) considers appropriate membrane-gas and membrane-water interfacial equilibrium conditions, and iii) uses microstructural data to estimate transport resistances. It is also well known that conventional gas-liquid absorbers are prone to issues of flooding and water entrainment, which

pose serious concerns regarding their use in gas humidification [15]. For example, liquid water entering the gas stream can prove detrimental to applications such as fuel cell since it causes undesirable flooding inside the cells. None of the previous studies on porous membrane humidifiers has investigated the important issue of entrainment in porous humidifiers and the causes for the same.

In this background, the emphasis of the present work is twofold:

- i. To investigate gas humidification using asymmetric porous polysulfone hollow fiber membranes prepared from solutions of varying polymer concentrations so as to optimize the membrane micro-structure for preventing water entrainment while still ensuring good humidification performance, and
- ii. To develop a mathematical model for water-to-gas humidification in asymmetric hollow fiber membrane humidifiers and comprehensive experimental validation of the same.

4.2. Experimental

4.2.1. Materials

Polysulfone (PSF) was purchased from Solvay (Udel® P-3500) and was dried in a vacuum oven at 60 °C for 24 h before use. N, N Dimethyl acetate (DMAc) with a purity of >95% obtained from M/s. Merck-India was used as a solvent for preparing the dope solution. Iso-propanol and iso-butanol were obtained from M/s. Merck-India for post-treatment of fibers and pore size distribution studies respectively. Distilled water was used as the bore fluid and filtered tap water was used as non-solvent in the precipitation tank. Compressed air with RH of $\approx 10\%$ was used for humidity studies.

4.2.2. Preparation of spinning dope

Weighed amounts of PSF were added to DMAc to prepare 25, 27 and 30 wt % concentration spinning dopes. The solutions were stirred for 32 h to ensure complete dissolution of the polymer in the solvent. After stirring, the dopes were left undisturbed overnight before using for spinning.

4.2.3. Spinning of hollow fibers

The hollow fibers were prepared using dry-wet phase inversion process on our in-house spinning machine (discussed in detail in Appendix A, Fig. 4A.1.). The spinneret annulus, needle

dimensions and ID/OD of the fibers were measured using Zeiss AxioCam MRc5 optical microscope. The type of spinneret, dope pressure, bore fluid flow rate, and take-up speed of the spool together contribute to the fiber microstructure and macro-dimensions (ID/OD and thickness). The spinning parameters for each polymer concentration were chosen to allow extrusion of geometrically similar fiber dimensions. The hollow fibers once collected were left immersed in water for 24 h for complete removal of residual solvent. After this, the fibers were dried at room temperature for 24 h followed by oven drying at 60 °C for 4 h. The oven dried fibers were then stored in sealed plastic bags at room temperature until further use. The spinning conditions for each polymer concentration are provided in Table 4.1.

Table 4.1: Hollow fiber spinning parameters.

Process parameters	Membrane: HFM25	Membrane: HFM27	Membrane: HFM30
Dope composition (wt %)	PSF : DMAc 25 : 75	PSF : DMAc 27 : 73	PSF : DMAc 30 : 70
Dope viscosity (Pa s)	4	5.8	10
Dope pressure (kPa)	98	119	298
Bore fluid	DI Water	DI Water	DI Water
Bore fluid flow rate (ml/min)	7	26	18
Average take up speed (m/min)	5	4	5
Air gap (cm)	3	3	3
Spinneret needle ID:OD (mm)	0.3 : 0.5	0.3 : 0.5	0.3 : 0.5
Spinneret annulus OD (mm)	1.28	1.28	1.28

4.2.4. Preparation of hollow fiber membrane modules

For each of the three membranes HFM25, HFM27, and HFM30, different modules were made with varying tube number and tube length as listed in Table 4.2. The modules are named as PS(polysulfone)-Nx(number of tubes)-Lx(length of tubes). A PVC tube of 0.5-inch diameter (D_s) was used for making the housing of each module. Fibers were cut to appropriate lengths and glued at the ends using epoxy resin. Initially, the pores of the fibers are air-filled. This prevents penetration of water into the pores due to its large interfacial tension. Therefore, to facilitate

water transport through the partially hydrophobic membrane, the hollow fiber bundle inside the modules were injected with iso-propyl alcohol (IPA) for 4 h followed by immersion in DI-water for 24 h. IPA being miscible in water gets eventually displaced thereby enabling the pores to fill with water. Before using the modules for any test, excess amount of water in the lumen of the hollow fibers was removed by passing air through the tubes till no water drops appeared from the ports.

Table 4.2: Details of modules and test parameters.

Experiment	Module identification	Membrane type		
		HFM25	HFM27	HFM30
Bubble point test	PS-N3-L20	$N = 3$ $L = 20 \text{ cm}$	$N = 3$ $L = 20 \text{ cm}$	$N = 3$ $L = 20 \text{ cm}$
Pore size distribution	PS-N10-L20	$N = 10$ $L = 20 \text{ cm}$	$N = 10$ $L = 20 \text{ cm}$	$N = 10$ $L = 20 \text{ cm}$
Water flux and entrainment tests	PS-N30-L20	$N = 30$ $L = 20 \text{ cm}$ $T_w = RT^*$ $T_w = 60^\circ\text{C}^{**}$ $\dot{Q}_w = 0.38 \text{ lpm}$	$N = 30$ $L = 20 \text{ cm}$ $T_w = RT^*$ $T_w = 60^\circ\text{C}^{**}$ $\dot{Q}_w = 0.38 \text{ lpm}$	$N = 30$ $L = 20 \text{ cm}$ $T_w = RT^*$ $T_w = 60^\circ\text{C}^{**}$ $\dot{Q}_w = 0.38 \text{ lpm}$
Humidity test	PS-N30-L20	$N = 30$ $L = 20 \text{ cm}$ $T_w = 60^\circ\text{C}$ $\dot{Q}_w = 0.38 \text{ lpm}$ $\dot{Q}_a = 3, 5, 7, 10 \text{ lpm}$	$N = 30$ $L = 20 \text{ cm}$ $T_w = 60^\circ\text{C}$ $\dot{Q}_w = 0.38 \text{ lpm}$ $\dot{Q}_a = 3, 5, 7, 10 \text{ lpm}$	$N = 30$ $L = 20 \text{ cm}$ $T_w = 60^\circ\text{C}$ $\dot{Q}_w = 0.38 \text{ lpm}$ $\dot{Q}_a = 3, 5, 7, 10 \text{ lpm}$
Effect of tube length	PS27-N30-L	—	$N = 30$ $L = 10, 15, 20 \text{ cm}$ $T_w = 60^\circ\text{C}$ $\dot{Q}_w = 0.38 \text{ lpm}$ $\dot{Q}_a = 3, 5, 7, 10 \text{ lpm}$	—
Effect of tube number	PS27-N-L15	—	$N = 10, 30, 60$ $L = 15 \text{ cm}$ $T_w = 60^\circ\text{C}$ $\dot{Q}_w = 0.38 \text{ lpm}$ $\dot{Q}_a = 3, 5, 7, 10 \text{ lpm}$	—
Effect of water temperature	PS27-N30-L15	—	$N = 30$ $L = 15 \text{ cm}$ $T_w = 40, 50, 60^\circ\text{C}$ $\dot{Q}_w = 0.38 \text{ lpm}$ $\dot{Q}_a = 3, 5, 7, 10 \text{ lpm}$	—

Effect of water flow rate	PS27-N30-L15	—	$N = 30$ $L = 15 \text{ cm}$ $T_w = 60 \text{ }^\circ\text{C}$ $\dot{Q}_w = 0.38, 0.84, 1.22$ lpm $\dot{Q}_a = 3, 5, 7, 10 \text{ lpm}$	—
----------------------------------	--------------	---	-----------------------------------------------------------------------------------------------------------------------------------------------------------------	---

* Flux test at room temperature (RT); ** Entrainment test; T_w = Water bath temperature

4.2.5. Field emission scanning electron microscopy (FE-SEM) of hollow fiber membranes

The microstructure of membranes was investigated using a field emission scanning electron microscope (FE-SEM, Nova NanoSEM 450). Specimens of membrane cross-section were prepared by fracturing the dry HFM in liquid nitrogen followed by gold sputtering and mounting on a sample holder.

4.2.6. Water flux and entrainment tests

Water flux was measured for representative modules PS-N30-L20 made using the three types of membranes: HFM25, HFM27, and HFM30. Flux was measured gravimetrically at different trans-membrane pressures by circulating DI water at ambient temperature on the shell side and collecting permeate on the tube side. Flux was calculated using Eq. (1).

$$\text{Flux} = \frac{m_w}{\rho_w t A_m} (3.6 \times 10^6) \text{ Lm}^{-2} \text{ h}^{-1} \dots\dots\dots(1)$$

Here, m_w (kg) is the weight of water collected as permeate, ρ_w (kg/m³) is the density of water, t (s) is the time taken to collect permeate and A_m is the surface area of the fibers.

Entrainment tests were performed on the same modules by circulating hot water at 60 °C on the shell side at a flow rate of 380 ml/min without applying any transmembrane pressure. The reason for using water at 60 °C for entrainment test is to estimate entrainment at high humidity conditions which is achieved at high water temperature. Each entrainment test was conducted for 15 min. The liquid water permeate was measured on the outlet of the tube side and calculated using Eq. (2).

$$\text{Entrainment rate} = \frac{60 \times V_{\text{permeate}}}{t} \text{ ml/min} \dots\dots\dots(2)$$

Here, V_{permeate} (ml) is the volume of permeate collected and t (s) is the time over which permeate was collected.

4.2.7. Bubble point, pore size distribution and membrane porosity tests

Bubble point test gives a crude estimation of the largest pore size in the skin of the membrane which will allow gas to displace the liquid inside the membrane pores at some applied pressure [16]. The test procedure is provided in the Appendix A, Fig. 4A.2.

Pore size distribution was determined using liquid-liquid displacement method, which is known to characterize the porosity of dense skin layer [21,22,23]. Details of the methodology are discussed in Appendix A, Fig. 4A.3. The pore sizes and their distribution were estimated using the Young-Laplace equation (3) and Hagen Poiseuille's equation (4).

$$r_p = \frac{2\gamma}{\Delta P} \dots\dots\dots(3)$$

$$n = \frac{8 \eta l J}{\pi \Delta P r_p^4} \dots\dots\dots(4)$$

Here, γ is the surface tension (N/m) of the displacing fluid, ΔP is the trans-membrane pressure (Pa), η is the dynamic viscosity of the displacing fluid (Pa s), l is the pore length (assumed equal to skin thickness for asymmetric membranes) (m), r_p is the pore radius (m), J is the flux ($\text{m}^3\text{m}^{-2}\text{h}^{-1}$) and n is the number density of pore of radius r_p ($\#/\text{m}^2$). Finally, based on the total pore density for each polymer concentration, we can estimate the number average pore size (\bar{r}_p) as given in Eq. (5).

$$\bar{r}_p = \frac{\sum_{i=1}^N n_i r_{pi}}{\sum_{i=1}^N n_i} \dots\dots\dots(5)$$

Here $n_i (\#/\text{m}^2)$ is the number density of pores (number of pores per unit membrane area) having radius r_{pi} (m), which is calculated for each pressure step i .

The surface porosity of the membranes is estimated as[24,25]

$$\theta_{surface} = \frac{\text{total pore area}}{\text{membrane area}} \times 100 = \sum_{i=1}^N n_i \pi r_{pi}^2 \times 100 \dots\dots\dots(6)$$

Membrane bulk porosity and tortuosity together determine the rate of mass transfer across the membrane. Higher the porosity higher is the flux, whereas higher tortuosity leads to increased mass transfer resistance and reduced flux [21,22]. Membrane bulk porosity can be estimated gravimetrically by Eq. (7).

$$\theta_{bulk} = \frac{V_m - V_p}{V_m} \times 100 = \frac{\pi H(r_o^2 - r_i^2) - (W_m / \rho_p)}{\pi H(r_o^2 - r_i^2)} \times 100 \dots\dots\dots (7)$$

Here, $V_m(m^3)$ is the volume of the sample, $V_p(m^3)$ is the volume occupied by the polymer, $\rho_p (kg/m^3)$ is the density of the polymer, $W_m(kg)$ is the weight of a fiber sample of length $H (m)$, and $r_o (m)$ and $r_i (m)$ are the outer and inner radii of the fiber.

4.2.8. Measuring humidifier performance

The test setup to measure humidifier performance is shown in Fig. 4.1. The setup comprises a water bath supplying hot water to the shell side of the membrane module at the required flow rate using a peristaltic pump. Water temperature was measured in-line near the inlet of the humidifier using a Mextech DT-9 digital thermometer having a resolution of 0.1 °C and an accuracy of ± 1 °C. Air from the compressor is supplied to the tube side of the module. The flow rate of air is regulated using a rotameter having a resolution of 0.5 L/min. The tube side outlet is connected to a Testo 6681 humidity transmitter for measuring the outlet air temperature in °C and absolute humidity (kg H₂O / kg air). For safe operation of the sensor and preventing condensation of water on it, the distance between the air outlet of the humidifier and the transmitter probe was kept as 10 cm. Various modules listed in Table 4.2 were tested on the setup for studying the effect of polymer concentration, number of tubes, tube length, water temperature, water flow rate, and air flow rate on humidifier performance.

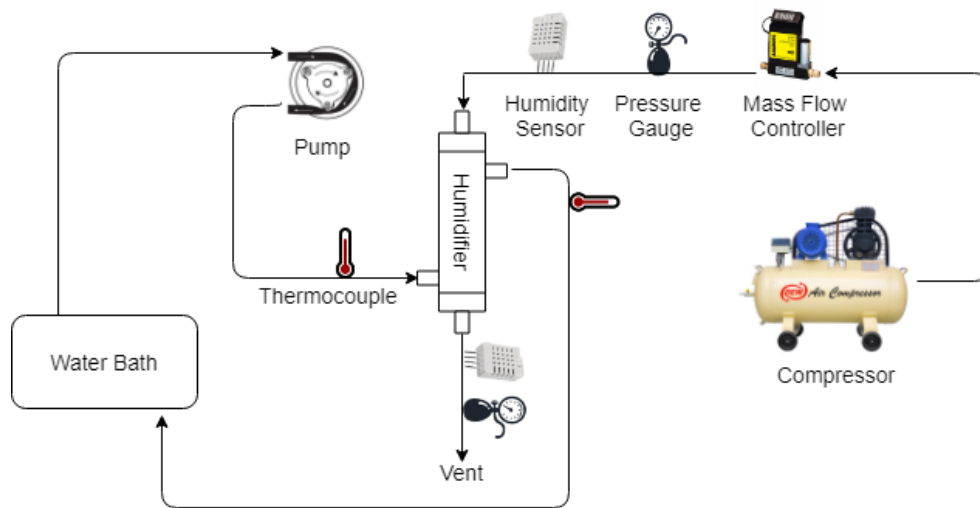


Fig. 4.1. Humidification test setup.

4.3. Mathematical model

We begin by asking ourselves: what is the physical state of water transported across the membrane? While it is very likely that water in the liquid state is present inside the membrane owing to the IPA treatment followed by washing in water, it is also possible that water evaporates at the shell side owing to the high water temperature on shell side and the vapor diffuses across the membrane. In our modeling effort we have considered the two extreme cases:

i) The pores are filled with liquid water and it is the liquid water in the membrane phase that simultaneously diffuses through the porous matrix and the dense polysulfone across a concentration gradient developed at steady state, and

ii) The water evaporates at the membrane-shell interface and fills the pores, and only water vapor that diffuses across the membrane.

The consequence of these two approaches would reflect in the determination of the effective diffusion coefficient of water or water vapor in the membrane, effective thermal conductivity and water concentration at the respective membrane interfaces.

In the following sections, we will consider Case (i) in detail. Case ii) is developed in the Appendix B section where we have also compared the model results for both cases for a reference polymer concentration. While a third case of simultaneous liquid+vapor transport is perhaps the most probable, it is difficult to quantify the amount of vaporization taking place within the membrane pores. Hence, for now, we have considered only the two limiting cases i) and ii). The transport of water (liquid or vapor) through asymmetric membranes used in this study is modelled using resistance in series approach as shown in Fig. 4.2a below. The model is based on the following assumptions:

- Cartesian coordinate system is chosen for transport across membrane despite the cylindrical nature of the membrane geometry. This is reasonable because the membrane thickness is much smaller than the tube diameter so that the local curvature can be neglected.

- The humidification process is modeled as a quasi-2D process with local heat and mass transfer gradients in the transverse (x-) direction and the overall addition of heat and moisture occurring along the axial (z-) direction (see Fig. 4.2b).
- Flow is laminar and fully developed.
- The interfacial resistance to heat transfer at the membrane-water interface is neglected.
- The model assumes the asymmetric membrane to be a macro-homogeneous phase characterized by effective transport coefficients, which are estimated from details of the porous microstructure. It is assumed that transport of heat and water through the membrane happens due to gradients of temperature and concentration that have average values at any x- and z- in the membrane.
- The water concentration in the membrane at either interface is an average concentration over the entire interface and is not specific to the dense polysulfone phase or the pores on the membrane interface. This assumption is reasonable owing to extremely low surface porosities in the asymmetric membrane skin.
- At steady state, the concentration gradient arises in the membrane due to the drying of membrane near the membrane-gas interface which is in equilibrium with the gas phase on tube side. Hence, dual equilibrium laws have been incorporated at respective membrane interfaces to estimate the concentration gradient in the membrane.
- The latent heat lost to evaporation is gained from the hot water on the shell side [23–25].
- Thermal losses from the humidifier to the surroundings in terms of convection and radiation are neglected i.e. the humidifier is assumed to be perfectly insulated.
- Changes in air and water mass flow rates across the length of the tubes are neglected. This is reasonable for temperatures under consideration based on our earlier work [24] which was described in Chapter 3.
- Physical properties such as density, thermal conductivity, specific heat, and viscosity remain constant.

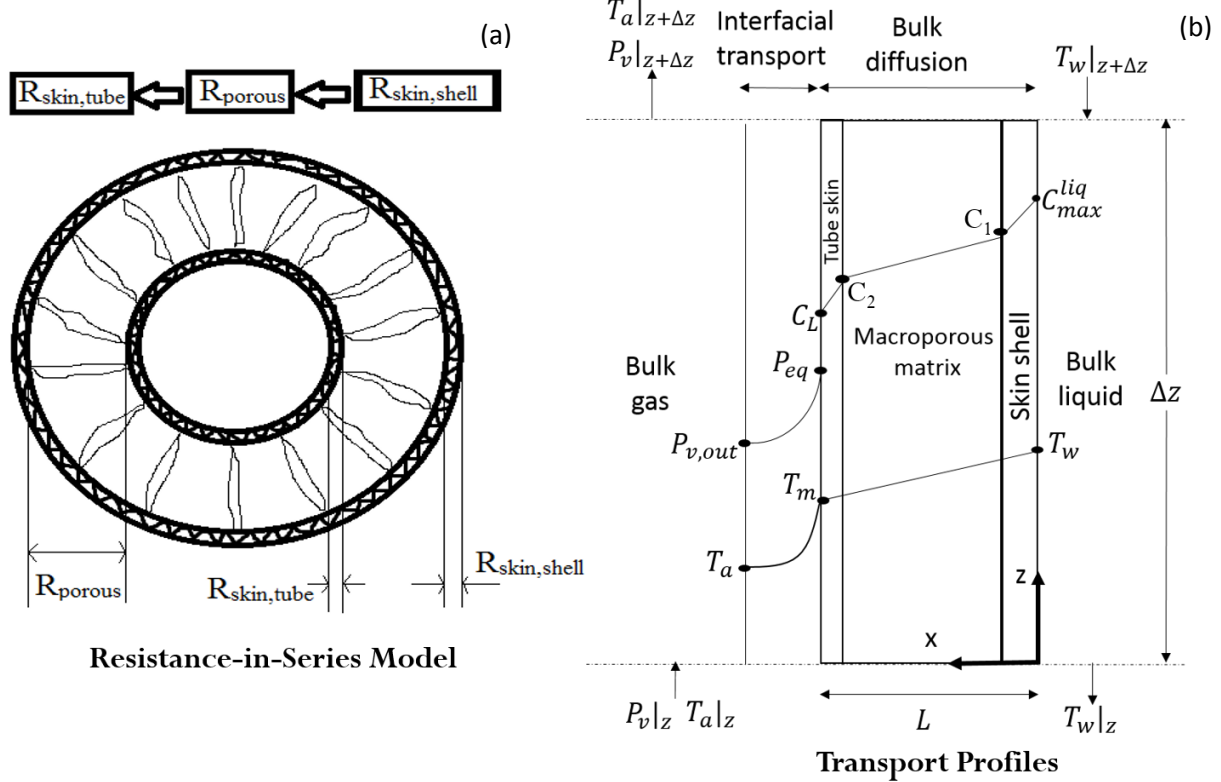


Fig. 4.2. Schematic representation of (a) resistance-in-series model for asymmetric membranes (b) temperature and concentration profiles along transverse (x-) direction.

The transport resistance across an asymmetric hollow fiber membrane is modeled using the following morphological and equilibrium considerations:

- i) The microstructure of asymmetric hollow fiber membranes consists of thin nano-porous skin layers on the tube side and shell side, and a macro-porous bulk region in between (details of this microstructure will be elucidated in Section 4.1).
- ii) The pore size distribution in the skin layers is described as N_i nano-capillaries of radius r_{pi} . This information is obtained from experimental data as described later in Section 4. Since the minimum radius of the nano-capillaries is estimated to be above 4 nm, the pore confinement effects are not expected, and water will undergo self-diffusion inside the capillary under a concentration gradient [26]. On the other hand, water will also diffuse through the dense portion of the skin analogous to water diffusion across dense PSF as suggested by [31]. Both these transport resistances are in parallel and hence the total skin resistance is given by Eqs. (11) and (12).

- iii) Water also self-diffuses in the bulk through the tortuous macro-porous matrix.
- iv) The membrane surfaces are in equilibrium with water on the shell side and with moist air on the tube side thereby allowing liquid-vapor permeation (LVP).

We can now model the transport resistance across the asymmetric hollow fiber membrane as given by Eq. (9).

$$R_{total} = R_{skin,shell} + R_{bulk} + R_{skin,tube} \dots\dots\dots(9)$$

Where, $R_{skin,shell}$ and $R_{skin,tube}$ are the resistances offered by the respective skins on shell and tube sides and R_{bulk} is the resistance offered by the macro-porous region sandwiched in between the two skin layers.

In Eq. (9), the individual skin resistances can be obtained from Eqs. (10) and (11) based on equivalent resistance for a parallel circuit.

This gives,

$$\frac{1}{R_{skin,shell}} = \left[\frac{1}{R_{diff,shell}} + \frac{1}{R_{pore,shell}} \right] \dots\dots\dots(10)$$

$$\frac{1}{R_{skin,shell}} = \frac{1}{A_{od}} \left[\frac{D_p(A_{od} - \sum_{i=1}^N \pi r_i^2 N_i)}{t_{skin,shell}} + \frac{\sum_{i=1}^N \pi r_i^2 N_i D_w}{t_{skin,shell}} \right] \dots\dots\dots(11)$$

Where, $R_{diff,shell}$ and $R_{pore,shell}$ are respectively the resistances to moisture diffusion in the dense polymer phase and nanopores of the shell-skin, D_p is the diffusion coefficient of water in the dense polysulfone, D_w is the self-diffusion coefficient of water, $t_{skin,shell}$ is the skin thickness, r_i is the radius of the i^{th} pore obtained from pore size distribution data and A_{od} is the outer membrane surface area.

Similarly, for tube side skin we get

$$\frac{1}{R_{skin,tube}} = \frac{1}{A_{id}} \left[\frac{D_p(A_{id} - \sum_{i=1}^N \pi r_i^2 N_i)}{t_{skin,tube}} + \frac{\sum_{i=1}^N \pi r_i^2 N_i D_w}{t_{skin,tube}} \right] \dots\dots\dots(12)$$

Combining Eqs. (9)-(12) gives

$$R_{total} = \frac{A_{od} t_{skin,shell}}{D_p(A_{od} - \sum_{i=1}^N \pi r_i^2 N_i) + \sum_{i=1}^N \pi r_i^2 N_i D_w} + R_{bulk} + \frac{A_{id} t_{skin,tube}}{D_p(A_{id} - \sum_{i=1}^N \pi r_i^2 N_i) + \sum_{i=1}^N \pi r_i^2 N_i D_w} \dots\dots\dots(13)$$

In Section 4.2 we show how R_{bulk} can be rigorously estimated from the asymmetric porous morphology of the bulk region of the membrane.

The effective diffusivity of water in asymmetric membrane can be written as

$$D_{eff} = \frac{L}{R_{total}} \dots\dots\dots(14)$$

Substituting Eq. (13) in (14), we get

$$D_{eff} = \frac{L}{\left[\frac{A_{od}t_{skin,shell}}{Dp(A_{od}-\sum_{i=1}^N \pi r_i^2 N_i) + \sum_{i=1}^N \pi r_i^2 N_i D_w} + R_{bulk} + \frac{A_{id}t_{skin,tube}}{Dp(A_{id}-\sum_{i=1}^N \pi r_i^2 N_i) + \sum_{i=1}^N \pi r_i^2 N_i D_w} \right]} \dots\dots\dots(15)$$

Eq (15) characterizes the transport of moisture through the asymmetric membrane by accounting for its microstructural details.

We now look at equilibrium considerations at the membrane interfaces on the shell side and tube side. Fig. 4.2b shows schematic of the local concentration and temperature profiles along the membrane thickness and at the membrane-air interface at any axial position z . It is assumed that interfacial equilibrium of moisture at the membrane-air interface is governed by Henry's law, which relates water concentration in membrane phase with water vapor pressure in air at the interface. Instead of direct isopiestic measurements for estimating Henry's constant, which is beyond the scope of this work, we use here a modified form of Henry's law as proposed by Monroe et al. [27] in Eq. (16) below.

$$P_{eq} = \frac{P_{v,sat}}{C_{max}^{liq}} C_L \dots\dots\dots(16)$$

Here, C_L (mol/m^3) is the concentration of water in the membrane phase at the membrane-air interface, P_{eq} (Pa) is the partial pressure of vapor in air at the membrane-air interface which is in equilibrium with C_L , C_{max}^{liq} (mol/m^3) is the maximum concentration of water in the membrane phase given by Eq. (17) in case of liquid water transport and $P_{v,sat}$ (Pa) is the saturation vapor pressure of water at temperature T_w (K) as given in Eq. (18)[28].

$$C_{max}^{liq} = \frac{\theta \rho_w}{M_w} + \frac{S \rho_p (1-\theta)}{M_w} \dots\dots\dots(17)$$

Where, θ is the bulk porosity estimated from gravimetric measurements (see Table 4.3), ρ_w and M_w are the respective density and molecular weight of water, S is the solubility of water in

dense polysulfone (grams of water sorbed at equilibrium/gram of membrane ~ 0.0085 g/g) [29]. Since the second term on right side of Eq. (17) \ll first term, we proceed with neglecting the second term.

$$P_{v,sat} = A \times 10^{\left(\frac{mT_w}{T_w + T_n}\right)} \dots \dots \dots (18)$$

Where $A = 611.6441$ (Pa), $m = 7.591386$, $T_n = 240.7263$ °C for $-20 \leq T_w \leq 50$ °C and
 $A = 600.4918$ (Pa), $m = 7.337936$, $T_n = 229.3975$ °C for $50 \leq T_w \leq 100$ °C

The rationale of choosing Henry's law given by Eq. (16) is based on the fact that it provides a better description of equilibrium in the case of a liquid-vapor permeation system [24,27], such as the one studied here, over generic polynomial expressions of equilibrium which are better suited to describe equilibrium in vapor-vapor permeation systems [30,31]. Detailed discussion on the validity of modified Henry's law is also presented in the previous chapter (Chapter-3).

Next, we consider the microscopic water and heat balance across the membrane at any axial location z , and also the overall addition of moisture and heat along the length of the membrane. The boundary conditions for heat and mass transfer (Eqs. (23), (27), (29)) across the membrane are given by Eqs. (19) and (20) respectively.

$$\begin{aligned} x = 0, T &= T_w \\ x = L, -k_m \frac{\partial T}{\partial x} \Big|_L &= h_t(T_m - T_a) \dots \dots \dots (19) \end{aligned}$$

$$\begin{aligned} x = 0, C &= C_{max}^{liq} \\ x = L, -D_{eff} \frac{\partial C}{\partial x} \Big|_L &= K_t \left(\frac{P_{eq}}{RT_m} - \frac{P_v}{RT_a} \right) \dots \dots \dots (20) \end{aligned}$$

Here, $T_w(K)$ is the water temperature, $L(m)$ is the membrane thickness, $k_m(W/mK)$ is the effective thermal conductivity of the porous membrane which is estimated from Eq. (21)[32], $h_t(W/m^2K)$ is the convective heat transfer coefficient on the tube side, $T_m(K)$ is the membrane temperature at the membrane-air interface, $T_a(K)$ is the bulk air temperature, $K_t(m/s)$ is the convective mass transfer coefficient on the tube side and $P_v(Pa)$ is the partial pressure of vapor in bulk air (see Fig. 4.2b for the locations of various temperatures and pressures described above). It must be noted that while the water evaporates at the membrane-gas interface, the

loss of heat to evaporation is reflected by the drop in shell side temperature. Hence, we have included this heat loss in the shell side energy balance equation (see Eq. (26)) instead of including it in Eq. (19). This is also in agreement with the several literature reports[24,25,33].

$$k_m = k_{polymer}^{1-\theta} \times k_{water}^{\theta} \dots\dots\dots(21)$$

Writing a mass balance equation for water vapor along the axial direction on the tube side in a control volume of length Δz , we get

Mass balance equation:

$$\frac{\pi d_{id}^2}{4RT_a} v_a (P_v|_z - P_v|_{z+\Delta z}) = -K_t \left(\frac{P_{eq}}{RT_m} - \frac{P_v}{RT_a} \right) \pi d_{id} \Delta z \dots\dots\dots(22)$$

Here, $d_{id}(m)$ is the inner diameter of tube, $v_a (m/s)$ is the average superficial velocity of air in the tube, and $K_t(m/s)$ is the tube side convective mass transfer coefficient. In differential form, Eq. (22) becomes

$$\frac{dP_v}{dz} = \frac{4K_t}{v_a d_{id}} \left(P_{eq} \left(\frac{T_a}{T_m} \right) - P_v \right) \dots\dots\dots(23)$$

The tube side convective mass transfer coefficient K_t is obtained in terms of Sherwood number and is calculated using standard correlations given below for laminar flow in smooth tubes[34] as given in Eqs. (24) and (25).

$$Sh = \frac{K_t d_{id}}{D_a} \dots\dots\dots(24)$$

Where Sherwood number (Sh) is given as

$$Sh = 3.658 + \left[\frac{0.0668 (Re Sc \frac{d_{id}}{H})}{1 + (0.04 (Re Sc \frac{d_{id}}{H})^{2/3})} \right] \dots\dots\dots(25)$$

The energy balance on shell side can be written as

$$\dot{m}_a C_{pw} T_w|_{z+\Delta z} - \dot{m}_w C_{pw} T_w|_z = NU \pi d_{od} \Delta z (T_w - T_a) + NK_t M_w \lambda_{vap} \pi d_{od} \Delta z \left(\frac{P_{eq}}{RT_m} - \frac{P_v}{RT_a} \right) \dots\dots\dots(26)$$

Here, $\dot{m}_w (kg/s)$ is the mass flow rate of water on the shell side, $C_{pw} (J/kg K)$ is the specific heat of water, $U (W/m^2 K)$ is the overall heat transfer coefficient, $d_{od}(m)$ is the outer diameter

of tube, N is number of tubes, M_w (kg/mol) is molecular weight of water, and λ_{vap} (J/kg) is the latent heat of vaporization of water.

Equation (26) incorporates the energy loss from the shell side due to latent heat of evaporation of water as well as the heat transferred by conduction and convection in the membrane. In differential form, Eq. (26) becomes

$$\frac{dT_w}{dz} = \frac{NU\pi d_{od}(T_w - T_a)}{\dot{m}_w c_{pw}} + \frac{NK_t M_w \lambda_{vap} \pi d_{od}}{\dot{m}_w c_{pw}} \left(\frac{P_{eq}}{RT_m} - \frac{P_v}{RT_a} \right) \dots\dots\dots (27)$$

Energy balance on tube side accounts for the increase in air temperature due to the heat gained from conductive and convective heat transfer and the sensible heat gained due to the addition of water vapor. Since specific heat of air varies significantly with the addition of moisture, it is also considered to vary in the z -direction. The tube side energy balance can thus be written as Eq. (28).

$$\dot{m}_a (C_{pa} T_a) \Big|_z - \dot{m}_a (C_{pa} T_a) \Big|_{z+\Delta z} = -NU\pi d_{id} \Delta z (T_w - T_a) - NK_t M_w C_{pv} (T_m - T_a) \pi d_{id} \Delta z \left(\frac{P_{eq}}{RT_m} - \frac{P_v}{RT_a} \right) \dots\dots\dots (28)$$

The tube side energy balance in differential form is given by

$$\frac{dT_a}{dz} = \frac{NU\pi d_{id}(T_w - T_a)}{\dot{m}_a C_{pa}} + \frac{NK_t M_w C_{pv} \pi d_{id}(T_m - T_a)}{\dot{m}_a C_{pa}} \left(\frac{P_{eq}}{RT_m} - \frac{P_v}{RT_a} \right) - \frac{2.488 K_t C_{pv} T_a P_T}{v_a d_{id} (P_T - P_v)^2} \left(P_{eq} \left(\frac{T_a}{T_m} \right) - P_v \right) \dots\dots\dots (29)$$

The last term on the right side of Eq. (29) arises because $C_{pa} = 1005 + 1820\omega_{a,out}$ [35] and $\omega_{a,out} = \frac{0.622P_v}{P_T - P_v}$ [28], where C_{pa} ($J / kg K$) is the specific heat capacity of moist air and $\omega_{a,out}$, $kg H_2O/kg air$ is the absolute humidity defined as the mass of water vapor per unit mass of air. P_T is the total gas pressure which is 101325 Pa.

Equations (23), (27) and (29) form the main set of coupled mass and heat transfer equations of the model, which when solved together yield the output parameters: outlet air temperature $T_{a,out}(K)$, vapor pressure of outlet air P_v (Pa), and outlet water temperature $T_{w,out}(K)$. The boundary conditions are the known inlet operating conditions $P_{v,in}$ (Pa), $T_{a,in}(K)$ and $T_{w,in}(K)$.

The other input model parameters are: (a) the operating parameters: \dot{m}_w, \dot{m}_a ; (b) the design parameters: d_{id}, d_{od}, L, H, N ; and (c) the physical properties like $C_{pw}, C_{pv}, \rho_a, \rho_w, \mu_a, \mu_w, k_a, k_w, k_m$ of the fluids. The values of these input parameters are provided in Table 4.3. The overall heat transfer coefficient is treated as a fit parameter of the model because the effect on heat transfer coefficient due to the heat lost from humidifier to the surroundings could not be measured independently. The variation of overall heat transfer coefficient with experimental conditions are discussed in the following section.

Table 4.3: Value of input parameters.

Property	Value	Reference
Specific heat of water, C_{pw} (J/kg K)	4186	[34]
Specific heat of water vapor, C_{pv} (J/kg K)	1820	[34]
Density of air, ρ_a (kg/m ³)	1.166	[34]
Density of water, ρ_w (kg/m ³)	1000	[34]
Viscosity of water, μ_w (Pa s)	8.9×10^{-4}	[34]
Viscosity of air, μ_a (Pa s)	1.83×10^{-5}	[34]
Thermal conductivity of air, k_a (W/m K)	0.0264	[34]
Thermal conductivity of water, k_w (W/m K)	0.6	[34]
Thermal conductivity of polysulfone, k_p (W/m K)	0.24	[36]
Diffusivity of water in polysulfone, D_p (m ² /s)	5×10^{-12}	[29]
Diffusivity of water vapor in polysulfone, D_{pv} (m ² /s)	9×10^{-12}	[39]
Diffusivity of water in air, D_{wa} (m ² /s)	2.52×10^{-5}	[34]
Self-diffusivity of water, D_w (m ² /s)	4.74×10^{-9}	[37]
Latent heat of vaporization of water, λ_{vap} (J/kg)	2.265×10^6	[34]
Tube ID (mm) of as-spun wet fibers of 25:27:30 wt% polymer concentration*	0.6 : 0.57 : 0.67	
Tube OD (mm) of as-spun wet fibers of 25:27:30 wt% polymer concentration*	1.1 : 1.0 : 1.03	
Tube ID of oven-dried membranes of 25:27:30 wt% polymer concentration, d_{id} (mm) *	0.50: 0.52 : 0.72	
Tube OD of oven-dried membranes of 25:27:30 wt% polymer concentration, d_{od} (mm) *	0.87 : 0.86 : 1.02	
Fiber thickness for 25:27:30 wt% polymer concentration, L (mm) *	0.19 : 0.17 : 0.15	
Mean pore radius estimated from pore size distribution, \bar{r}_p (nm) **	6	
Volumetric bulk porosity for 25:27:30 wt% polymer concentration, θ ***	0.65±0.06: 0.52±0.08: 0.37±0.12	
C_{max}^{liq} for 25:27:30 wt% polymer concentration (mol/m ³)	36140 : 28846 : 20614	

*Measured on stereo-optical microscope; **Calculated using Eq. (5); ***Calculated using Eqs. (7);

In the next section, model calculations are compared with experimentally measured temperature and absolute humidity of outlet air for different membrane modules (listed in Table 4.2 earlier) at varying air and water flow rates and water inlet temperatures. The humidifier performance is quantified in terms of two performance indices viz., thermal effectiveness factor and humidity effectiveness factor which are defined below in Eq. (30) and Eq. (31). While the thermal effectiveness factor describes the efficacy with which the air picks up heat within the humidifier and approaches inlet water temperature, the humidity effectiveness factor takes into account the humidity difference between the shell and tube sides and determines the efficacy of moisture transfer. In Eq. (31), the equivalent humidity on the shell side ($\omega_{w,in}$, $kg\ H_2O/kg\ air$) is considered to be the equilibrium humidity of air that is saturated with water at temperature $T_{w,in}(K)$. This is determined using Eq. (32) below [35,38].

$$\varepsilon_t = \frac{T_{a,out} - T_{a,in}}{T_{w,in} - T_{a,in}} \dots\dots\dots(30)$$

$$\varepsilon_h = \frac{\omega_{a,out} - \omega_{a,in}}{\omega_{w,in} - \omega_{a,in}} \dots\dots\dots(31)$$

$$\omega_{w,in} = \frac{10^6}{\exp\left(\frac{5294}{T_{w,in}}\right)} \dots\dots\dots(32)$$

4.4. Results and discussion

4.4.1. Membrane Microstructure

The average porosity of the membranes was calculated from the measured values of geometrical dimensions and dry weight of fiber samples as per Eq. (7). The HFM25, HFM27, and HFM30 membranes had an average porosity of 0.65, 0.52 and 0.37, respectively. This trend agrees with the intuitively expected decrease in porosity as the polymer concentration in the spinning dope is increased. More details of the porous microstructure were obtained from the FE-SEM micrographs. Fig. 4.3(a1 – c1, a2 – c2) shows the FE-SEM images of the cross-section of membrane fibers made from dopes having 25%, 27%, and 30 % polymer concentrations by weight. In general, as can be seen from the images, three types of pores are observed – individual macrovoids in the bulk macro-porous region of the membrane, a continuous network of macropores of micron to sub-micron range in the bulk macro-porous region of the membrane

and a continuous network of very small pore (nanopores) in the skin layers. The nanopores in the skin layers are not clearly observed in the FE-SEM images however, their quantification by bubble point and liquid-liquid displacement methods is described later. While for HFM25 the macrovoids are present on both shell and tube sides, for HFM27 and HFM30 the macrovoids are concentrated only towards the tube side. In general, the microstructure in the bulk of the fiber thickness is sponge-like. The dry fiber thicknesses are observed to decrease with increasing polymer concentration. At the two interfaces (tube side and shell side), skin like structures can also be observed from Fig. 4.3(a3 – c3, a4 – c4). The total average skin thickness (shell + tube skin thickness) was observed to be around 290 nm, 310 nm and 288 nm for HFM 25, HFM27 and HFM30 respectively. These skin thicknesses account for 0.15, 0.18 and 0.19 % of the total membrane thickness of HFM25, HFM27, and HFM30 respectively. The skin thickness values were used in the calculation of the overall diffusion coefficient in the model as discussed later.

It is well known in the literature of asymmetric hollow fiber membranes that when a non-solvent is used as the bore fluid the internal coagulation process (on the tube or lumen side) starts immediately after the fiber exits from the spinneret. However, in the air-gap region near the spinneret only partial phase separation occurs on the outer surface (shell side) of the hollow fiber due to the presence of moisture in the air gap [39]. Eventually, when the fiber is fully immersed in the coagulation bath, complete phase separation takes place at the outer surface. Consequently, the inner surface is almost immediately frozen while the outer surface skin is susceptible to shrinking. The ID of as-spun wet fibers (reported in Table 4.3) is close to the OD of the needle (0.5 mm), which confirms rapid quenching of the two membranes on the tube side. The OD of the membranes is less than the OD of the annulus (1.28 mm) because of shrinking by slower phase separation on the shell side coupled with small amount of stretching due to gravity/take-up speed. Further shrinking of the ID and OD occurs during the post-treatment when the membranes are kept immersed in water followed by air drying and oven drying thereby consolidating the porous microstructure.

Microstructure development in the HFMs can be understood from physics of phase separation of polymer solution (PSF in DMAc in the present case) when it is brought in contact

with a non-solvent (water). As mentioned earlier, freezing and formation of a thin skin first occurs at the inner wall of the membrane. The steep concentration gradient across the skin causes DMAc to diffuse through the thin skin and dissolve into the bore fluid. Simultaneously, water from the bore diffuses inwards reducing the solvating power and initiating phase separation. Water from the polymer lean phase nucleates out to form droplets, which eventually form the macrovoids. The droplets near the inner wall are smaller since their growth is arrested by rapid phase separation. However, those away from the wall can ripen/coalesce to form larger droplets because of the slower phase separation, and they thus form larger macrovoids. The peculiar pointedness of the macrovoids is a result of orientation caused by flow, which is induced by a surface tension gradient as the lower surface tension DMAc transports out into the higher surface tension water phase. At the outer wall of the membrane, incipient phase separation begins as the membrane encounters moisture present in the air gap. Thicker skin is formed because of slower phase separation in the air gap. Higher the polymer concentration in the dope, higher is the skin fraction in the membrane as is verified by FE-SEM measurements. As the membrane enters the coagulation bath, outward diffusion of DMAc and inward diffusion of water occurs through the outer surface skin leading to further phase separation. When the polymer concentration in the dope is low (HFM25) the larger amount of polymer lean phase nucleates out to form small droplets near the outer skin. As a result, macrovoids are seen near the outer wall for these membranes. However, membranes made from higher polymer concentrations (HFM27 and HFM30) have a greater amount of polymer rich phase resulting in the formation of spongy structure of smaller interconnected pores (sub-microns to few microns) rather than macrovoids.

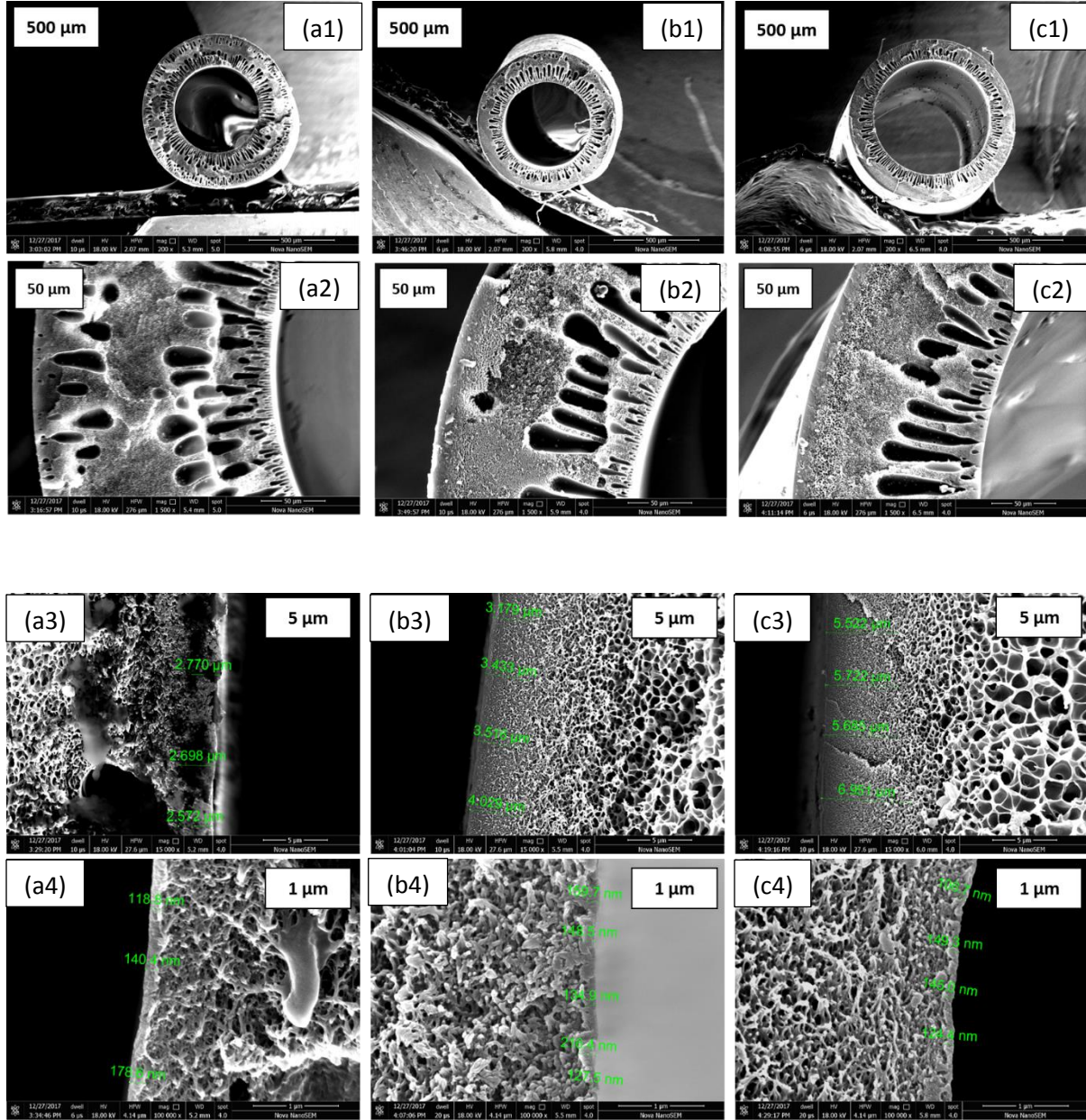


Fig. 4.3. FE-SEM images of entire fiber cross-section (top row; left to right: (a1) HFM25, (b1) HFM27, (c1) HFM30), fiber thickness cross-section (second row; left to right: (a2) HFM25, (b2) HFM27, (c2) HFM30), shell-side membrane microstructure (third row; left to right: (a3) HFM25, (b3) HFM27, (c3) HFM30) and tube-side membrane microstructure (bottom row; left to right: (a4) HFM25, (b4) HFM27, (c4) HFM30).

4.4.2. Quantification of porosity

The membrane microstructure influences the transport of moisture (liquid or vapor) and therefore has direct implications on humidification performance. While in most applications, macrovoid formation is considered undesirable due to their susceptibility to failure under high-

pressure operation [40], the presence of macrovoids may actually prove beneficial for moderate pressure applications like that of gas humidification because of their ability to act as water reservoirs. At the same time, the nanopores in the skin layers and macropores in the bulk membrane are expected to modulate moisture transport rate across the membrane. With the eventual goal of correlating transport properties with the microstructure, we use here image processing tool (ImageJ) to quantify the average volume fractions of the macrovoids and macropores (note the difference between macrovoid and macropore, size of macrovoids \gg macropores). It is assumed in this method that the volume fractions of macrovoids and smaller pores are equal to the areal fractions calculated above. Three rectangular segments were chosen at randomly selected locations along the membrane circumference. Two such cross-sections were taken at different lengths along the fibers. Thus, in all, six rectangular segments were analysed by image processing. Figure 4.4a shows representative images for each membrane type. The boundaries of the macrovoids inside each segment were marked manually and the area of macrovoids was calculated with ImageJ. This gave the areal fraction ($\theta_{mv} = \frac{\text{macrovoid area}}{\text{segment area}}$) of the macrovoids in each segment. The areal fraction of macrovoids averaged over six segments are reported in Table 4.4 along with standard deviation for each of the three membranes. Table 4.4 shows that the overall macrovoid porosity θ_{mv} decreased slightly as the polymer concentration in the dope increased. The higher macrovoid porosity of HFM25 is owing to the fact that macrovoids are present on both tube side and shell side. Next, the volume fraction of macropores was estimated by subtracting from the total segment area the areal macrovoid fraction and the area occupied by the polymer. The latter was calculated as $A_p = \frac{W_m}{H\rho_p}$, where $\frac{W_m}{H}$ is the measured weight per unit length of fiber and ρ_p is the known density of polysulfone. The variation incurred in calculating pore volume fraction by this assumption is estimated to be about 25-30% based on the comparison of porosity calculated from the SEM micrographs (as shown in Table 4.4) and the gravimetric average porosity calculated earlier in Section 4.1. This difference is most likely due to the assumption that the volume average porosity can be estimated from 2D image analysis. It can be seen from Table 4.4 that total porosity and volume fraction of

macropores of the membranes decrease in the order HFM25>HFM27>HFM30, which correlates with increasing polymer concentration in the spin dope.

Table 4.4: Estimated porosity for each membrane type.

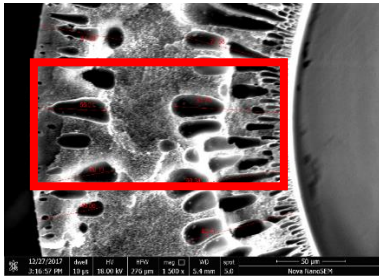
Membrane Type	HFM25	HFM27	HFM30
Total segment area, μm^2	13477 \pm 3199	11161 \pm 2854	6675 \pm 1325
Macrovoid area in segment, μm^2	3485 \pm 383	2595 \pm 553	1531 \pm 488
θ_{mv}	0.259 \pm 0.051	0.233 \pm 0.025	0.229 \pm 0.042
Total cross-section area (CSA) of HFM, μm^2	397917	368322	502851
Total macrovoid area, A_{mv} , μm^2	106376 \pm 20355	86678 \pm 9054	114231 \pm 21378
Weight/Length (W/H) of fiber (kg/m)	1.47 x 10 ⁻⁴ \pm 8.84 x 10 ⁻⁶	1.62 x 10 ⁻⁴ \pm 5.76 x 10 ⁻⁶	3.17 x 10 ⁻⁴ \pm 5.85 x 10 ⁻⁵
Area occupied by polymer, $A_p = \frac{W}{H\rho_p}$, μm^2	118683 \pm 7130	130645 \pm 4647	255376 \pm 47208
$\theta_{pore} = \frac{CSA - A_p - A_{mv}}{CSA}$	0.434 \pm 0.054	0.41 \pm 0.03	0.265 \pm 0.098
Total porosity, $\theta_{total} = \theta_{mv} + \theta_{pore}$	0.702 \pm 0.018	0.645 \pm 0.013	0.492 \pm 0.094

The macro-porous bulk region of the membrane i.e., the region between the skin layers can be sub-divided into two/three domains as shown in Fig. 4.4b. Domains 1 and 3 near the skin layers have macrovoids along with the spongy microstructure in between them. Domain 2, which is away from the skin layers, has only the spongy microstructure containing small interconnected macropores. HFM25 has all three domains whereas HFM27 and HFM30 have only domain 1 and domain 2. Using the same image processing procedure discussed earlier, we estimated the macrovoid porosity ($\theta_{1,mv}$, $\theta_{3,mv}$) in domains 1 and 3 respectively. The porosity of the spongy microstructure (macropores) is assumed the same in all three domains as is already shown in Table 4.4. Thus, the calculated porosity in the three domains of the bulk membrane is shown in Table 4.5 below.

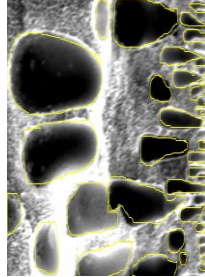
Table 4.5: Calculation of porosity in the macro-porous bulk of the membranes.

Membrane Type	HFM25	HFM27	HFM30
Domain 1 (near tube side)			
Segment area, μm^2	5574 \pm 644	6163 \pm 1092	5487 \pm 254
Macrovoid area, μm^2	2420 \pm 162	2905 \pm 793	2495 \pm 168
t_1 , μm	83.60	83.0	68.98
$\theta_{1,mv}$	0.434 \pm 0.024	0.471 \pm 0.054	0.455 \pm 0.040
$\theta_{1,pore} = \theta_{pore}$	0.434 \pm 0.054	0.41 \pm 0.03	0.265 \pm 0.098
Domain 2 (middle area)			
t_2 , μm	44.95	82.0	82.02
$\theta_{2,pore} = \theta_{pore}$	0.434 \pm 0.054	0.41 \pm 0.03	0.265 \pm 0.098
Domain 3 (near shell side)			
Segment area, μm^2	4247 \pm 392		
Macrovoid area, μm^2	1329 \pm 311		
t_3 , μm	56.46		
$\theta_{3,mv}$	0.313 \pm 0.048		
$\theta_{3,pore} = \theta_{pore}$	0.434 \pm 0.054		

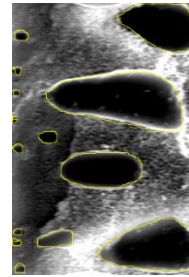
$\theta_{i,mv}$ is the macrovoid volume fraction of domain i ($i=1,2,3$); $\theta_{i,pore}$ is the volume fraction of macro-pores in domain i ($i=1,2,3$); t_i is the thickness of domain i ($i=1,2,3$)



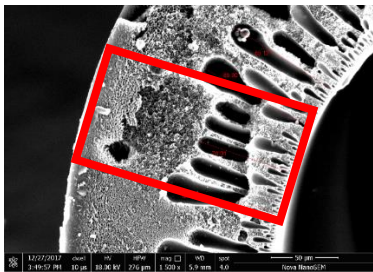
(a1) HFM25: Total segment



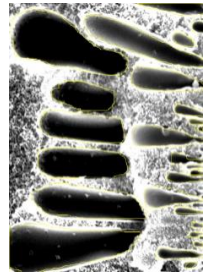
Domain 1



Domain 3



(a2) HFM27: Total Segment



Domain 1

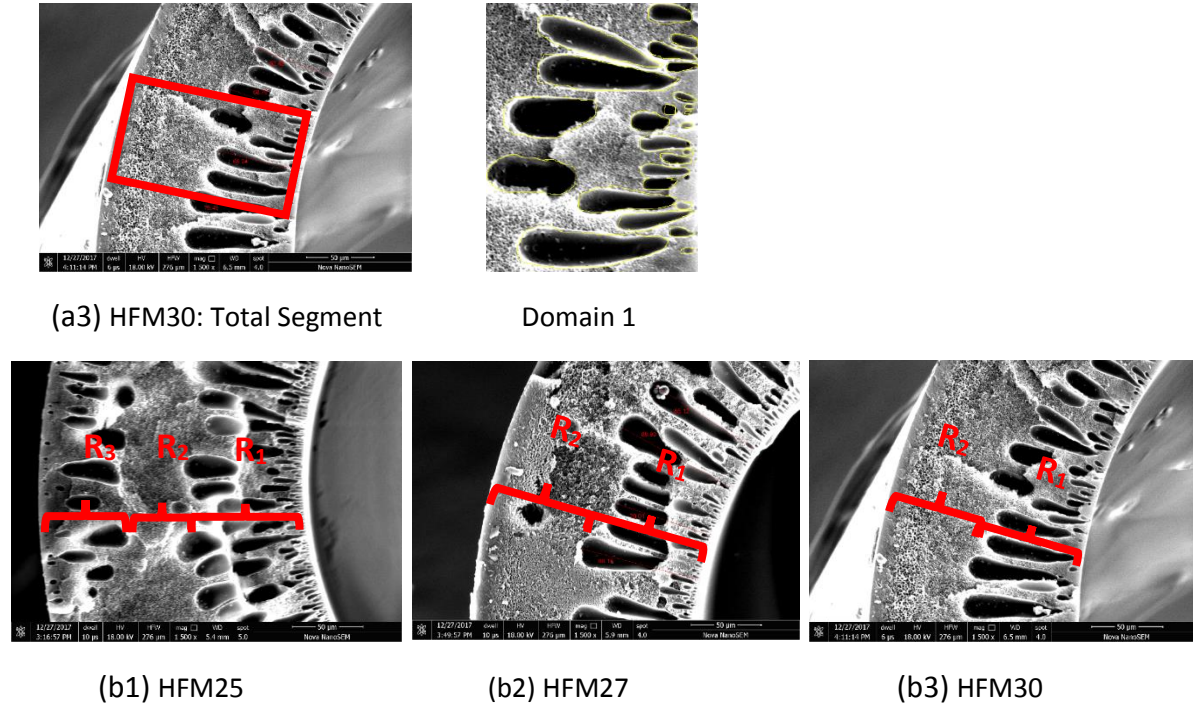


Fig. 4.4. (a) Representative images for HFM25 (a1), HFM27 (a2), and HFM30 (a3) used for image processing. The representative rectangular segment of the cross-section marked in red is used for calculations presented in Table 4.4. The zoomed-in image of macrovoids in the segment is presented as domains (1, 2, and 3) which were used for calculating areal fractions using ImageJ as shown in Table 4.5. (b) Representative micrographs for HFM25 (b1), HFM27 (b2), and HFM30 (b3) are shown with the spatial domains (marked as R_1 , R_2 , and R_3) containing macrovoids and smaller interconnected pores.

4.4.3. Estimating resistance for transport of moisture through porous microstructure

Using the quantification of bulk microstructure given in Table 4.5 we can now estimate the mass transport resistance offered by the bulk macro-porous membrane as follows. In the case of HFM25 membrane, since the three domains are in series, therefore the bulk resistance can be written as

$$R_{bulk,25} = R_{25,1} + R_{25,2} + R_{25,3} \dots\dots\dots(33)$$

Where, $R_{25,i}$; ($i = 1,2,3$) are the resistances offered by the microstructure in domain i ; ($i = 1,2,3$). Domain 1 contains macrovoids and spongy porous network, which offer two resistances in parallel. Therefore $R_{25,1}$ is given by Eq. (34).

$$\frac{1}{R_{25,1}} = \frac{\theta_{25,1,mv} D_w}{t_{25,1}} + \frac{(1-\theta_{25,1,mv}) D_w \theta_{25,1,pore}^{1.5}}{t_{25,1}} \dots\dots\dots(34)$$

Here, $t_{25,1}(m)$ is the thickness of domain 1. The first term represents resistance offered by macrovoids in which transport is governed by self-diffusion. The second term corresponds to resistance to diffusion in the interconnected macropores of the spongy region between macrovoids. The form of this term accounts for tortuosity of the diffusional path (Bruggemen's correlation) in the spongy matrix.

Using similar arguments, the resistances $R_{25,2}$ and $R_{25,3}$ in the domains 2 and 3 can be estimated by Eq. (35) and Eq. (36).

$$R_{25,2} = \frac{t_{25,2}}{D_w \theta_{25,2,pore}^{1.5}} \dots\dots\dots(35)$$

$$\frac{1}{R_{25,3}} = \frac{\theta_{25,3,mv} D_w}{t_{25,3}} + \frac{(1-\theta_{25,3,mv}) D_w \theta_{25,3,pore}^{1.5}}{t_{25,3}} \dots\dots\dots(36)$$

Here, $t_{25,2}(m)$ and $t_{25,3}(m)$ are the thicknesses of domains 2 and 3.

For the membranes HFM27 and HFM30, the total bulk resistance becomes

$$R_{bulk,27} = R_{27,1} + R_{27,2} \dots\dots\dots(37)$$

$$R_{bulk,30} = R_{30,1} + R_{30,2} \dots\dots\dots(38)$$

These are given by Eqs. (39) - (42).

$$\frac{1}{R_{27,1}} = \frac{\theta_{27,1,mv} D_w}{t_{27,1}} + \frac{(1-\theta_{27,1,mv}) D_w \theta_{27,1,pore}^{1.5}}{t_{27,1}} \dots\dots\dots(39)$$

$$\frac{1}{R_{30,1}} = \frac{\theta_{30,1,mv} D_w}{t_{30,1}} + \frac{(1-\theta_{30,1,mv}) D_w \theta_{30,1,pore}^{1.5}}{t_{30,1}} \dots\dots\dots(40)$$

$$R_{27,2} = \frac{t_{27,2}}{D_w \theta_{27,2,pore}^{1.5}} \dots\dots\dots(41)$$

$$R_{30,2} = \frac{t_{30,2}}{D_w \theta_{30,2,pore}^{1.5}} \dots\dots\dots(42)$$

The bulk resistances R_{bulk} for HFM25, HFM27, and HFM30 obtained from Eqs. (33), (37), and (38) respectively, can now be substituted in Eq. (15) of the model described in Section 4.3.

4.4.4. Bubble point and pore size distribution analysis

Having quantified the macrovoid porosity and macropore porosity in the bulk region, we now look at quantification of porosity in the skin layer. This is done using the bubble point and liquid-liquid displacement methods, both of which work on the same principle of fluid displacement

from inside the pore due to another fluid under pressure. However, the distinction between the two methods arises from the different displacing fluids used. While bubble point uses pre-wetted membranes and air as the displacing fluid, the liquid-liquid displacement method makes use of the difference in surface tension between the displacing fluid (water saturated IBA) and the displaced fluid (liquid water) in the membrane pores. The bubble point method is useful for quick and easy estimation of the largest pore size in the skin whereas, the pore size distribution gives a more detailed estimation of the number density of pores of a particular size present in the skin. Fig. 4.5a shows bubble point obtained for the three different membranes. As can be seen from the graph, the bubble points of the membranes are in the order $HFM25 < HFM27 < HFM30$. This suggests that increasing the polymer concentration reduces the largest pore size available in the skin and hence requires higher pressure to push the water out from the pores. The maximum pore radii of skin layers prepared from dopes containing 25, 27 and 30 wt % polymer are estimated to be 22.2, 20.4, 18.3 nm respectively.

IBA flux and the corresponding pore size distribution for different membranes is shown in Fig. 4.5(b, c). As expected, the flux shown in Fig. 4.4b was found to increase with increasing pressure for all HFMs. The flux decreased in the order $HFM25 > HFM27 > HFM30$. As can be seen from Fig. 4.5c, the distribution of pore size in the skin layers varies from 4.8 to 22.4 nm for membranes prepared from dopes of different polymer concentrations. The maximum pore radii measured using this method was ~ 22.4 nm for HFM25, HFM27, and HFM30 which agrees closely with the bubble point measurement. It is to be noted that the measured minimum pore radius in all cases is same due to limitations on the maximum pressure that could be reached with our experimental setup without bursting the fibers or the connection tubes. It was found that the number density of pores decreased by an order of magnitude as polymer concentration in the dope increased from 25 wt% to 30 wt%. Thus, increasing polymer concentration led to the formation of denser skin layers in which the larger pores were less. The total pore density was 6.43×10^{12} , 4.15×10^{11} and 2.66×10^{11} (number of pores / m^2) for HFM25, HFM27, and HFM30 respectively. However, since the number density is the highest for the smaller pores, the number average pore radius obtained from the measurements as given by Eq. (5) was ~ 6 nm for all polymer concentrations. Surface porosities of 0.0788, 0.0054 and 0.0036 % were estimated from Eq. (6) for HFM25,

HFM27, and HFM30 respectively. As expected, HFM27 and HFM30 have nearly one order low surface porosity than HFM25 which also agrees well with the pore density calculations. As discussed earlier, the implication of low surface porosity is in increasing the skin resistance contribution to mass transport.

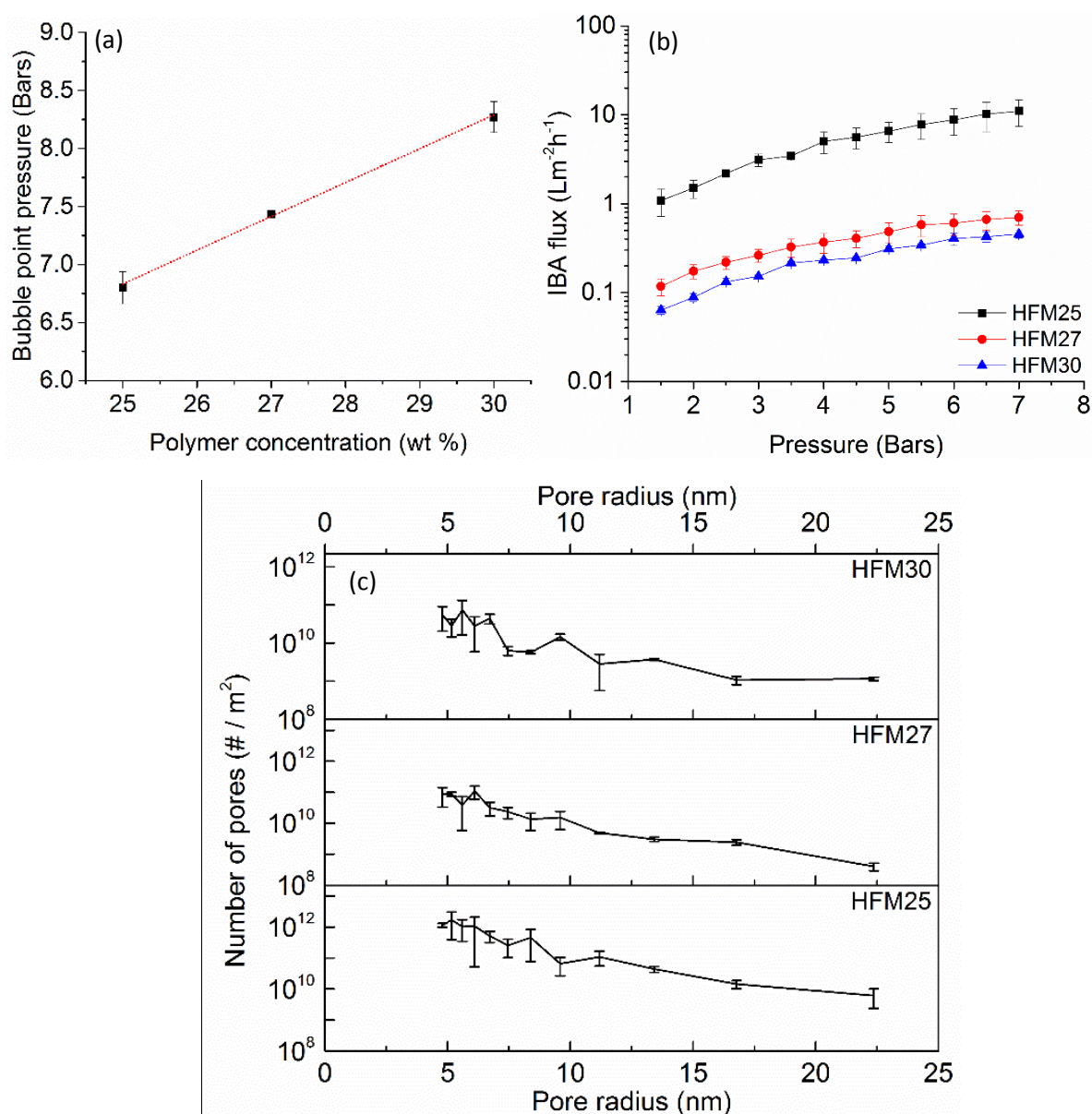


Fig. 4.5. (a) Bubble point (b) IBA flux and (c) Pore size distribution of PSF hollow fiber membranes.

The microstructure data as obtained from FE-SEM and pore size distribution analyses also help in the estimation of limiting rates of transport phenomena. For example, the individual resistances to transport of water through the skin layers and the porous bulk of the membrane

can be estimated from Eqs. (11), (12), (33), (37), (38) by substituting parametric values from Table 4.5. The estimates for resistances offered by each membrane type are listed in Table 4.6. A primary observation from Table 4.6 is that both skin and bulk offer significant resistance to mass transfer for each membrane type and neither can be neglected. This is in partial agreement with Zhang's model[14] for vapor transport across flat asymmetric membrane, which showed spongy porous layer resistance to be dominant. However, Zhang concluded that skin resistance is small enough and may not actually affect vapor transport if the skin is extremely thin and porous (in Zhang's model the skin thickness was 2.1 μm and the porosity was 35 %). Therefore, for a less porous skin as in our case, both bulk and skin resistances are significant and increase with increasing polymer concentration. This is because of decreasing skin and bulk porosities as we increase polymer concentration. The skin contribution to resistance increases as polymer concentration is increased from 25 to 27 wt% and then decreases with further increase in polymer concentration to 30 %. This happens because the skin porosity (and hence skin resistance) decreases only marginally from 27% to 30% polymer concentration, whereas the bulk porosity (and hence bulk resistance) decreases more substantially in the same range of polymer concentration. The effective diffusion coefficient obtained from Eq. (15) for different HFMs decreases in the order HFM25>HFM27>HFM30. Similarly, the resistance to heat transfer in HFM27 and HFM30 are likely to be higher than for HFM25.

Table 4.6: Individual resistances and effective diffusion coefficient of liquid water for different HFMs.

Membrane type	HFM25	HFM27	HFM30
Domain 1 resistance, R_1 (s/m)	29597.55	28642.41	27491.86
Domain 2 resistance, R_2 (s/m)	33167.81	65896.1	126844.78
Domain 3 resistance, R_3 (s/m)	23389.12	NA	NA
$R_{tot,bulk} = R_1 + R_2 + R_3$ (s/m)	86154.48	94538.51	154336.64
$R_{skin,shell}$ (s/m)	30176	47790	48384
$R_{skin,tube}$ (s/m)	23124	46452	47872
R_{total} (s/m)	139454.48	188780.51	250592.64
D_{eff} (m^2/s)	13.27×10^{-10}	9.01×10^{-10}	5.63×10^{-10}
% contribution of skin resistance	38.22 %	49.92 %	38.41 %
% contribution of bulk resistance	61.78 %	50.08 %	61.59 %

4.4.5. Water flux and entrainment

Water flux was measured at ambient water temperature at four different pressures which are typically within the operation range for gas humidification in several applications like PEM fuel cells, respiratory gas, and environment air. At these pressures, the measured water fluxes are shown in Fig. 4.6a. As can be seen in the figure for modules based on HFM25, the water flux increases with increasing trans-membrane pressure from 0.5 to 2 bars. However, no flux was recorded for modules based on HFM27 and HFM30. This is because of the denser membrane and high skin fraction leading to low pore density in these fibers. The presence of more number of smaller pores in HFM27 and HFM30 demands significantly higher trans-membrane pressure for water to penetrate the pores. It must be noted that typical trans-membrane pressures do not exceed 2 bars in gas humidification.

In water entrainment measurements, the module based on HFM25 led to water entrainment without applying any back pressure. No entrainment was seen for modules based on HFM27 and HFM30 as can be seen in Fig. 4.6b. The entrainment in HFM25 is attributed to higher porosity and skin defects observed in the FE-SEM images. Based on these data, most of the experiments studying the effect of design and operating parameters on humidifier performance were done using modules made from HFM27. The results from humidity experiments are discussed later in detail in Section 4.6 – 4.8.

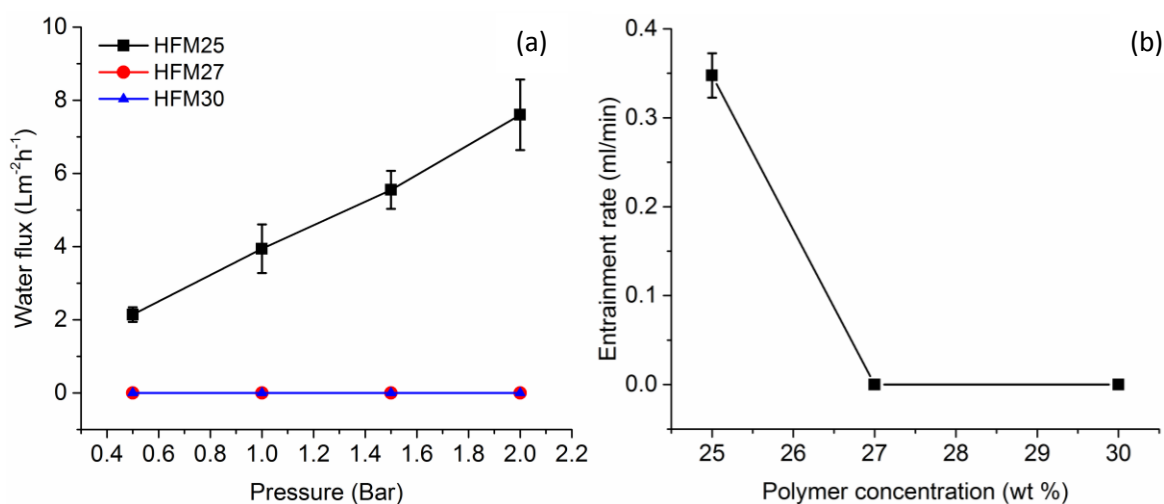


Fig. 4.6. (a) Water flux and (b) Entrainment rate for membranes made with different polymer concentration in the dope.

4.4.6. Humidifier performance: Effects of air flow rate and membrane type

The performances of humidifier modules built using HFM25, HFM27, and HFM30 membranes are shown in Fig. 4.7(a-d). Experimental data for normalized outlet air temperature ($T_{a,out}/T_{a,in}$) and normalized absolute humidity of outlet air ($\omega_{a,out}/\omega_{a,in}$) as a function of air flow rate are presented in Figs. 4.7a and 4.7b. For all three modules, the outlet air temperature and humidity were observed to decrease with increasing air flow rate. This is a consequence of decrease in residence time of air in the humidifier with increasing air flow rate. Also, for a given flow rate, the outlet air temperature decreased with increase in polymer concentration of the dope that was used to prepare the hollow fibers. As discussed in the earlier sections, increasing polymer concentration of spinning dope resulted in decreasing porosity and increasing skin fraction, which consequently leads to higher membrane resistance to heat and mass transfer and hence lower air outlet temperature and humidity. This however does not imply that having higher porosity is better for gas humidification. As was seen in the entrainment tests in Fig. 4.6b, HFM25 suffered from liquid water entrainment which is unacceptable in applications like PEM fuel cells and respiratory gases. Therefore, among the three polymer concentrations studied here, we consider HFM27 as optimal since it prevents entrainment of liquid water while still providing enough humidification. Figs. 4.7c and 4.7d show the thermal and humidity effectiveness factors, respectively. These are also seen to decrease with increasing air flow rate and increasing polymer concentration of the dope due to the reasons discussed above.

Fig. 4.7. also shows the model fits with experimental data along with the values of Pearson's correlation coefficients (r , calculated from Eq. (43)). The overall heat transfer coefficients were calibrated for experimental data points corresponding to 5 L/min of air flow rate for each membrane type. The fitted values of overall heat transfer coefficient were found to decrease in the order HFM25>HFM27>HFM30. This decrease is expected to arise from the difference in the skin microstructure of the HFMs. Similar to diffusion coefficient, the overall heat transfer coefficient also reduces for membranes with lower porosity and a high fraction of skin thus confirming the role of microstructure in heat transport. Further, the overall heat transfer coefficient for all HFMs was seen to increase slightly and linearly with air flow rate (see Fig. 4.8.).

This is likely due to the contribution of tube side heat transfer coefficient on the overall heat transfer coefficient. The tube side heat transfer coefficient increases with increase in air flow rate as per known correlations.

$$r = \frac{\sum_{i=1}^n (X_i - \bar{X})(Y_i - \bar{Y})}{\sqrt{\sum_{i=1}^n (X_i - \bar{X})^2} \sqrt{\sum_{i=1}^n (Y_i - \bar{Y})^2}} \dots\dots\dots(43)$$

Where, X_i is model value and Y_i is experimental value indexed with i , \bar{X} and \bar{Y} are the sample mean values, n is the sample size (4 in this study).

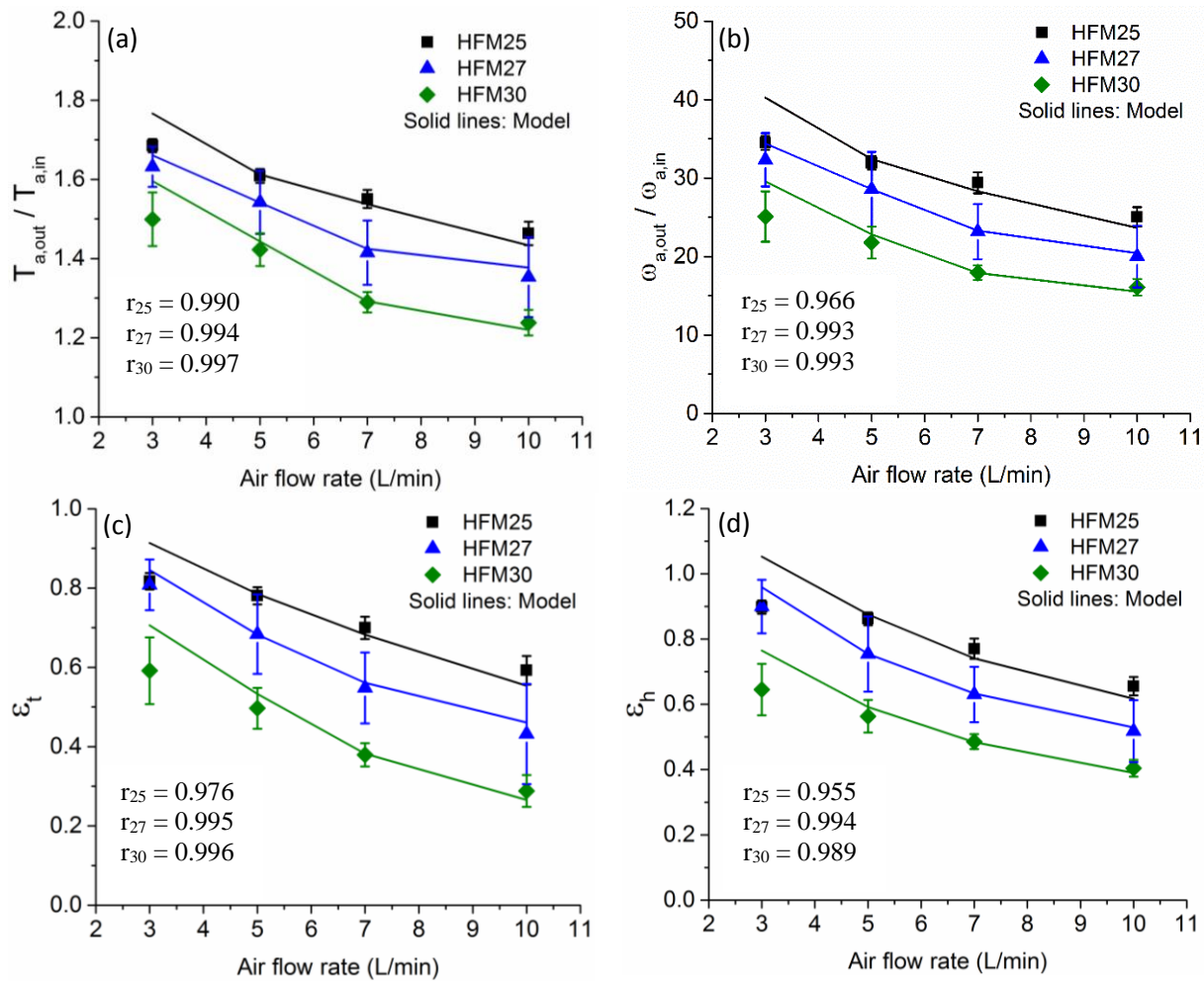


Fig. 4.7. (a) Air outlet temperature, (b) Absolute humidity of outlet air, (c) Thermal effectiveness factor, and (d) Humidity effectiveness factor. Solid lines through the data are model fits. The Pearson's correlation coefficients (r_{25} , r_{27} and r_{30}) close to 1 suggests a positive correlation between model and experimental results.

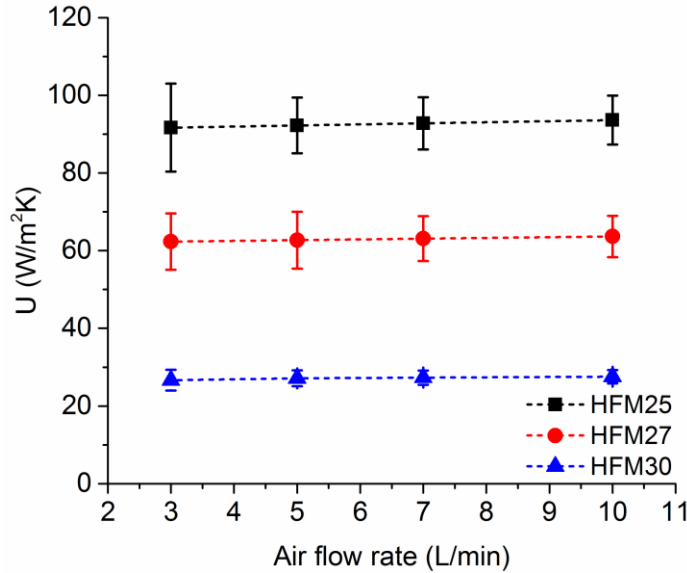


Fig. 4.8. Overall heat transfer coefficient variation with air flow rate for different HFMs. The error bars represent 1 standard deviation from the mean values.

4.4.7. Humidifier performance: Effects of water temperature and water flow rate

Water on the shell side is the source of heat and humidity for the dry air entering the humidifier. It is therefore important to check the effects of inlet temperature and inlet flow rate of water on humidification performance. Figures 9(a,b) show the experimental results for varying water temperatures during humidity experiments conducted on PS27-N30-L15 modules. The outlet air temperature and absolute humidity increases with increase in water temperature and decreases with increase in air flow rate. Fig. 4.9c shows that the thermal effectiveness increases with increasing water temperature. Although an increase in water temperature will increase the denominator in Eq. (38) i.e. $(T_{w,in} - T_{a,in})$, the greater increase in air temperature by virtue of larger thermal gradients causes the thermal effectiveness to increase. On the contrary, the humidity effectiveness shown in Fig. 4.9d decreases with increasing water temperature. This is because of the coupled nature of heat and mass transfer. As water temperature increases, the simultaneous increase in air temperature increases its saturation vapor pressure and hence increases the equilibrium partial pressure of water at the membrane-air interface (see Eq. (16)) thereby causing increased transport of moisture into the air. However, at the same time, the equivalent humidity increases on the shell side based on Eq. (32). The result is that the net amount of vapor added in the air stream is lower than the overall increase in vapor content on the shell side and hence the humidity effectiveness factor decreases. It must be noted that the performance parameters also depend on the air inlet conditions of temperature and absolute

humidity. Therefore, a change in the air inlet conditions would also change the effectiveness. In this study, the change in air inlet conditions at different water temperatures was not significant enough to have caused a dramatic change in thermal or humidity effectiveness.

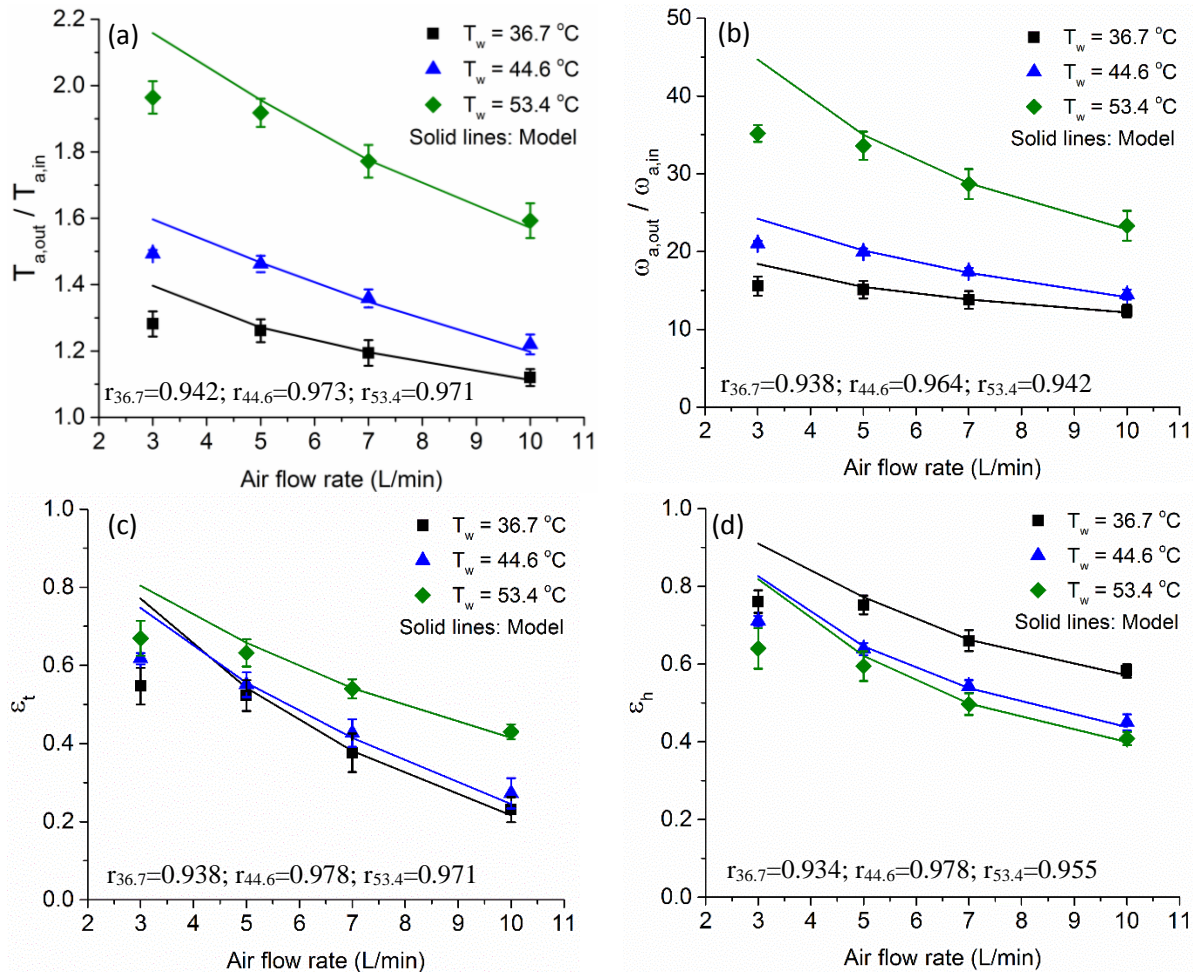


Fig. 4.9. (a) Air outlet temperature, (b) Absolute humidity of outlet air, (c) Thermal effectiveness factor and (d) Humidity effectiveness factor measured on PS27-N30-L15 modules for different water inlet temperatures. Lines through the data are model fits. The Pearson's correlation coefficient (r) greater than 0.9 suggests an excellent positive correlation between model and experimental results.

Fig. 4.10(a-d) shows experimental data and model fits for different water flow rates on the shell side. In Figs. 4.10a and 4.10b, the outlet air temperature and absolute humidity are seen to increase with increasing water flow rate. This is expected because of the higher average shell side temperature (i.e. reducing the ΔT_w on shell side), and to a smaller extent because of higher thermal flux caused by increasing the overall heat transfer coefficient. The higher outlet air temperature increases the saturation vapor pressure thereby allowing for an increase in

transport of moisture into the air. It is worth noting that increasing the water flow rate from 840 ml/min to 1220 ml/min causes only a minor increase in outlet air temperature and absolute humidity. This is because beyond a certain water flow rate, the heat transfer is limited solely by the residence time of air in the tubes.

Figures 4.10c and 4.10d show the thermal and humidity effectiveness factors respectively for different water flow rates. Interestingly, the effectiveness parameters do not show a significant improvement with increase in water flow rate. This is because any increase in air temperature with increase in water flow rate is nearly compensated by the increase in average shell side temperature. Similarly, any increase in air humidity is compensated by the increase in shell side equivalent humidity, hence resulting in similar humidification effectiveness.

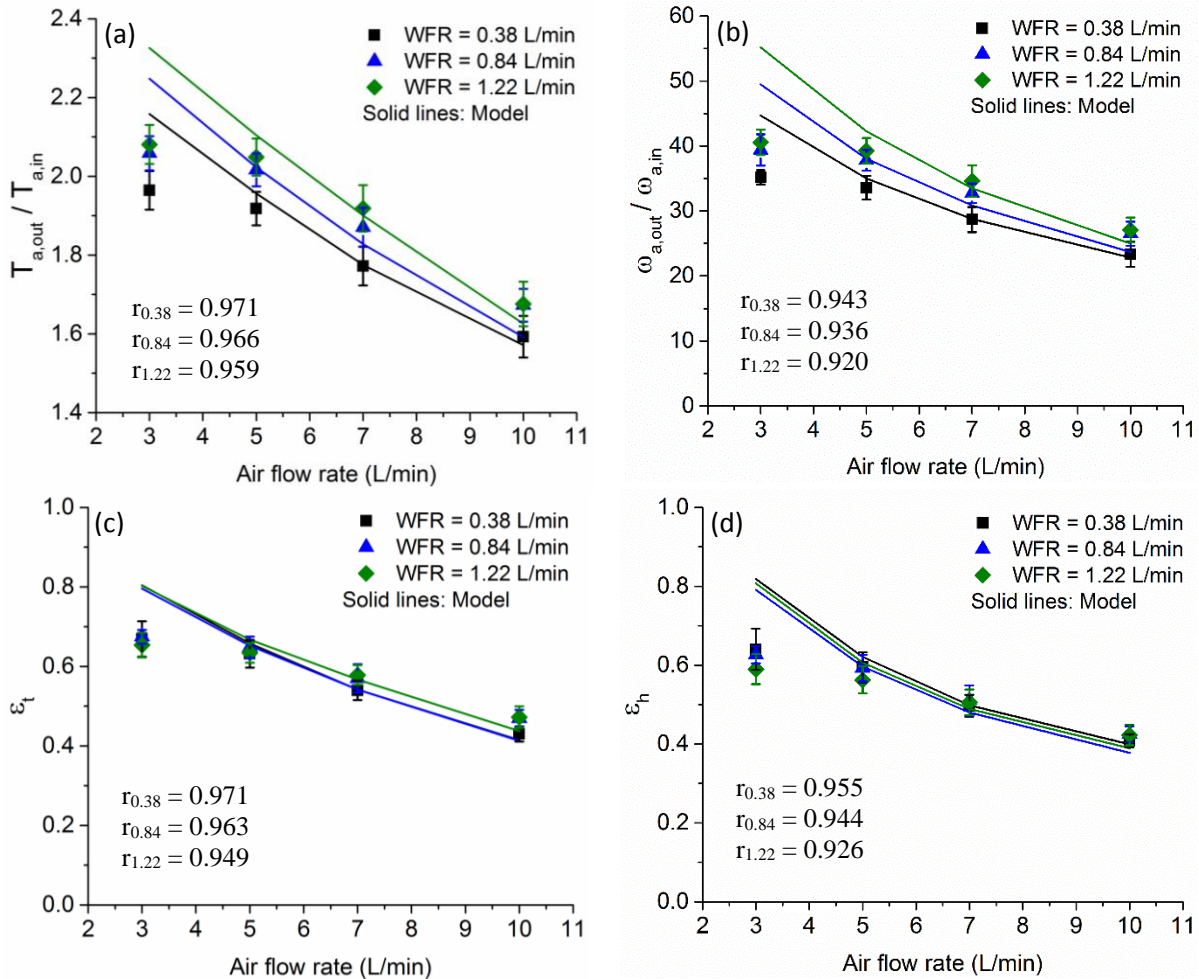


Fig. 4.10. (a) Air outlet temperature, (b) Absolute humidity of outlet air, (c) Thermal effectiveness factor and (d) Humidity effectiveness factor measured on PS27-N30-L15 modules for different water inlet flow

rates. Lines through the data are model fits. The Pearson's correlation coefficient (r) greater than 0.9 suggests an excellent positive correlation between model and experimental results.

The values of overall heat transfer coefficient obtained by fitting the model to experimental data for different water inlet temperatures is shown in Fig. 4.11. The heat transfer coefficient is expected to be independent of the inlet water temperature. Indeed it is seen that the values of U are similar for $T_w = 36.7$ & 44.6 °C. However, the slight increase in case of $T_w = 53.4$ °C is likely a manifestation of uncertainty of ± 1 °C in water temperature measurement. This is confirmed by the overlapping error bars showing 1 standard deviation from the mean values. The variation of U with air flow rate is as discussed earlier.

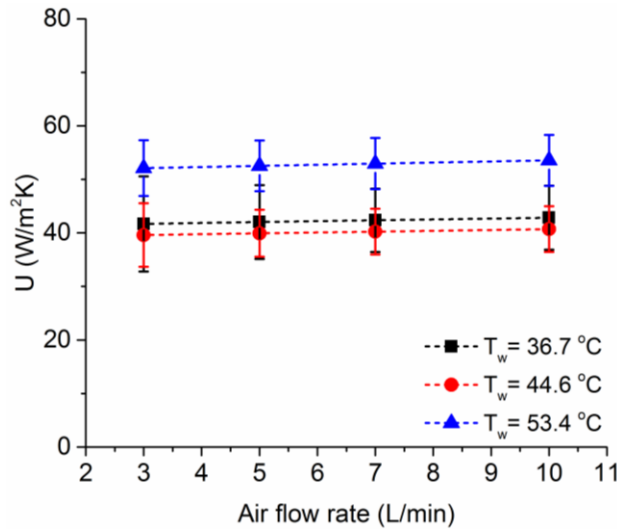
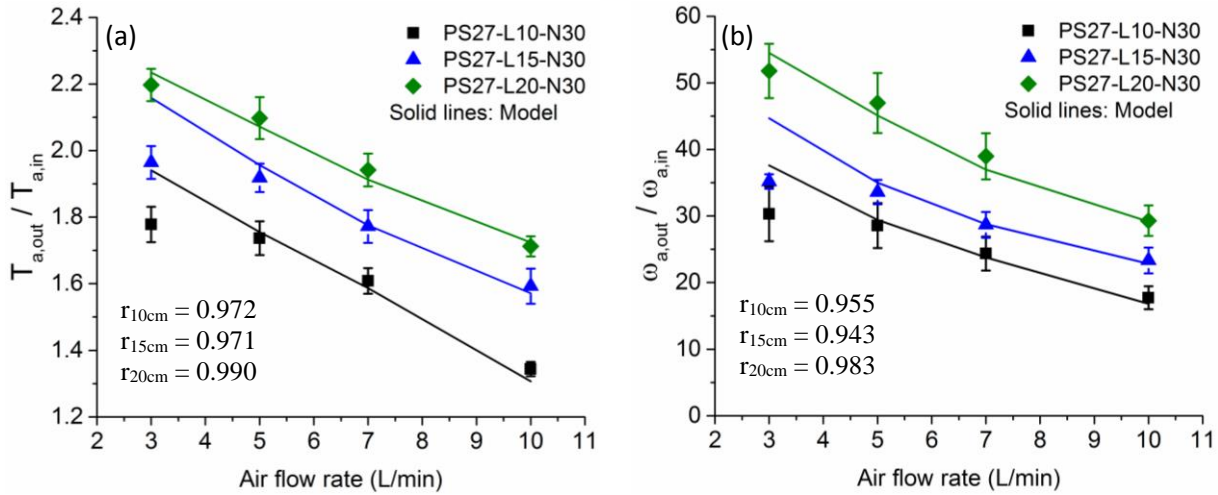


Fig. 4.11. Overall heat transfer coefficient variation with air flow rate for different inlet water temperatures in HFM27 test module. The error bars represent 1 standard deviation from the mean values.

4.4.8. Effect of tube length and tube number

When it comes to designing the humidifier for a particular application, tube length and tube number play a critical role by virtue of determining the available surface area and the residence time that the dry air gets for humidification[23]. In Figs. 4.12(a-d) and 4.13(a-d), we show the experimental data and the corresponding model fits for varying tube lengths and tube numbers respectively. As expected, in both cases the normalized air temperature and absolute humidity increased with increasing available surface area i.e. by increasing the tube length or by increasing the tube number. Increasing the tube number from 10 to 60 increased the available surface area by six folds, whereas increasing the tube length from 10 cm to 20 cm increased the surface area by two folds. One would therefore expect higher normalized outlet air temperature for the PS27-

L15-N60 compared to PS27-L20-N30. This is however not observed because, for the experimental conditions investigated here, it turns out that $0.04(RePr \frac{d_{id}}{H})^{2/3} \ll 1$ and $0.04(ReSc \frac{d_{id}}{H})^{2/3} \ll 1$ so that the convective heat and mass transfer coefficient scale as $h_t, K_t \sim (constant + \frac{1}{NH})$ (see Eq. (25)). Therefore, when tube number (N) increases from 10 to 60, the percentage decrease in convective coefficients is ~ 3 folds higher in comparison to when the tube length (H) increases from 10 cm to 20 cm. In either case, the residence time (t_R) increases due to increase in membrane surface area. Consequently, $U \times t_R|_{PS27-L20-N30} > U \times t_R|_{PS27-L15-N60}$ at all air flow rates. For instance, at an air flow rate of 5 L/min, $U \times t_R|_{PS27-L20-N30} = 0.962 J/m^2 K$ whereas $U \times t_R|_{PS27-L15-N60} = 0.718 J/m^2 K$. Hence, the corresponding increase in outlet gas temperature and humidity is higher in the case when the tube length is increased than when the number is increased.



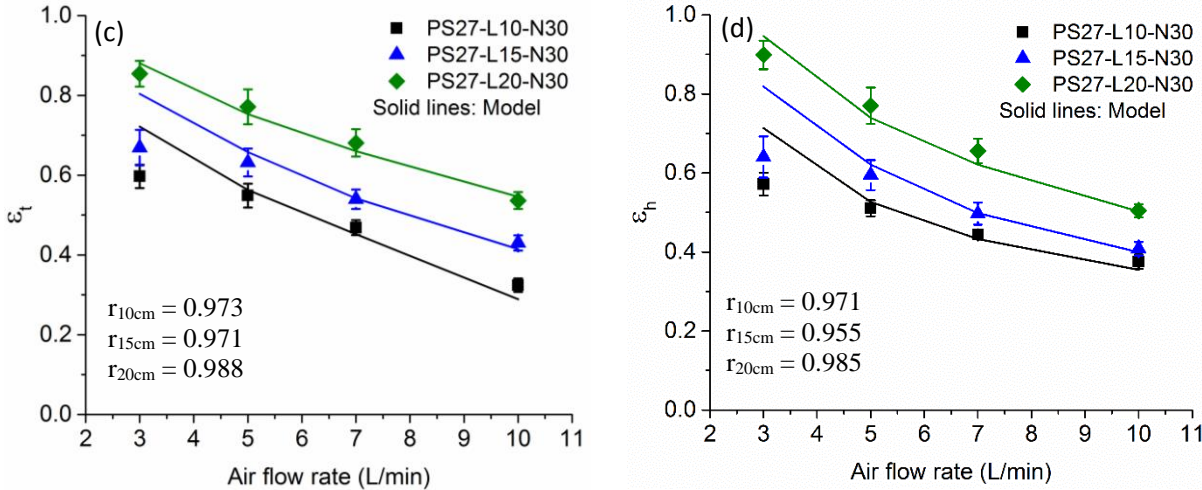


Fig. 4.12. (a) Air outlet temperature, (b) Absolute humidity of outlet air, (c) Thermal effectiveness factor and (d) Humidity effectiveness factor for modules having different tube lengths. Lines through the data are model fits. The Pearson's correlation coefficient (r) greater than 0.9 suggests an excellent positive correlation between model and experimental results.

The corresponding thermal and humidity effectiveness factors in both cases also follow similar trends and are seen to increase with increasing surface area (Fig. 4.12(c, d) and 4.13(c, d)). Increasing the surface area allows for a prolonged residence time of air inside the module to exchange heat and mass, which results in higher thermal and humidity effectiveness. An interesting and unusual observation is made for PS27-L15-N10 modules having 10 number of tubes (Fig. 4.13.). In this case, the thermal effectiveness decreases as expected with flow rate until it reaches a flow rate of 7 L/min beyond which the thermal effectiveness factor is seen to increase sharply. This is coupled with a sharp decrease in humidity effectiveness factor beyond air flow rate of 7 L/min. While the decrease in humidity effectiveness factor can be attributed to the decrease in residence time of air with increase in flow rate, the same argument does not explain the increase in thermal effectiveness factor. One possible explanation is that for the small tube number of 10, a high flow rate of 10 L/min causes the membrane to dry out faster than its capacity to transport vapor across. Hence at these flow rates, the membrane pores are dry and possibly partially filled with air instead of water. Essentially, the water concentration in the membrane reduces with increasing air flow rate due to drying of the membrane. This leads to a decrease in outlet air humidity. Additionally, this reduces the latent heat loss from the shell side which leads to increasing the heat content on the shell side. This increasing heat content on shell

side leads to increasing air temperature with increasing air flow rate, and hence the higher thermal effectiveness factor.

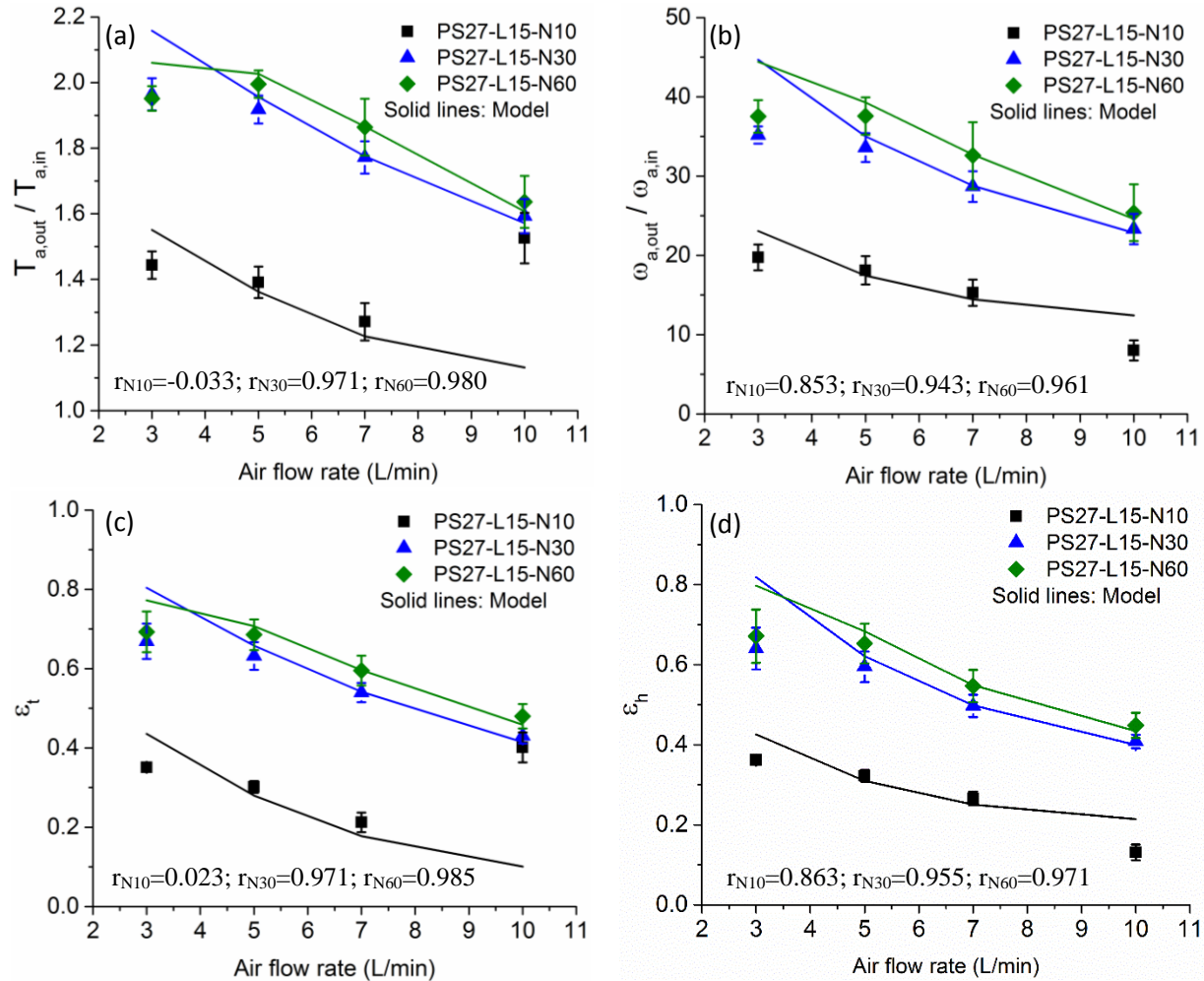


Fig. 4.13. (a) Air outlet temperature, (b) Absolute humidity of outlet air, (c) Thermal effectiveness factor and (d) Humidity effectiveness factor for modules having different tube numbers. Lines through the data are model fits. The Pearson's correlation coefficient (r) greater than 0.9 suggests an excellent positive correlation between model and experimental results for $N=30$ and $N=60$. However, for $N=10$, a good correlation could not be obtained due to the anomalous behaviour observed at AFR=10 L/min (see text).

The effects of varying tube number and tube length can be combined into a single parameter namely, membrane area. Figure 4.14. illustrates the effect of increasing membrane area (by increasing either tube length or tube number) on thermal/humidity effectiveness factor. The graph is presented for the reference case of AFR = 5 L/min for HFM27. As can be seen in Fig. 4.14., thermal and humidity effectiveness factors of the humidifier increase rapidly initially with increasing membrane area. However, the effects of the two parameters differ at high membrane

area. While increasing tube length beyond this membrane area results in an increase in effectiveness factor, an increase in tube number beyond this limiting area results in decreasing the effectiveness factor. This is because of the reasons discussed earlier for varying tube length and tube number. Till the bifurcation point, the reduction in U due to increase in tube number is compensated by the increase in residence time. However, beyond the bifurcation point, this compensation is not warranted, hence resulting in decreasing the effectiveness. In case of increasing tube length, such counter-effect is likely to be observed at $H \geq 60 \text{ cm}$ when the convective coefficients reduce significantly. Hence, for $H = 30 \text{ cm}$, the decrease in U is still compensated by increasing residence time which results in further increase in effectiveness beyond the bifurcation point. In summary, membrane area is not the only important parameter that decides effectiveness factor; the length and diameter both play a role in deciding ε_t .

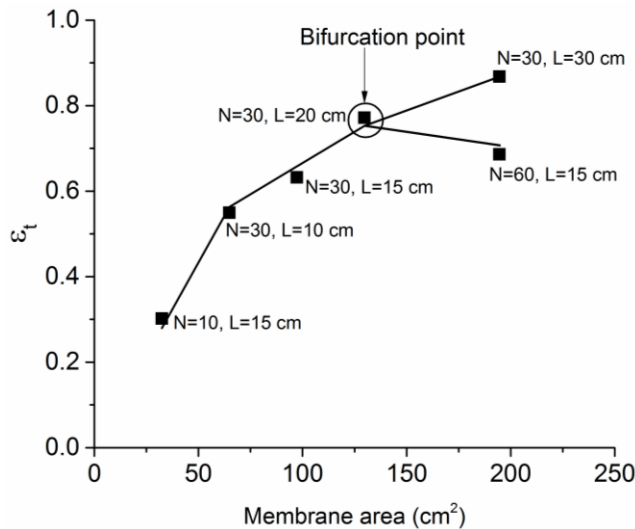


Fig. 4.14. Effect of membrane area on thermal effectiveness. The solid line and data point for $N=30$, $L=30 \text{ cm}$ are model fits. The humidity effectiveness factor also follows a similar trend.

Another perspective for choosing membrane area and desired performance is driven by cost. In Fig. 4.14., the cost of membrane keeps increasing with increasing membrane area. Thus it must be kept in mind while designing membrane systems, to establish a trade-off between performance expectations and cost especially when the performance gains are marginal beyond a specific membrane area.

4.4.9. Comparison of humidifier performance with literature

Table 4.7 compares the performance of our humidifier with different types of humidifiers published in the literature. Most of the earlier work does not report thermal performance of humidifiers, hence the comparison of thermal effectiveness is not possible. However, comparison of moisture transfer performance between porous membrane humidifiers reported in earlier work and present work is possible on the basis of relative humidity of outlet gas. In order to do a quantitative comparison with literature data, the performance of our humidifier was extrapolated to smaller or larger membrane areas using the model. Given the reasonable comparison between experimental data and model predictions shown in Figs. 4.10. - 4.13., such an extrapolation is justified. For a comparable membrane area of 25 cm², our humidifier performance is better than the Nafion flat sheet based membrane humidifier reported by Park et al.[9]. This is primarily because the diffusion coefficients of our porous membranes are much higher than typical diffusion coefficients of a Nafion membrane ($2 - 5 \times 10^{-10}$ m²/s). A similar comparison for a membrane area of 1517 cm² with those reported by Chen et al.[41] for Nafion hollow fiber membrane also suggests that our humidifier performance is better. Further, the performance of our humidifier also compares favourably over Nafion based hollow fiber membranes and bubble humidifiers as well, both in terms of thermal as well as vapor transfer effectiveness. The observed improved performance of porous membrane-based humidifiers over dense membrane-based humidifiers is in agreement with literature reports which were summarized in Section 1. Yet another comparison of our humidifier performance with PES and PSF flat sheet membrane-based humidifiers reported by Samimi et al.[21] for the same membrane area of 57 cm² also suggests that our humidifier performance is better. While the reasons for this observation are not entirely clear since PES and PSF flat sheet membrane are also porous, similar to our HFMs, it may be possible that there are subtle differences in the membrane microstructures. In general, improvements in humidifier performance results in an advantageous reduction in parasitic power loss (typically pumping and heating load) in operation of these systems for any desired outlet gas relative humidity.

Table 4.7: Comparison of humidifier performance between this study and the literature.

Humidifier type	Membrane area or Interfacial area (cm ²)	Liquid flow rate (L/min)	Air flow rate (L/min)	Liquid inlet temp. (°C)	Air inlet temp. (°C)	Outlet air temp. (°C)	Outlet air RH (%)	Reference
HFM25 Hollow fiber	70.23	0.38	5	57.3	RT	51.8	~100	This study (experiment)
HFM27 Hollow fiber	73.62	0.38	5	57.5	RT	49.5	~99	This study (experiment)
HFM30 Hollow fiber	102.87	0.38	5	56.0	RT	43.1	~99	This study (experiment)
HFM27 Hollow fiber	25	0.38	5	60	RT	33.4	99	This study (model fits)
HFM27 Hollow fiber	57	0.38	3	25	RT	24	100	This study (model fits)
HFM27 Hollow fiber	1517	0.38	10	19	26	19	100	This study (model fits)
Nafion™ 112 Flat sheet	25	NA	5	60	RT	NA	39.4	[9]
Nafion™ 117 Flat sheet	25	NA	5	60	RT	NA	9.3	[9]
Nafion™ Hollow fiber	1517	NA	10	19	26	NA	~89	[41]
PES Hollow fiber	NA	NA	3	60	RT	30.9	62.4	[10]
PES Flat sheet	56.76	NA	3	25	RT	NA	~68	[21]
PSF Flat sheet	56.76	NA	3	25	RT	NA	~70	[21]
Bubble column humidifier	NA	N/A	5	60	RT	36.6	95	[42]

NA: Not available; N/A: Not applicable; RT: Room temperature; PES: Polyethersulfone; PSF: Polysulfone

4.5. Conclusions

A detailed experimental study of water-to-air humidification using polysulfone-based asymmetric hollow fiber membrane modules was conducted. Based on judiciously optimized process parameters, hollow fiber membranes (HFM25, HFM27, and HFM30) having different asymmetric microstructures were spun from dopes of three different polymer concentrations using a dry-wet phase inversion process. Rigorous microstructural characterization of these membranes using FE-SEM, water flux test, entrainment test, bubble point measurement, pore

size distribution measurement and gravimetric measurement of porosity, suggests that the porosity and pore density decrease while the total skin fraction increases with increasing polymer concentration of the spin dope. As a result, HFM25 membranes showed water entrainment at ambient pressure and water flux at higher transmembrane pressures whereas HFM27 and HFM30 membranes showed no entrainment or water flux. The microstructure also plays an important role in determining the heat and vapor transfer across the membrane thickness. A rigorous methodology was proposed to estimate the effective diffusion coefficient of moisture through the asymmetric membranes by quantifying the macrovoidage and macro-pore porosity using image processing, gravimetric measurements and pore size distribution analyses by effectively invoking resistance-in-series approach. The model predicts that vapor transfer through asymmetric membranes is limited by both diffusion through the skin and bulk of the hollow fiber membrane, and hence the efficacy of humidification decreases with increasing skin fraction and decreasing bulk porosity. Similarly, the thermal effectiveness factor was observed to decrease with increasing skin fraction and decreasing bulk porosity. Although the difference in thermal effectiveness might also arise due to different tube diameters for each polymer concentration (which would affect the heat transfer coefficient), it was seen that HFM25 and HFM27 membranes which had similar tube IDs ($\approx 500 \mu\text{m}$) had different thermal effectiveness thereby confirming the role of microstructure in heat transport. In general, it was found that humidification of air decreased with increasing air flow rate and increased with increasing water flow rate, water temperature, membrane length and number of tubes. Overall, our model predictions backed with our experimental data show that asymmetric hollow fiber polysulfone membranes (HFM27) of adequate membrane area and having a defect-free skin thickness of $200 \text{ nm} < t_{\text{skin}} < 400 \text{ nm}$ and total bulk porosity of $\sim 52 \%$ gave excellent humidification performance measured in terms of thermal and humidity effectiveness factors, or equivalently measured in terms of relative humidity of outlet air ($75 \% \leq RH \leq 100 \%$). While, this prediction is specific to HFM27 membranes, such predictions can be extended to other types of membranes in future.

A microscopic mathematical model incorporating the effects of skin and porous matrix resistances inside the membrane was also presented in this work. The model accounts for

appropriate equilibrium conditions at the membrane-gas interface along with heat and mass transport. The experimental results and model predictions ascertain that heat transport and mass transport are intricately coupled in the membrane humidification process. The model can aid in scale up or scale down of humidifiers by providing the users with specific values of different material, geometric and flow parameters for any desired application.

Nomenclature

a	Air
A	Area (m ²)
AFR	Air flow rate (L/min)
C_L	Concentration of water or water vapor in the membrane at the membrane-gas interface (mol/m ³)
C_{max}^{liq}	Maximum concentration of liquid water in the membrane (mol/m ³)
C_{max}^{vap}	Maximum concentration of water vapor in the membrane (mol/m ³)
C_{pa}	Specific heat of air (J/kg K)
C_{pv}	Specific heat of water vapor (J/kg K)
C_{pw}	Specific heat of water (J/kg K)
d_{id}	Tube inner diameter (mm)
d_{od}	Tube outer diameter (m)
\bar{d}_p	Mean pore diameter (m)
D_S	Shell diameter (m)
D_{wa}	Diffusion coefficient of water in air (m ² /s)
D_p	Diffusion coefficient of liquid water in polymer (m ² /s)
D_{pv}	Diffusion coefficient of water vapor in polymer (m ² /s)
D_w	Self-diffusion coefficient of water (m ² /s)
D_{eff}	Effective diffusion coefficient of water in membrane (m ² /s)
h_t	Tube side heat transfer coefficient (W/m ² K)
h_s	Shell side heat transfer coefficient (W/m ² K)
L	Membrane thickness (m)
J	Flux (m ³ /m ² s) or (L/m ² h)
K_t	Tube side mass transfer coefficient (m/s)
k_a	Thermal conductivity of air (W/m K)
k_w	Thermal conductivity of water (W/m K)
k_p	Thermal conductivity of polymer (W/m K)
k_{eff}	Effective thermal conductivity of membrane (W/m K)
l	Pore length (m)
H	Tube length (m)
\dot{m}_a	Mass flow rate of air (kg/s)
\dot{m}_w	Mass flow rate of water (kg/s)
M_w	Molecular weight of water (kg/mol)

mv	Macrovoid
n	Number density of pores (# /m ²)
N	Number of tubes
ΔP	Trans-membrane pressure (Pa)
P_v	Vapor pressure of water (Pa)
$P_{v,out}$	Outlet vapor pressure of water in air (Pa)
$P_{v,sat}$	Saturation vapor pressure of water at T_w (Pa)
P_{eq}	Equilibrium vapor pressure of water at the membrane-gas interface (Pa)
r_p	Pore radius (m)
\bar{r}_p	Mean pore radius (m)
R	Universal gas constant (J/mol K)
$R_{skin,shell}$	Resistance of shell side skin (s/m)
$R_{skin,tube}$	Resistance of tube side skin (s/m)
R_{bulk}	Resistance of porous membrane matrix (s/m)
R_{total}	Total membrane resistance (s/m)
$T_{a,in}$	Inlet air temperature (K)
T_w	Water-bath temperature (K)
$T_{w,in}$	Inlet water temperature (K)
$T_{a,out}$	Outlet air temperature (K)
$T_{w,out}$	Outlet water temperature (K)
T_m	Membrane temperature at membrane-gas interface (K)
U	Overall heat transfer coefficient (W/m ² K)
v	Vapor
v_a	Velocity of air through the tubes (m/s)
V_m	Volume of membrane (m ³)
V_p	Volume of polymer (m ³)
w	Water
W_m	Weight of fiber (m ³)
WFR	Water flow rate (L/min)

Greek letters

η	Dynamic viscosity (Pa.s)
γ	Surface tension (N/m)
θ	Porosity
λ_{vap}	Latent heat of vaporization (J/kg)
ρ	Density (kg/m ³)
ω	Mixing ratio or absolute humidity (g/kg)
ε	Effectiveness

Appendix A

Spinning of hollow fibers:

The dope reservoir filled with spinning dope was connected to a spinneret. The dope reservoir was pressurized with air for pushing dope through the spinneret's annulus. The hollow fiber membrane formation starts with the dope solution and the bore fluid (distilled water) extruding simultaneously through a tube-in-orifice arrangement. The fiber extruded from spinneret then passes through an air gap and enters a coagulation bath or precipitation tank where the solvent is exchanged with a non-solvent (filtered tap water) and the polymer precipitates in the shape of hollow fibers. The hollow fibers are then collected over a spool at a rate that enables smooth wind-up without breakage. The schematic representation of the phase inversion process is shown in Fig. 4.A1.

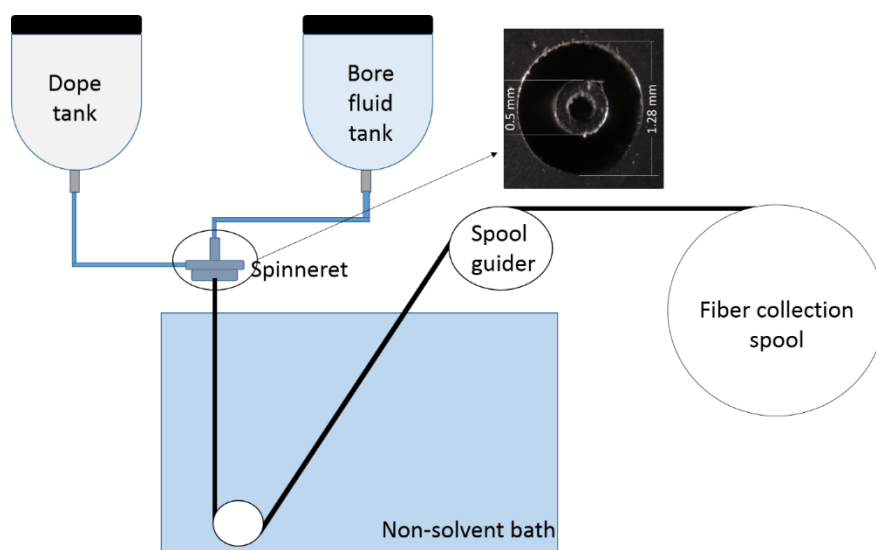


Fig. 4.A1. Schematic representation of phase inversion hollow fiber spinning setup and microscope image of the annular spinneret.

Bubble point test:

HFM modules were kept immersed in DI water for 24 h before the test. These modules with pre-wetted fibers were then subjected to increasing air pressure on the tube side until a continuous

stream of bubbles was observed through a water column placed outside the module. The schematic representation of the bubble point setup is shown in Fig. 4.A2.

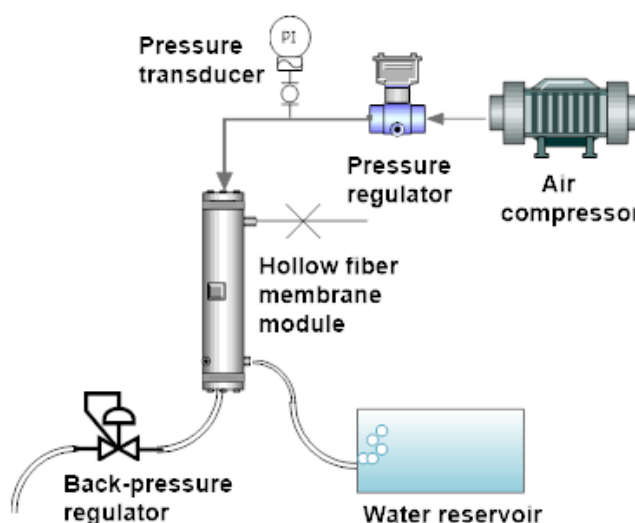


Fig. 4.A2. Schematic representation of Bubble Point Setup

Pore size distribution using Liquid-liquid displacement:

Liquid-liquid displacement was carried out with water-saturated iso-butyl alcohol (IBA) (surface tension, $\gamma = 0.0019 \text{ N/m}$) displacing water in the water under applied pressure. Hollow fibers inside the module were pre-wetted with water (surface tension, $\gamma = 0.072 \text{ N/m}$) by immersing the module in distilled water for 24 h and then used on the pore size distribution test setup as shown in Fig. 4.A3. Water-saturated IBA was stored in an elevated tank which was connected to the air compressor via pressure regulator having a resolution of 0.01 bar. The IBA was pushed through the tubes at different pressures and the corresponding fluxes were measured from the shell side outlet.

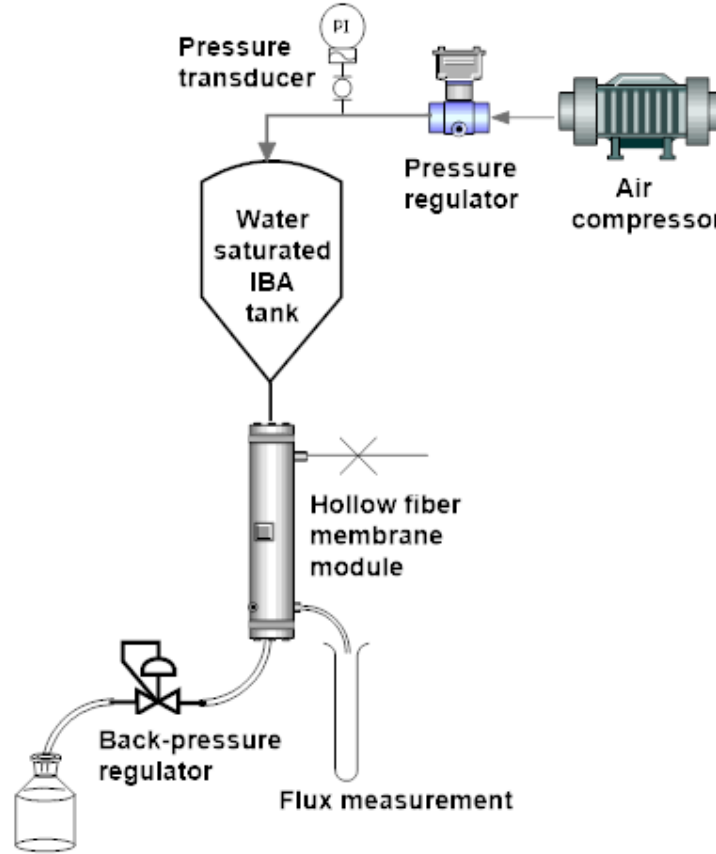


Fig. 4.A3. Schematic representation of pore size distribution setup using liquid-liquid displacement method

Appendix B

Case ii) Humidification by transport of water vapor across the membrane. The following changes were made to the model to obtain the results:

1. In Eqs. (15) and (34) - (42), D_p and D_w are replaced by D_{pv} and D_{wa} respectively. Where, D_{pv} and D_{wa} are the diffusion coefficient of water vapor in dense polysulfone and air respectively.
2. Maximum vapor concentration in the membrane (moles of water vapor per unit volume of membrane) at the membrane-water interface is estimated using Eq. (B1).

$$C_{max}^{vap} = \frac{\theta P_{v,sat}}{RT_w} \dots \dots \dots (B1)$$

Where, θ is membrane porosity, $P_{v,sat}$ is the saturation vapor pressure at water temperature T_w and R is the gas constant.

The individual resistances and effective diffusivity values for water vapor transport are shown in Table 4.B1. As expected, the membrane resistance is drastically reduced for vapor transport due to much higher water vapor diffusivity values. In contrast to liquid water transport, the vapor transport in general is observed to be limited by skin resistance due to very low skin porosity; the presence of macro-porous bulk imparts negligible resistance to vapor diffusion.

Table 4.B1: Individual resistances and effective diffusion coefficient of water vapor for different HFMs

Membrane type	HFM25	HFM27	HFM30
Domain 1 resistance, R_1 (s/m)	5.57	5.39	5.17
Domain 2 resistance, R_2 (s/m)	6.24	12.39	23.86
Domain 3 resistance, R_3 (s/m)	4.40	NA	NA
$R_{tot,bulk} = R_1 + R_2 + R_3$ (s/m)	16.21	17.78	29.03
$R_{skin,shell}$ (s/m)	7.56	114	161
$R_{skin,tube}$ (s/m)	7.53	113	159
R_{total} (s/m)	31.30	243.78	349
D_{eff} (m ² /s)	5.91×10^{-6}	6.97×10^{-7}	4.04×10^{-7}
% contribution of skin resistance	48.22 %	92.71 %	91.68 %
% contribution of bulk resistance	51.78 %	7.29 %	8.32 %

In Fig. 4.B1a, we compare the normalized gradients obtained from the two approaches for the reference case of HFM27 for different air flow rates and inlet water temperature of 60 °C. Interestingly, the vapor transport suffers larger concentration gradients than for liquid transport despite having few orders higher diffusion coefficients than for liquid water diffusion. This is because the gas phase water concentrations even at saturation are much smaller than in liquid state. Hence, even though vapor fluxes are higher than water fluxes as shown in Fig. 4.B1b, the low water vapor concentration at the membrane-gas interface during vapor transport leads to small gradients for vapor transport in the tubes and hence results in lower outlet gas humidity as shown in Fig. 4.B1d. The heat transport is not affected significantly by vapor transport due to small length scale of membrane thickness over which conduction has to happen as shown in Fig. 4.B1c. The higher gas temperature in case of vapor transport is a consequence of the effect of humidity on specific heat of air. Higher the humidity, higher is the specific heat of air. Hence, raising the temperature of the humid air requires more thermal energy than for dry air stream, thereby limiting the increase in gas temperature.

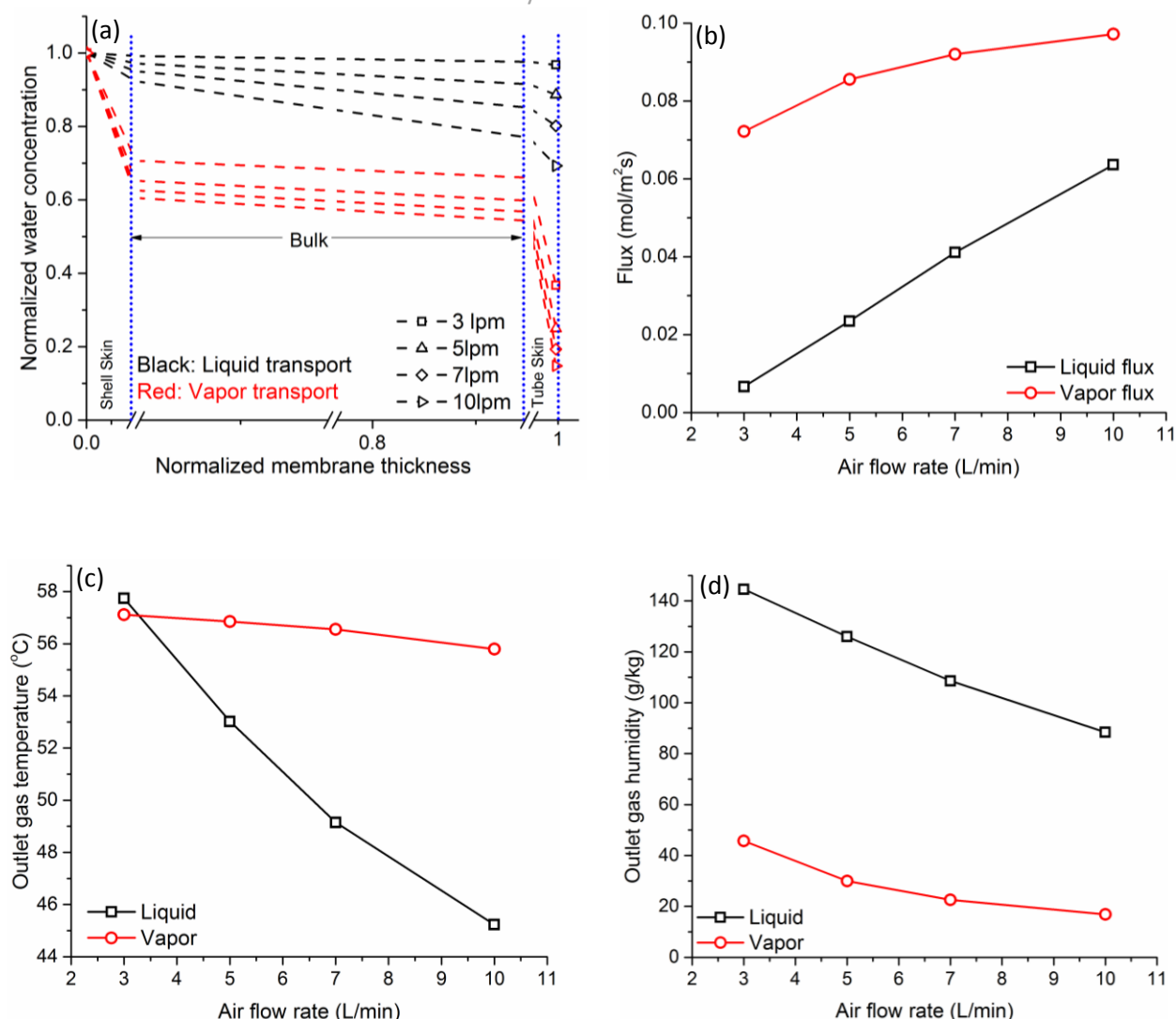


Fig. 4.B1. Comparison of model predictions for the cases of liquid water vs water vapor transport for the reference membrane HFM27 (a) Normalized concentration gradients; (b) flux of liquid water (blue line) vs water vapor (red line); (c) outlet gas temperature and (d) outlet gas humidity in the two cases. The normalization in (a) is done using C_{max}^{liq} for liquid water and using C_{max}^{vap} for water vapor.

Finally, based on the comparison shown above and the experimental results, we conclude that the approach used in this work considering liquid water transport resembles closer to the physical system than the vapor transport approach for modelling water-to-gas humidification through asymmetric membranes.

References

- [1] N. Valentínyi, E. Cséfalvay, P. Mizsey, Modelling of pervaporation: Parameter estimation and model development, Chem. Eng. Res. Des. 91 (2013) 174–183. doi:10.1016/j.cherd.

2012.07.001.

- [2] J.G. Wijmans, R.W. Baker, The solution-diffusion model: a review, *J. Memb. Sci.* 107 (1995) 1–21. doi:10.1016/0376-7388(95)00102-I.
- [3] M. Adachi, T. Navessin, Z. Xie, F.H. Li, S. Tanaka, S. Holdcroft, Thickness dependence of water permeation through proton exchange membranes, *J. Memb. Sci.* 364 (2010) 183–193. doi:10.1016/j.memsci.2010.08.011.
- [4] A. Kusoglu, A.Z. Weber, New Insights into Perfluorinated Sulfonic-Acid Ionomers, *Chem. Rev.* 117 (2017) 987–1104. doi:10.1021/acs.chemrev.6b00159.
- [5] M. Canghai, Development of Polysulfone Asymmetric Membrane Using Pneumatically-Controlled Membrane Casting System and Study of The Effects of Shear Rate and Forced Convection Residence Time on Gas Separation Membranes Performance, (2011).
- [6] T.S.N. Chung, Fabrication of Hollow-Fiber Membranes by Phase Inversion, *Adv. Membr. Technol. Appl.* (2008) 821–839. doi:10.1002/9780470276280.ch31.
- [7] P. Radovanovic, S.W. Thiel, S.T. Hwang, Formation of asymmetric polysulfone membranes by immersion precipitation. Part I. Modelling mass transport during gelation, *J. Memb. Sci.* 65 (1992) 213–229. doi:10.1016/0376-7388(92)87024-R.
- [8] M. Cheryan, *Ultrafiltration and Microfiltration Handbook*, 1998. doi:97-62251.
- [9] S.K. Park, E.A. Cho, I.H. Oh, Characteristics of membrane humidifiers for polymer electrolyte membrane fuel cells, *Korean J. Chem. Eng.* 22 (2005) 877–881. doi:10.1007/BF02705668.
- [10] G. Bakeri, S. Naeimifard, T. Matsuura, A.F. Ismail, A porous polyethersulfone hollow fiber membrane in a gas humidification process, *RSC Adv.* 5 (2015) 14448–14457. doi:10.1039/C4RA14180F.
- [11] J.R. Du, L. Liu, A. Chakma, X. Feng, Using poly(N,N-dimethylaminoethyl methacrylate)/polyacrylonitrile composite membranes for gas dehydration and humidification, *Chem.*

- Eng. Sci. 65 (2010) 4372–4381. doi:10.1016/j.ces.2010.05.005.
- [12] K. Ramya, J. Sreenivas, K.S. Dhathathreyan, Study of a porous membrane humidification method in polymer electrolyte fuel cells, *Int. J. Hydrogen Energy*. 36 (2011) 14866–14872. doi:10.1016/j.ijhydene.2010.12.088.
- [13] M. Yang, S.M. Huang, X. Yang, Experimental investigations of a quasi-counter flow parallel-plate membrane contactor used for air humidification, *Energy Build.* 80 (2014) 640–644. doi:10.1016/j.enbuild.2014.07.058.
- [14] L.Z. Zhang, Coupled heat and mass transfer through asymmetric porous membranes with finger-like macrovoids structure, *Int. J. Heat Mass Transf.* 52 (2009) 751–759. doi:10.1016/j.ijheatmasstransfer.2008.07.029.
- [15] A. Gabelman, S.-T. Hwang, Hollow fiber membrane contactors, *J. Memb. Sci.* 159 (1999) 61–106. doi:10.1016/S0376-7388(99)00040-X.
- [16] W. Piatkiewicz, S. Rosiński, D. Lewińska, J. Bukowski, W. Judycki, Determination of pore size distribution in hollow fibre membranes, *J. Memb. Sci.* 153 (1999) 91–102. doi:10.1016/S0376-7388(98)00243-9.
- [17] G. Capannelli, F. Vigo, S. Munari, Ultrafiltration membranes - characterization methods, *J. Memb. Sci.* 15 (1983) 289–313. doi:10.1016/S0376-7388(00)82305-4.
- [18] H.R. Lohokare, Y.S. Bhole, U.K. Kharul, Effect of support material on ultrafiltration membrane performance, *J. Appl. Polym. Sci.* 99 (2006) 3389–3395. doi:10.1002/app.23039.
- [19] G. Bakeri, A.F. Ismail, M.R. DashtArzhandi, T. Matsuura, Porous PES and PEI hollow fiber membranes in a gas-liquid contacting process-A comparative study, *J. Memb. Sci.* 475 (2015) 57–64. doi:10.1016/j.memsci.2014.09.037.
- [20] M. Khayet, A. Velázquez, J.I. Mengual, Modelling mass transport through a porous partition: Effect of pore size distribution, *J. Non-Equilibrium Thermodyn.* 29 (2004) 279–299. doi:10.1515/JNETDY.2004.055.

- [21] A. Samimi, S.A. Mousavi, A. Moallemzadeh, R. Roostaazad, M. Hesampour, A. Pihlajamäki, M. Mänttari, Preparation and characterization of PES and PSU membrane humidifiers, *J. Memb. Sci.* 383 (2011) 197–205. doi:10.1016/j.memsci.2011.08.043.
- [22] L.Z. Zhang, Mass diffusion in a hydrophobic membrane humidification/dehumidification process: The effects of membrane characteristics, *Sep. Sci. Technol.* 41 (2006) 1565–1582. doi:10.1080/01496390600634723.
- [23] S. Kang, K. Min, S. Yu, Two dimensional dynamic modeling of a shell-and-tube water-to-gas membrane humidifier for proton exchange membrane fuel cell, *Int. J. Hydrogen Energy.* 35 (2010) 1727–1741. doi:10.1016/j.ijhydene.2009.11.105.
- [24] R. Pandey, A. Lele, Modelling of water-to-gas hollow fiber membrane humidifier, *Chem. Eng. Sci.* 192 (2018) 955–971. doi:10.1016/j.ces.2018.08.015.
- [25] L.Z. Zhang, S.M. Huang, Coupled heat and mass transfer in a counter flow hollow fiber membrane module for air humidification, *Int. J. Heat Mass Transf.* 54 (2011) 1055–1063. doi:10.1016/j.ijheatmasstransfer.2010.11.025.
- [26] I.C. Bourg, C.I. Steefel, Molecular dynamics simulations of water structure and diffusion in silica nanopores, *J. Phys. Chem. C.* 116 (2012) 11556–11564. doi:10.1021/jp301299a.
- [27] C.W. Monroe, T. Romero, W. Mérida, M. Eikerling, A vaporization-exchange model for water sorption and flux in Nafion, *J. Memb. Sci.* 324 (2008) 1–6. doi:10.1016/j.memsci.2008.05.080.
- [28] Vaisala, Humidity Conversion Formulas - Calculation formulas for humidity, (2013).
- [29] K.A. Schult and D.R. Paul, Water sorption and transport in a series of polysulfones, *Journal of Polymer Science: Part B: Polymer Physics*, Vol. 34, 2805–2817 (1996).
- [30] T.A. Zawodzinski, M. Neeman, L.O. Sillerud, S. Gottesfeld, Determination of water diffusion coefficients in perfluorosulfonate ionomeric membranes, *J. Phys. Chem.* 95 (1991) 6040–6044. doi:10.1021/j100168a060.

- [31] J.T. Hinatsu, Water Uptake of Perfluorosulfonic Acid Membranes from Liquid Water and Water Vapor, *J. Electrochem. Soc.* 141 (1994) 1493. doi:10.1149/1.2054951.
- [32] R. Pandey, B. Pesala, Heat and Mass Transfer Analysis of a Pot-in-Pot Refrigerator Using Reynolds Flow Model, *J. Therm. Sci. Eng. Appl.* 8 (2016) 031006. doi:10.1115/1.4033010.
- [33] L.-Z. Zhang, Coupled heat and mass transfer in an application-scale cross-flow hollow fiber membrane module for air humidification, *Int. J. Heat Mass Transf.* 55 (2012) 5861–5869. doi:10.1016/j.ijheatmasstransfer.2012.05.083.
- [34] J.H. Perry, Chemical engineers' handbook, *J. Chem. Educ.* 27 (1950) 533. doi:10.1021/ed027p533.1.
- [35] L.Z. Zhang, Total heat recovery : heat and moisture recovery from ventilation air, Nova Science Publishers, Inc, 2008.
- [36] J. Drobny, Specialty Thermoplastics, Springer Publications 2015. doi:10.1007/978-3-662-46419-9.
- [37] M. Holz, S.R. Heil, A. Sacco, Temperature-dependent self-diffusion coefficients of water and six selected molecular liquids for calibration in accurate ¹H NMR PFG measurements, *Phys. Chem. Chem. Phys.* 2 (2000) 4740–4742. doi:10.1039/b005319h.
- [38] J.L. Niu, L.Z. Zhang, Membrane-based Enthalpy Exchanger: Material considerations and clarification of moisture resistance, *J. Memb. Sci.* 189 (2001) 179–191. doi:10.1016/S0376-7388(00)00680-3.
- [39] N. Widjojo, T.S. Chung, Thickness and air gap dependence of macrovoid evolution in phase-inversion asymmetric hollow fiber membranes, *Ind. Eng. Chem. Res.* 45 (2006) 7618–7626. doi:10.1021/ie0606587.
- [40] N. Peng, T.S. Chung, K.Y. Wang, Macrovoid evolution and critical factors to form macrovoid-free hollow fiber membranes, *J. Memb. Sci.* 318 (2008) 363–372. doi:10.1016/j.memsci.2008.02.063.

- [41] D. Chen, W. Li, H. Peng, An experimental study and model validation of a membrane humidifier for PEM fuel cell humidification control, *J. Power Sources*. 180 (2008) 461–467. doi:10.1016/j.jpowsour.2008.02.055.
- [42] G. Vasu, A.K. Tangirala, B. Viswanathan, K.S. Dhathathreyan, Continuous bubble humidification and control of relative humidity of H₂ for a PEMFC system, *Int. J. Hydrogen Energy*. 33 (2008) 4640–4648. doi:10.1016/j.ijhydene.2008.05.051.

Chapter 5

Flow Distribution in Humidifiers Using Flow Simulations

The microscopic transport model presented in chapter 4 was shown to appropriately capture the physics of humidification from asymmetric membranes in the flow regime where the humidifier performance decreased monotonically with increasing air flow rate. The humidifier performance in this regime is limited by the residence time of gas inside the hollow fibers membranes. However, it was observed that the humidifier performance is lower than expected when the air flow was reduced below a specific value despite having larger residence times. Figure 5.1. below provides an illustration of this interesting and counter-intuitive observation. The region of the curve highlighted in green is the monotonic performance curve of the humidifiers which is also predicted by the microscopic transport model. The region highlighted in red is the non-monotonic behavior of humidifier performance, which is not predicted by the microscopic model. In order to arrive at an explanation for the non-monotonic behavior, we hypothesized that in a random tube arrangement (which resembles the case of a real humidifier module), uniform flow distribution of air could be severely compromised i.e., some tubes receive less flow than the others thereby adversely affecting the convective heat and mass transport and residence time in such tubes. Essentially, we hypothesize that a decrease in convective coefficients for heat and mass transport along with non-uniform residence time distribution across the tubes at such low gas flow rates is expected to reduce the humidifier performance.

This chapter aims to check the possibility of flow maldistribution at a low gas flow rate of 1 L/min, by reporting flow simulation studies performed on several 3D CAD models of our humidifier. The 3D model is designed to simulate the flow inside a real humidifier developed with HFM27 membranes having tube ID = 0.5 mm, $N = 30$ (number of tubes) and $L = 20$ cm (length of tubes), wherein the tubes are randomly placed inside the shell. We report here the effect of symmetry in tube arrangement with a cylindrical header design. Additionally, the effect of different header

designs on flow distribution in tubes is also presented. Finally, based on the simulation results, we propose certain design guidelines for minimizing flow maldistribution in shell and tube humidifiers at low gas flow rates.

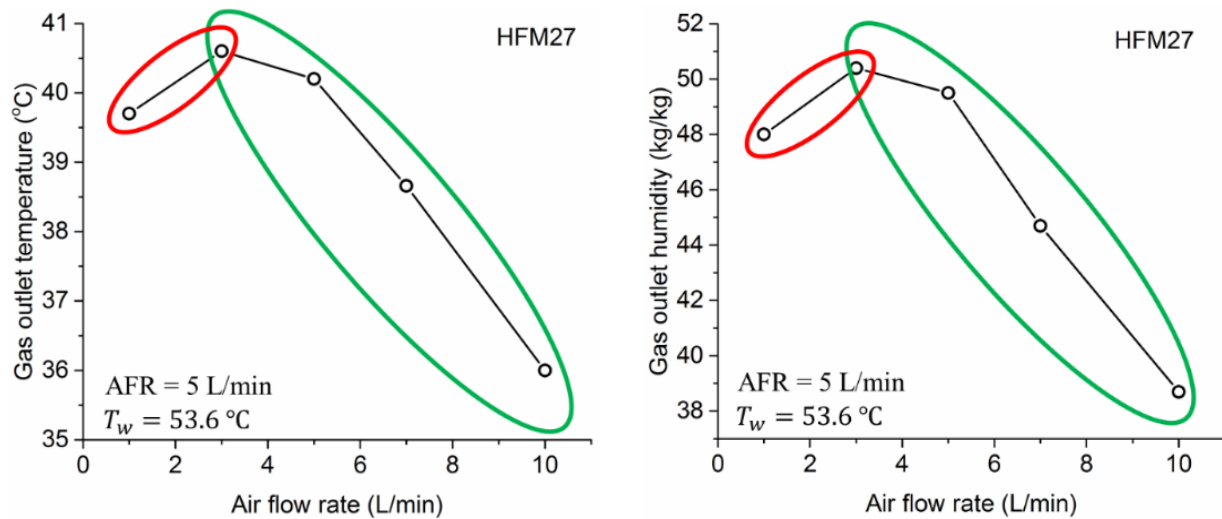


Fig. 5.1. Variation of outlet gas temperature and humidity with air flow rate. The green region is the monotonic region which is captured by the transport model presented in Chapter-4 and the red region corresponds to low humidifier performance which is studied in this chapter.

5.1. Introduction

Computational fluid dynamics is a powerful tool to simulate fluid flow in complex geometries and aids in minimizing the cost of experiments. In an isothermal CFD simulation, Navier Stokes equation and the equation of continuity are solved simultaneously to predict the transport of momentum and mass respectively. Since the nature of flow distribution in a hollow fiber membrane module is expected to affect its performance [1–3], CFD as a tool can be used to simulate flow distribution in a hollow fiber membrane module and provide design guidelines to reduce or eliminate the same.

Park et al. [2] studied the flow distribution in the header (cylindrical and conical) of a hollow fiber membrane module using CFD. They also studied residence time distribution for flow inside the lumen. They concluded that the maldistribution was a consequence of the larger size of the eddy formed in a cylindrical manifold compared to that formed in a conical manifold. The reason for the formation of smaller eddies and hence more uniform flow distribution in a conical manifold was attributed to the smaller drop in radial velocity with increasing distance and narrow flow

path. Zhang et al. [3] studied flow maldistribution in a cross-flow hollow fiber membrane module using CFD. They concluded that the packing fraction affects flow distribution significantly and suggested to have higher packing fraction for uniformity in shell side flow. They also concluded that compared to heat exchangers, flow maldistribution has a greater impact on humidifier efficiencies due to mass exchange. To minimize flow maldistribution, it was suggested to use straight headers for shell side flow without any converging or diverging sections and a higher packing fraction. Zhuang et al. [4] studied the effect of inlet header on the performance of a hollow fiber membrane module and concluded that an evenly distributed tubular arrangement offers a relatively uniform flux distribution in comparison to a random arrangement.

Building on the earlier studies on flow behavior in HFMs, in this work, we report the CFD simulation studies of flow inside hollow fibers and shell to understand its implications on the lower humidifier performance at low gas flow rates. In addition, we have studied the effect of symmetry and header design on flow distribution on the tube side.

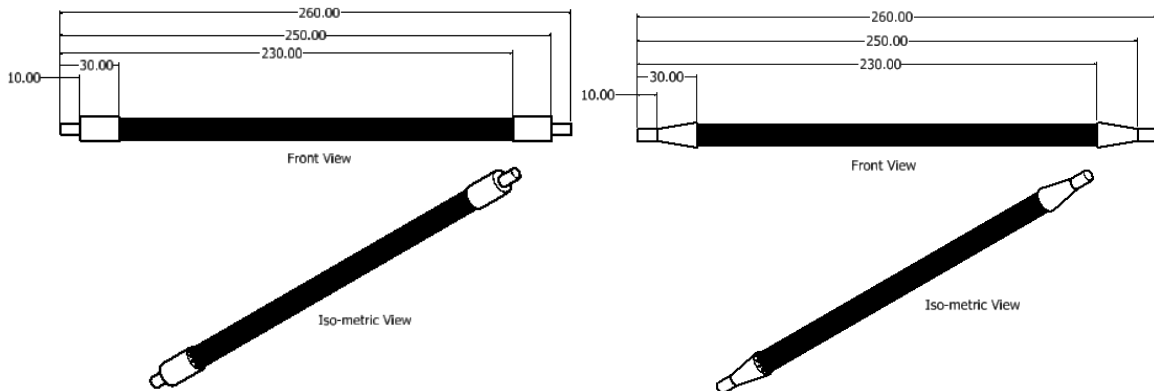
5.2. CAD models

CAD models for humidifiers were built using Autodesk Inventor v18 software. The shell and tube geometries were built for different tube arrangements viz. random, axially symmetric and axially + radially symmetric. While the random tube arrangement is most common in a real humidifier system, realization of axial or axial + radial symmetry in practical systems without spacers or guides is difficult. Still, studying these three geometries can help provide guidelines towards the extent of symmetry desirable for minimizing flow maldistribution. In addition, as suggested by Park et al. [2], we also study the flow distribution with a truncated conical header to verify if the flow maldistribution is indeed reduced. The design parameters are listed in Table 5.1 for the different geometries made.

Table 5.1: Design parameters for different CAD models

Model	Tube length, number, diameter	Tube arrangement	Inlet Header geometry	Outlet header geometry	Port Length, Diameter
Tube_C1	20 cm, 30, 0.5 mm	Random symmetry	2 cm cylinder	2 cm cylinder	1 cm, 0.6 cm
Tube_C2	20 cm, 30, 0.5 mm	Axially symmetric	2 cm cylinder	2 cm cylinder	1 cm, 0.6 cm
Tube_C3	20 cm, 30, 0.5 mm	Axially+Radially Symmetric	2 cm cylinder	2 cm cylinder	1 cm, 0.6 cm
Tube_C4	20 cm, 30, 0.5 mm	Axially+Radially Symmetric	2 cm cone	2 cm cone	1 cm, 0.6 cm
Tube_C5	20 cm, 30, 0.5 mm	Axially+Radially Symmetric	1 cm cone	1 cm cone	1 cm, 0.6 cm
Shell_C1	20 cm, 30, 0.5 mm	Random	-	-	1 cm, 0.5 cm
Shell_C2	20 cm, 30, 0.5 mm	Axially symmetric	-	-	1 cm, 0.5 cm
Shell_C3	20 cm, 30, 0.5 mm	Axially+Radially Symmetric	-	-	1 cm, 0.5 cm

The front and isometric views of the CAD models listed in Table 5.1 for tube side are shown in Fig. 5.2(a-c) and the cross-sections of the different tube arrangements are shown in Fig. 5.3(a-c).



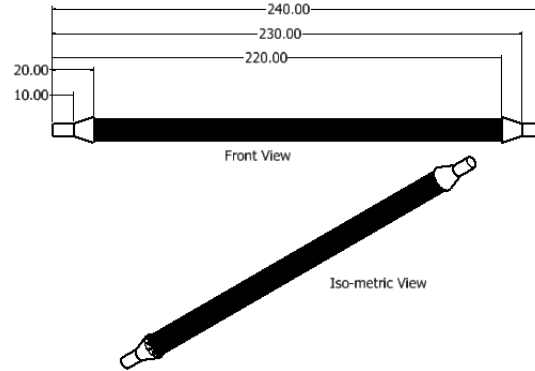


Fig. 5.2. Front and isometric views of the CAD models (a) Tube_C1/C2/C3 (b) Tube_C4 and (c) Tube_C5

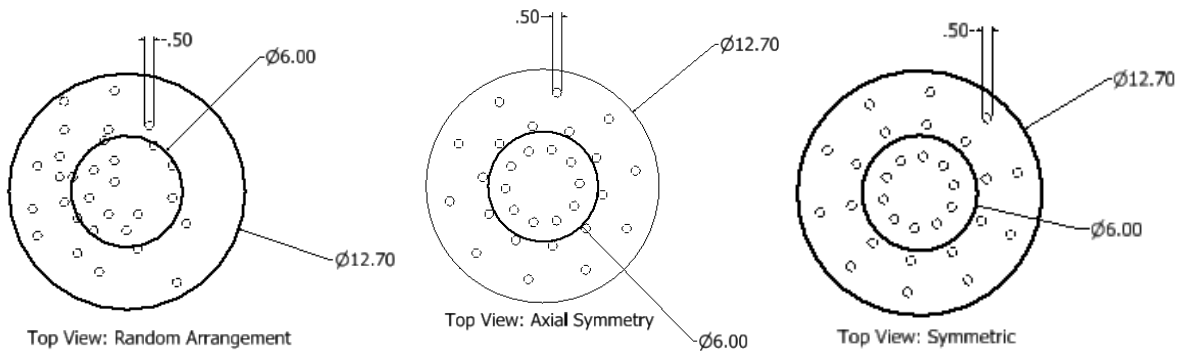


Fig. 5.3. Cross-sectional view of CAD models (a) Tube_C1 (b) Tube_C2 and (c) Tube_C3/C4/C5

The front and isometric views of the CAD models for the shell side are shown in Fig. 5.4a and the cross-sections of the different tube arrangements are shown in Fig. 5.4(b-d).

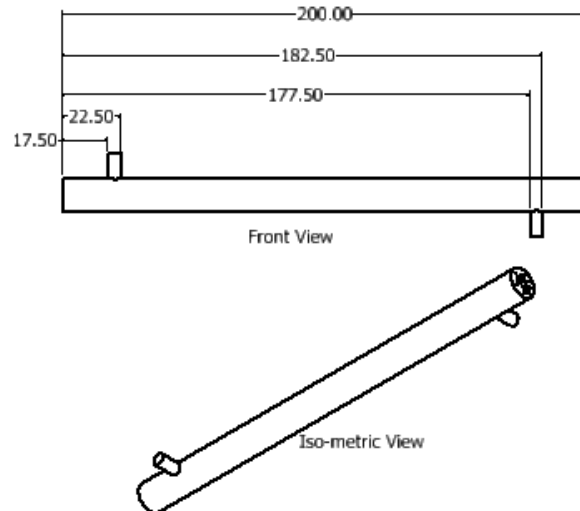


Fig. 5.4. (a) Front and isometric views of Shell_C1/C2/C3, (b) Cross-sectional/Top view of Shell_C1, Shell_C2, and Shell_C3

5.3. Governing Equations

For Reynolds number < 2100, considering laminar flow of a Newtonian fluid (air on tube side and water on shell side), the mass and momentum balances expressed in a fixed reference frame are written as follows:

$$\nabla \cdot \mathbf{u} = 0 \dots\dots\dots(1)$$

$$\rho \frac{\partial \mathbf{u}}{\partial t} + \rho(\mathbf{u} \cdot \nabla) \mathbf{u} = -\nabla P + \mu \nabla^2 \mathbf{u} \dots\dots\dots(2)$$

Navier Stokes equations were solved under boundary conditions related to the fluid domain, which describe real working conditions. The main assumptions in the simulation are:

- No slip boundary
- Heat and vapor transport across the membrane are not considered. Thus the effect of mass flow changes on shell and tube sides are neglected. This is reasonable because for the temperatures considered in this study, fluid density is not expected to change significantly through heat and mass transport. Consequently, flow simulations without heat and mass transport considerations are likely to suffice for establishing the causes for flow distribution.
- Gravity effects are neglected

5.4. Simulation Methodology

CFD simulations for all the geometries mentioned in Table 5.1 were performed on COMSOL multiphysics version 5.3 (a finite element solver). Once the geometry was imported, the boundary conditions were mentioned for the inlet and outlet ports. A velocity boundary condition for the inlet and a zero exit pressure boundary condition for the outlet was used. A physics controlled structured mesh was generated over the entire geometry as shown in Fig. 5.5(a,b) for shell and tube flow. Mesh independence studies were performed leading to the choice of an optimized mesh. All results reported here are for fully converged and mesh independent simulations. The simulation was performed for an air flow rate of 1 L/min equivalent to an inlet velocity of 0.6 m/s, and water flow rate of 380 ml/min equivalent to a flow velocity of 0.23 m/s. Figure 5.6. below shows a schematic of the simulation methodology.

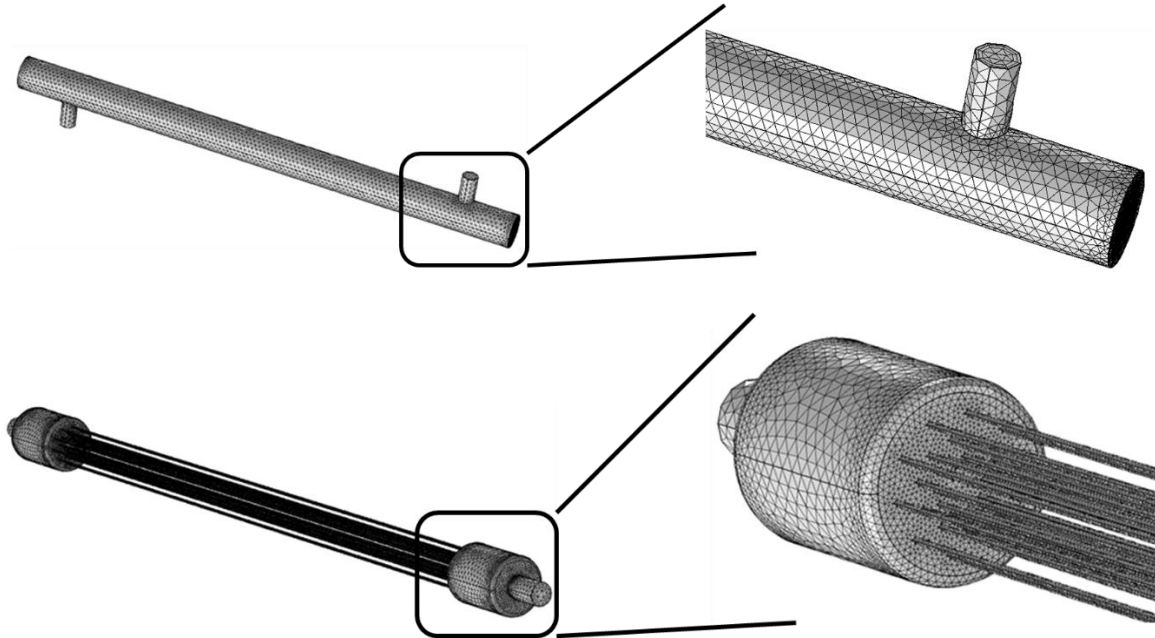


Fig. 5.5. Physics controlled mesh for (a) shell side geometry and (b) tube side geometry

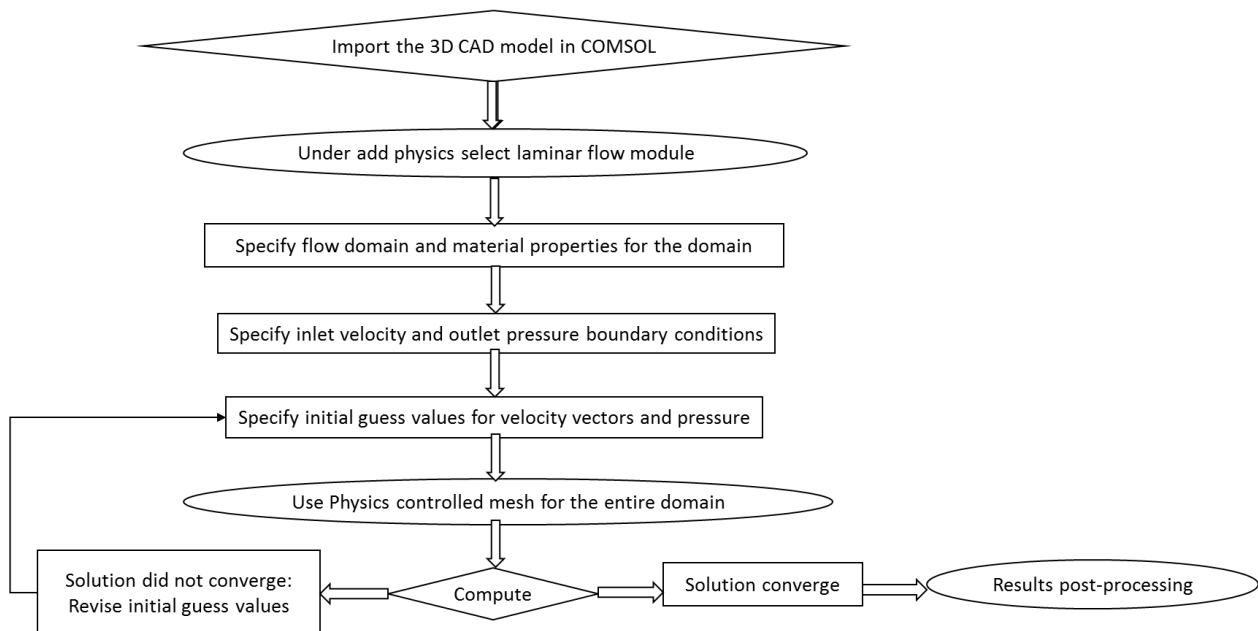


Fig. 5.6. Schematic illustration of the simulation procedure

5.5. Results and Discussion

5.5.1. Effect of symmetry on tube flow distribution

Under laminar flow, fluids tend to flow without lateral mixing and adjacent layers slide past one another. There are neither cross-currents nor eddies. However, due to the presence of sequence of diverging and converging sections (inlet port followed by a header followed by the small diameter tubes) and the presence of the potting resin (which holds the fibers in its place) perpendicular to the direction of flow, lateral mixing is possible between flow streamlines thereby leading to formation of eddies. In our simulations, it is the arrangement of tubes and the header design that dictates the formation and size of eddies and thereby dictate the flow through the tubes. For Tube_C1 model (random tube geometry), Fig. 5.7a shows the velocity profile inside the hollow fibers at a distance of 10 cm from the inlet. The size of the red mark determines the flow velocity above 5 m/s i.e. larger the red mark, higher is the flow through that particular tube. As can be seen from the figure, few tubes marked with a red circle, receive a higher flow than the rest. The reason for such a flow distribution can be understood from Fig. 5.7(b-c) which captures the flow inside the inlet and outlet headers by tracing the flow streamlines. As discussed above, the formation of eddies is clearly seen in both the headers (inlet and outlet) which is the primary reason for flow maldistribution. As suggested by Zhang et al. [3] the flow maldistribution inside the module is a manifestation of the contribution from both the headers and the core of the module. Thus, larger the size of eddies in the headers, higher is the maldistribution. This can further be verified from Figs. 5.8. and 5.9. which show the velocity profiles and flow streamlines for Tube_C2 (axial symmetry geometry) and Tube_C3 models (axial + radial symmetry geometry). It can be seen from Fig. 5.8(b,c) and 5.9(b,c) that the eddies beside being smaller are also observed to assume symmetry along the central axis as the tube arrangement is made more symmetric. While just an axial symmetry alone can reduce the flow maldistribution and increase the flow inside tubes as can be seen from Fig. 5.8a, the axial + radial symmetry can improve the situation further and minimize flow maldistribution with a cylindrical header as seen in Fig. 5.9a. Interestingly, in the case of Tube_C2, we observe that the maximum flow velocity is higher than for Tube_C1 and Tube_C3. In addition, as evident from Fig. 5.8a, it was observed that all the tubes had a velocity of >5 m/s despite having flow maldistribution. While perfect symmetry is desirable,

it is not always practically feasible to achieve. Hence, based on earlier literature reports by Zhuang et al. [4] which are further endorsed in this study, it is suggested that any improvement in symmetry (radial or axial) is expected to improve flow distribution.

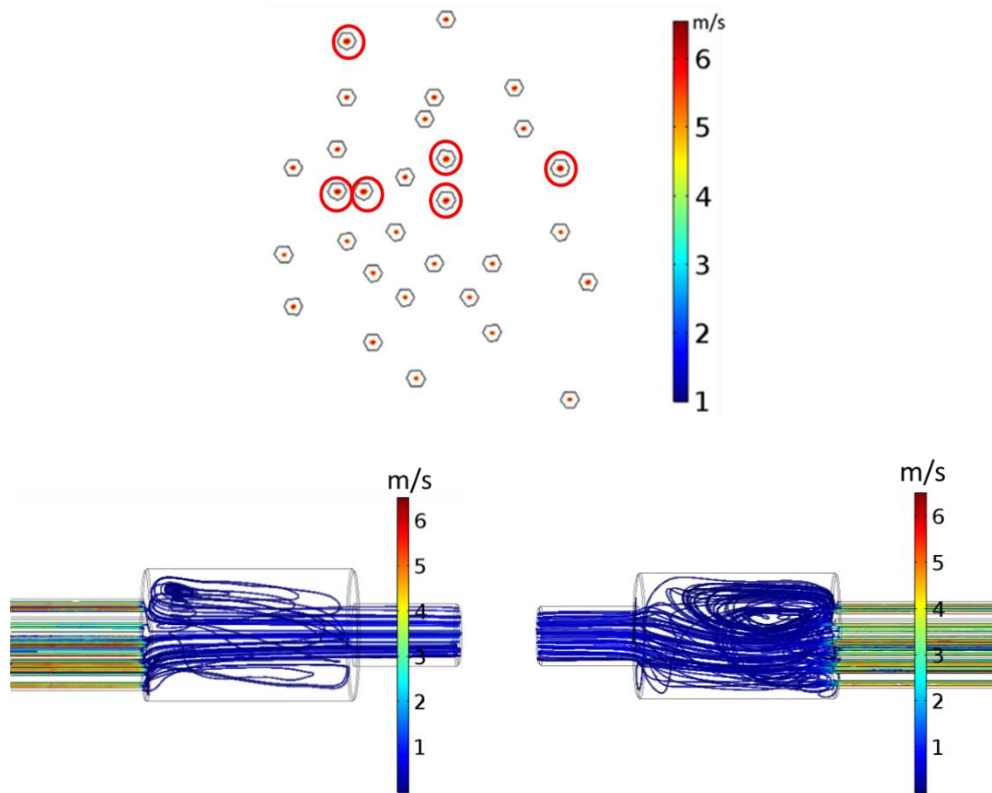
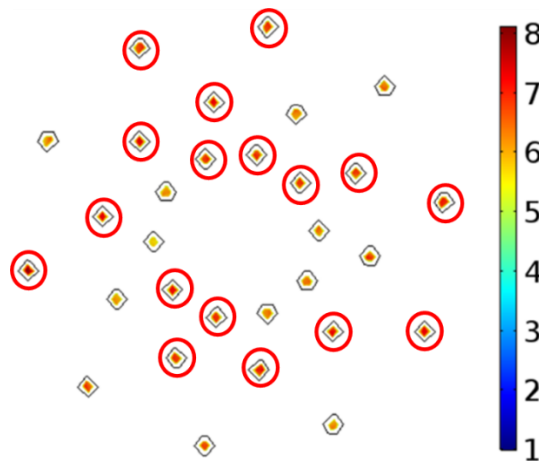


Fig. 5.7. (a) Velocity distribution inside tubes (b) flow velocity streamlines inside inlet header and (c) flow streamlines inside outlet header for Tube_C1 model. The red circles represent tubes receiving higher flow than other tubes.



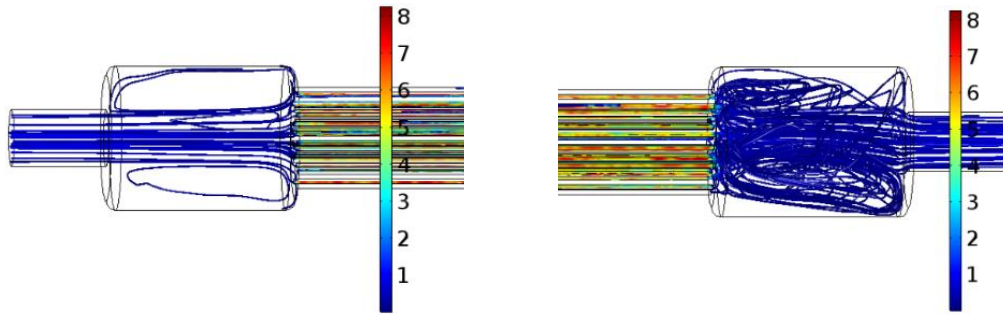


Fig. 5.8. (a) Velocity distribution inside tubes (b) flow velocity streamlines inside inlet header and (c) flow streamlines inside outlet header for Tube_C2 model. The red circles represent tubes receiving higher flow than other tubes.

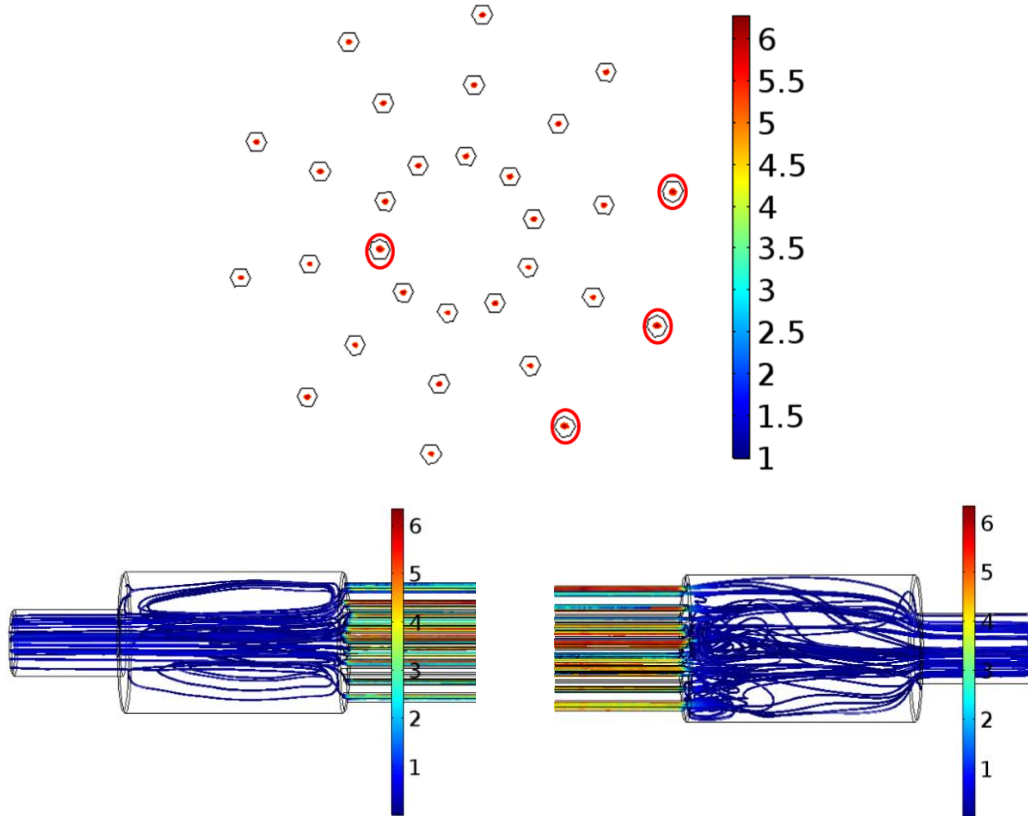
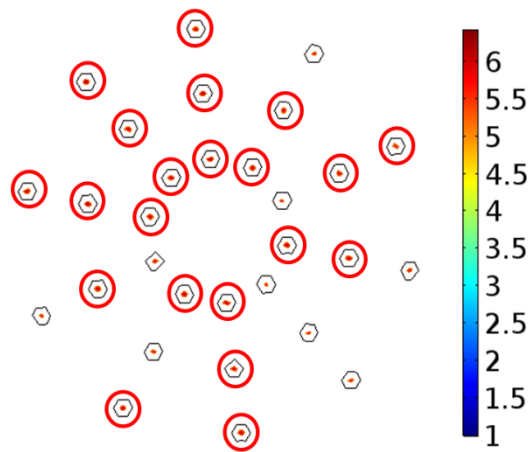


Fig. 5.9. (a) Velocity distribution inside tubes (b) flow velocity streamlines inside inlet header and (c) flow streamlines inside outlet header for Tube_C3 model. The red circles represent tubes receiving higher flow than other tubes.

5.5.2. Effect of header design

As discussed above, it is evident that the flow maldistribution can be reduced by minimizing eddy formation. While we have shown that improving the symmetry in tube arrangement can aid in the cause, altering the header design in addition to the tube symmetry can assist in further minimization of maldistribution. In Figs. 5.10(a-c) and 5.11(a-c), we show the velocity profiles inside tubes and flow streamlines in the headers for Tube_C4 (2 cm conical header with axial + radial symmetry) and Tube_C5 models (1 cm conical header with axial + radial symmetry), respectively. As can be seen from Fig. 5.10a, the number of tubes receiving highest tube flow has increased significantly in comparison to a cylindrical header. Fig. 5.10(b,c) shows that the eddy formation is reduced with this header which is beneficial for flow distribution. Further, Fig. 5.11a suggests that reducing the header length aids in improving flow distribution because of minimizing eddy formation further. The conical shape of the header is expected to reduce the lateral mixing due to streamlining of the flow. In addition, the length of the conical header also decides the available volume for eddy formation which is found to be lower for smaller header lengths. Thus, in order to improve flow distribution, it is suggested to have conical headers with small height especially for low gas flow rate operation.



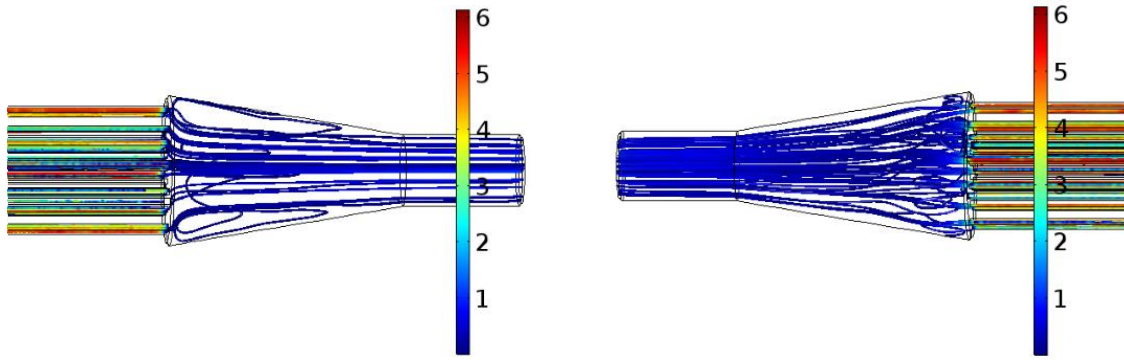


Fig. 5.10. (a) Velocity distribution inside tubes (b) flow velocity streamlines inside inlet header and (c) flow streamlines inside outlet header for Tube_C4 model. The red circles represent tubes receiving higher flow than other tubes.

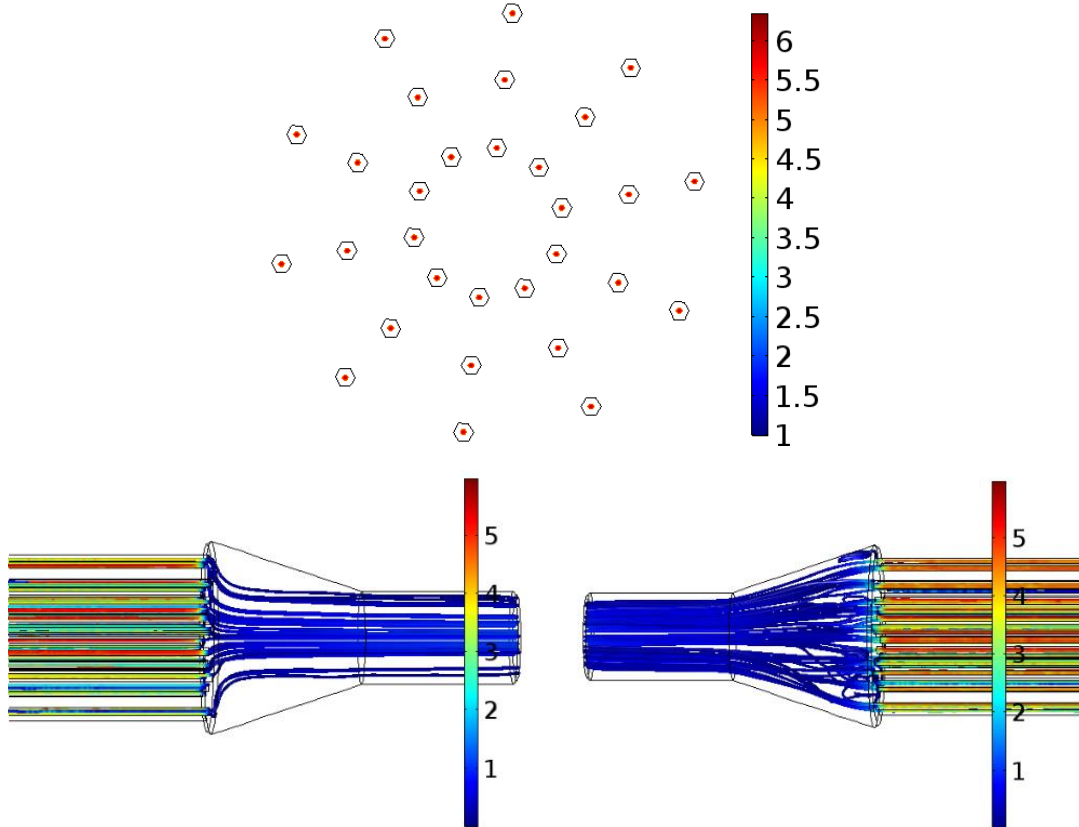


Fig. 5.11. (a) Velocity distribution inside tubes (b) flow velocity streamlines inside inlet header and (c) flow streamlines inside outlet header for Tube_C5 model

5.5.3. Effect of symmetry on shell flow distribution

The arrangement of tubes and the inlet/outlet port location on the shell affects the flow distribution of fluid inside the shell. With the current lab scale humidifier design, the location of

inlet/outlet ports is restricted at approximately 2 cm distance from either end of the shell in order to accommodate the headers. This is expected to create a region of dead volume inside the shell where water flow is low or absent and does not contribute to the humidifier performance. This is verified by CFD simulations for the Shell_C1 (random tube arrangement), Shell_C2 (axial tube symmetry) and Shell_C3 models (axial + radial tube symmetry) as shown in Fig. 5.12(a-c) and 5.13(a-c). In general, from Fig. 5.12(a-c), it is seen that the flow velocities are minimum near the tube surface and more so for inner tubes than for tubes placed near the periphery. As expected, in Shell_C1 model which has randomly placed tubes, the flow distribution is poor in the radial direction which improves upon improving the tube symmetry and attains better flow uniformity for a perfectly symmetric tube arrangement (Shell_C3 model). However, the flow persists to remain unevenly distributed in the radial direction with flow velocities decreasing along the shell radius. This is expected but unavoidable because of the resistance to flow provided by the presence of tubes inside the shell. A possible consequence of such maldistributed flow is that the overall heat transfer coefficient may vary with tube arrangement and is expected to increase in the order Shell_C1 < Shell_C2 < Shell_C3. Therefore, while a symmetric arrangement is likely to achieve higher overall heat transfer coefficient and uniform residence time distribution, the random arrangement could suffer from a loss in overall heat transfer coefficient and uneven residence time distribution thus affecting the humidifier performance.

Additionally, from Fig. 5.13(a-c) it is observed that a dead volume near the inlet/outlet ports is developed because of the placement of the inlet/outlet ports away from the shell ends. These dead zones are the regions inside humidifier where the contribution to humidification is the least due to no shell side flow. As a result, it is suggested to have the inlet/outlet ports for shell side on the headers to minimize dead volume.

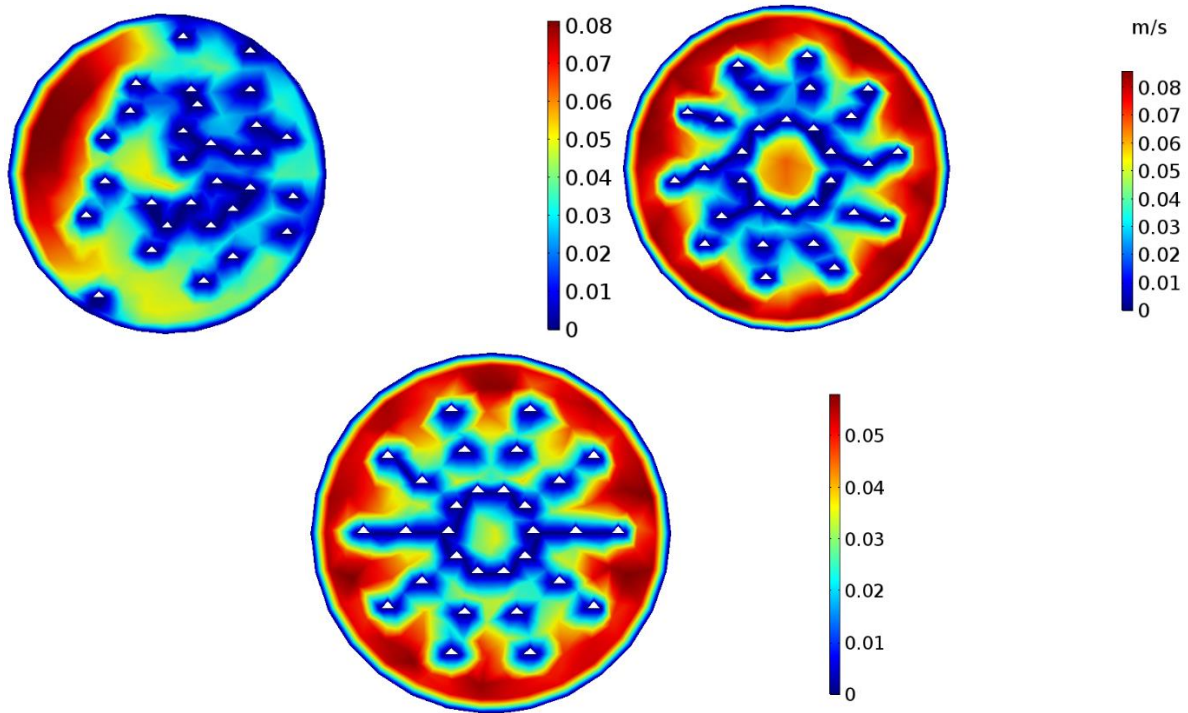


Fig. 5.12. Velocity profile inside the shell for (a) Shell_C1 (b) Shell_C2 and (c) Shell_C3

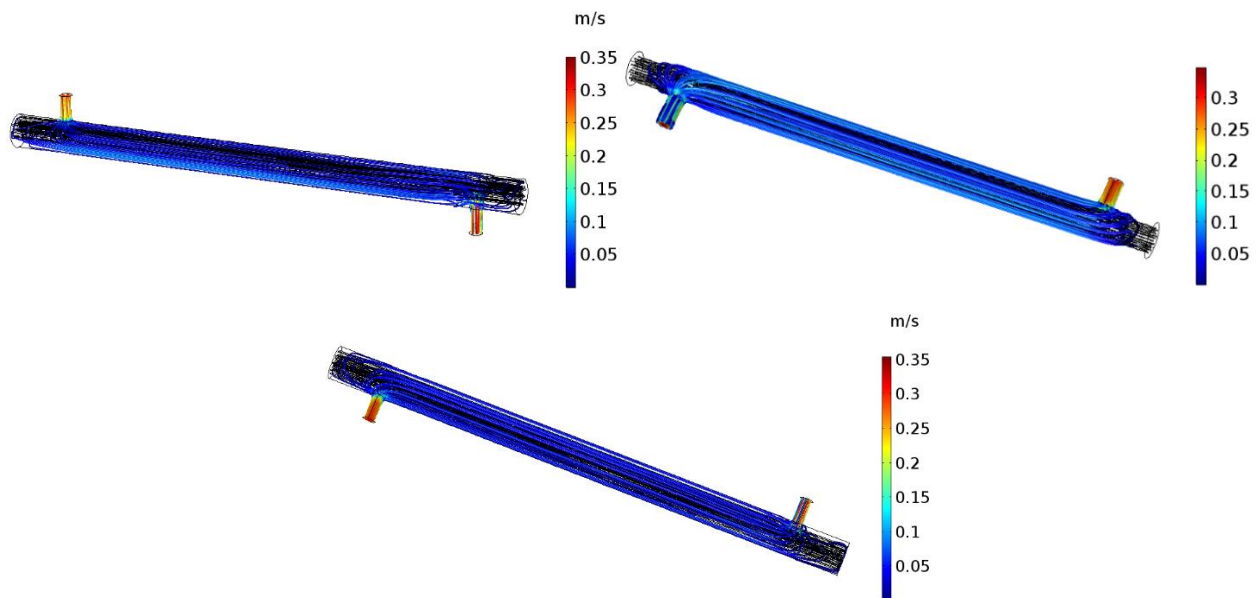


Fig. 5.13. Flow velocity streamlines inside the shell for (a) Shell_C1 (b) Shell_C2 and (c) Shell_C3

5.6. Conclusions

Minimizing flow maldistribution in hollow fiber membrane humidifiers is important for achieving optimal performance. Formation of eddies as a consequence of random tube arrangement and

converging-diverging sections is the primary cause behind flow maldistribution. Thus, it is necessary to modify the present humidifier design. The following design guidelines are proposed for improving the flow distribution in hollow fiber membrane modules.

- A symmetric arrangement of tubes can help alleviate flow maldistribution in tubes and shell side.
- Conical header design is more suited to reduce flow maldistribution.
- Reducing header length can also improve flow distribution.
- The inlet/outlet ports for the shell side should be placed on the headers to minimize dead volume and increase effective area for heat and mass transport.

References

- [1] J. Zhang, Y. Xu, Z. Xu, Flow distribution in a randomly packed hollow fiber membrane module, *J. Memb. Sci.* 211 (2003) 263–269.
- [2] J.K. Park, H.N. Chang, Flow Distribution in the Fiber Lumen Side of a Hollow-Fiber Module, *AIChE Journal*, 32 (1986) 1937–1947.
- [3] L. Zhang, Z. Li, T. Zhong, L. Pei, Flow maldistribution and performance deteriorations in a cross flow hollow fiber membrane module for air humidification, *J. Memb. Sci.* 427 (2013) 1–9. doi:10.1016/j.memsci.2012.09.030.
- [4] L. Zhuang, H. Guo, G. Dai, Z. Xu, Effect of the inlet manifold on the performance of a hollow fiber membrane module - A CFD study, 526 (2017) 73–93. doi:10.1016/j.memsci.2016.12.018.

Chapter 6

Internal Humidification in PEM Fuel Cells Using Wick-Based Water Transport

In this chapter, the feasibility of a wick-based technique for direct humidification of the membranes in proton exchange membrane fuel cells (PEMFC) operating under dry feed operation is investigated. In the experimental work described in this chapter, single cells and multi-cell stacks of PEM fuel cells were operated in several configurations using a wicking material laid over the active area to facilitate water transport directly to the membrane electrode assembly (MEA) through capillary action. The performance obtained due to the incorporation of such a wick in the conventional fuel cell system was analyzed by means of electrochemical impedance measurements from which the Ohmic and charge transfer resistances were estimated in different configurations.

The content of this chapter is published in,

"Journal of Electrochemical Society 2015 volume 162, issue 9, F1000-F1010".

Reproduced with permission from Journal of Electrochemical Society.

6.1. Introduction

Proton exchange membrane fuel cells (PEMFCs) have gained worldwide attention for power generation in various sectors due to their low temperature operation, high power density and high efficiency [1]. Fuel cell efficiency can reach as high as 60% for electricity generation and up to 80% when heat is also utilized. It also provides ~ 90% reduction in major pollutants released in the atmosphere [2]. Despite having several positives, two greatest barriers that have hindered its mass commercialization are durability and cost [3].

Water and thermal management are critical for achieving maximum performance and durability of PEMFC [4-8]. Water management requires on the one hand maintenance of high moisture content in the membrane to ensure good ionic conductivity [9] while ensuring on the other hand that flooding in the catalyst layer, GDL and/or flow field channels is avoided. Avoiding liquid water

accumulation on catalyst layer (flooding) is of critical importance for optimal performance and durability [6, 10]. The excessive presence of liquid water due to reaction and/or external humidification results in concentration polarization and can raise concerns of durability and performance reduction [10]. The accumulation of liquid water is the major cause of the oxygen mass transport limitation in a PEM fuel cell. If the water removal rate does not comply with the generation rate (especially at cathode), excessive water will accumulate. This hinders the transport of oxygen by blocking the pores in the porous cathode catalyst layer (CCL) and gas diffusion layer (GDL), masking the active sites in the catalyst layer and blocking the gas transport channels in the flow field. Moreover, auxiliary compressors and humidifier units required for external humidification together can account for up to 20 % of the total fuel cell system volume and thereby reduce its power density [11] and increase system complexity [12-14]. Under continuous operation, insufficient humidification of gases may lead to dehydration of the membrane which results in higher Ohmic resistance [15] and finally breakdown of cell due to reduced proton conductivity of the membrane [16].

Water movement in the cell is mainly governed by back diffusion (from cathode to anode) at low current density operation and by electro-osmotic drag (from anode to cathode) at high current densities [17]. Problems related to dehydration of the membrane are especially crucial at the anode side of the membrane due to electro-osmotic drag. In a dry ionomer phase, protons cannot migrate effectively since the sulfonic acid bond cannot be dissociated, leading to decrease in ionic conductivity. This further reduces the access of protons to the catalyst surface thus increasing the activation polarization [18]. A fully hydrated membrane on the other hand can achieve as much as 300 times higher ionic conductivity as compared to the dry ionomer [15]. Possibilities are that both electrodes get accumulated with liquid water (flooding) at different current densities [19, 20], but flooding is more crucial at cathode where significant amount of water is produced by oxygen reduction reaction (ORR) at higher current densities [21]. Therefore, an optimal balance is required between humidification and drying of membrane [22].

Several methods have been reported in the literature that have addressed the issue of water management by (i) maintaining optimal operational conditions, (ii) by cell system design consisting of gas humidification system and flow field design and/or (iii) MEA material and

structure design [22]. Nguyen et al. [23] used a technique wherein direct liquid water was injected in conjunction with an interdigitated flow field for effective water management. On the positive aspect, the method offers compactness, control and less energy consumption for humidification. However, the negative aspect of this technique is the possibility of flooding inside the flow fields. Another common technique addresses this issue by using water vapor saturated inlet gas streams on serpentine cathode flow fields for air delivery [12] where excess water is removed by advection caused due to increased pressure drop over the long channel length and high air velocities due to reduced air channel cross-sectional area. Although stable performance is achieved, this approach results in large parasitic power losses accounting for as high as 35% of stack power and increased system complexity [14].

Passive water management techniques have gained recent attraction among fuel cell system developers as it renders reduced parasitic power loss, low operational costs and less system complexity [24]. Several fuel cell manufacturers like Intelligent Energy, UTC Ltd., General Motors, etc. have carried out years of research in successfully developing PEMFC stacks using passive techniques for water and thermal management [25-29]. US Patent 6,960,404 [25] describes the wicking action over the cathode in the form of channels in order to supply the water inside the cell for internal humidification. EP 1,530,813 [26] describes a technique for direct supply of water to the bipolar plate channels for internal humidification of membrane. The technique uses an extremely thin metal foil (~40 microns) assembly; designed to be placed over the top and bottom portions of active area of the flow field plate. Water is supplied to the metal foil directly through a complicated design of bipolar plate. The water when reaches the flow field evaporates into the gas stream thereby humidifying it. US Patent 7,799,453 [27] demonstrates a fuel cell with electroosmotic pump for driving liquid water generated at the cathode out of the fuel cell, for achieving stable and flooding-free performance over a wide range of current densities. US Patent 8,211,592 [28] showcases a corrosion-resistant, super-hydrophilic fluoropolymer layer over the flow field for effective water management in fuel cells. The layer is surface modified by plasma activation of fluoropolymer and is claimed to have a porosity of greater than 40 %. US Patent 8,685,593 [29] proposes use of a silicon oxide/carbon bilayer over metallic bipolar plates for water management. Yi et al. [30] made use of hydrophilic, porous water transport plates (WTPs)

in which the pores remain filled with water. The WTP allows water exchange while preventing gas permeation into the coolant stream. The excess water from the gas streams would be wicked into the WTP due to the pressure differential created across the plates. Buie et al. [31] used an electroosmotic (EO) pump directly integrated into a fuel cell cathode and applied an electric field to drive liquid water from the GDL to an external reservoir. Santiago's research group has extensively studied wick-based techniques for active and passive water management in PEM fuel cells [32-35]. Litster et al. [32] used an electroosmotic pump in concert with integrated porous SGL carbon wicks to prevent flooding and facilitate stable performance nearly at all current densities. Fabian et al. [33] demonstrated active water management at the cathode of a planar air-breathing PEM fuel cell using an electroosmotic pump. The methodology used therein uses less than 2 % of the fuel cell power to provide stable operation with higher net power performance. Another work of Fabian et al. [34] demonstrates passive water management at the cathode of a planar air-breathing PEM fuel cell using electrically conducting and hydrophilic wicks. They successfully demonstrated fuel cell operation under severe flooding conditions, ambient temperature of 10 °C and relative humidity of 80%, for up to 6 h with no observable cathode flooding or loss of performance. Litster & Santiago [35] also studied dry gas operation with parallel cathode channels and compared fuel cell performance of porous & hydrophilic carbon plates with the control case of non-porous carbon plates. They concluded that porous plates provide significant improvements in fuel cell performance due to enhanced uniformity in water distribution over the active area by capillary action. Incorporation of special hydrophilic wicking structure into the cathode flow channels can redistribute liquid water and accelerate water removal [36-38]. For instance, a cathode serpentine flow field mounted with one or two strips of absorbent wicking materials such as PVA sponge, cotton cloth, cotton paper etc. has been used to achieve improved water removal at a current density of 1.2 A/cm² [38]. Strickland et al. [24] used in situ polymerized wicks on a 25 cm² parallel channel flow field design at low air stoichiometry, to provide a liquid water transport pathway from reaction sites to outside of the fuel cell by leveraging air pressure gradients.

To the best of our knowledge, almost all of these techniques have so far been used to address water management at the cathode with or without dry feed operation. None of the previous

studies has investigated the effect of water management over the anode side using such methodologies. Moreover, almost all previous researches have been carried out on smaller active areas such as 25-50 cm². Here we study internal humidification in fuel cells of 100 cm² active area using wick-based techniques. Therefore, the present study deals with the use of an electrically conducting & porous material for its ability to provide direct membrane humidification using several configurations of wick based 100 cm² PEM fuel cell setup. The performance of the cell using this humidification technique is compared with a conventional PEM fuel cell wherein humidification is achieved using external bubble humidifiers and by maintaining operational conditions in PEMFCs. Such wick-based techniques can leverage upon reduced parasitic power loads as well as system compactness, which could yield dividends in several stationary and automotive applications.

6.2. Experimental

6.2.1. Determination of pore size, permeability, contact angle and thermal stability

Pore size distribution, gas permeability and contact angle play an important role for wicking action to take place in a porous hydrophilic material. These parameters also govern the possibility of flooding of electrodes due to excess wicking. In order for a wick to supply water to the fuel streams internally, it is essential that a positive wicking velocity be continuously maintained. Hence, optimum pore size distribution and permeability are critical for flood-free cell performance. Wicking action is in turn determined by using two important factors namely differential capillary pressure and wicking velocity. Differential capillary pressure (dP_{cap}) is a function of surface tension of water, contact angle and pore diameter, whereas wicking velocity depends on the difference between dP_{cap} and differential flow field pressure ($dP_{flowfield}$), permeability, viscosity of fluid and channel length.

HCB grade carbon cloth (~99.5 % carbon) was used as a wicking material (AvCarb[®], US) and was characterized for its pore size and permeability using a capillary flow porometer instrument (Porous Materials Inc., US). The technique works based on the displacement of a wetting liquid from the sample pores by applying a gas at increasing pressure. . Average pore size, air flow rate and permeability through the wick were measured in relation to varying differential air pressure. Sessile drop method was used to measure the contact angle over the wick surface using Surface

Electro Optics Instrument (Model Phoenix-300, Korea). Surface wetting energy of the wick was also measured which defines the ability of the fluid to wet the surface. Since the wick has heterogeneous pore structure, contact angle was measured at five different locations on a 5 x 5 cm² area and was averaged. Thermal stability of the wicking material was studied for a temperature range of 30 °C to 250 °C using a Thermo-gravimetric analyzer (TGA) (NETZSCH, STA 449, Germany). Change in mass percentage with respect to temperature was recorded. In addition, Differential Scanning Calorimetry (DSC) was performed simultaneously on the sample to determine the differential heat flow as a function of temperature.

Existing literature on wicking techniques make use of lands or channels formed from wick which may be either conducting or non-conducting [24-25, 37-38]. Most of these techniques limit themselves to parallel flow-field designs, which are not very effective in terms of fuel utilization. For example, Strickland et al. [24] demonstrated in situ polymerized wicks as parallel channels over the cathode for improved water management in a 25 cm² fuel cell setup. Ge et al. [38] used two strips of wicks on the entry and exit ends of a serpentine flow field over a 50 cm² area and demonstrated improved single cell performance over the control setup with dry feed. However, since the methodology relies solely on water produced by the electrochemical reaction, it renders limitations on scaling up to larger active areas where uniform distribution of water over the active area is certainly a concern. Moreover, since back diffusion for anode humidification is only limited to lower current densities therefore operation at higher current densities is bound to be restricted [17]. Another lacuna in the literature is that the materials used for wicking are not rigorously characterized. This leads to an incomplete understanding of the capacity of wicking materials to provide internal humidification in PEM fuel cells under dry feed operation. Therefore, in this study, a systematic methodology is adopted wherein the chosen wicking material is first characterized for its ability to undergo capillary action. This is followed by theoretical estimation of the amount of water uptake possible by the material under the fuel cell gas flow conditions. Finally, a single cell setup with the wicking material covering either anode or cathode or both electrodes is experimentally investigated for its ability to internally humidify as well as prevent drying and flooding events inside the fuel cell.

The study has been done with respect to two flow modes i.e., counter-flow and co-flow. Co-flow mode in this study implies that the gas flow direction is parallel to the capillary action in the wicking material. In case of counter-flow mode, the gas flow is in opposite direction of the capillary action. It was important to check these flow modes in order to confirm the role of capillary action in membrane humidification inside the cell. The schematic representation of these flow modes is given in Fig. 6.1. The trough shown in Fig. 6.1. was designed to accommodate a single cell with only the extended portion of the wick dipping inside the trough. The configurations and their respective details have been mentioned in Table 6.1. The control setup Configuration-A does not use any wick and is always operated in counter-flow mode. Other configurations (B – D) include a layer of wick over the anode (configuration-B), layer of wick over the cathode (configuration-C) and a layer of wick each over both electrodes (configuration-D). These configurations were operated by varying inlet gas humidity, inlet gas temperature and flow modes. These configurations have been schematically represented in Fig. 6.2. Further, in order to check for excess wicking in co-flow mode, the effect of stoichiometry was studied in case of configuration-C with and without external water supply to the wick. It is to be noted that configurations C₁ and C₂ as mentioned in Table 6.1 are same in terms of placement of wick and thus have been represented in a single schematic as configuration-C in Fig. 6.2.

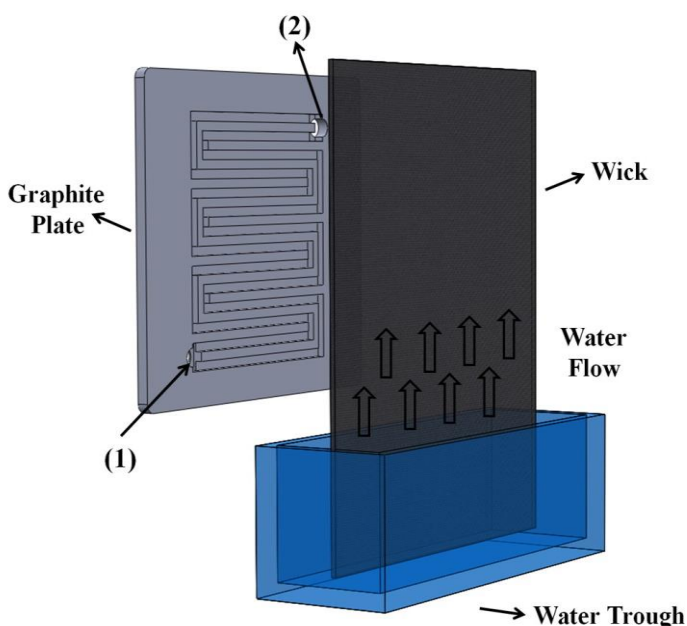


Fig. 6.1. Schematic representation of the flow modes in a single cell. Counter-flow: Gas inlet – (2), Gas out – (1); Co-flow: Gas inlet – (1), Gas outlet – (2). In counter-flow mode, the gas flow is opposite to the capillary action while in co-flow mode, the gas flow is in the direction of capillary action.

Table 6.1: Description of (a) anode conditions and (b) cathode conditions for different configurations

(a) Anode Conditions					
Configuration	A	B	C₁	C or C₂	D
Placement of wick	No wick	Over anode	Over cathode	Over cathode	Over anode and cathode
External water supply to wick	No	Yes	No	Yes	Yes
Flow mode at anode	Counter	Counter / Co-flow	Counter	Counter	Counter / Co-flow
Means of humidification at anode	Bubble humidifier	Through wick	Bubble humidifier	Bubble humidifier	Through wick
Feed at anode	Humidified	Dry	Humidified	Humidified	Dry
Inlet fuel temperature (°C)	50 - 52	28 - 30	50 - 52	50 - 52	28 - 30

(b) Cathode Conditions					
Configuration	A	B	C₁	C or C₂	D
Placement of wick	No wick	Over anode	Over cathode	Over cathode	Over anode and cathode
External water supply to wick	No	Yes	No	Yes	Yes
Flow mode at cathode	Counter	Counter	Counter / Co-flow	Counter / Co-flow	Counter / Co-flow
Means of humidification at cathode	Bubble humidifier	Bubble humidifier	Through wick	Through wick	Through wick
Feed at cathode	Humidified	Humidified	Dry	Dry	Dry
Inlet oxidant temperature (°C)	45 - 47	45 - 47	28 - 30	28 - 30	28 - 30

*Counter: Top to bottom flow; Co-flow: Bottom to top flow

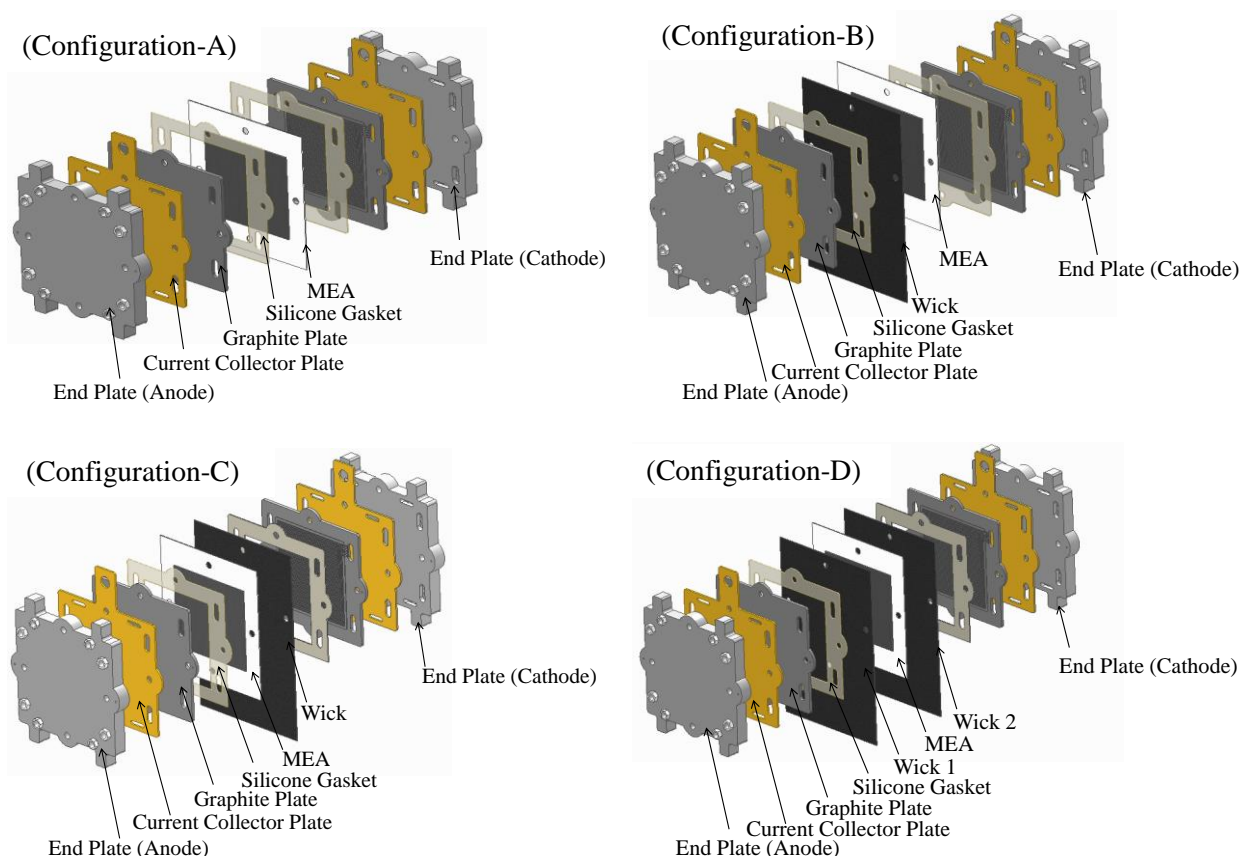


Fig. 6.2. Schematic representation of different configurations in a single cell.

A single cell assembly for configuration-A consists of a central membrane-electrode assembly (MEA) that is flanked on either sides by silicone gaskets, cathode and anode flow fields, gold coated copper current collectors, Teflon® layers for electrical insulation, and stainless steel end plates support for compression. In other configurations (B - D), the MEA was covered on either or both sides by a layer of wick over the entire plate area with the bottom portion of the wick extending outwards by 5 cm. A monopolar plate each at anode and cathode having 7-channel, 7-pass serpentine flow field were used for the experiments. MEA (Alfa Aesar, Johnson Matthey, UK) consisting of Pt catalyst loading of 0.4 mg/cm^2 , non-woven teflonized carbon fiber as gas diffusion layer and polyfluorosulphonic acid ionomer membrane electrolyte was used for all the single cell experiments. MEAs were evaluated using a 100 cm^2 fuel cell fixture fabricated in our laboratory workshop with parallel serpentine flow field machined on graphite plates obtained from M/s Schunk Kohlenstofftechnik GmbH, Germany. The testing was performed on a BioLogic

fuel cell test station (Model FCT-50/150S, France) for cell polarization and AC impedance measurements in a single cell setup. Reactant gases were fed from compressed air cylinders (~99.99 % purity) and hydrogen cylinders (~99.99 % purity) to the test station and their flow rates were monitored. De-ionized water was supplied to the trough for configurations-B, C & D. For cases wherein gas humidification was required externally, the temperature of the bubble humidifiers was maintained constant in order to achieve 80 - 85 % humidification for anode and 50 - 55 % humidification for cathode. The gas line temperature was maintained slightly above the humidified gas temperature in order to prevent condensation. Each experiment was repeated for a minimum of three times to check for the variation in fuel cell performance with each configuration. Table 6.2 enlists all the experimental parameters used for the fuel cell testing.

Table 6.2: Experimental parameters for fuel cell testing.

Parameter	Value
Fuel cell temperature	55 °C
Cathode humidifier temperature	45 °C
Anode humidifier temperature	52 °C
Cathode gas line temperature	55 °C
Anode gas line temperature	60 °C
Hydrogen stoichiometry	1.2
Air stoichiometry	3
Number of channels	7
Number of passes	7
Length of each channel	84.8 cm
Active area	100 cm ²
Anode/Cathode outlet pressure	1 atm (abs)
Wick thickness	0.31 mm
MEA thickness	0.41 mm
Trough capacity	220 ml

6.3. Results and Discussion

6.3.1. Determination of pore size, permeability, contact angle and thermal stability of wicking material

Fig. 6.3(a,c) respectively shows the average pore diameter and gas permeability of the wick in relation to differential air pressure. Lower pore diameters as well as higher gas permeability were measured at higher differential air pressures across the wick because of the increase in capillary displacement of the fluid. The average pore size in relation to varying differential pressure was found to be in the range of 25.7 to 94.5 μm for the wick with an average pore size of 61 μm , while the average permeability value was found to be 25 Darcys. The standard deviation (SD) error bars represent the spread of the measured values across the mean. Goebel [25] has reported acceptable material parameters for selection of wicking material in a fuel cell setup. The values measured in the present study are in the acceptable range reported by Goebel and are provided in Table 6.3. Figure 6.3b shows the contact angle data for a 5 x 5 cm^2 area wick at five different locations. The pattern suggests that the contact angle varies with respect to location due to the variation in pore size distribution. The average contact angle was found to be 77 degrees. This value is acceptable for choosing carbon cloth as a wicking material. In general, contact angle lower than 90 degrees is termed as hydrophilic. Strickland et al. [24] also reported a contact angle of 55 degrees for their photo-polymerized wick channels over the cathode. Contact angle is inversely proportional to the wetting energy and decreases with time as the hydrophilic surface of the wick sorbs the water. Surface wetting energy on the other hand usually increases with decrease in contact angle.

Table 6.3: Comparison of properties for selection of wicking material.

Property	Value reported *	Actual Value of Wick Used
Pore size (μm)	5 - 30	$25 \pm 1(\text{SD}) - 95 \pm 1(\text{SD})$
Void fraction (%)	0.60 - 0.80	0.50 - 0.60
Thickness (mm)	0.2 - 1	0.31 ± 0.01
Thermal conductivity (W/m.K)	> 2	1.7
Electrical resistivity (mOhm-cm)	< 500	1.1

* [30]; SD: Standard deviation

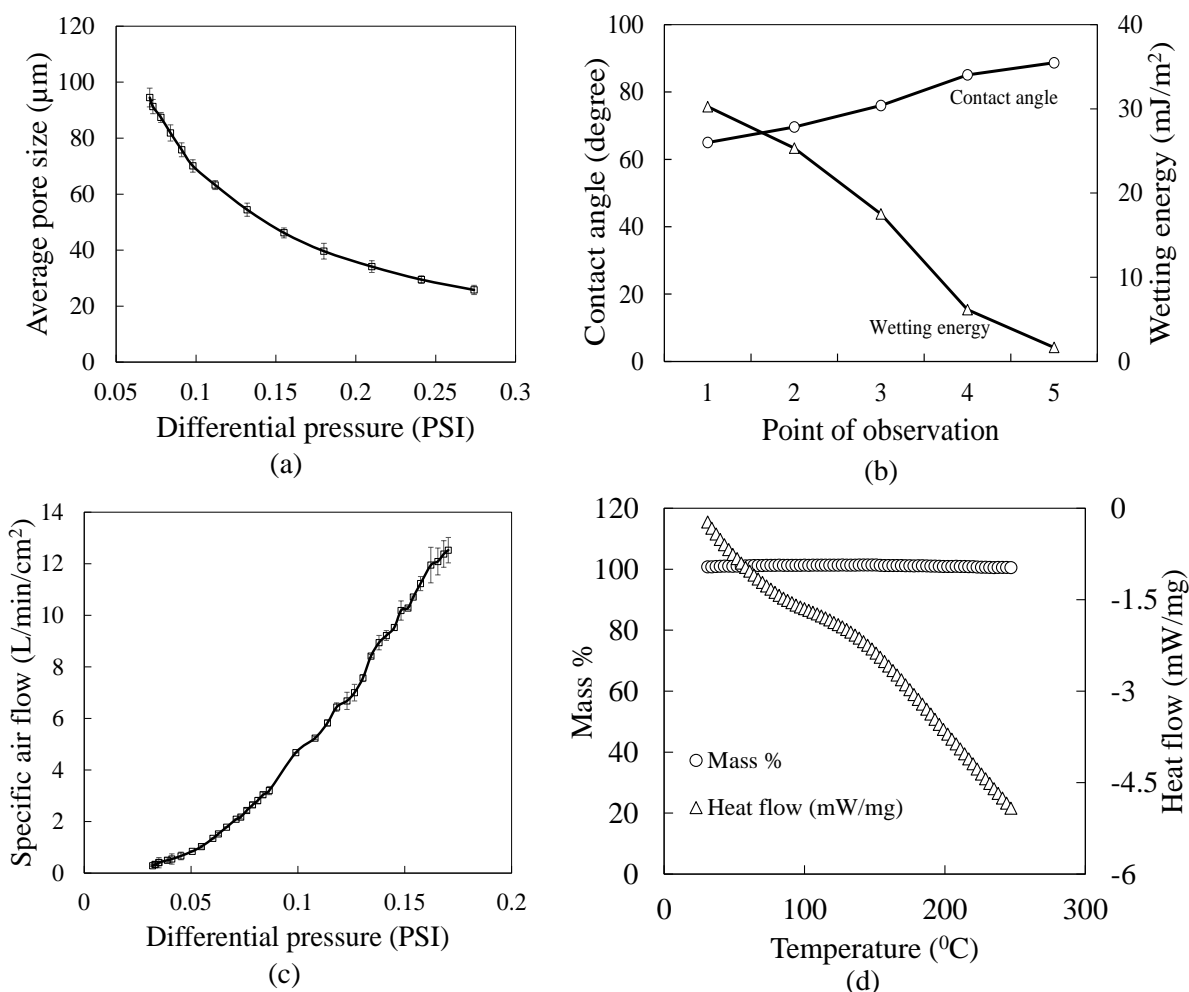


Fig. 6.3. Wick characterization: (a) Pore diameter vs. differential air pressure across the wick, (b) Gas permeability through wick vs. differential air pressure across the wick, (c) Contact angle measurement and (d) TGA/DSC plot for variation in mass % and heat flow with respect to temperature. The error bars represent the standard deviation values for a data set of average pore diameter and gas permeability.

It is important that the wicking material used for water transport be thermally stable for the PEMFC temperature operation range. In general, wicking materials like cotton loose about 5 - 7 % of their mass in the temperature range of 30 - 250 $^{\circ}\text{C}$ [39, 40]. Hence, long duration operation with such wicking materials are not likely to provide stable performance. From Fig. 6.3d of TGA/DSC, no loss in mass percentage was observed for the entire temperature range. Heat flow pattern with increase in temperature observed no peaks indicating absence of any sort of phase transitions in this temperature range. The material was thus found stable for the entire range of fuel cell temperature.

6.3.2. Theoretical calculation for water uptake from capillary action of wick

The rise of water in a capillary depends on surface tension of water, contact angle between water and surface, density of water and capillary radius. The height (h) of liquid in a capillary is given by Eq. (1)

$$h = \frac{2\sigma \cos\theta}{r\rho g} \dots\dots\dots(1)$$

Where, ' σ ' is the surface tension of water (N/m), ' θ ' is the contact angle (degree), ' r ' is the capillary radius (m), ' ρ ' is the density of water (kg/m³) and ' g ' is the acceleration due to gravity (m/s²). Based on the above equation, the height to which water would rise in a wick having a contact angle of 77 degrees and average pore diameter of 61 μ m is estimated to be 21 mm. Clearly, this height is not sufficient for uniform water distribution over the 100 cm² active area having a side length of 100 mm, more so in case of Configurations-B & D where the water rise from the wick is the sole source of water for humidification over the anode. It is however to be noted that the above estimate is under quiescent condition of air. However, in a fuel cell setup, the rise of liquid is also affected by the gas flow over the wick. Strickland et al. [24] have provided correlations for estimating the water uptake rate in the wick. We reproduce those relations with some modifications that are suitable for this context. Therefore, in case of wicks used in fuel cells, Eqs. (2) - (3) can theoretically calculate the flow rate of water uptake in different configurations.

$$Q_{wick} = \frac{A_w}{\mu_{H_2O}} k_w \frac{dP_{cap} - dP_{flowfield}}{L_c} \quad \text{Counter-flow mode} \dots\dots\dots(2)$$

$$Q_{wick} = \frac{A_w}{\mu_{H_2O}} k_w \frac{dP_{cap} + dP_{flowfield}}{L_c} \quad \text{Co-flow mode} \dots\dots\dots(3)$$

Where, ' A_w ' is the channel wick cross-sectional area (m²) , ' μ ' is the dynamic viscosity of water (Pa-s), ' k_w ' is the wick permeability (m²), ' dP_{cap} ' is the differential capillary pressure (N/m²), ' $dP_{flowfield}$ ' is the differential pressure between inlet and outlet of the gas flow field (N/m²) and ' L_c ' is the channel length (m). For counter-flow mode, dP_{cap} and $dP_{flowfield}$ are opposite in direction and hence the difference between them will dictate the rise of water through the wick. In contrast, dP_{cap} and $dP_{flowfield}$ are in the same direction in co-flow mode and hence add up to facilitate the wicking action. Figure 6.4. represents the block diagrams for the measurement of

$dP_{flowfield}$ in counter and co-flow modes. The setup includes a gas cylinder, which supplies the gas to the mass flow controller (MFC) which then feeds the gas to the fuel cell inlet. The measurement of anode and cathode flow field pressure drops is made by recording the differential gas pressure at the respective inlets and outlets. Differential capillary pressures for the wick based on its pore size and contact angle can be estimated using Eq. (4).

$$dP_{cap, avg} = \frac{4\sigma \cos \theta}{d_{pore}} \dots \dots \dots (4)$$

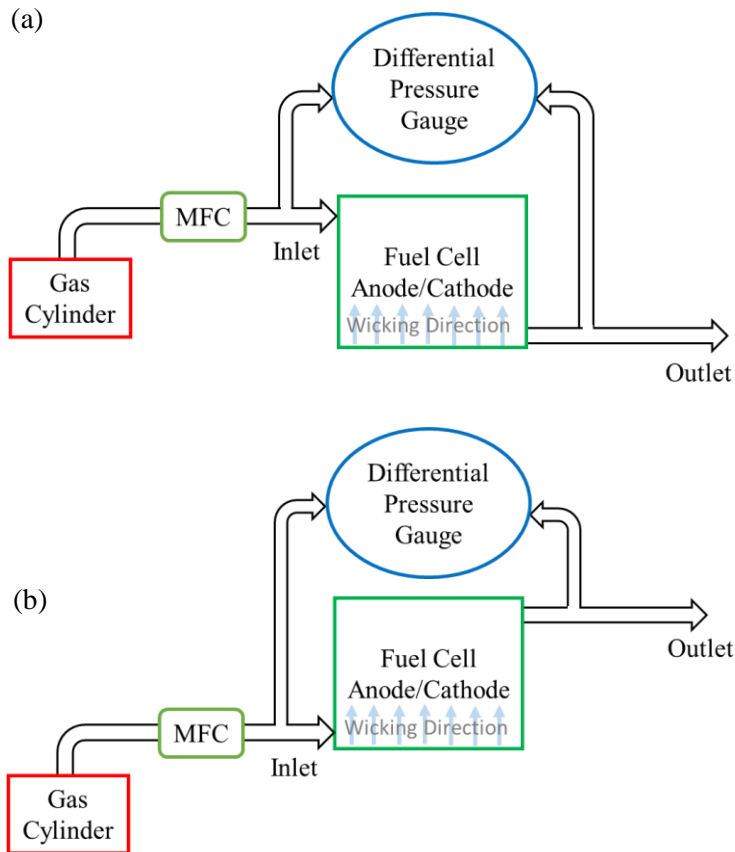


Fig. 6.4. Block diagram representation of the differential pressure measurement for (a) Counter-flow and (b) co-flow mode, in a 100 cm² PEM fuel cell.

The cross-sectional area average wicking velocities for wicks placed over the anode and cathode differ due to their respective stoichiometry and gas flow rates. In addition, the mode of flow further alters the velocity that can be calculated using Eqs. (5) – (6).

$$V_{wick} \text{ (mm/s)} = \frac{k_w (dP_{cap,avg} - dP_{flowfield})}{\mu L_c} \quad \text{Counter-flow mode(5)}$$

$$V_{wick} \text{ (mm/s)} = \frac{k_w (dP_{cap,avg} + dP_{flowfield})}{\mu L_c} \quad \text{Co-flow mode(6)}$$

It is to be noted that while $dP_{cap,avg}$ in wick does not change due to mode of gas flow, the $dP_{flowfield}$ does differ with the mode of gas flow due to gravity effects. Thus, wicking velocities vary for anode and cathode in case of counter and co-flow modes. Once, the wicking velocities are known, the rate of water uptake in wick can be calculated for anode and cathode under different flow modes by multiplying the velocity with the cross-sectional area of wick. This is given by Eqs. (7).

$$Q_{wick} = V_{wick} \times A_w \times \text{no. of channels(7)}$$

Table 6.4 shows the various parameters that were calculated using the data obtained from contact angle measurements and capillary flow porometry, for determining the water uptake in the wick. It can be noted that the wicking velocity for both anode as well as cathode is much higher in co-flow mode as compared to counter-flow mode due to differential flow field pressure acting in favor of the capillary rise. Further, it can also be seen that due to higher differential flow field pressures opposite to the capillary rise, water does not rise at all for cathode under counter-flow mode. Thus, it is confirmed that the counter-flow mode for Configuration-C would make use of only the water produced at the cathode by electrochemical reaction.

Table 6.4: Determination of water uptake through capillary action in counter-flow and co-flow modes.

Parameter	Value
Surface Tension (σ) of water at 30 °C (N/m)	0.0712
Average contact angle (θ) (degree)	77 ± 1 (SD)
Average pore diameter (μm)	61 ± 1 (SD)
Average permeability for wick (Darcy) (1 Darcy ~ 10 ⁻¹² m ²)	25 ± 1 (SD)
Viscosity of water (μ) at 30 °C (Pa-s)	0.000798
$dP_{flowfield}$ (N/m ²) for anode side: counter-flow mode	426.26

$dP_{flowfield}$ (N/m ²) for anode side: co-flow mode	593.974
$dP_{flowfield}$ (N/m ²) for cathode side: counter-flow mode	5799.98
$dP_{flowfield}$ (N/m ²) for cathode side: co-flow mode	5869.86
Average differential capillary pressure ' $dP_{cap,avg}$ ' (N/m ²)	1050.26
V_{wick} (mm/min) at anode: counter-flow mode	1.383
V_{wick} (mm/min) at anode: co-flow mode	3.645
V_{wick} (mm/min) at cathode: counter-flow mode	-10.528
V_{wick} (mm/min) at cathode: co-flow mode	15.339
Cross sectional area of wick (m ²) ($A_w = \pi r^2$)	2.92×10^{-9}
Q_{wick} (ml/min) at anode: counter-flow mode	2.827×10^{-5}
Q_{wick} (ml/min) at anode: co-flow mode	7.450×10^{-5}
Q_{wick} (ml/min) at cathode: counter-flow mode	-2.152×10^{-4}
Q_{wick} (ml/min) at cathode: co-flow mode	3.135×10^{-4}

SD: Standard deviation

6.3.3. Polarization curves

During PEMFC operation with dry reactant gases, dry hydrogen and oxygen (or air) can be humidified by water produced in the cathode along the flow channels and then saturated near the outlet region of the gases. This is possible due to the back diffusion of water from cathode to anode at lower current densities. Therefore, in principle, it is possible to operate a fuel cell with dry gases in the correct operating conditions. In this section, polarization curves for all the configurations operated under counter-flow and co-flow modes, which were fed with dry or humidified streams as per the details given earlier in Table 6.1, are presented. Each polarization curve experiment was carried out after equilibration of the cell in galvanostatic and constant stoichiometry (anode=1.2; cathode=3) mode to maintain cell temperature of 55 °C for 8 h. The polarization data for the single cell was obtained at 55 °C at varying load current densities with hydrogen stoichiometry of 1.2 and air stoichiometry of 3, set for a current density of 0.8 A/cm².

Figure 6.5a shows the cell polarization curves for all the Configurations (B, C and D) under counter-flow mode in comparison with Configuration-A which by default is operated in counter-

flow mode. The curves are represented along with their standard deviation (SD) error bars obtained from 5 set of polarization experiments performed for each configuration. The bars represent 1 SD for each data point recorded. The comparison suggests that the open circuit voltage (OCV) remains unaffected in various configurations and stabilizes at about 0.9 V. In case of counter-flow mode of experiments, the wicking action is resisted by the opposing gas flow as predicted by theoretical calculations. This resistance is even more predominant if the gas flow rates are high as in case of configuration-C and therefore, might even stop capillary action completely. The control setup (configuration-A) after equilibration could give a maximum power density of 407 mW/cm². The potential drop at high current densities above 900 mA/cm² is due to mass transfer limitations, as the flow rate was set for a load of 0.8 A/cm². Possibility of flooding, as also reported by Pasaogullari et al. [41] and Baschuk et al. [42] above current densities of 1000 mA/cm², could also cause a sudden potential drop. At higher current densities, electro-osmotic drag becomes predominant and draws more water from the anode towards the cathode leading to flooding of cathode catalyst layers, which causes mass transport losses. Small amount of water was wicked up in case of Configuration-B even under the counter-flow mode where the maximum power density was restricted to only 344 mW/cm². This was mainly due to increased gas diffusion resistance provided by the wet wick and can also be attributed to the dry feed of hydrogen which can lead to increase in membrane resistance despite the wicking action in counter-flow mode. In case of Configuration-C, the maximum power density was measured at 465 mW/cm². This was expected, as the air stoichiometry was kept sufficiently high which would prevent any significant gas diffusion resistance and the water produced at the cathode was more uniformly distributed by the air flow over the wick thereby preventing any flooding events over the cathode. Similar improvements in performance have been reported earlier by Strickland et al. [24] and Ge et al. [38] using wicks over the cathode. Litster et al. [35] also reported performance improvements of 3.5 times with hydrophilic porous carbon cathode plates over non-porous carbon plates under dry gas operation. Configuration-D had wicking action only at the anode while wick at the cathode did not observe any capillary action. Since, both the electrodes were operated with dry feed, the performance was consistently lower than other configurations. The fuel cell performance is strongly dependent on the water content in the

membrane, which is further dependent on water activity. Local drying out of the membrane occurs as soon as the water partial pressure at the membrane/electrode interface becomes lower than its equilibrium pressure [43]. As the water supplied to the membrane remained insufficient in case of Configuration-D, most of which is attributed to the dry feed and very limited capillary rise on the anode side, the maximum power density was found to be only 297 mW/cm².

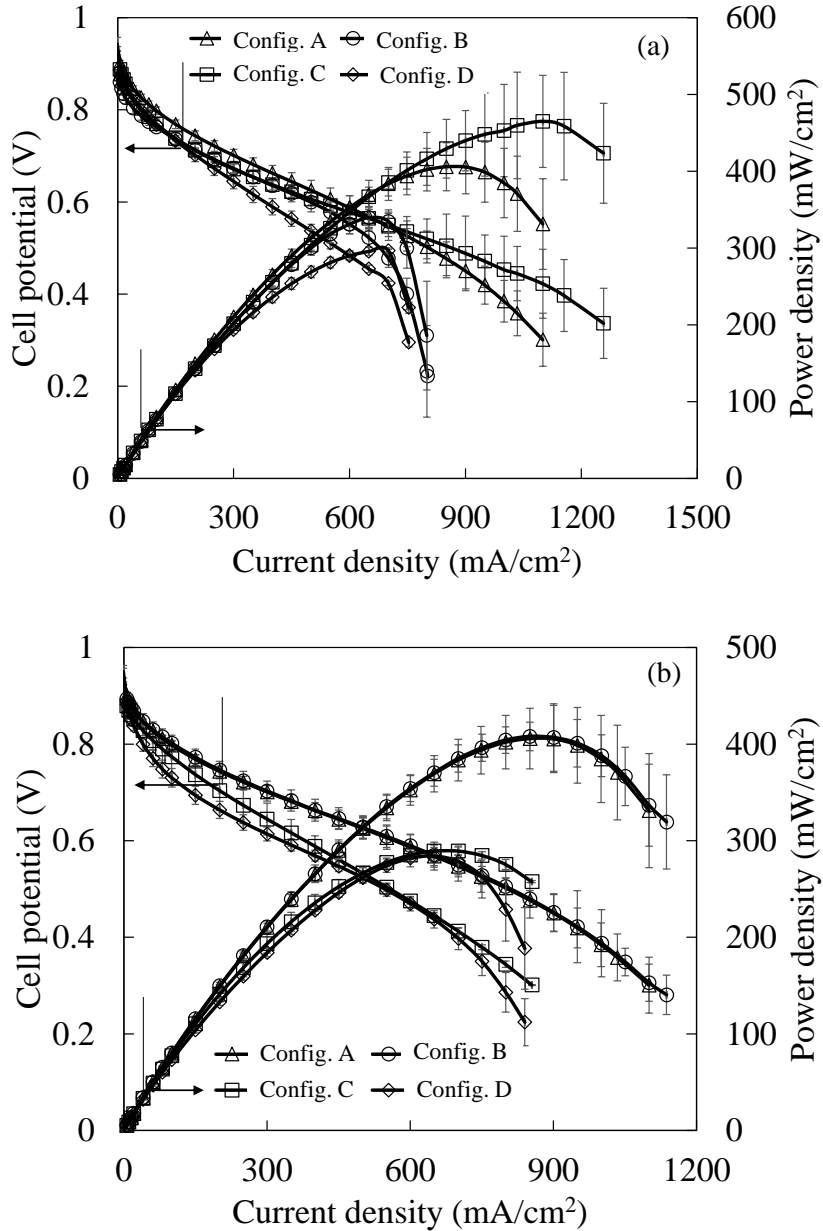


Fig. 6.5. Polarization curves for different single cell configurations at $\lambda_{H_2} = 1.2$ and $\lambda_{Air} = 3$: (a) Counter-flow mode and (b) Co-flow mode. Error bars represent the standard deviation values obtained for the set of experiments performed for each configuration.

Figure 6.5b shows the polarization curves along with their standard deviation error bars obtained for Configurations-B, C & D under co-flow mode and are compared with configuration-A. In this mode, all the configurations with wick undergo enhanced capillary action in comparison to counter-flow mode. Here, Configuration-B could match the performance of the control Configuration-A and gave a maximum power density of 409 mW/cm^2 which is attributed to the enhanced capillary action in the co-flow mode thereby providing sufficient water to the membrane for good proton conductivity. Flooding at anode is possible at low current densities ($< 300 \text{ mA/cm}^2$) where the back diffusion from cathode is predominant. Configuration-C was found to give maximum power density of nearly 284 mW/cm^2 , which was much lower than its performance observed in counter-flow mode. This can only be attributed to the possibility of flooding due to excess water transport and/or localized sluggish ORR kinetics due to ambient air and wicking water temperature, which was fed to the cathode. Configuration-D which is a combination of Configurations-B & C, did not observe any significant variation in performance from the counter-flow mode and gave a maximum power density of 285 mW/cm^2 . The most critical reason for lower performance of Configuration-D is the high gas diffusion resistance provided by the wet wick on both sides of MEA along with dry and ambient temperature feed of gases and wicking water, which leads to slower reaction kinetics at the electrodes, especially at the cathode. There needs to be a balance between the water supplied from wick and that generated or supplied from external systems in order to obtain a stable and flood-free performance that deserves further investigation in future work. It is difficult to have visual access of the internal fuel cell process which could further elucidate water transport mechanisms in wicks inside the fuel cell. However, possible diagnostic tools for further investigation include neutron imaging [45-47], X-ray radiography [48], and magnetic resonance imaging [49] for water distribution measurements or cell segmentation methods to spatially resolve flooding events [50].

6.3.4. Effect of air stoichiometry on wicking action

Air stoichiometry plays a vital role in obtaining stable and flood-free performance. Lower air stoichiometry can lead to cathode flooding while higher air stoichiometry can lead to higher compressor/pump loads. Moreover, dry feed operation becomes extremely difficult at high air

stoichiometry due to the risk of rapid membrane drying. Therefore, in principle, dry feed operation must take care of membrane hydration whilst preventing flooding of cathode. In this section, the effect of air stoichiometry on the fuel cell performance with wicks (Configuration-C) under dry air feed is studied for co-flow mode with and without external water supply. From the polarization data for the Configuration-C in co-flow mode, which was found to be much lower than counter-flow mode, it still remains unclear as to whether external water supply is required at the cathode or not for better fuel cell performance. In this regard, another set of experiments were carried out with co-flow mode in Configuration-C wherein the effect of air stoichiometry was studied for two cases:

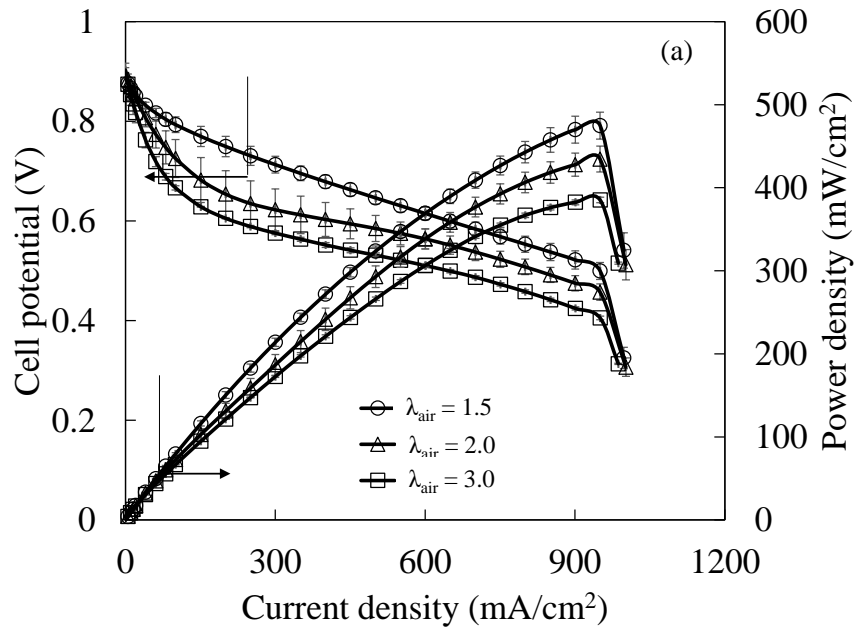
Case 1: without external water supply from trough (Configuration C_1)

Case 2: with external water supply from trough (Configuration C_2)

These cases were studied only with co-flow mode to check for the need of external water supply for cathode. Figure 6(a,b) show the polarization curves obtained at air stoichiometries of 1.5, 2 and 3 for cases 1 & 2. Interestingly for case 1, it was found that lower air stoichiometry of 1.5 showed improved performance as compared to higher air stoichiometry of 2 or 3. The maximum power density for air stoichiometry of 1.5 reached up to 475 mW/cm²; while the performance for air stoichiometry of 2 and 3 could only reach 435 mW/cm² and 385 mW/cm² respectively. The fact that higher air flow rates under dry conditions can lead to faster dehydration of the membrane thereby leading to reduced performance. Lower air flow rates help in retaining the moisture in the membrane and therefore perform better. Strickland et al. [24] also demonstrated improved fuel cell performance with in situ polymerized wicks at the cathode for a very low air stoichiometry of 1.15 using humidified gas streams. Litster et al. [35] also reported superior fuel cell performance at air stoichiometry of 1.3 using hydrophilic porous carbon plates under dry gas operation. In yet another work of Litster et al. [32], significant performance improvements were achieved using porous carbon plates integrated with external electroosmotic pump. Another interesting observation in case 1 is that the fuel cell performance at air stoichiometry of 1.5 does not see a significant decrease in the low current density region (< 300 mA/cm²) while the fuel cell operating at stoichiometries of 2 and 3 experiences this initial loss in performance. The lower performance at higher stoichiometry is hypothesized to be due to the rate of water removal

being higher at lower current densities than the rate of water generation at the cathode, which causes drying. This is an extremely interesting observation, which confirms that the cathode need not be operated with external water supply to the wick. The water produced at the cathode itself is sufficient lest the air flow rate is properly regulated.

For case 2, where external water supply was provided to the wick, the peak performance was found to be close to 300 mW/cm² for all the air stoichiometries. However, this performance was much lower than what was obtained with all air stoichiometries in case 1. This indicates that excess wicking has possibly led towards flooding of electrodes under co-flow mode in Configuration-C₂. On the contrary, the initial potential loss in the low current density region was not seen in case 2. This observation clearly points towards the need for an optimum balance required between the external water supply by wick, which is useful for low current density operation, and the water generated at the cathode at high current densities where no external water supply is required.



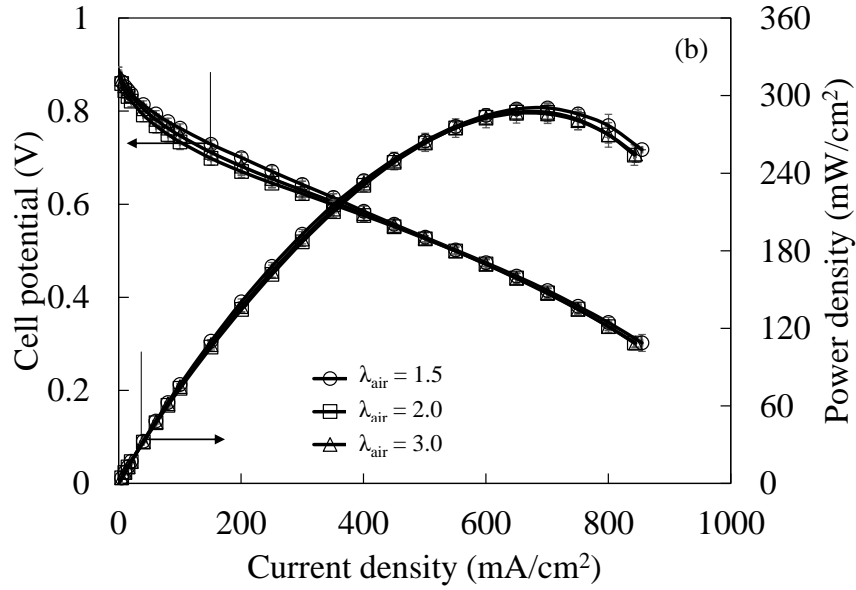


Fig. 6.6. Polarization curves for configuration-C in co-flow mode at air stoichiometry of 1.5, 2 & 3: (a) without external water supply to the wick (configuration-C₁) and (b) with external water supply to the wick (configuration-C₂). Error bars represent the standard deviation values obtained for the set of experiments performed for each air stoichiometry.

6.3.5. Electrochemical impedance spectroscopy (EIS) measurements

EIS technique can be used to distinguish between different failures in a PEM fuel cell under load conditions. Membrane dehydration reduces the proton conductivity, which can be approximated by changes in Ohmic resistances. In contrast, the impedances associated with mass transport (e.g., diffusion within the electrode layers) require simulation via distributed circuit elements whose response varies with frequency [51-54]. In this section, EIS analysis is presented by means of Nyquist plots obtained at 0.6 V with cell temperature of 55 °C in the frequency range of 0.1 Hz to 10 kHz. The equivalent circuit for the single cell is presented in Fig. 6.7. The circuit comprises of three resistances (R1, R2 and R3) associated with Ohmic resistance, charge transfer resistance at the anode and charge transfer resistance at the cathode respectively. Double layer capacitances linked to anode and cathode are represented by C1 and C2 respectively. The simulated curves based on the equivalent circuit are obtained from EC-lab software and are presented along with the experimental curves.

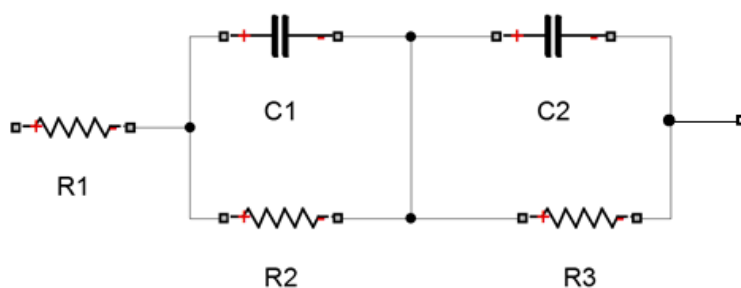


Fig. 6.7. Equivalent circuit for the Nyquist plots.

Figure 6.8(a - d) shows the Nyquist plots for different configurations under counter-flow mode along with their simulated curves. The Ohmic resistance is measured as the intersection of the curve at the high frequency with the real axis, while the charge transfer resistance is measured as the difference in the real axis intercepts at low and high frequency ends. Understandably, the Ohmic resistance, which is predominated by membrane resistance [55], is found to vary among different configurations due to the variation in amount of water supplied to the membrane in each configuration. In addition, it is obvious that the addition of wick over the active area in a fuel cell would add its internal resistance to the electron transfer within the cell and thereby would reflect in an increase of Ohmic resistance. For instance, for a 10 cm long carbon cloth having an electrical resistivity of 1.1 mOhm-cm, area specific resistance would be equal to 11 mOhm-cm², which is a very small value in comparison to the overall Ohmic resistance of the fuel cell. Therefore, in this work, the increase in Ohmic resistance is attributed majorly to the change in membrane resistance, which is dependent on moisture content of the membrane. As expected, Configuration-A offers the least Ohmic resistance followed by Configurations-B, C & D. A small increase in Ohmic resistance in case of Configuration-B is attributed to the presence of wick as well as to the small capillary rise in the wick in counter-flow mode, which could not provide sufficient water to the membrane through wick. The trend however is in good agreement with the polarization data where performance of A is maximum followed by B & C which give close to 300 mW/cm² at 0.6 V. Mérida et al. [56] proposed fuel cell failure characterization based on two frequency bands where a single frequency in each band could suffice to diagnose the failure. Large impedance variation (> 5 %) at high frequencies (> 103 Hz) can be associated with

dehydration while smaller variations (< 10 %) at low frequencies without concurrent changes at high frequencies can be associated with flooding. Based on this observation, it is seen that membrane dehydration effect is significant only in case of Configuration-D while Configuration-C undergoes minor dehydration at cell potentials close to 0.6 V. The values for the Ohmic and charge transfer resistance obtained from experimental and simulated data are given in Table 6.5. Tables 6.6 and 6.7 compare the Ohmic and charge transfer resistances respectively for different configurations along with the reasons for the observed trends. The χ^2/N (Chi^2/N) values which reflects on test of goodness of fit are also provided. Where, $\chi^2 = \sum \frac{(\text{observed-expected})^2}{\text{expected}}$ and N ($N=n-1$, where n is the number of items in a set) is the degrees of freedom. Very small values of χ^2/N indicate that the fit obtained using this equivalent circuit is the best possible fit. In addition, it is noted that both the Ohmic and charge transfer resistances observed and estimated are in good agreement. The variations seen in the charge transfer resistance are attributed to the electrode kinetics and diffusion of reactants both towards and away from the electrode, which are temperature dependent and are likely to be affected by electrode hydration levels as well [18]. In addition, it is possible for the water accumulated at the cathode to block the pores of the wick and thereby result in flooding event, which can also cause a change in the charge transfer resistance. Hence, it can be seen that in Configurations-C & D where the cathode is fed with air at ambient temperature and where dehydration effect is also observed (marked by the shift in the high frequency intercept); the charge transfer resistance is found to be much higher. The same is not seen in case of Configuration-B as the hydrogen oxidation reaction (HOR) kinetics are much faster even at lower temperatures as compared to oxygen reduction reaction (ORR).

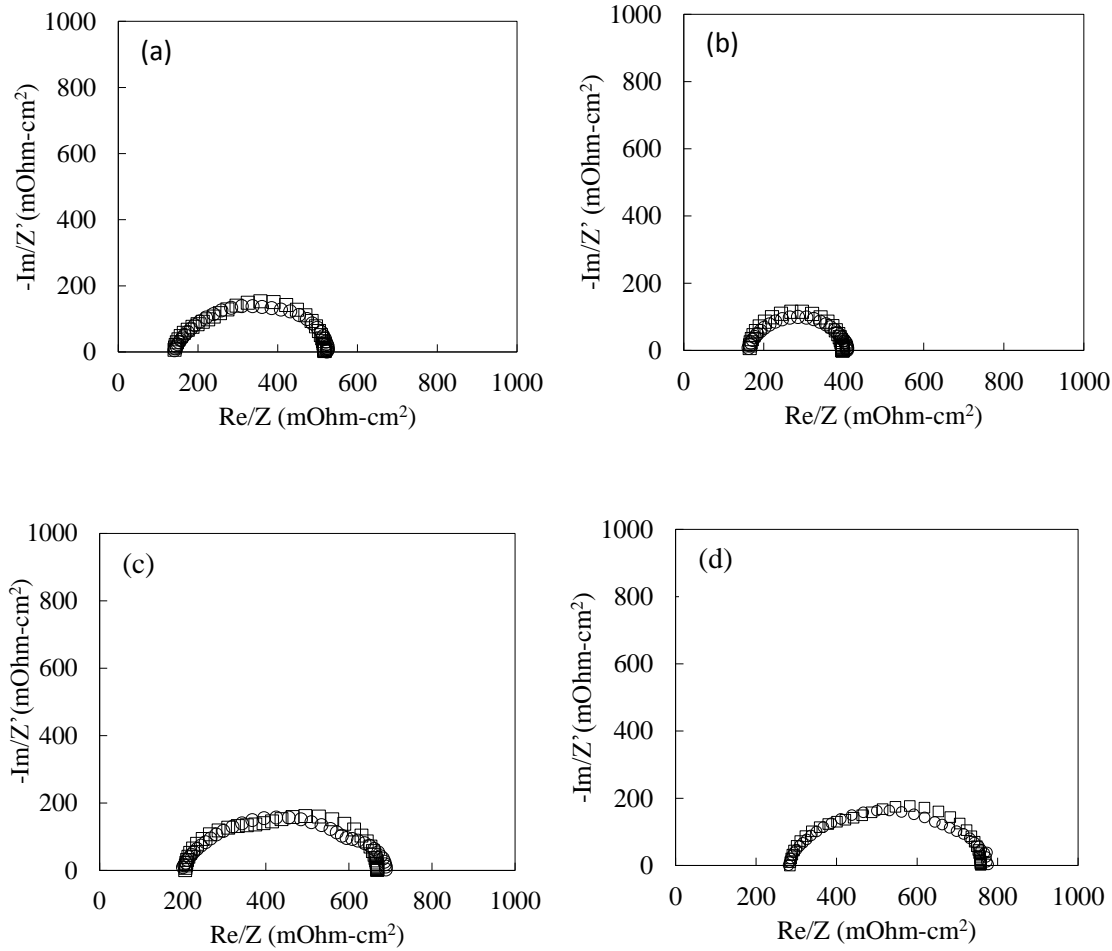


Fig. 6.8. Nyquist plots under counter-flow mode: (a) configuration-A (b) configuration-B (c) configuration-C and (d) configuration-D. Experimental data (o) and simulated curve (\square) are compared for their Ohmic resistance and charge transfer resistance values, which are the major losses incurred in the experimental setup.

Table 6.5: Experimental and simulated values of Ohmic and charge transfer resistances for different configurations.

Configuration	Counter-flow				Co-flow				$\frac{\chi^2}{N}$	
	Ohmic resistance (mOhm-cm ²)		Charge transfer resistance (mOhm-cm ²)		Ohmic resistance (mOhm-cm ²)		Charge transfer resistance (mOhm-cm ²)			
	Expt.	Sim.	Expt.	Sim.	Expt.	Sim.	Expt.	Sim.	Counter-flow	Co-flow
A	139	141	385	376	NA	NA	NA	NA	0.00125	-

B	160	164	248	233	166	169	346	338	0.00185	0.00091
C	198	206	490	462	217	221	445	434	0.00194	0.00088
D	278	283	498	475	236	249	718	678	0.00115	0.00301

Table 6.6: Comparison of Ohmic resistances between different configurations

Configuration	Counter-flow	Co-flow	Remarks
A	139	NA	This Configuration observed the lowest Ohmic resistance compared to others. This is attributed to operation of cell without wick under humid feed operation.
B	160	166	In this Configuration, the slight increase in Ohmic resistance with co-flow can be attributed to resistance contribution of wet wick at anode.
C	198	217	In this Configuration, the increase in Ohmic resistance with co-flow can be attributed to resistance contribution of wet wick at cathode. The resistance however is higher than Configuration B suggesting that MEA hydration levels were lower in this Configuration possibly due to dry feed operation at cathode.
D	278	236	In this Configuration, the decrease in Ohmic resistance with co-flow can be attributed to better hydration of MEA. The resistance however is still higher than other configurations due to resistance of wick and dry feed operation at both anode and cathode.

Table 6.7: Comparison of charge transfer resistances (CTR) between different configurations

Configuration	Counter-flow	Co-flow	Remarks
A	385	NA	The charge transfer resistance was found to be lower than Configuration-C, D and higher than Configuration-B. While a lower resistance is expected for this configuration owing to absence of wick and humid feed operation maintaining optimal conditions for fuel cell operation, the observation of higher CTR than Configuration-B is counter-intuitive and requires further investigation.
B	248	346	Configuration-B observed the lowest CTR in both flow modes possibly due to avoiding flooding at anode in this case while the cathode conditions were maintained through external humidifiers. The increase in CTR with co-flow is attributed to increase in diffusion resistance due to wet wick.
C	490	445	The increase in CTR in this configuration is attributed to the increase in diffusion resistance due to drying in counter-flow and due to flooding in co-flow mode.
D	498	718	The increase in CTR for co-flow mode is attributed to wet wick resistance to diffusion caused due to possible flooding of electrodes. In counter-flow mode, the resistance is still higher than other configurations owing to drying of electrodes under dry feed operation with minimal wicking.

For the co-flow mode, Fig. 6.9(a - d) shows the Nyquist plots for different configurations along with their simulated curves. Since enhanced wicking action is expected in co-flow mode, the Ohmic resistance is found to decrease in case of Configurations-C & D while Configuration-B does not reflect significant variation in Ohmic resistance from the counter-flow mode. The increasing order of Ohmic resistance remains as Configuration-A followed by B, C & D respectively, which is

in accordance with the polarization data. In case of charge transfer resistance, Configurations-B & D experienced significant increase from that obtained in counter-flow mode. This is again attributed to the electrode kinetics, which are affected by the ambient temperature of fuel or oxidant supplied to the fuel cell and possibly due to water rising up the wicking material at ambient temperature.

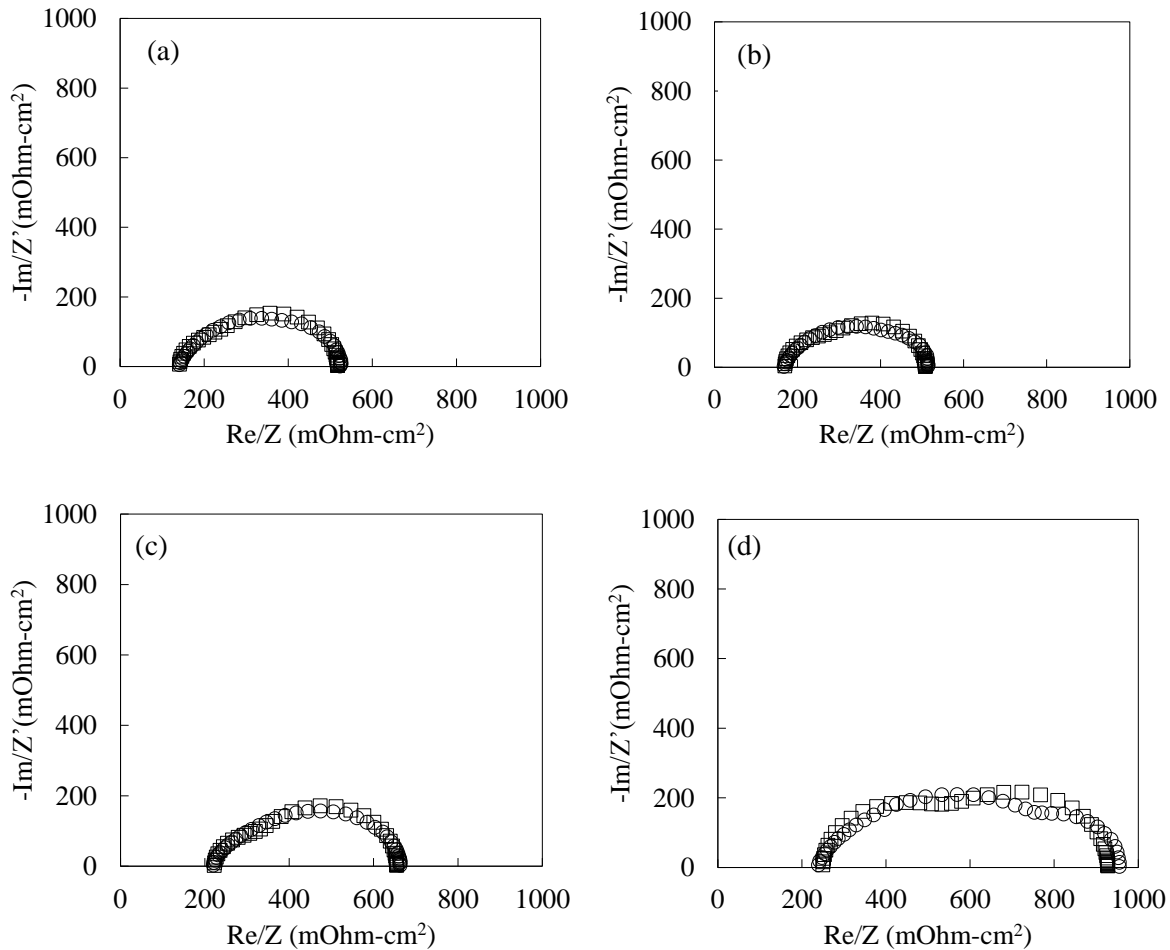


Fig. 6.9. Nyquist plots under co-flow mode: (a) Configuration-A (b) Configuration-B (c) Configuration-C and (d) Configuration-D. Experimental data (o) and simulated curve (\square) are compared for their Ohmic resistance and charge transfer resistance.

Impedance measurements were also carried out for cases 1 and 2 in configuration-C discussed earlier. Figure 6.10(a, b) show the AC impedance spectra for Configurations-C₁ & C₂ respectively. As expected, the Ohmic resistance was found to be the lowest for air stoichiometry of 1.5 for the case C1 followed by stoichiometry of 2 and 3. The same is reflected in case of charge transfer

resistance where increase in air stoichiometry increases the charge transfer resistance because of drying of electrodes under dry feed operation. Highest Ohmic resistance values obtained for air stoichiometry of 3 indicate that higher flow rate of air can be detrimental to fuel cell performance during low current densities operation under ambient dry feed in Configuration-C1. For the case C2, the Ohmic resistance was found to be similar for all the air stoichiometry, which is in accordance with the polarization data. Similar trend was observed for charge transfer resistance where the variation was found to be lower than that observed in counter-flow mode. However, as co-flow mode provides enhanced wicking action, the charge transfer resistance was found to be higher than that of counter-flow mode due to the ambient water temperature, which can reduce the ORR kinetics.

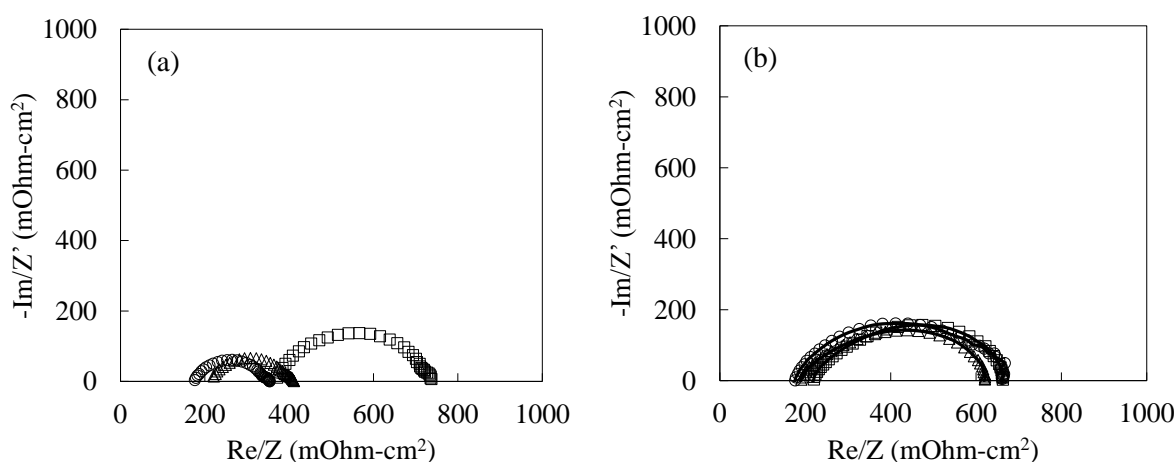


Fig. 6.10. Nyquist plots for configuration (a) C₁ and (b) C₂ compared at air stoichiometry of 1.5 (o), 2 (Δ) and 3 (\square).

6.4. Conclusions

The concept of wick-based humidification is derived based on the principle of evaporative cooling, which can render simultaneous humidification, and cooling of PEM fuel cells. The water produced at the cathode is found to be sufficient for stable flood-free performance under dry air feed in Configuration-C. Compact arrangement of trough in the present study can also facilitate wick based humidification at the anode (Configuration-B) giving a peak power density of 409 mW/cm² in co-flow mode which is comparable to the control which gives 408 mW/cm². Configuration-D does not show performance comparable to Configuration-A in both the flow

modes. The primary reason for this behavior is the dry ambient temperature feed of gases along with ambient wicking water temperature, which leads to sluggish reaction kinetics. In addition, as having wick on both sides of MEA provides some diffusion resistance due to extended path before reaching the catalyst layer; the limiting current densities were always found to be lower than other configurations. The possibility of flooding due to excess wicking could only arise in case of co-flow mode. Thus, Configurations-C & D perform poorly at high current densities in the co-flow mode. Performance loss is more predominant in the low current density region for Configurations-C & D in the co-flow mode whereas the same is not observed in case of counter-flow mode. The stoichiometric variation study shows that wick based technique can provide better water management at very low air stoichiometry of 1.5 in the PEM fuel cell. The hydration levels of the membrane in each configuration is confirmed by means of variation in Ohmic resistance through electrochemical impedance spectroscopy. The variation in charge transfer resistance between different configurations is attributed to the dry & ambient temperature feed of gases, water wicked up at room temperature, and to the membrane hydration levels.

The proposed humidification technique in order to operate under dry feed with Configuration-D needs further investigation and insight into the water flow regimes inside the cell. In addition to identifying these transport mechanisms, ongoing work is focused on scaling up this methodology to fuel cell stacks and leveraging composite designs of wicks to enable high performance dry gas operation with Configuration-D. Work is under progress to couple this technique for achieving simultaneous cooling through controlled evaporation of water over the wick surface inside the fuel cell.

References

- [1] S. Gottesfeld, T.A. Zawodzinski, *Advances in Electrochemical Science and Engineering*, Volume 5, Wiley-VCH Verlag GmbH, Weinheim, Germany, doi: 10.1002/9783527616794. ch4.
- [2] D. Papageorgopoulos, *An Introduction to the 2010 Fuel Cell Pre-Solicitation Workshop in: DOE fuel cell technologies program overview*. Department of Energy, Lakewood, Colorado, 2010.

- [3] C. Gittleman, D. Masten, S. Jorgensen, J. Waldecker, S. Hirano, M. Mehall, Automotive fuel cell R&D needs in: DOE fuel cell pre-solicitation workshop. Department of Energy, Lakewood, Colorado, 2010.
- [4] J.M.L. Canut, R.M. Abouatallah, D.A. Harrington, Detection of Membrane Drying, Fuel Cell Flooding, and Anode Catalyst Poisoning on PEMFC Stacks by Electrochemical Impedance Spectroscopy, *J. Electrochem. Soc.* 153 (2006) A857-A864.
- [5] T.V. Nguyen, M.W. Knobbe, A liquid water management strategy for PEM fuel cell stacks, *J. Power Sources* 114 (2003) 70-79.
- [6] H. Li, Y. Tang, Z. Wang, Z. Shi, S. Wu, D. Song, J. Zhang, K. Fatih, J. Zhang, H. Wang, Z. Liu, R. Abouatallah, A. Mazza, A review of water flooding issues in the proton exchange membrane fuel cell, *J. Power Sources* 178 (2008) 103-117.
- [7] J.R. Yu, T. Matsuura, Y. Yoshikawa, M.N. Islam, M. Hori, Lifetime behavior of a PEM fuel cell with low humidification of feed stream, *Phys. Chem. Chem. Phys.* 7 (2005) 373-378.
- [8] N.Y. Steiner, P. Mocoteguy, D. Candusso, D. Hissel, A. Hernandez, A. Aslanides, A review on PEM voltage degradation associated with water management: Impacts, influent factors and characterization, *J. Power Sources* 183 (2008) 260-274.
- [9] T.A. Zawodzinski, C. Derouin, S. Radzinski, R.J. Sherman, V.T. Smith, T.E. Springer, S. Gottesfeld, Water Uptake by and Transport Through Nafion® 117 Membranes, *J. Electrochem. Soc.* 140 (1993) 1041-1047.
- [10] Y. Wang, K.S. Chen, J. Mishler, S.C. Cho, X.C. Adroher, A review of polymer electrolyte membrane fuel cells: Technology, applications, and needs on fundamental research, *Applied Energy* 88 (2011) 981-1007.
- [11] F.N. Buchi, S. Srinivasan, Operating Proton Exchange Membrane Fuel Cells Without External Humidification of the Reactant Gases Fundamental Aspects, *J. Electrochem. Soc.* 144 (1997) 2767-2772.
- [12] X. Li, I. Sabir, J. Park, A flow channel design procedure for PEM fuel cells with effective water removal, *J. Power Sources* 163 (2007) 933-942.
- [13] D.P. Wilkinson, H.H. Voss, K. Prater, Water management and stack design for solid polymer fuel cells, *J. Power Sources* 49 (1994) 117-127.

- [14] R.K. Ahluwalia, X. Wang, A. Rousseau, R. Kumar, Fuel economy of hydrogen fuel cell vehicles, *J. Power Sources* 130 (2004) 192-201.
- [15] Y. Sone, P. Ekdunge, D. Simonsson, Proton Conductivity of Nafion 117 as Measured by a Four-Electrode AC Impedance Method, *J. Electrochem. Soc.* 143 (1996) 1254-1259.
- [16] J. Larminie, A. Dicks, M.S. McDonald. *Fuel cell systems explained*. New York: Wiley, 2003.
- [17] F. Barbir, *PEM Fuel Cells Theory and Practice*, 2nd Edition, Academic Press 2013.
- [18] J. Stumper, M. Löhr, S. Hamada, Diagnostic tools for liquid water in PEM fuel cells, *J. Power Sources* 143 (2005) 150-157.
- [19] F. Barbir, H. Gorgun, X. Wang, Relationship between pressure drop and cell resistance as a diagnostic tool for PEM fuel cells, *J. Power Sources* 141 (2005) 96-101.
- [20] D. Natarajan, T.V. Nguyen, Current distribution in PEM fuel cells. Part 1: Oxygen and fuel flow rate effects, *AIChE Journal* 51 (2005) 2587-2598.
- [21] H. Meng, C.Y. Wang, Model of Two-Phase Flow and Flooding Dynamics in Polymer Electrolyte Fuel Cells, *J. Electrochem. Soc.* 152 (2005) A1733-A1741.
- [22] M. Ji, Z. Wei, A Review of Water Management in Polymer Electrolyte Membrane Fuel Cells, *Energies* 2 (2009) 1057-1106.
- [23] T.V. Nguyen, M.W. Knobbe, C.K. Dyer, A liquid water management strategy for PEM fuel cell stacks, *J. Power Sources* 114 (2003) 70-79.
- [24] D.G. Strickland, J.G. Santiago, In situ-polymerized wicks for passive water management in proton exchange membrane fuel cells, *J. Power Sources* 195 (2010) 1667-1675.
- [25] S.G. Goebel, Evaporative cooled fuel cell, General Motors Corporation, U.S. Patent 6,960,404 B2 (2005).
- [26] P. David, Fuel cell direct water injection, Intelligent Energy Ltd., EP 1530813 B (2012).
- [27] J.G. Santiago, J. Posner, F.B. Prinz, T. Fabian, J. Eaton, S.W. Cha, C. Buie, D. Kim, H. Tsuru, J. Sasahara, T. Kubota, Y. Saito, Fuel cell with electroosmotic pump, The board of trustees of the Leland Stanford Junior University and Honda Motors Co. Ltd., US Patent 7,799,453 (2010).
- [28] G. Vyas, Y.M. Mikhail, T.A Trabold, Hydrophilic layer on flowfield for water management in PEM fuel cell, GM Global Technology Operations LLC, US8211592 B2 (2012).

- [29] G.V. Dadheech, M.J. Lukitsch, Carbon based bipolar plate coatings for effective water management, GM Global Technology Operations LLC, US8685593 B2 (2014).
- [30] J.S. Yi, J.D.L. Yang, C. King, Water management along the flow channels of PEM fuel cells, *AIChE J.* 50 (2004) 2594-2603.
- [31] C.R. Buie, J.D. Posner, T. Fabian, C.A. Suk-Won, D. Kim, F.B. Prinz, J.K. Eaton, J.G. Santiago, Water management in proton exchange membrane fuel cells using integrated electroosmotic pumping, *J. Power Sources* 161 (2006) 191-202.
- [32] S. Litster, C.R. Buie, T. Fabian, J.K. Eaton, J.G. Santiago, Active Water Management for PEM Fuel Cells, *J. Electrochem. Soc.* 154 (2007) B1049-B1058.
- [33] T. Fabian, R. O'Hayre, S. Litster, F.B. Prinz, J.G. Santiago, Active water management at the cathode of a planar air-breathing polymer electrolyte membrane fuel cell using an electroosmotic pump, *J. Power Sources* 195 (2010) 3640 – 3644.
- [34] T. Fabian, R. O'Hayre, S. Litster, F.B. Prinz, J.G. Santiago, Passive water management at the cathode of a planar air-breathing proton exchange membrane fuel cell, *J. Power Sources* 195 (2010) 3201 – 3206.
- [35] S. Litster, J.G. Santiago, Dry gas operation of proton exchange membrane fuel cells with parallel channels: Non-porous versus porous plates, *J. Power Sources* 188 (2009) 82 – 88.
- [36] R. Eckl, W. Zehntner, C. Leu, U. Wagner, Experimental analysis of water management in a self-humidifying polymer electrolyte fuel cell stack, *J. Power Sources* 138 (2004) 137 – 144.
- [37] S.H. Ge, X.G. Li, I.M. Hsing, Internally humidified polymer electrolyte fuel cells using water absorbing sponge, *Electrochim. Acta* 50 (2005) 1909-1916.
- [38] S.H. Ge, X.G. Li, I.M. Hsing, Water Management in PEMFCs Using Absorbent Wicks, *J. Electrochem. Soc.* 151 (2004) B523-B528.
- [39] K.S. Muralidhara, S. Sreenivasan, Thermal Degradation Kinetic Data of Polyester, Cotton and Polyester-Cotton Blended Textile Material, *World App. Sci.* 11 (2010) 184-189.
- [40] N. Abidi, E. Hequet, Characterization of cotton fibers using TGA and FTIR, *The World Cotton Research Conference – 4*, 2007.
- [41] U. Pasaogullari, C.Y. Wang, Liquid Water Transport in Gas Diffusion Layer of Polymer Electrolyte Fuel Cells, *J. Electrochem. Soc.* 151 (2004) A399–A406.

- [42] J.J. Baschuk, X.H. Li, Modelling of polymer electrolyte membrane fuel cells with variable degrees of water flooding, *J. Power Sources* 86 (2000) 181–196.
- [43] T. E. Springer, T. A. Zawodzinski, and S. Gottesfeld, Polymer Electrolyte Fuel Cell Model, *J. Electrochem. Soc.* 138 (1991) 2334–2342.
- [44] M. Pérez-Page, V. Pérez-Herranz, Effect of the Operation and Humidification Temperatures on the Performance of a Pem Fuel Cell Stack on Dead-End Mode, *Int. J. Electrochem. Sci.*, 6 (2011) 492 – 505.
- [45] R. Satija, D.L. Jacobson, M. Arif, S.A. Werner, In situ neutron imaging technique for evaluation of water management systems in operating PEM fuel cells, *J. Power Sources* 129 (2004) 238–245.
- [46] M.A. Hickner, N.P. Siegel, K.S. Chen, D.S. Hussey, D.L. Jacobson, M. Arif, In Situ High-Resolution Neutron Radiography of Cross-Sectional Liquid Water Profiles in Proton Exchange Membrane Fuel Cells, *J. Electrochem. Soc.* 155 (2008) B427–B434.
- [47] A. Turhan, K. Heller, J.S. Brenizer, M.M. Mench, Passive control of liquid water storage and distribution in a PEFC through flow-field design, *J. Power Sources* 180 (2008) 773–783.
- [48] C. Hartnig, I. Manke, R. Kuhn, S. Kleinau, J. Goebbels, J. Banhart, High-resolution in-plane investigation of the water evolution and transport in PEM fuel cells, *J. Power Sources* 188 (2009) 468–474.
- [49] S. Tsushima, K. Teranishi, S. Hirai, Magnetic Resonance Imaging of the Water Distribution within a Polymer Electrolyte Membrane in Fuel Cells, *Electrochem. Solid State* 7 (2004) A269–A272.
- [50] D.G. Strickland, S. Litster, J.G. Santiago, Current distribution in polymer electrolyte membrane fuel cell with active water management, *J. Power Sources* 174 (2007) 272–281.
- [51] D.R. Franceschetti, J.R. McDonanld, Diffusion of neutral and charged species under small-signal a.c. conditions, *J. Electroanal. Chem.* 101 (1979) 307–316.
- [52] J.R. Macdonald, Binary electrolyte small-signal frequency response, *J. Electroanal. Chem.* 53 (1974) 1–55.
- [53] J.R. Macdonald, Simplified impedance/frequency-response results for intrinsically conducting solids and liquids, *J. Chem. Phys.* 61 (1974) 3977–3996.

- [54] J.R. Macdonald, D.R. Franceschetti, Theory of small-signal ac response of solids and liquids with recombining mobile charge, *J. Chem. Phys.* 68 (1978) 1614–1637.
- [55] J. Zhang, L. Zhang, C.W.B. Bezerra, H. Li, Z. Xia, J. Zhang, A.L.B. Marques, E.P. Marques, EIS-assisted performance analysis of non-noble metal electrocatalyst (Fe–N/C)-based PEM fuel cells in the temperature range of 23–80 °C, *Electrochimica Acta*, 54 (2009) 1737-1743.
- [56] W. Mérida, D.A. Harrington, J.M. Le Canut, G. McLean, Characterisation of proton exchange membrane fuel cell (PEMFC) failures via electrochemical impedance spectroscopy, *J. Power Sources*, 161 (2006) 264–274.

Chapter 7

Conclusions and Future Scope

This chapter aims to highlight the salient conclusions of the research work on membrane-based active humidification and wick-based passive humidification of PEM fuel cells described in this thesis. In addition, based on the present understanding of the two means of humidification, certain perspectives on future scope for research work is presented.

7.1. Membrane-based active humidification

Membrane-based gas humidification was studied to facilitate humidifier design guidelines based on thorough understanding of

- coupling of heat and mass transport
- dual phase equilibria due to liquid-vapor permeation (LVP)
- role of membrane microstructure

Two types of membrane systems (dense and asymmetric) were studied each of which pave way for further research work.

7.1.1. Dense hollow fiber membranes

Nafion® based dense hollow fiber membranes are widely used for gas humidification. Despite the several models proposed in literature over the last decade, a comprehensive understanding of the mechanisms involved in a water-to-gas Nafion® membrane humidifier has remained elusive.

Water transport in Nafion® is dependent on the physical state of water (liquid or vapor) it is in equilibrium with. A phenomenon known as the Schroeder's paradox is reported to be prevalent for water sorption capacity of polymeric membranes including Nafion®. We have shown that, in the case of LVP, equilibrium at the membrane-gas interface was better captured by a modified form of Henry's law (Eq. (2)) as proposed by Monroe et al. [1] and the temperature dependent

membrane-water equilibrium sorption can be adequately modeled using an empirical correlation (Eq. (1)).

$$C_{\max}^{\text{liq}} = -99467.411 + 5312.483T_w - 70.255T_w^2 + 0.313T_w^3 \quad \dots\dots\dots(1)$$

$$P_{\text{eq}} = P_{v,\text{sat}} \frac{C_L}{C_{\max}^{\text{liq}}} \quad \dots\dots\dots(2)$$

A microscopic transport model for heat and mass exchange between water side and gas stream via Nafion® hollow fiber membranes was proposed. The heat transport took into the account evaporation of water, conduction within the membrane and convection at the interfaces along with the sensible heat due to moisture addition. The mass transport took into account the diffusion within the membrane and the convection at the interfaces. Dependence of specific heat of air on humidity was also invoked in the model. All the material, geometric and operational parameters were built into the model to realize their roles on humidification performance.

Key conclusions of the model are:

- The performance of the humidifier is limited by the residence time i.e., larger the residence time, better is the outlet gas temperature and humidity.
- Non-dimensionalization of the governing equations results in 11 dimensionless numbers which provide insights into the dominant processes affecting gas humidification.
- Heat transport is limited by the membrane-gas interfacial resistance.
- Mass transport is limited largely by diffusion in the membrane but has a significant contribution from interfacial resistance as well. The contributions of diffusion and interfacial resistance change with air flow rate. At very low air flow rates (~10 L/min for the membrane modules described in this work), interfacial resistance is limiting whereas at extremely high air flow rates (~1000 L/min), diffusion is the limiting process. At all other intermediate flow rates, both resistances govern the transport.
- For dimensionless tube length $\xi \leq 1$, mass transport is limited by residence time of gas in tubes. For $\xi > 1$, the mass transport is limited by the time scale for convection.
- Sensible heat of moisture has a negligible contribution in increasing outlet gas temperature.

- The coupled mass transport is suggested to be responsible for enhancing the convective heat transport at the membrane-gas interface as evidenced from the need for a correction factor of 2.3 in the overall heat transfer coefficient. This conclusion is in agreement with the works of Karlsson et al. [43] and Rautenbach et al. [44].

7.1.2. Asymmetric hollow membranes

Nafion based hollow fiber membrane humidifiers besides being costly were also observed to have a very low trans-membrane pressure (TMP) tolerance of just 5 psi [2]. In PEM fuel cell operation, typical operating pressures can range from 0 to 2.5 bar(g). Thus, using Nafion based hollow fiber membrane humidifiers are not always suitable for PEM fuel cell operation.

Through this research work, we proposed to develop indigenous membrane humidifiers which can address the issues of high cost and poor pressure tolerance of Nafion-based membrane humidifiers. Intuitively it is expected that by opting for a cost-effective polymer and increasing the membrane thickness, the issue of cost and poor pressure tolerance can be alleviated. However, a thick membrane means a higher heat and mass transport resistance. Thus, the membranes had to be porous. Additionally, a porous hydrophilic membrane like polyacrylonitrile would mean that liquid water could entrain into the gas stream. Thus, a partially hydrophobic asymmetric hollow fiber polymeric membranes made of polysulfone was hypothesized to address all the major issues associated with developing cost-effective and high TMP tolerant membranes for gas humidification. We showed that polysulfone hollow fiber membranes can be tuned for its skin and bulk porosity by varying the polymer concentration and spinning parameters.

Asymmetric polysulfone hollow fiber membranes were characterized for their bulk and skin porosities using gravimetric and pore size distribution analysis respectively. Both the porosities were found to decrease with increasing polymer concentration. For low polymer concentration of 25 wt%, SEM analysis observed the formation of cracks/skin defects at the outer boundary of the hollow fiber, thus leading to water entrainment in the gas stream. Higher polymer concentrations of 27 and 30 wt% were immune to such skin defects and provided entrainment free humidification performance. The humidifier performance with the three tested polymer

concentration was in the order HFM25>HFM27>HFM30. Fig. 7.1. below shows the test results of a single fuel cell (active area of 100 cm²) tested with the developed humidifiers and compared with the conventional bubble humidification. As can be seen from the figure, in the operating voltage range of the fuel cell i.e. 0.6-0.7 V, the fuel cell performance obtained with HFM27 is comparable with the conventional method of bubble humidification. HFM30 is observed to give low fuel cell performance due to its lower humidification effectiveness than HFM27. We could not test HFM25 humidifier for fuel cell testing due to issues faced with liquid water entrainment.

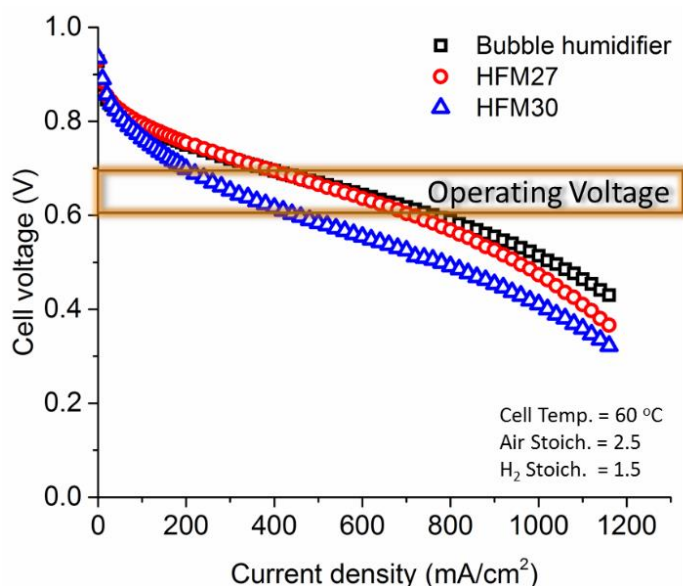


Fig. 7.1. Fuel cell performance comparison with different humidification systems (a) Bubble humidifier (black markers) (b) HFM27 (red markers) and (c) HFM30 (blue markers)

In terms of cost, a component-wise comparison is presented in Table 7.1 between our in-house developed humidifiers and other commercial benchmarks available today. The cost estimated for our humidifiers is based on the cost of membrane development with our own spinning setup as well as other commercially available polysulfone ultrafiltration membranes [3]. All other component costs are standard cost of the material available in the market. Based on the comparison, it is evident that the cost-performance benefit with polysulfone-based hollow fiber membrane humidifiers offers a lucrative option for gas humidification applications.

Table 7.1: Cost comparison of different membrane humidifiers

Humidifier Type	Nafion Based	Silicone Based	Polysulfone Based
Membrane cost	Nafion \$ 500/m ²	PDMS \$ 111/m ²	Polysulfone \$ 6 – 20/m ²
Housing cost	Polycarbonate \$ 6/m ²	Polycarbonate \$ 6/m ²	Polyvinyl chloride \$ 5/m ²
Potting cost	Epoxy \$10/kg	Polyurethane \$3/kg	Epoxy \$10/kg
TMP tolerance	0.4 bars	3 bars	> 7 bars
Lowest Net Cost/Module	\$ 500 – 740 Membrane area: 0.19 m ² Supplier: Perma Pure	\$ 350 - 400 Membrane area: 0.25 m ² Supplier: PermSelect	\$ 60 - 80 Membrane area: 0.25 m ²

7.1.2.1 Model development for asymmetric membrane humidifiers

In order to derive optimal performance from the in-house developed humidifiers, a mathematical model as a design guideline tool was developed taking into account the coupled heat and mass transport, the framework for which was built into the dense membrane model. In addition, the dual phase equilibria and the role of membrane microstructure were critical to the model development. While the membrane-gas interface was modeled using Eq. (2), the membrane-water interface was modeled using Eq. (3) under the assumption that membrane pores are filled with liquid water due to the pre-treatment protocol introduced in our work.

$$C_{\max}^{\text{liq}} = \frac{\theta \rho_w}{M_w} + \frac{s p_p (1-\theta)}{M_w} \dots\dots\dots (3)$$

The role of membrane microstructure in mass transport across the membrane was modelled with a resistance-in-series approach as shown in Fig. 7.2. The skin resistance was modelled as a parallel combination of transport through the nano-pores and the diffusion across the dense portion of the skin. The bulk resistance was modelled by quantifying the contribution of macrovoids to bulk porosity through image processing of the SEM micrographs. For HFM25, macrovoid contribution was present near both the skins, whereas for HFM27 and HFM30, macrovoid contribution was limited to near the tube side skin alone. In general, the resistance of the smaller pores in the bulk was dominant over the macrovoids. Since heat transport is largely limited by interfacial resistance, the effective thermal conduction through the membrane was modelled using a simple correlation (Eq. (4)) provided in the literature for heat transport through porous media [4].

$$k_m = k_w^\theta \times k_p^{1-\theta} \dots\dots\dots(4)$$

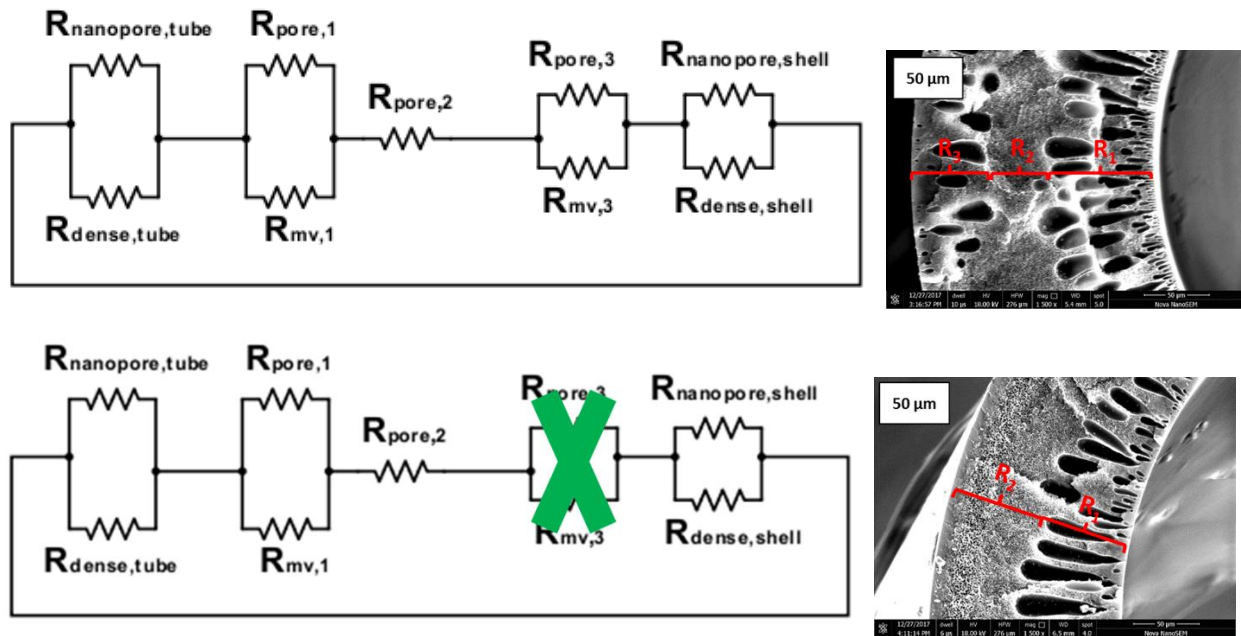


Fig. 7.2. Resistance-on-series model for (a) HFM25, (b) HFM27 / HFM30

Finally, the developed model along with the experimental data on pore size distribution, gravimetric measurements and SEM images of the hollow fiber membranes, allowed us to obtain excellent model fits to the humidification test data. Once the model was validated with different membrane microstructures, we tested its efficacy with rigorous validation over a series of experiments verifying the effect of different geometric and operating parameters.

The following key conclusions are drawn based on the experimental data and model predictions.

- The humidification performance decreased with decreasing membrane bulk and skin porosity.
- The humidification performance increases with increasing membrane area. However, beyond certain area the performance can be limited by decrease in the convective coefficients.
- With increasing polymer concentration from HFM25:HFM27:HFM30,
 - Skin resistance (s/m) to water transport increases in the ratio 1 : 1.77 : 1.81
 - Bulk resistance (s/m) to water transport increases in the ratio 1 : 1.10 : 1.79
 - Effective diffusivity (m^2/s) of water in membrane decreases in the ratio 2.36 : 1.6 : 1
 - Effective thermal conductivity (W/mK) of membrane decreases in the ratio 3 : 2 : 1
- Mass transport is limited more by membrane resistance than by interfacial resistance.
- With our humidifiers, at 5 L/min gas flow rate, obtaining an outlet gas RH of 75 – 100 % requires the following membrane properties
 - Polysulfone concentration of 27 wt%
 - Membrane thickness of 150 – 200 μm
 - Defect-free skin thickness of 200 – 400 nm
 - Bulk porosity of 50 – 55 %

7.1.2.2 Flow distribution in HFM humidifiers

Flow distribution was simulated using CFD simulations for multiple tube arrangements which provided insights into the effect of symmetry and header design. In general, it was observed that a random tube arrangement, especially at low packing fractions, could lead to severe flow maldistribution. An improvement in the symmetry of tube arrangement was shown to alleviate flow maldistribution both on tube and shell side. The flow distribution was found to be a cumulative effect of the flow developed in the headers and tubes. In general, larger the eddy formation in the headers, larger was flow maldistribution. Formation of dead volume inside the shell due to present humidifier design can be minimized by redesigning the headers to

accommodate inlet/outlet ports for shell side flow. Further work is required to provide quantifiable design guidelines.

7.2. Wick-based passive humidification

Passive humidification in PEM fuel cells offers huge advantage in terms of reducing parasitic power loss, system simplification and ease of operation. Among different passive humidification techniques, wick-based passive humidification offers advantage of uniform distribution of water over the entire active area and thereby aid in flooding prevention. In this thesis, we have proposed a novel wick based technique based on carbon cloth which is used for an active area of 100 cm^2 . We showed that the technique could be used in different configurations which allows for dry-feed operation of PEM fuel cell at either one or both the electrodes. The configurations tested in our research are described in Table 6.1 on page 179. It was found that the water generated at the cathode was sufficient for stable flood-free performance under dry air feed with Configuration-C. Configuration-B under co-flow mode also performed comparable to the control test cell. Only Configuration-D suffered from drop in performance in both the flow modes due to dry-free operation and water wicking at ambient temperature. Additionally, in co-flow mode, the performance could also be limited due to increased resistance to gas diffusion in the GDL and catalyst layer possibly due to presence of capillary driven liquid water. The stoichiometric variation of air in Configuration-C1 (without external water supply) resulted in achieving higher performance at a low air stoichiometry of 1.5. This suggests that at higher air stoichiometry, the rate of dehydration of the CCL and membrane is possibly higher than the rate of water generation and distribution, thereby significantly increasing the Ohmic resistance. This was also verified using electrochemical impedance spectroscopy (EIS), which clearly showed a drastic shift in the high frequency intercept in the Nyquist plot for air stoichiometry of 3. The hydration and flooding events were recorded with EIS measurements and were found to verify the variations observed under fuel cell polarization tests.

7.3. Future Scope

Based on the work presented in this thesis and the understanding developed over the course of this research work, we provide future perspectives and scope for furthering the research in each of the topics studied.

7.3.1. Dense Nafion™ hollow fiber membrane humidifier

The microscopic model developed for a Nafion™ hollow fiber membrane humidifier in this thesis is a comprehensive tool for predicting humidifier performance from a given set of geometric and operating conditions. However, while designing new humidifiers, often the task is to estimate the membrane area that would be required for achieving the desired outlet gas conditions. Hence, we propose that a humidifier manufacturer can be provided by design charts as shown in Fig. 7.3. The solid black line represents the model predictions for varying membrane area operating at 650 lpm of gas flow rate and water inlet temperature of 60 °C. The upper and lower bounds in the performance curve are represented by dashed blue and red lines for 1000 and 10 lpm respectively. For a particular desired set of outlet gas conditions, thermal and humidity effectiveness parameters can be calculated (see Eqs. (30-31) in chapter 4) a priori which is represented on the y-axis of the charts. Based on the operating conditions of water temperature and gas flow rate, a line parallel to x-axis intercepting the y-axis on the known value of effectiveness factor and intersecting the curve corresponding to the chosen gas flow rate would determine the required membrane area. For instance, for achieving a thermal and humidity effectiveness of 70% with a gas flow rate of 650 L/min and water temperature of 60 °C, one would need a membrane area of 0.38 m². However, since mass transport is governed largely by diffusion resistance, the humidity effectiveness increases sharply upon increasing the membrane area. Whereas, heat transport is limited by interfacial resistance and hence increase only gradually with increase in membrane area. For instance, 80 % humidity effectiveness can be achieved with a membrane area of 0.5 m², which consequently leads to a thermal effectiveness of only 75 %. Thus, achieving a higher thermal effectiveness would require a higher membrane area than that would be required for achieving similar humidity effectiveness. Once a series of similar graphs are developed for a wide range of operating conditions, the same can be used as a humidifier design guide.

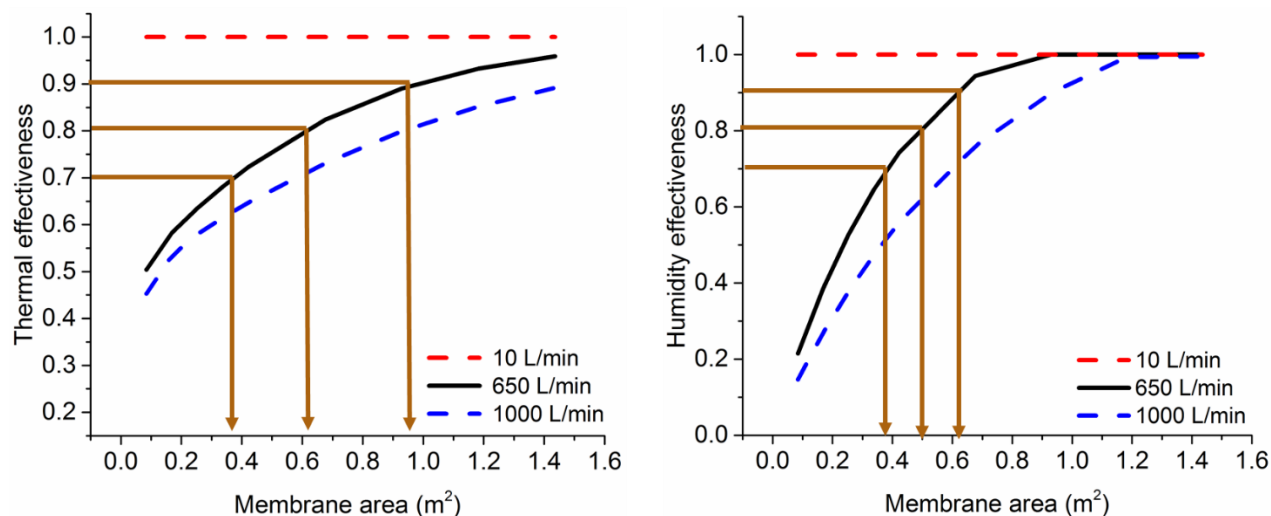


Fig. 7.3. Utility of the model. The black lines are the model predictions. The dashed red and blue lines represent the upper and lower bounds respectively for a wide range of flow conditions. In all cases, the water flow rate is 1/25th of air flow rate.

7.3.2. Asymmetric polysulfone membrane humidifier

Asymmetric membranes developed for membrane humidifiers have been tested for gas humidification in PEM fuel cell operation. With the current lab-scale humidifier design, issues like flow maldistribution, quality control at high membrane area, and entrainment issues with high performing humidifier HFM25 are to be addressed to bridge the gap between lab to market. At present, we have been able to develop humidifiers with a capacity of handling gas flow rates of 100 L/min. The next target is to address the above mentioned issues and scale up the membrane area for handling gas flow rates in excess of 1000 L/min without compromising the humidification performance. The target for successful humidifier development for PEM fuel cell application is shown schematically in Fig. 7.4.

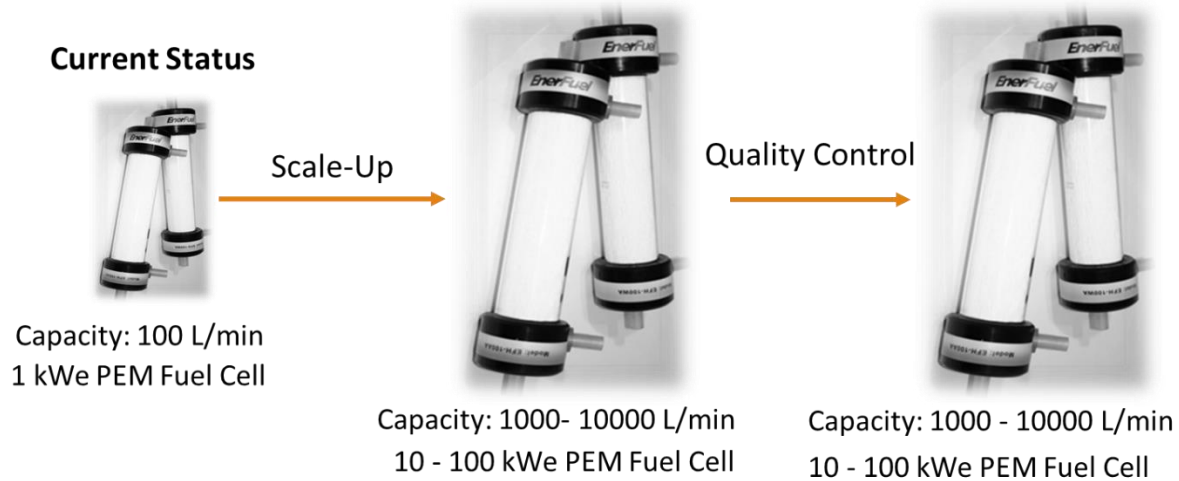


Fig. 7.4. Challenges to be addressed for asymmetric HFM humidifiers

The following directions could be helpful in addressing the issues:

- For flow distribution on tube side, a higher packing fraction along with use of spacers or guiders for tube placement can help improve symmetry and reduce flow maldistribution.
- For flow distribution on shell side, a modified header design as shown in Fig. 7.5. below, can help minimize the dead volume. The header design can be optimized further by additional CFD simulations.
- For quality control and eliminating the performance loss due to pin holes or defective skin, a dense hydrophilic polymer coating (thin film of few nm) or an in-situ gel formation to plug the pin-holes/defects could be investigated. A resultant composite membrane is also likely to have higher durability by virtue of delaying the fouling inside pores.
- Using the model to develop membranes for specific desired outlet gas conditions for different applications like ambient air humidification, respiratory medical devices etc.

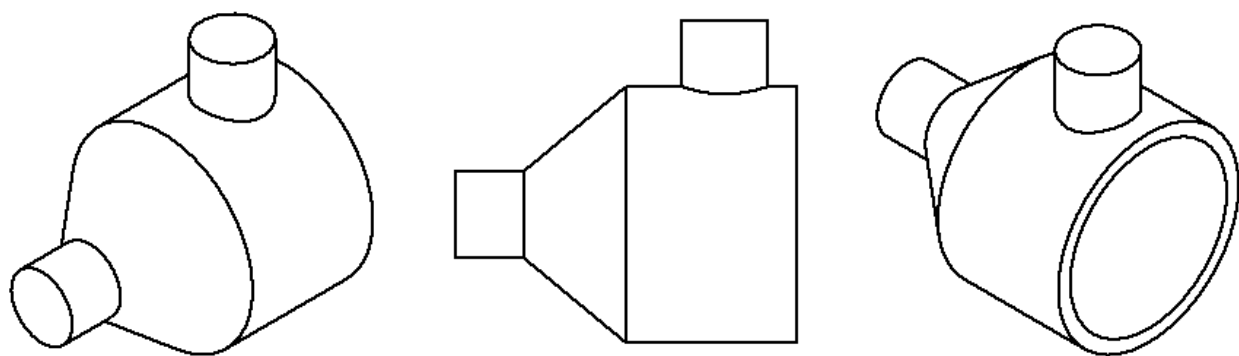


Fig. 7.5. Proposed header design for minimizing dead volume and improving flow distribution. The figure is not drawn to scale. The dimensions will be based on the flow capacity.

7.3.3. Wick based passive humidification

Passive humidification based on the proposed technique needs to be tested for larger fuel cell stacks. Additionally, the evaporative cooling potential of this technique also needs investigation. The challenges that the technique poses for scale up are:

- Preventing shorting of cells due to presence of conducting wicks in the same water header. The header design is critical in this regard. Compartmentalization of the header for anode and cathode wicks could alleviate this issue.
- Improving the hydrophilicity of the carbon cloth needs further investigation. This will facilitate rapid wicking and aid in better water management. Functionalization of carbon cloth can aid in improving the hydrophilicity.
- Larger stacks can be tested with Configuration-C1 at low air stoichiometry of 1.5. This alone will reduce the parasitic power loss significantly.

References

- [1] C.W. Monroe, T. Romero, W. Mérida, M. Eikerling, A vaporization-exchange model for water sorption and flux in Nafion, J. Memb. Sci. 324 (2008) 1–6. doi:10.1016/j.memsci.2008.05.080.
- [2] FC series humidifier datasheet, Perma Pure LLC..

- [3] S.-K. Park, E.A. Cho, I.-H. Oh, Characteristics of membrane humidifiers for polymer electrolyte membrane fuel cells, Korean J. Chem. Eng. 22 (2005) 877–881. doi:10.1007/BF02705668.
- [4] R. Pandey, B. Pesala, Heat and Mass Transfer Analysis of a Pot-in-Pot Refrigerator Using Reynolds Flow Model, J. Therm. Sci. Eng. Appl. 8 (2016) 031006. doi:10.1115/1.4033010.

List of Publications

1. R. Pandey and A.K. Lele, Modelling of Water-to-Gas Hollow Fiber Membrane Humidifier, Chemical Engineering Science Journal (2018) 192, 955-971. DOI:10.1016/j.ces.2018.08.015
2. R. Pandey, H. Agarwal, B. Saravanan, P. Sridhar and S.D. Bhat, Internal Humidification in PEM Fuel Cells Using Wick Based Water Transport, Journal of Electrochemical Society (2015) 162, F1000-F1010. DOI: 10.1149/2.0621509jes
3. R. Pandey and A.K. Lele, Experimental Investigation and Modelling of Asymmetric Hollow Fiber Membranes for Gas Humidification. (Manuscript under preparation)

Other Publications

1. R. Pandey and B. Pasela, Heat and Mass Transfer Analysis of a Pot-in-Pot Refrigerator Using Reynolds Flow Model, Journal of Thermal Science and Engineering Applications (2016) 8(3), 031006. DOI: 10.1115/1.4033010.
2. H. Agarwal, R. Pandey, S.D. Bhat, Improved polymer electrolyte fuel cell performance with membrane electrode assemblies using modified metallic plate: Comparative study on impact of various coatings, International Journal of Hydrogen Energy, DOI: 10.1016/j.ijhydene.2019.05.243.

Patents

1. R. Pandey, H. Agarwal, R. Kumar, P. Sridhar, S.D. Bhat, Internal humidification in low temperature PEM fuel cell by means of a wick, EP 3164 902 B1 (Granted)
2. R. Pandey, Asymmetric hollow fiber membranes for gas humidification, Indian Patent Application published online (No. 201611018484).